SPATIALLY STRUCTURED WAVES AND OSCILLATIONS IN NEURONAL NETWORKS WITH SYNAPTIC DEPRESSION AND ADAPTATION

by

Zachary Peter Kilpatrick

A dissertation submitted to the faculty of
The University of Utah
in partial fulfillment of the requirements for the degree of

Doctor of Philosophy

Department of Mathematics

The University of Utah

August 2010

ProQuest LLC
789 East Eisenhower Parkway
P.O. Box 1346
Ann Arbor, MI 48106-1346

The University of Utah Graduate School

STATEMENT OF DISSERTATION APPROVAL

The dissertation of **Zachary Peter Kilpatrick**

has been approved by the following supervisory committee members:

Paul Bressloff	, Chair	**4/12/2010** Date Approved
James Keener	, Member	**4/12/2010** Date Approved
Aaron Fogelson	, Member	**4/12/2010** Date Approved
Alla Borisyuk	, Member	**4/12/2010** Date Approved
Alessandra Angelucci	, Member	**4/14/2010** Date Approved

and by **Aaron Bertram**, Chair of the Department of **Mathematics**

and by Charles A. Wight, Dean of The Graduate School.

ABSTRACT

We analyze the spatiotemporal dynamics of systems of nonlocal integro–differential equations, which all represent neuronal networks with synaptic depression and spike frequency adaptation. These networks support a wide range of spatially structured waves, pulses, and oscillations, which are suggestive of phenomena seen in cortical slice experiments and *in vivo*. In a one–dimensional network with synaptic depression and adaptation, we study traveling waves, standing bumps, and synchronous oscillations. We find that adaptation plays a minor role in determining the speed of waves; the dynamics are dominated by depression. Spatially structured oscillations arise in parameter regimes when the space–clamped version of the network supports limit cycles. Analyzing standing bumps in the network with only depression, we find the stability of bumps is determined by the spectrum of a piecewise smooth operator. We extend these results to a two–dimensional network with only depression. Here, when the space–clamped network supports limit cycles, both target wave emitting oscillating cores and spiral waves arise in the spatially extended network. When additive noise is included, the network supports oscillations for a wider range of parameters. In the high–gain limit of the firing rate function, single target waves and standing bumps exist in the network. We then proceed to study binocular rivalry in a competitive neuronal network with synaptic depression. The network consists of two separate populations each corresponding to cells receiving input from a single eye. Different regions in these populations respond preferentially to a particular stimulus orientation. In a space–clamped version of the model, we identify a binocular rivalry state with limit cycles, whose period we can compute analytically using a fast–slow analysis. In the spatially–extended model, we study rivalry as the destabilization of double bumps, using the piecewise smooth stability analysis we developed for the single population model. Finally, we study the effect of inhomogeneities in the spatial connectivity of a neuronal network with linear adaptation. Periodic modulation of synaptic connections leads to an effective reduction in the speed of traveling pulses and even wave propagation failure when inhomogeneities have sufficiently large amplitude or period.

To my mom and dad who made a world of possibilities available to me, who always made sure I finished my homework, and who have given selflessly to me all my life.

CONTENTS

NOTATION AND SYMBOLS

$\mathbb{R}^n$	n–dimensional Euclidean space
$\mathbb{C}^n$	n–dimensional complex Euclidean space
$\mathcal{C}^n(\mathbb{R},\mathbb{R})$	Bounded, n–times continuously differentiable functions $f:\mathbb{R}\to\mathbb{R}$
$\mathcal{C}^n(\mathbb{R},\mathbb{C})$	Bounded, n–times continuously differentiable functions $f:\mathbb{R}\to\mathbb{C}$
Θ	Standard Heaviside function
δ	Dirac delta distribution
$\widehat{w}$	Hankel transform of the function w
J_ν	Bessel function of the first kind of order ν
I_ν	Modified Bessel function of the first kind of order ν
K_ν	Modified Bessel function of the second kind of order ν
exp	Exponential function e^x
$\mathbf{x}$	General vector in one– or two–dimensional space
x	One–dimensional spatial scalar
$\mathbf{r}$	Two–dimensional spatial vector set in polar coordinates
$u * v$	Convolution of u and v
$\mathcal{L}$	General linear operator
$\dot{g}$	Derivative of the function g
∇^2	Laplace operator
∇^4	Biharmonic operator

ACKNOWLEDGMENTS

Thanks to all the faculty and staff who have made my journey at the math department nurturing and enlightening by teaching great courses, getting me to conferences, and keeping my mind open to the boundlessness of mathematical research. Most of all, I would like to thank my advisor Paul Bressloff for his patience with me, for the frequent discussions we had to develop this work, and his constant guidance with my academic development. From the beginning, he has had a genuine willingness to work with me on exciting research. Thanks also to Jim Keener for his feedback and creative input whenever I brought research questions to him. In the mathematical biology program at Utah, there have been many colleagues that contributed to this work through informal chats, listening to practice talks, and constant encouragement including Jay Newby, Karin Leiderman, Lindsay Crowl, Courtney Davis, Elizabeth Copene, Will Nesse, Darci Taylor, and Berton Earnshaw.

Beyond the University of Utah, several people and institutions have supported me during the development of this work. In particular, I would like to thank the faculty, staff, postdocs, and graduate students at the Oxford Centre for Collaborative Applied Mathematics for the lovely two months I spent there. Conversations with other great researchers in the field of mathematical neuroscience have sparked ideas and polished results within this dissertation. Among them are Bill Troy, Stefanos Folias, Bard Ermentrout, Carlo Laing, Steve Coombes, and Markus Owen. In addition, both Steve Cox and Mark Embree at Rice University contributed greatly by giving me my start in academic research and pointing me in the right direction thereafter.

For my wonderfully supportive and caring family I have the deepest gratitude and love: my mom for being such a patient and compassionate listener whose humility amazes me; my dad for his loving advice, humor, and encouragement; Elisabeth for showing me what it means to have a big heart and honing my early math skills with the number guessing game and problems on the chalkboard; Charlie for always talking nerd-speak with me and never rubbing it in that he is way smarter than I am; and Alexandra for putting up with me way more than I deserve, being kind to me, and constantly checking in on me.

For Natalie, I am so thankful for your love, support, excitement, light-hearted humor, and ability to get my head out of "math–mode" for much needed respite. I owe much of my sanity to you reminding me a great deal of this world exists outside of my office. My life is richer since the day we met at brunch.

Thanks to the National Science Foundation for funding my education and research (NSF grants IGERT 0217424, RTG 0354259, and DMS 0813677).

CHAPTER 1

INTRODUCTION

The model one should use to describe phenomena of the brain largely depends upon the question one wishes to answer. There is an enormous wealth of models available for describing the currents, action potentials, firing rates, local field potentials, and electroencephalogram data one observes in experiment [87, 39]. The Hodgkin–Huxley model has been a very successful model for quantifying conduction of an action potential of a single neuron in certain cases [65]. However, there remain myriad other neural phenomena that have no definitive model attached to them. This is not to say that the many available models are poor descriptions of the biological situations they wish to mimic, simply that the appropriateness of each model is largely context dependent. There exist no equations in neuroscience that have the widespread definitive applicability that the Navier–Stokes equations do in fluid mechanics.

Often, a neural system can be modeled in a number of ways. For example, when modeling a very large network of neurons ($10^6 - 10^{11}$), one approach is to represent the detailed properties of every single neuron within the network [74, 112]. These models consider what kind of ionic currents each neuron possesses, how many synapses a neuron makes with its neighbors, and the precise temporal profile of the action potential. As a result, numerical simulations of such a system can be quite impressive, in that they readout thousands of membrane potential traces and give "data" that looks a great deal like a biological experiment. Usually such models allow one to manipulate the equations much faster and easier than one could the true biological system. Also, such methods do have the advantage of stating that they attempt to remain as true to the details of the biological system as possible. However, a closer look at such efforts reveals that there is no way to certainly quantify, in practice, all the specific characteristics of each neuron within a real network. Even if one could know all of these quantities and reconstruct the network within the confines of a physically accurate system of equations, simulating such a network may not inform one anymore than the biological system. The problem has not been

simplified in any way. An alternative approach is to use techniques of applied mathematics and informed intuition to distill out the essential properties of the large network of neurons to yield a simplified system of mean field equations [180, 39]. In essence, one represents the network as an excitable continuum, rather than a collection of discrete objects (i.e. the neurons). Rather than keeping track of the entirety of the network's microstructure, a mean field approach is concerned only with the coarse–grained structure of the network. The behavior of these models can then represent the type of activity witnessed on a coarser scale than the single neuron [25, 136, 67, 141]. Additionally, such models are more amenable to mathematical analysis and arguably inform the theorist much more than a massive system that can be simulated only numerically. This is due to the fact that one can often then find relationships between biologically pertinent parameters and different behaviors of the model [136, 92, 79].

In this dissertation, we analyze a series of models of the latter, mean field type. In doing so, we are able to recover many behaviors that have been observed experimentally in networks of neurons [83, 27, 79, 80, 81, 82].

1.1 Neurons, networks, and negative feedback

Neurons are the fundamental cells of the brain. Many brain functions employ a neuron's ability to generate electrical pulses called action potentials or spikes [31]. These action potentials occur due to rapid changes in their internal concentration of certain ions (i.e. potassium, sodium, and chloride) [65]. A neuron is activated upon the opening of some of its ionic channels (i.e. sodium), which leads to a flow of ions into the cell and a displacement of the membrane potential from its resting value, a depolarization. Quite quickly, the change in voltage will result in other ion channels opening (i.e. potassium), allowing those ions to flow out, which will counteract this depolarization and bring the internal ionic concentrations back to their baseline level. Thus, an action potential is completed.

The complicated signaling in the brain relies on an extensive structure of connections between individual neurons, called synapses [153]. The average neuron makes synaptic connections with roughly 7,000 of its neighbors [134]. While there are many different kinds of synapses, we will be primarily concerned with two categories for this thesis: excitatory and inhibitory. Neurons with excitatory synapses make their neighbors more likely to fire action potentials when activated. Neurons with inhibitory synapses make their neighbors less likely to fire when activated. Many studies have found, in general, the likelihood of

a neuron being connected to its neighbor often depends on the distance between the two neurons [181, 105, 153]. Networks of even a few neurons, some excitatory some inhibitory, can lead to very complicated dynamics when stimulated or allowed to fire spontaneously [31]. Thus, to understand the brain, it is important to not simply study neurons in isolation, but within the architecture of intricate network connectivity.

Whether in the brain or isolated in slices, large networks of neurons can support well structured spatiotemporal activity [51, 126, 32, 182]. In this disseration, we are mainly concerned with activity that arises in the presence of minimal inhibitory connections. Therefore, there must be some form of negative feedback other that inhibition that leads to nonmonotonic spatial structure of activity like traveling pulses and oscillations. We will discuss two main types of local negative feedback. Mostly, we study the effects of synaptic depression [169]. In particular, short–term synaptic depression, is the process by which resources in the synapse are exhausted due to continual usage [113, 189]. These resources can include neurotransmitter like glutamate, vesicles that hold the neurotransmitter, or scaffolding proteins which fix vesicles to the active zone of the presynapse. As these resources are used up, the synapse becomes less effective at transmitting its signal from the presynaptic to the postsynaptic neuron. Thus synaptic depression is a mechanism for curtailing the positive feedback of excitatory connections in a network in the absence of any inhibition [164, 66, 80]. Additionally, spike frequency adaptation acts as a negative feedback mechanism by reducing the maximal firing rate of a neuron [109, 162]. Essentially, some hyperpolarizing ionic current is activated due to the repetitive firing of a neuron. For example, voltage activated calcium channels may bring in calcium which switches on a shunting potassium current. As a result, the neuron requires more input to fire [9]. Both synaptic depression and adaptation follow dynamics at least an order of magnitude slower than the membrane time constant of a neuron (10ms). It has recently been proposed that in cortical networks with minimal inhibition, depression and adaptation may be ideal mechanisms for generating different types of spatially structured activity such as traveling pulses, spiral waves, and self–sustained oscillations [136, 67, 144, 57, 93, 79]. We will now describe in detail the generation and functional purpose of such phenomena as observed in experiment.

1.2 Cortical network dynamics in experiment

The advent of more accurate methods of recording neural activity has allowed the observation of more intricate spatiotemporal activity in neuronal networks. Since voltage–sensitive dye imaging was pioneered over forty years ago, experimentalists have begun using it more frequently for a highly responsive characterization of coarse–grained membrane potential in large networks of neurons [38, 182]. Additionally, multielectrode techniques continue to improve to allow many neurons' membrane potentials to be simultaneously resolved [139]. A great deal of information concerning working memory, epilepsy, sensory coding, and motor control has been collected using these ever improving experimental methods [58, 46, 183, 147, 67, 184]. We review a number of these findings below.

1.2.1 Standing pulses or bumps

Persistent, localized regions of neural activity have been proposed as substrates of several memory and sensory processes in the brain. Experiments in primate prefrontal cortex show that sensory cues can often lead to spatially localized groups of neurons persistently firing during the delay period of an oculomotor–delayed response task [58, 125]. Monkeys are usually trained in such experiments to fixate on a central spot on a display monitor, on which a peripheral cue is presented in some area of the screen. The stimulus is then removed and the monkey must wait a second before making a saccadic eye movement to the position of the target. Electrode recordings of the monkey's prefrontal cortex suggest that the position of the peripheral cue is encoded as a "bump" of activity localized to a specific group of neurons. This bump of activity disappears once the task is complete. Both experimentalists and theoreticians have been interested in studying this phenomenon because it is a clear example of neural activity that is not simply representing sensory stimuli, but remembering it [177, 95, 99, 144, 42].

It has also been suggested that the brain may keep the eyes still by representing eye position as an activity bump in the medial vestibular nucleus (MVN) and the prepositus hypoglossi (PH) [152]. Essentially, the MVN and PH maintain a memory of eye position based on the position of the bump. In order that the eyes be held in place, this memory is then read out by motor neurons in the abducens and oculomotor nuclei. These nuclei in turn control the extraocular muscles. Thus, bumps are useful for not only maintaining positions of visual stimuli, but also for maintaining working motor memory.

Finally, visual stimuli, fed from the retina through the lateral geniculate nucleus, to the primary visual cortex (V1) are often represented as bumps within local regions of V1.

Although the stimulus itself may be a bump of activity, due to some preprocessing in early visual region, the recurrent connections and V1 provide further sharpening of the stimulus due to the orientation selectivity of recurrent connections [8, 54].

In general, it is presumed that stationary bumps of activity in cortex rely on a lateral inhibition structure of synaptic connectivity. That is, excitatory neurons in a network exhibiting bumps have short–range connections and inhibitory neurons have longer range connections. In addition, Wang has proposed that the excitatory neurons in networks that support persistent bumps of activity must be dominated by a slow synaptic component [177]. This is due to the fact that there is interplay between local negative feedback, like spike frequency adaptation and synaptic depression, and the excitatory synaptic dynamics. Therefore, Wang suggests that slow NMDA receptors dominate dynamics in these working memory networks. The verification of the precise mechanisms for bumps is an ongoing research area.

1.2.2 Self–sustained oscillations

Neuronal oscillations are a ubiquitous feature of many networks of the brain [31]. Their suggested roles include temporally binding sensory neurons into assemblies [158, 142], memory consolidation during sleep [70, 114], and epileptic seizures [126]. Spatially localized oscillations arise both *in vivo* and *in vitro* and may be observed experimentally using multielectrode arrays or voltage–sensitive dye imaging [182].

A variety of sensory stimuli have been linked to oscillations *in vivo* [51, 100]. For example, studies of vertebrate and invertebrate olfactory bulbs have shown odor stimuli can elicit oscillations [101]. Similarly, a small visual stimulus can evoke oscillations in visual cortex, one way of addressing the problem of binding different pieces of a visual image together [158, 184]. Populations of neurons that respond to parts of a stimulus with the same features may oscillate synchronously [142, 10]. Binocular rivalry stimuli can also generate oscillations in the firing rate of neurons in the visual cortex [13]. When two different stimuli are presented to either eye, such as differently oriented gratings, the neurons in V1 corresponding to either eye may switch back and forth between possessing the dominant firing rate. This is thought to be a measurable substrate of the perceived phenomenon of either image actually being seen by the subject [103]. In the auditory cortex, oscillating ensembles are a hallmark of sound response as well [100]. Since oscillations carry with them a characteristic time–scale, they are a prime code for storage of time–dependent

signals like sound.

Such organizing activity in the brain has been purported to play a role in both working and long term memory [86]. Whether or not large–scale brain oscillations are epiphenomena or the cause of such events remains an open question in many cases. The encoding of new information as well as the retrieval of long–term memory is reflected by the period of oscillations [86]. Recall of a previous memory is often accompanied by an increase in oscillatory power [151]. There must likely be some negative feedback mechanism in existence to stabilize and generate persistent oscillations over a period of seconds. Both experiment and modeling continue to devote efforts to understanding the mechanisms that generate sustained oscillations [32].

Pathological phenomena, like epileptic seizures, have also been linked to self–sustained oscillations. Electrophysiology has been used to study epilepsy in humans as well as animal models, and seizures are usually accompanied by measurable structured oscillations in population activity. In fact, the nature of such oscillations as recorded by electroencephalagram can indicate the nature of the seizure mechanism [102]. As in cortical slice studies, some seizures have hallmark electrical activity traces consisting of focused localized synchronous oscillations that emit traveling pulses [126]. Thus, it is useful to understand the mechanisms behind population oscillations in large scale neuronal networks due to their important functional and pathological implications.

1.2.3 Traveling waves

Traveling waves of electrical activity have been observed *in vivo* in a number of sensory and motor cortical areas [182]. Such waves are often seen during periods without sensory stimulation; the subsequent presentation of a stimulus then induces a switch to synchronous oscillatory behavior [51]. Waves can also arise from spatially localized groups of neurons whose population activity oscillates around 1–10Hz [183, 126]; each oscillation cycle may emit elevated activity that propagates as a traveling plane wave [183, 37, 67, 182]. A common experimental paradigm is to record electrical activity *in vitro* using thin slices of cortical tissue, in which inhibition has been suppressed by blocking GABA_A receptors with an antagonist such as bicuculline [37, 183, 141, 139]. Synchronized discharges can then be evoked by a weak electrical stimulus from any site on the cortical slice. Following rapid vertical propagation, each discharge propagates away from the stimulus in both horizontal directions at a mean velocity of about $6 - 9$ cm/s.

A variety of sensorimotor stimuli and tasks have been linked to propagating waves *in*

vivo. For example, a number of studies of vertebrate and invertebrate olfactory bulbs have shown odor stimuli can elicit oscillations and propagating waves [101, 46]. Similarly, a small visual stimulus can evoke a propagating wave in visual cortex [140, 184, 10, 64], and stimulating a single whisker can trigger a wave in rat barrel cortex [135]. Spatiotemporal activity is not only a neural correlate of sensory stimuli, but can also precede motor commands. For example, evoked waves have been found in monkey motor cortex during movement preparation and execution [145]. Several organizing mechanisms for such spatiotemporal activity have been suggested, including a single pacemaker oscillator exciting successive neighbors in an excitable network, or coupled oscillators propagating gradual phase delays in space [51, 182]. Traveling waves are also a characteristic feature of certain neurological disorders in humans including epilepsy [118]. Therefore, investigating the mechanisms underlying wave propagation in neural tissue is important for understanding both normal and pathological brain states. Although the conditions for wave propagation may differ from the intact cortex due to the removal of some long–range connections during slice preparation, the *in vitro* slice is more amenable to pharmacological manipulation and to multielectrode recordings.

Kleinfeld and colleagues studied the presence of waves of electrical activity in the terrestrial mollusk's procerebral lobe, largely responsible for olfaction [85]. Groups of neurons oscillate at the same frequency and a phase shift propagates through the network as a wave. Interestingly, application of an odor stimulus leads to a quick transition from traveling waves to synchronous activity. Thus, Ermentrout and Kleinfeld hypothesize that traveling waves may act as a "searchlight" for novel stimuli [51]. When an input arrives, time and location of the stimulus may be marked by a unique phase in the continuum of phase–shifts of the wave. Traveling pulses are an ideal construct for scanning cortex since only a fraction of cortex is rendered inactive at any given time.

The Pinto lab has extensively studied excitable traveling waves, also known as epileptiform events, in rodent cortical slices [136, 139]. Excitable waves occur when activity spreads across subthreshold neural tissue as a pulse or front. Recently Pinto and colleagues sought to understand the characteristics of different stages of this epileptiform activity in thalamocortical slice as pictured in Figure 1.1. They found that initiation of waves is an all–or–none event with a sharp threshold. Functional architecture of excitatory connections determines the threshold of activity required for wave onset. When the stimulus is near threshold, the delay between application of the stimulus and initiation is variable. The

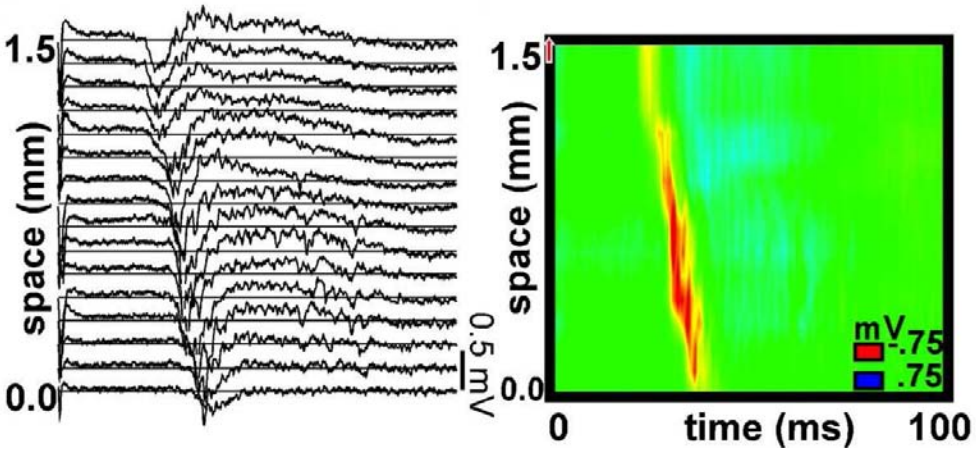

Figure 1.1. Traveling pulse of activity in local field potential recordings following electrode stimulation in a slice from rat somatosensory cortex. The slice was bathed in picrotoxin to block most inhibitory connections. (Left) Raw electrode recordings and (Right) pseudo-color plot show the data are relatively invariant along a space–time characteristic. Adapted from [139]. Compare with Figure 2.4, which models this phenomenon in a network with synaptic depression and spike frequency adaptation.

velocity and amplitude of waves seem to be unaffected by stimulus amplitude, so long as it is above threshold and the wave is initiated far enough from the recording sites. Termination of waves is a strong depolarizing shift and recovery of all neurons involved in superthreshold activity. This may arise from a combination of intrinsic single neuron recovery or excessive inhibition at the population level. Another possibility is that cortical waves may fail when entering a region of the neural medium that is sufficiently inhomogeneous in its synaptic connection architecture [20, 83]. Thus, waves in cortical slice can reveal a great deal about the physiological basis of epileptiform event phases.

Cortical waves can exhibit more exotic properties than simply initiating, propagating, and terminating. Recently, Xu and colleagues studied whether cortical waves can cross the border of the primary (V1) and secondary (V2) areas of visual cortex, using optical imaging on rats [184]. Drifting gratings visually evoked propagating activity in the monocular area of V1. When the wave reached V2, it was "compressed," the pulse width decreased, and sometimes another wave propagated backwards into V1. This only occurred for visually evoked waves, not spontaneous waves, which suggests that the mechanism for this activity is related to visual processing. Studying area–dependent changes to spatiotemporal activity, such as this, may be another means for revealing how different areas of the brain transfer

information between one another.

1.2.4 Spiral waves

Huang and colleagues explored the emergence of spiral waves of neural activity in a recent study in tangentially cut slices of rat neocortex [67]. As discussed in section 1.2.3, experiments employing slices cut normal to the surface of the cortex often produce unidirectionally propagating waves [37, 33, 183, 139]. Due to the use of a voltage sensitive dye technique, it was possible for them to recover an accurate spatiotemporal signal of average membrane potential in two dimensions. As pictured in Figure 1.2, Huang and colleagues found that 4–15Hz oscillations spontaneously arose within the slice, following the application of bicuculline and carbachol to block inhibition. Both plane waves, ring waves, and irregular waves would arise intially due to spatially localized oscillating cores. However, the interaction of these propagating waves would often eventually lead to spiral waves that could last for up to 30 cycles.

Spiral waves may be a means to spatially organize extensive episodes of periodic activity. Recently, Schiff and colleagues showed that the organization of spatiotemporal activity into a spiral wave effectively reduces the dimensionality of the dynamics [148]. As with traveling waves, spiral waves may be a mechanism for binding sensory information together in a spatially connected region of cortex. Such organization may also extend the duration of the activity and in *vivo* contribute to seizure generation. Since they arise in networks without inhibition, some local feedback mechanism, such as synaptic depression or spike frequency adaptation, must be employed as an alternative to interneurons' role in curtailing excitatory activity.

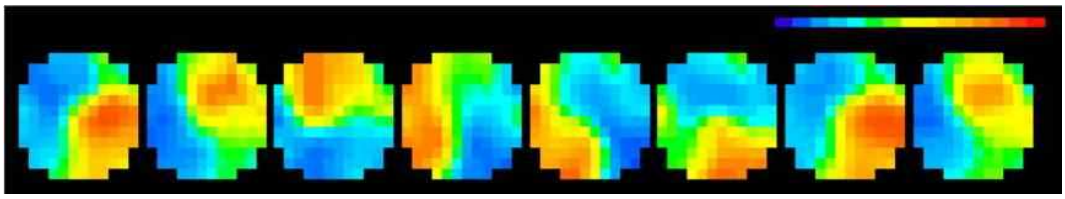

Figure 1.2. Spiral wave of activity in a tangential slice of rat neocortex. Color follows the linear scale in the top right and represents the amplitude of a voltage sensitive dye signal read by an array of optical detectors. Adapted from [67]. Compare with Figure 3.8, which models this phenomenon in a neuronal network with synaptic depression.

1.3 Cortical network models

There have been many theoretical studies regarding stationary pulses or bumps, traveling waves, spiral waves, self–sustained oscillations, and other spatially structured solutions using spatially extended firing rate models of cortical tissue [181, 3, 25, 136, 67, 55, 39, 5, 168]. Often, networks are studied on an infinite domain, which is a reasonable approximation that makes these models amenable to analysis. Despite individual neurons being discrete objects, the assumption that these networks are continuous is justified when examining large–scale networks of $10^6 - 10^9$ neurons containing 10^5 neurons per 1 mm^2. Ignoring boundary effects is reasonable when the space occupied by the modeled brain activity is relatively smaller than the entirety of the network. This is indeed the case for standing bumps, traveling pulses, and localized oscillations. Also, due to the capacitive nature of individual neurons, one usually assumes activity evolves according to first order dynamics. Other assumptions are sometimes necessary, in order to study the existence and stability of standing and traveling waves, which we will discuss as they arise.

Perhaps the most studied equations that describe a spatially extended neuronal network are those derived by Wilson and Cowan [180, 181]. They represent the time evolution of synaptic drive to excitatory and inhibitory populations and are coupled nonlocally to one another in space

$$\tau_e \frac{\partial u_e}{\partial t} = -u_e + w_{ee} * f(u_e) - w_{ei} * f(u_i), \tag{1.1a}$$

$$\tau_i \frac{\partial u_i}{\partial t} = -u_i + w_{ie} * f(u_e) - w_{ii} * f(u_i), \tag{1.1b}$$

where

$$\left(w_{ab} * f(u_b)\right)(x) \quad = \quad \int_{-\infty}^{\infty} w_{ab}(x,y) f(u_b(y,t)) \mathrm{d}y.$$

Systems of this type are often referred to as *neural fields*, since they describe the mean field or average interactions of a neuronal network.[1] The synaptic drive of the excitatory (inhibitory) population is represented by u_e (u_i) and evolves with time constant τ_e (τ_i). The weight function w_{ab} represents the strength of connection or weight from population b to population a. Often, but not always, it is taken to be a homogeneous, isotropic, monotone decreasing function of Euclidean distance so that $w(x,y) = w(|x-y|)$. The

[1] The systems we study in this dissertation describe the evolution of a neural field, which is a quantity that informs us of how the neuronal network — the physical system we are modeling — is behaving.

nonlinearity f denotes an output firing rate function. A typical choice for f is a bounded, positive monotonic function such as the sigmoid

$$f(u) = \frac{1}{1 + \mathrm{e}^{-\eta(u-\theta)}} \tag{1.2}$$

with gain η and threshold θ. In numerical simulations, Wilson and Cowan found that initial stimuli can give rise to standing pulses or bumps as well as traveling pulses, depending on the structure and strength of excitatory and inhibitory connections [181]. Following up on this, Amari carried out an analytical study of a scalar system with short range excitation and long–range inhibition, assuming inhibition acts much faster than excitation, so that the excitatory drive $u \equiv u_e$ evolves as [3]

$$\tau_e \frac{\partial u(x,t)}{\partial t} \quad = \quad -u(x,t) + \int_{-\infty}^{\infty} w(x-y) f(u(y,t)) \mathrm{d}y. \tag{1.3}$$

Most analytical studies of the existence and stability of spatially structured solutions of equation (1.3) and its generalizations have been obtained by taking the high–gain limit $\eta \to \infty$ of the nonlinearity f, such that it becomes a Heaviside function [3, 136, 137, 39]

$$f(u) = \Theta(u-\theta) \quad = \quad \begin{cases} 0 & \text{if } u < \theta \\ 1 & \text{if } u > \theta. \end{cases} \tag{1.4}$$

By analyzing stationary bump solutions, Amari found that lateral inhibition was indeed necessary to stabilize them [3]. In Appendix A, we briefly review the analysis of bumps in the scalar neural field equation (1.3) with $f \equiv \Theta$.

Studying traveling fronts in a more general form of equation (1.3), Ermentrout and McLeod derived results for their existence and uniqueness [52]. Therein, they analyze a purely excitatory scalar firing rate model with smooth activation function f like (1.2) and also include general temporal dynamics

$$u(x,t) \quad = \quad \int_{-\infty}^{t} \alpha_f(t-\tau) \int_{-\infty}^{\infty} w(|x-y|) f(u(y,\tau)) dy d\tau, \tag{1.5}$$

where w is a non–negative, even functions, and α_f is a positive, monotonically decreasing function. When the α_f function is a decaying exponential, they found first order temporal dynamics, as α_f represents synaptic time course. f is a monotonically increasing so that $F(v) = -v + f(v)$ has three roots, $u_1 < u_2 < u_3$ with $F'(u_1), F'(u_3) < 0$ and $F'(u_2) > 0$. This is essentially a reformulation of equation (1.3). They prove that there exist two stable states to the system u_1 and u_3. A unique monotone traveling wave front joins these two

stable states, and it approaches u_3 at $-\infty$ and u_1 at ∞. The speed of the front has the same sign as

$$\int_{u_1}^{u_3} F(u)\mathrm{d}u.$$

Wave fronts will travel with a positive (negative) speed when the threshold of f is low (high), and stationary fronts exist when the negative and positive areas of the cubic–like function $F(v)$ in the domain $[u_1, u_3]$ are equal. Fronts form heteroclinic orbits — trajectories between two different stable states. Although stability of this wave front can be proved, it is structurally unstable [60]. Therefore, perturbations to the system which supports this front may lead to large changes in the wave front profile.

The Amari model (1.3) of a neural field can also be extended by considering the effects of finite signal propagation velocity along axons [71]. As a result, the argument of the firing rate function f will include a time delay which depends on the distance between two cortical positions. Incorporating this into the system (1.3) yields [136, 40]

$$\tau_e \frac{\partial u(x,t)}{\partial t} = -u(x,t) + \int_{-\infty}^{\infty} w(x-y) f(u(y, t-|x-y|/\nu))\mathrm{d}y, \tag{1.6}$$

where ν is the propagation velocity of membrane potentials in the network. As with many differential equations that include time delay, the model (1.6) can support oscillations. Depending on the form of the weight function w, this system can support multiple bumps, bulk oscillations, and propagating patterns [40, 5, 26].

In a purely excitatory network, such as when w is non–negative in (1.3), with no axonal delays, the only spatially structured solutions that seem to exist are traveling fronts, that shift the entire medium from an "off" to an "on" state. However, experimental studies of disinhibited cortical tissue suggest that traveling pulses can arise even with the inhibition blocked [183, 136, 141]. Pinto and Ermentrout were the first to address this issue in a mathematical model of cortical tissue with local negative feedback [136]. They considered a network of purely excitatory neurons u with a local negative feedback variable v, meant to represent either synaptic depression or spike frequency adaptation. Synaptic depression is a phenomenon by which usage of a particular synapse depletes the signal it is capable of sending at a later time. Spike frequency adaptation is the attenuation of a neuron's firing rate over time due to activation of an ion channel that shunts current out of the cell. Many recent theoretical studies of spatiotemporal dynamics

in neuronal networks have employed Pinto and Ermentrout's model of linear recovery [136, 137, 67, 55, 57, 56, 39, 93, 168, 83, 155, 167]:

$$\frac{\partial u(x,t)}{\partial t} = -u(x,t) + \int_{-\infty}^{\infty} w(x,x')\Theta(u(x',t)-\theta)\mathrm{d}x' - v(x,t) + I(x,t), \tag{1.7a}$$

$$\frac{1}{\alpha_p}\frac{\partial v(x,t)}{\partial t} = \beta_p u(x,t) - v(x,t), \tag{1.7b}$$

where u is synaptic input current, w represents the synaptic weighting between neurons, Θ is a Heaviside firing rate function with θ the firing threshold, $I(x,t)$ is an external input, v is a slow local negative feedback component and α_p and β_p are the rate and strength of the feedback, respectively. In essence, this formulation of linear recovery is analogous to that found in the Fitzhugh–Nagumo equations. Though here, the recovery variable represents spike frequency adaptation or synaptic depression. Pinto and Ermentrout established that for zero input and large enough negative feedback, traveling pulses exist. Using a shooting method, they were able to demonstrate the existence of a pair of traveling pulses by setting $\beta_p = 0$ and α_p quite small.

Results on traveling pulses were extended to a more general class of weight functions in a recent paper by Pinto, Jackson, and Wayne [138], in which they make relatively weak assumptions on the pattern of spatial connectivity defined by w. They found that in the case where neurons have a single stable state, there are two traveling pulse solutions. When neurons are bistable, they show the existence of a stationary pulse, and sometimes, a single traveling pulse solution. They also carried out a linear stability analysis of all of these pulse solutions by constructing an Evans function — essentially a characteristic equation for the eigenvalues of perturbations of the pulses. Such Evans function approaches have been used to study the stability of traveling pulses in neural fields in several other studies [41, 57, 187].

Other recent extensions of this work have explored various scenarios for the occurrence of spatiotemporal oscillations. For example, Folias and Bressloff have shown that in the presence of a localized Gaussian input I, standing and traveling pulses of activity can transition to spatially localized oscillators or breathers, which can then act as wave emitters [55, 57, 56]. Spiral waves have been studied numerically as a means of explaining data from voltage sensitive dye experiments in disinhibited cortical slice [67]. Also, Laing has used numerical continuation methods in order to find how the angular velocity of spiral waves depends on parameters such as the feedback strength β_p. Precise measurements of quantities relating to self–sustained oscillations are more difficult to find, but initial efforts have begun to explain them in numerical simulation. Troy and Shusterman [168]

have shown that for large enough negative feedback β_p, the complex eigenvalues of the homogeneous fixed point lead to multi–pulse solutions. When simulated in two dimensions, the spatially extended system supports a re–entrant localized rotor that periodically emits target waves. In a subsequent study, they showed that making β_p even larger can lead to a stable limit cycle about the low activity state [155]. Thus, in one dimension, periodic oscillations emit a traveling pulse at each cycle, mimicking EEG data of epileptic seizures [126].

Coombes and Owen have recently introduced a nonlinear model of negative feedback [42] in which the firing threshold θ is treated as a variable representing spike frequency adaptation. One way of conceptualizing an adaptation current is that it increases the synaptic input drive necessary to produce a spike in a single neuron. In order that one might find interesting dynamics, different thresholds are taken for the nonlinearity of the neural population input u and the feedback variable h equations

$$\frac{1}{\alpha_a}\frac{\partial u(x,t)}{\partial t} = -u(x,t) + \int_{-\infty}^{\infty} w(x,x')\Theta(u(x',t) - h(x',t))\mathrm{d}x' \tag{1.8a}$$

$$\frac{\partial h(x,t)}{\partial t} = -(h(x,t) - h_0) + \kappa_a \Theta(u - \theta_a). \tag{1.8b}$$

The input to the neural population $u(x,t)$ evolves at a rate α_a and is superthreshold at a local point when $u(x,t) > h(x,t)$. In the dynamical equation for the adaptation variable $h(x,t)$, h_0 is the baseline threshold value, which dynamically increases with strength κ_a once synaptic drive u rises above θ_a at a local point in the network. The fact that $h_0 > \theta_a$ leads to many different exotic solutions arising in this seemingly simple model. Standing bumps as well as traveling pulses can destabilize via a Hopf bifurcation to breathing solutions. Additionally, a single standing bump can split into two standing bumps via a destabilization, which continues until the self–replicating process fills the domain with bumps [42]. We revisit the system (1.8) in Appendix B, bringing out the subtleties of stability analysis of standing bumps in the network, due to its piecewise smoothness.

While all of these studies use reasonable models to reconstruct spatiotemporal dynamics observed *in vitro* and *in vivo*, they are not necessarily the most physiologically plausible models of local negative feedback in cortical tissue. Indeed the Wilson–Cowan equations can be derived from more biophysical models of a neuronal network, but the negative feedback found in the above equations was inserted heuristically after the fact. However, there have been recent studies that more systematically derive sets of equations for spike frequency adaptation [9] and synaptic depression [169] in firing rate models. We are inter-

ested in the qualitative differences between dynamics observed in the Pinto–Ermentrout model and those observed in a model with more biophysically suggestive negative feedback.

1.4 Content of the dissertation

Despite the extensive and rigorous work that has been completed thusfar on spatially structured solutions in neural field equations, there remain many open questions regarding the link between microscopic processes and large scale activity. For example, the Pinto–Ermentrout equations (1.7) can support spatially localized oscillations that emit traveling pulses if the parameter β_p is above some critical value [155, 167]. A natural question then is, what does β_p represent? Does this quantify the conductance of an adaptive current? Or does it provide the rate at which neurotransmitter is depleted from the presynaptic bouton? In the case that we cannot link such parameters to some physiologically meaningful quantity, then it is hard to say if the model is in a physically accurate regime. Therefore, it is useful to try to derive models whose parameters are physiologically meaningful. Thus, for most of this dissertation, we consider alternative models to those presented in section 1.3, paying particular attention to the forms we take for local negative feedback. These forms have been derived in previous studies of more physiologically detailed models of negative feedback in neurons [169, 9].

Motivated by this, in Chapters 2, 3 and 4, we study a neuronal network model which includes up to two forms of physiologically justified negative feedback. We model synaptic depression in our system of equations by considering a reduction derived from a biophysically reasonable multiple synaptic resource pool model [169, 7, 116, 164]. Essentially, we include the effects of synaptic depression by scaling the influence of a particular network location's synapses dynamically in time. Additionally, we sometimes include the effects of spike frequency adaptation. We employ this mechanisms in our model by considering the rate based description derived from detailed conductance based models of a universal adaptation current [9, 109, 162]. The result is that the adaptation current appears in the argument of the firing rate function f. As opposed to the usual Pinto–Ermentrout formulation of negative feedback in spatially extended neural fields [136, 168, 167], our negative feedback accounts for two separate physiological mechanisms, both of which depend on the output firing rate f. Hence, the basic formulation of the Amari neural field equation (1.3) is modified according to the following system of equations, which now includes firing rate dependent synaptic depression and spike frequency adaptation:

$$\tau \frac{\partial u(\mathbf{x},t)}{\partial t} = -u(\mathbf{x},t) + \int_{\mathbb{D}} w(\mathbf{x},\mathbf{x}')q(\mathbf{x}',t)f(u(\mathbf{x}',t)-a(\mathbf{x}',t))\mathrm{d}\mathbf{x}', \tag{1.9a}$$

$$\frac{\partial q(\mathbf{x},t)}{\partial t} = \frac{1-q(\mathbf{x},t)}{\alpha} - \beta q(\mathbf{x},t)f(u(\mathbf{x},t)-a(\mathbf{x},t)), \tag{1.9b}$$

$$\epsilon \frac{\partial a(\mathbf{x},t)}{\partial t} = -a(\mathbf{x},t) + \gamma f(u(\mathbf{x},t)-a(\mathbf{x},t)), \tag{1.9c}$$

where the spatial domain $\mathbb{D}$ may be in either one or two dimensions, and thus $\mathbf{x}$ would be a scalar or two component vector respectively. Equation (1.9a) describes the evolution of the synaptic current $u(x,t)$ in the presence of synaptic depression and spike frequency adaptation, which take the form of a synaptic scaling factor $q(x,t)$ evolving according to equation (1.9b) and an outward hyperpolarizing adaptation current $a(x,t)$ evolving according to equation (1.9c). The factor $q(x,t)$ can be interpreted as a measure of available presynaptic resources, which are depleted at a rate βf [169, 7, 164], and are recovered on a timescale specified by the constant α (experimentally shown to be 200–1500ms [2, 170, 169]). The adaptation current $a(x,t)$ is activated with strength γ and time constant ϵ (experimentally shown to be 40–120ms [109, 162]). As derived from a universal adaptation current by Benda and Herz [9], spike frequency adaptation is switched on as a linear function of a neuron's firing rate.[2]

It will be convenient for us to fix parameters so that f is interpreted as the fraction of the maximum firing rate, that is $0 \leq f \leq 1$. For a great deal of our analytical results in the paper, we employ a Heaviside firing rate function for f, which allows us to relate parameters in the model to quantities like traveling wave speed and bump sizes. From an experimental perspective, it would at first sight seem inexact to approximate the firing rate of a volume of neurons as either zero or at its maximum depending of whether the input drive is sub– or super–threshold. However, it is possible to numerically simulate neuronal networks with more physiologically accurate smooth firing rate functions and often these results are qualitatively similar to those found for the Heaviside firing rate. In fact, a high gain sigmoid is well approximated by a Heaviside firing rate. Additionally, from a mathematical perspective, very little analytical progress can be made with networks having smooth sigmoidal firing rates. Nonetheless, some methods have been developed to derive analytical results for the existence of spatially structured solutions in networks with smooth firing rate function, such as the sigmoid (1.2) [84, 136, 53, 44]. We are indeed able

[2]Our model of adaptation differs from Coombes and Owen [42], who take the nonlinear part of equation (1.9c) to be of the form $\gamma f(u(x,t)-\kappa)$ for a fixed κ.

to numerically simulate the system (1.9) in the presence of a continuous firing rate function, like a sigmoid or piecewise linear function. The dynamics exhibited by the system can in some case be dependent on the firing rate function, and which we shall discuss further in this dissertation.

It is important to point out that a convenient feature of the model system (1.9) is that most of its parameters can be linked to biologically meaningful quantities. Since the time constant of the fast form of resource dependent synaptic depression has been shown to be anywhere between 200–1500ms, if we consider fixing the membrane time constant, experimentally shown to be 10ms, by setting $\tau = 1$, we know that α should range between 20 and 150. Additionally, we know from experimental results that the strength of a synapse is reduced due to depression by a factor $\eta = 0.05 - 0.4$ of its maximal value [2, 169, 189]. In response to a sustained input of rate $f = 1$, a simple steady–state calculation shows that $\beta \approx (1-\eta)/(\eta\alpha) \approx 0.001 - 0.1\ (ms)^{-1}$ for the given range of values of α. Experimentalists have also identified a slower form of synaptic depression that recovers on a timescale of roughly 5–10s [174, 34], so we would wish to set α to be 500 to 1000 for this phenomenon and $\beta \approx 0.0001 - 0.005$ correspondingly. Additionally, we know similar quantities for the adaptation parameters. Since adaptation currents typically have time constants between 40–120ms, then ϵ should lie between 4 and 12 [109, 162]. As for the strength of adaptation γ, this may be more difficult to link to physiological parameters, since data usually gives the fraction of the adapted maximum is to the baseline maximum firing rate, which is about 1/3 [109, 162, 9]. However, in the case of a smooth firing rate function, it is possible to derive appropriate values for γ based on this estimate using a simple steady state analysis, which links parameters to the equilibrium values of our variables. We are then confident that we can learn a great deal about how synaptic depression and adaptation affect cortical network dynamics by analyzing the system (1.9) since we have methodical ways of relating our results to biological parameters and vice versa.

Thus, in Chapter 2 we proceed by analyzing the full system (1.9) in one–dimension (so $\mathbf{x} = x$, a scalar) for a number of different spatially structured waves and oscillatory solutions. We also consider the effects of employing two different types of firing rate function for f, a Heaviside step function and a piecewise linear function. Our analysis begins with a treatment of traveling waves in the network (1.9) in the case of a purely excitatory network, so that the weight function $w > 0$ everywhere. We derive conditions for the existence of traveling fronts and pulses in the case of a Heaviside step firing rate,

and show that adaptation plays a relatively minor role in determining the characteristics of traveling waves. We then proceed by considering the network with only synaptic depression and lateral inhibition weight function. We derive conditions for the existence and stability of stationary pulses or bumps, and show that bumps will destabilize for sufficiently strong synaptic depression. Interestingly, since we take a Heaviside firing rate function, we must treat the stability analysis of stationary bumps in an alternate way to the usual linear stability calculation of spatial structures. Since there arises a jump discontinuity in our depression variable, we must keep track of the sign of perturbations in our stability analysis of this piecewise smooth system. This leads to novel stability results for bumps in a biologically based model. Finally, in the case of a piecewise linear firing rate function, we complete a phase plane analysis of the space clamped system with both synaptic depression and adaptation, and show that the network can support self–sustained oscillations for a physiological range of synaptic depression strengths. We show numerically that the spatially extended network exhibits self–sustained oscillations between an Up state and a Down state, in which a spatially localized oscillating core periodically emits pulses each cycle. All of these results are significant in that they link to experimentally observed phenomena *in vitro* and *in vivo*. We are able to relate the existence of these spatially structured states to experimentally justified values of the model parameters.

We follow this in Chapter 3 by characterizing the behavior of a two–dimensional neuronal network ($\mathbf{x} = \mathbf{r}$, a two–dimensional vector) with synaptic depression (consider setting adaptation strength $\gamma = 0$). We ignore spike frequency adaptation in this study, due to the minor role it played in influencing traveling wave and oscillation properties in Chapter 2. We show that the two–dimensional network supports a wide range of spatially structured oscillations, which are suggestive of phenomena seen in cortical slice experiments and *in vivo*. The particular form of the oscillations depends on initial conditions and the level of background noise. As shown through phase plane analysis, the space clamped network with a piecewise linear firing rate can support limit cycles. Additionally, low levels of additive noise in the activity variable can induce self–sustained oscillations in parameter regimes where the continuous system does not. We then show the results of a number of numerical simulations of the spatially extended system in the presence of an excitatory weight function. An initial, spatially localized stimulus evolves network activity to a spatially localized oscillating core that periodically emits target waves. Low levels of noise can spontaneously generate several pockets of oscillatory activity that interact via

their target patterns. Periodic activity in space can also organize into spiral waves, provided that there is some source of rotational symmetry breaking due to external stimuli or noise. In the high gain limit where the firing rate function becomes a Heaviside, no oscillatory behavior exists, but a transient stimulus can lead to a single, outward propagating target wave. Additionally, we analyze the existence of standing bumps of activity in the spatially extended network with lateral inhibition. We find that bumps certainly destabilize due to radially symmetric perturbations in the two–dimensional network for sufficiently strong depression. Due to the piecewise smooth nature of the network, as is the case in Chapter 2, we must keep track of the sign of perturbations everywhere along the bump boundary. However, we leave the analysis of radially nonsymmetric perturbations an open problem, due to its excessive complexity. Thus, our relatively simple model of a neuronal network with local negative feedback is able to support a wide variety of spatially structured waves and oscillations in both one and two dimensions.

In Chapter 4, we analyze a two–population network with synaptic depression modifying connections within and between populations (again setting adaptation strength $\gamma = 0$) and time–independent inputs to either population. This network is meant to represent two hypercolumns in primary visual cortex, where each hypercolumn receives input from a single eye. Neurons within the hypercolumn respond preferentially to a specific orientation of a visual stimulus. With this model, we can study some of the spatiotemporal dynamics of neural activity that arise in binocular rivalry, the phenomenon in which perception switches between two images presented to either eye. Due to cross–inhibition between populations, the model can support slow oscillations in the activity of either population, usually on a time–scale of seconds. Using a Heaviside firing rate function, for the space–clamped version of the model, we are able to compute expressions that determine the amount of time, each period, either eye's neural activity spends in dominance. Using these expressions, we can examine how these dominance times depend on parameters like the strength of input to either eye's neural population. In the spatially extended system, we can study the onset of oscillations using stability analysis of the different stationary bump solutions supported by the model. First, we analyze the existence and stability of single bump or winner–take–all solutions, where only one population supports superthreshold activity. Next, we examine the existence and stability of double bump solutions, where both populations support superthreshold activity. We find, by employing the piecewise smooth stability analysis we develop in Chapter 2, that linear stability predicts the onset of a binocular rivalry–type

solution when a perturbation that expands one bump and contracts the other is unstable.

In Chapter 5, we proceed by returning to the Pinto–Ermentrout model (1.7) with linear negative feedback and analyze the effects that an inhomogeneous weight function has on the propagation of traveling pulses. Such an analysis is motivated by the fact that many regions of the cortex do have an intricate periodic microstructure in their nonlocal synaptic connectivity, such as the prefrontal cortex [106, 122] and the visual cortex [105, 186]. In a previous study of the Amari equation with periodic inhomogeneities, it was found that inhomogeneity could cause reduction in speed and even failure of traveling fronts [20]. Motivated by this result and an interest in addressing more intricate activity structure, we study the propagation of traveling pulses in an inhomogeneous excitatory neuronal network using averaging and homogenization theory. By employing perturbation theory and the Fredholm alternative, the equation representing the modified wave speed is essentially found as a solvability condition for a hierarchy of equations. We show how a spatially periodic modulation of homogeneous synaptic connections leads to an effective reduction in the speed of a traveling pulse. Interestingly, when this predicted traveling pulse speed is compared with pulse speeds for the upper and lower limit of associated homogeneous systems, the pulse speed tends to the lower limit. In the case of a Heaviside firing rate function, we are able to derive explicit formulae to approximate how the traveling wave speed depends on model parameters. In the case of a smooth firing rate function, we are able to derive a general form for this relation. Finally, we show a series of results from numerical simulations of our inhomogeneous neuronal network with local negative feedback. The predictions for the wave speed match reasonably well with these simulations. Interestingly, in the case of large amplitude modulations, the traveling pulse represents the envelope of a multibump solution, in which individual bumps are nonpropagating and transient. Therefore, the pulses can in fact become saltatory in nature composed of a disconnected active region. The appearance (disappearance) of bumps at the leading (trailing) edge of the pulse generates the coherent propagation of the pulse. Wave propagation failure occurs when activity is insufficient to maintain bumps at the leading edge. Such results may be significant since traveling waves are often associated with brain pathologies like epilepsy, so inhomogeneity may be a means of preventing such propagation.

Finally, in Chapter 6, we discuss several future research directions of the work presented in this dissertation. Mainly, this involves exploring the effects of synaptic plasticity in different models of neuronal networks. First we propose to study synaptic facilitation, a

dynamic strengthening of synapses, in the context of a spatially extended network. We also discuss a model of spiking neurons with synaptic plasticity. This contains not only short–term synaptic plasticity but also spike–timing–dependent plasticity, which is the process by which the relative timing of two coupled neurons' spiking determines a strengthening of weakening of the synapse between them. Finally, we introduce a plan to study a stochastic neuronal network with synaptic depression. Considering the finite size effects within smaller networks of neurons may lead to new insights. These could potentially include the role that noise has in generating oscillations and waves in neuronal networks.

CHAPTER 2

ONE–DIMENSIONAL NEURONAL NETWORK WITH SYNAPTIC DEPRESSION AND ADAPTATION

In this chapter, we analyze the spatiotemporal dynamics of a one–dimensional neural field model that takes into account two physiologically based forms of nonlinear negative feedback, namely, synaptic depression [169, 7, 116, 164] and spike frequency adaptation [9, 109, 162]. The details of both forms of negative feedback, including their associated time constants, are likely to be important in determining conditions for the existence and stability of spatially structured activity states such as traveling waves, standing bumps, or focused oscillations. Thus, as opposed to the usual Pinto–Ermentrout formulation of negative feedback in spatially extended neural fields [136, 168, 167], our negative feedback accounts for two separate physiological mechanisms, both of which depend on the output firing rate f as

$$\tau \frac{\partial u(x,t)}{\partial t} = -u(x,t) + \int_{-\infty}^{\infty} w(x,x')q(x',t)f(u(x',t)-a(x',t))\mathrm{d}x', \tag{2.1a}$$

$$\frac{\partial q(x,t)}{\partial t} = \frac{1-q(x,t)}{\alpha} - \beta q(x,t)f(u(x,t)-a(x,t)), \tag{2.1b}$$

$$\epsilon \frac{\partial a(x,t)}{\partial t} = -a(x,t) + \gamma f(u(x,t)-a(x,t)). \tag{2.1c}$$

Equation (2.1a) describes the evolution of the synaptic current $u(x,t)$ in the presence of synaptic depression and spike frequency adaptation, which take the form of a synaptic scaling factor $q(x,t)$ evolving according to equation (2.1b) and an outward hyperpolarizing adaptation current $a(x,t)$ evolving according to equation (2.1c). The factor $q(x,t)$ can be interpreted as a measure of available presynaptic resources, which are depleted at a rate βf and are recovered on a timescale specified by the constant α. The adaptation current $a(x,t)$ is activated with strength γ and time constant ϵ. We fix the temporal scale of the network by setting $\tau = 1$. The membrane time constant is typically around 10 ms.

Following Amari's original work on scalar networks [3], most analytical studies of the Pinto–Ermentrout model take the nonlinear firing–rate function f to be a Heaviside step function [136, 137, 155, 55, 57, 56, 168, 167] (although see [53] for a functional analytic study of neural field models with smooth nonlinearities):

$$f(J) \quad = \quad \Theta(J-\theta) = \begin{cases} 0, & J \in (-\infty, \theta), \\ 1, & J \in (\theta, \infty). \end{cases} \tag{2.2}$$

We will use such a function in order to study the existence and stability of traveling waves and bumps (see sections 2.1 and 2.2). However, as we show in section 2.3, the network can only support self–sustained oscillations if we consider a more general firing rate function such as the piecewise linear function (see Figure 2.1)

$$f(J) \quad = \quad \begin{cases} 0, & J \in (-\infty, \theta), \\ \sigma(J-\theta), & J \in (\theta, \theta+\sigma^{-1}), \\ 1, & J \in [\theta+\sigma^{-1}, \infty). \end{cases} \tag{2.3}$$

(One could also consider a firing rate function with a step followed by linear increase [61, 62]). Here σ specifies the slope or gain of the firing rate function such that in the limit $\sigma \to \infty$, we recover the Heaviside function (2.2). Note that taking the firing rate to be a linear function close to threshold is consistent with the observation that spike frequency adaptation tends to linearize the firing frequency–input current curve [50, 176]. One important point is that even if the firing threshold θ is the same in equations (2.3) and (2.2), a more intuitive threshold for the piecewise linear function should match the half height threshold θ_S usually defined for the sigmoidal function

$$f_\sigma(J) = \frac{1}{1+\mathrm{e}^{-\sigma(J-\theta_S)}} \tag{2.4}$$

as illustrated in Figure 2.1. Treating the Heaviside function as the high–gain limit of a sigmoid also implies that $\Theta(0) = 1/2$. However, we have found that the qualitative results on existence and stability of spatially structured solutions are unaffected by the value taken for $\Theta(0)$. In numerical simulations, the single value $\Theta(0)$ is very unlikely to ever be computed.

We consider two different forms for the weight function w. To represent a homogeneous excitatory network, we take w to be the normalized exponential

$$w(|x-x'|) \quad = \quad \frac{1}{2d}\mathrm{e}^{-|x-x'|/d}, \tag{2.5}$$

where d is the effective range of the excitatory distribution. The use of this weight function (2.5) is motivated by studies of traveling waves and self–sustained oscillations (sections 2.1

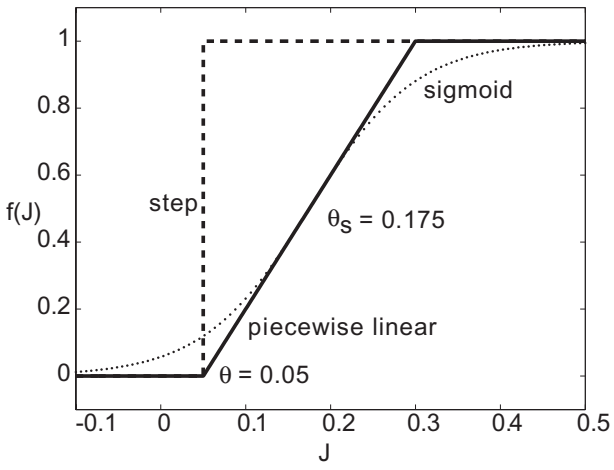

Figure 2.1. Comparison of the step, piecewise linear, and sigmoid firing rate functions. Parameter values are $\theta = 0.05$ and $\sigma = 4$. The sigmoid function has the same slope and value as the piecewise linear function at their mean values. When compared to the sigmoid function, it is apparent that the piecewise linear function's true threshold is more accurately given by $\theta_s = 0.175$, rather than θ, the point at which nonzero firing occurs.

and 2.3) of activity in epileptiform tissue *in vivo* or cortical slices, where inhibition is mostly blocked. In our studies employing the excitatory weight function (2.5), we fix the spatial scale by setting $d = 1$, noting that length–scale of synaptic connections is typically 1 mm. We represent a homogenous network with lateral inhibition by taking w to be the difference of exponentials

$$w(|x - x'|) \quad = \quad \mathrm{e}^{-|x-x'|} - A_i \mathrm{e}^{-|x-x'|/\sigma_i}, \tag{2.6}$$

where A_i is the relative strength of inhibition, σ_i is the relative scale of inhibition, and the spatial scale of excitation is taken to be 1mm. Use of this so called Mexican hat weight function (2.6) is motivated by experimental studies of standing pulses of activity in prefrontal cortex where lateral inhibition is present and required for stabilization of pulses (section 2.2). Since both weight functions are symmetric, depending only on Euclidean distance, we can write $w(x, x') = w(|x - x'|)$.

With this model in hand, we carry out a systematic study of the spatiotemporal dynamics that it supports. We proceed by first deriving conditions for the existence of traveling fronts and pulses in the case of a Heaviside firing rate function (see section 2.1). We show that adaptation plays a relatively minor role in determining the characteristics of the waves. For example, the wavespeed of a propagating front is independent of the

adaptation parameters, whilst both the width and speed of a traveling pulse are only weakly dependent on adaptation. As in the case of linear adaptation [136], there coexists a stable branch of fast/wide pulses and an unstable branch of slow/narrow pulses. The existence and stability of standing pulses or bumps is analyzed in section 2.2, where we show that care must be taken in treating the piecewise smoothness that arises in stability calculations. Finally, in section 2.3, we consider a more realistic piecewise linear firing rate function for which self–sustained oscillations can occur; these oscillations persist in the absence of adaptation.

2.1 Traveling waves

Several experimental studies of disinhibited cortical slices and *in vivo* cortical regions have exhibited traveling fronts and pulses of superthreshold activity [183, 182, 67, 184] (see also section 1.2.3 for a discussion of experimentally observed traveling waves). Neural field models of excitatory networks have sought to give heuristic explanations of such phenomena from a dynamical systems point of view [136, 55, 57, 39, 168, 155, 167]. In this section we present to our knowledge the first neural field study of traveling waves in a spatially extended network that includes physiologically justified terms for both synaptic depression and spike frequency adaptation. As we are concerned with phenomena that arise in the absence of inhibition, we take w to be the excitatory weight function (2.5) in this section. In the case of the Heaviside firing rate function (2.2), we can carry out the analysis along similar lines to previous modeling studies. We look for solutions to the system (2.1), $u(x,t) = U(\xi)$, $q(x,t) = Q(\xi)$, $a(x,t) = A(\xi)$, where $\xi = x - ct$ is the traveling wave coordinate.

2.1.1 Fronts

We specify conditions for a traveling front in our neural field model as follows. The total current $J(\xi) = U(\xi) - A(\xi)$ must cross the threshold θ of the activation function at exactly one point. We can conveniently fix this point to be $\xi = 0$ due to translation invariance. For concreteness, we consider a right moving front by taking the current J to be superthreshold (subthreshold) to the left (right) of $\xi = 0$. We then have

$$J(\xi) = U(\xi) - A(\xi) = \theta, \qquad \text{at } \xi = 0, \tag{2.7}$$

$$J(\xi) = U(\xi) - A(\xi) \gtrless \theta, \qquad \text{for } \xi \lessgtr 0, \tag{2.8}$$

$$\{U(\xi), Q(\xi), A(\xi)\} \to \{0, 1, 0\}, \qquad \text{as } \xi \to \infty, \tag{2.9}$$

$$c \geq 0. \tag{2.10}$$

It follows from our model system (2.1) that such a traveling front will evolve according to

$$-cU'(\xi) = -U(\xi) + \int_{-\infty}^{0} Q(\xi')w(|\xi - \xi'|)\mathrm{d}\xi', \tag{2.11}$$

$$-c\alpha Q'(\xi) = 1 - Q(\xi) - \alpha\beta Q(\xi)\Theta(-\xi), \tag{2.12}$$

$$-c\epsilon A'(\xi) = -A(\xi) + \gamma\Theta(-\xi). \tag{2.13}$$

Equations (2.12) and (2.13) can be solved explicitly to give

$$Q(\xi) = \begin{cases} 1, & \text{for } \xi > 0, \\ \frac{1}{1+\alpha\beta}\left(1 + \alpha\beta \mathrm{e}^{(1+\alpha\beta)\xi/(c\alpha)}\right), & \text{for } \xi \leq 0 \end{cases} \tag{2.14}$$

and

$$A(\xi) = \begin{cases} 0, & \text{for } \xi > 0, \\ \gamma(1 - \mathrm{e}^{\xi/(c\epsilon)}), & \text{for } \xi \leq 0. \end{cases} \tag{2.15}$$

Substituting (2.14) back into (2.11), we have

$$-cU'(\xi) = -U(\xi) + F(\xi), \tag{2.16}$$

$$F(\xi) = \frac{1}{1+\alpha\beta}\int_{-\infty}^{0}\left(1 + \alpha\beta \mathrm{e}^{(1+\alpha\beta)\xi'/(c\alpha)}\right) w(|\xi - \xi'|)\mathrm{d}\xi'. \tag{2.17}$$

In the case of the exponential weight function (2.5), we can explicitly evaluate $F(\xi)$ and thus solve equation (2.16) after imposing the appropriate asymptotic behavior. The threshold condition $J(0) = U(0) - A(0) = \theta$ then leads to the following relationship between front speed c and the threshold θ:

$$\theta = \frac{(c\alpha + 1)}{2(c+1)(c\alpha + (1+\alpha\beta))}. \tag{2.18}$$

A front solution is shown in Figure 2.2.

We can derive an explicit expression for the wavespeed c in terms of other parameters from (2.18) by finding the roots of the quadratic

$$2\alpha\theta c^2 + (2\theta(\alpha + (1+\alpha\beta)) - \alpha)c + 2\theta(1+\alpha\beta) - 1 = 0, \tag{2.19}$$

which are

$$c_\pm = \frac{1}{4\alpha\theta}\left(\alpha - 2\theta(\alpha + (1+\alpha\beta)) \pm \sqrt{\mathcal{D}_f}\right), \tag{2.20}$$

$$\mathcal{D}_f = \alpha^2 - 4\alpha\theta(\alpha + (1+\alpha\beta)) + 4\theta^2(\alpha + (1+\alpha\beta))^2 - 16\alpha\theta^2(1+\alpha\beta) + 8\alpha\theta.$$

In order for a front to exist with wavespeed $c_\pm$ as we have constructed it, $c_\pm$ must be real and nonnegative. None of the adaptation parameters ϵ or γ enter into the dispersion

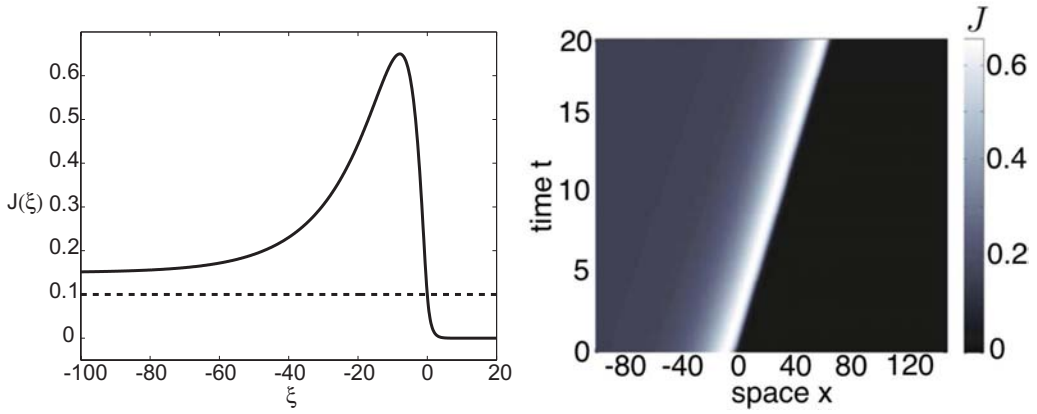

Figure 2.2. Traveling front solution in neuronal network with synaptic depression and adaptation. (Left): Profile of analytical front solution $J(\xi) = U(\xi) - A(\xi)$ for parameter values $\theta = 0.1$, $\alpha = 20$, $\beta = 0.2$, $\epsilon = 5$, and $\gamma = 0.05$. Wavespeed c_+ is specified by equation (2.20). Note that, as $\xi \to -\infty$, $J(\xi) \to 1/(1+\alpha\beta) - \gamma$. (Right): Corresponding space–time plot of a traveling front obtained by solving the system (2.1) numerically with the analytical front solution taken as the initial condition.

relation for fronts. However, in order for a front to exist, we must also satisfy $J(\xi) > \theta$ for $\xi < 0$ as given by (2.8) to make sure the trailing edge of the front does not cross back below threshold as identified in a similar analysis in [168]. Therefore, we impose the necessary condition

$$\lim_{\xi\to-\infty}[U(\xi) - A(\xi)] \quad = \quad \frac{1}{1+\alpha\beta} - \gamma > \theta \quad \Longrightarrow \gamma < \frac{1}{1+\alpha\beta} - \theta,\ \beta < \frac{1}{\alpha(\gamma+\theta)} - \frac{1}{\alpha}. \tag{2.21}$$

Otherwise, the trailing edge of the front dips below threshold, the superthreshold region has finite width, and therefore the profile evolves into a pulse. We quantify the dependence of wavespeed c on synaptic depression parameters in Figure 2.3.

2.1.2 Pulses

For a traveling pulse, the total current $J(\xi) = U(\xi) - A(\xi)$ must cross the threshold θ of the activation function at exactly two points. Once again, fix these points to be $\xi = -\Delta, 0$. Total current J must be superthreshold between these two points, and subthreshold otherwise. Imposing this, as well as boundary conditions, we have

$$J(\xi) = U(\xi) - A(\xi) = \theta, \qquad \text{at } \xi = -\Delta, 0, \tag{2.22}$$

$$J(\xi) = U(\xi) - A(\xi) > \theta, \qquad \text{for } \xi \in (-\Delta, 0), \tag{2.23}$$

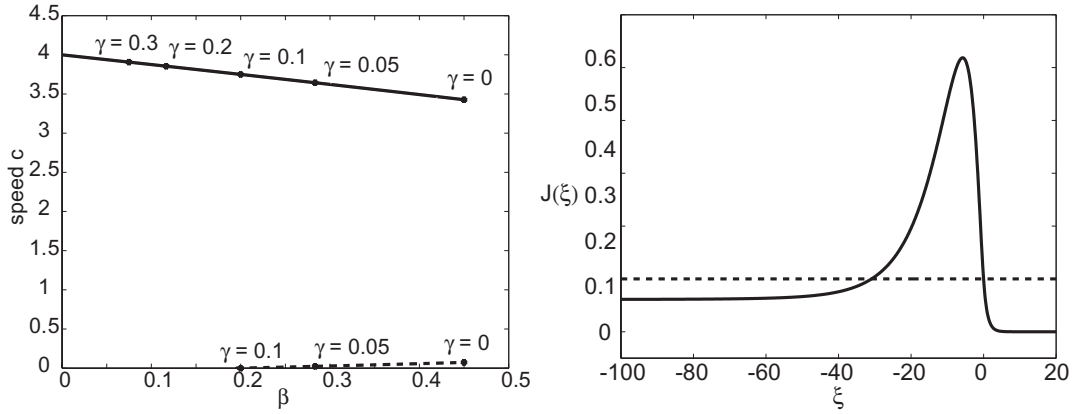

Figure 2.3. Synaptic depression and adaptation effects on front speeds. (Left): Dispersion curve of wavespeed c_+ (solid) and c_- (dashed) versus depression strength β. Numerical results show the fast front (c_+) is stable and the slow front (c_-) is unstable. The maximal value of β for which the superthreshold condition (2.21) is satisfied is given by a dot on each dispersion curve for a particular value of γ. Parameters are $\theta = 0.1$, $\alpha = 20$, and $\epsilon = 5$. (Right): A front that violates the superthreshold condition (2.21), despite its construction being specified by all other conditions. When the system (2.1) is solved numerically with such an initial condition, the solution settles into a traveling pulse.

$$J(\xi) = U(\xi) - A(\xi) < \theta \qquad \text{for } \xi \in (-\infty, -\Delta) \cup (0, \infty) \tag{2.24}$$

$$U(\xi) - A(\xi) \to 0, \qquad \text{as } \xi \to \pm\infty, \tag{2.25}$$

$$Q(\xi) \to 1, \qquad \text{as } \xi \to \infty. \tag{2.26}$$

Thus, it follows from our system (2.1) that a traveling pulse will evolve according to

$$-cU'(\xi) = -U(\xi) + \int_{-\Delta}^{0} Q(\xi')w(|\xi - \xi'|)\mathrm{d}\xi', \tag{2.27}$$

$$-c\alpha Q'(\xi) = 1 - Q(\xi) - \alpha\beta Q(\xi)(\Theta(-\xi) - \Theta(-\xi - \Delta)), \tag{2.28}$$

$$-c\epsilon A'(\xi) = -A(\xi) + \gamma(\Theta(-\xi) - \Theta(-\xi - \Delta)), \tag{2.29}$$

As in the front case, we can solve the system of equations by solving equations (2.28) and (2.29) individually, and then plugging $Q(\xi)$ back into equation (2.27). Using integrating factors, we find that

$$Q(\xi) = \begin{cases} 1, & \xi > 0, \\ \frac{1}{1+\alpha\beta}\left(1 + \alpha\beta \mathrm{e}^{(1+\alpha\beta)\xi/(c\alpha)}\right), & \xi \in (-\Delta, 0), \\ 1 - \frac{\alpha\beta}{1+\alpha\beta}\left(\mathrm{e}^{(\Delta+\xi)/(c\alpha)} - \mathrm{e}^{(\xi-\Delta\alpha\beta)/(c\alpha)}\right), & \xi < -\Delta \end{cases} \tag{2.30}$$

and

$$A(\xi) = \begin{cases} 0, & \xi > 0 \\ \gamma\left(1 - \mathrm{e}^{\xi/(c\epsilon)}\right), & \xi \in (-\Delta, 0), \\ \gamma\left(\mathrm{e}^{\Delta/(c\epsilon)} - 1\right)\mathrm{e}^{\xi/(c\epsilon)}, & \xi < -\Delta. \end{cases} \tag{2.31}$$

Substituting (2.30) back into (2.27),

$$-cU'(\xi) = -U(\xi) + G(\xi), \tag{2.32}$$

$$G(\xi) = \frac{1}{1+\alpha\beta}\int_{-\Delta}^{0}\left(1 + \alpha\beta\mathrm{e}^{(1+\alpha\beta)\xi/(c\alpha)}\right) w(|\xi - \xi'|)\mathrm{d}\xi'. \tag{2.33}$$

Notice that in the limit $\Delta \to \infty$, we recover the equations (2.16) and (2.17) for $U(\xi)$ in the front case. Again we can find the explicit solution for $U(\xi)$ when $w(|\xi - \xi'|)$ is taken to be the exponential weight function. The threshold conditions $J(-\Delta) = J(0) = \theta$ then lead to the following pair of equations for the wavespeed c and pulsewidth Δ:

$$\theta = K_0 - K_1\mathrm{e}^{-\Delta} - K_2\mathrm{e}^{-(1+\alpha\beta)\Delta/(c\alpha)}\mathrm{e}^{-\Delta}, \tag{2.34}$$

$$\theta = L_0 + L_1\mathrm{e}^{-\Delta} + L_2\mathrm{e}^{-(1+\alpha\beta)\Delta/(c\alpha)} - L_3\mathrm{e}^{-\Delta/c} + \gamma\mathrm{e}^{-\Delta/(c\epsilon)}, \tag{2.35}$$

where

$$K_0 = \frac{(c\alpha+1)}{2(c+1)(c\alpha+(1+\alpha\beta))}, \qquad K_1 = \frac{1}{2(c+1)(1+\alpha\beta)},$$

$$K_2 = \frac{\beta c\alpha^2}{2(c+1)(1+\alpha\beta)(c\alpha+(1+\alpha\beta))},$$

$$L_0 = \frac{2c+1}{2(c+1)(1+\alpha\beta)} - \gamma, \qquad L_1 = \frac{(c\alpha-1)}{2(c-1)(c\alpha-(1+\alpha\beta))},$$

$$L_2 = \frac{\beta c^2\alpha^4}{(1+\alpha\beta)(c^2\alpha^2-(1+\alpha\beta)^2)(\alpha-(1+\alpha\beta))} - \frac{\beta c\alpha^2}{2(c+1)(1+\alpha\beta)(c\alpha+(1+\alpha\beta))},$$

$$L_3 = \frac{1}{1+\alpha\beta}\left[1 + \frac{\beta c^2\alpha^4}{(c^2\alpha^2-(1+\alpha\beta)^2)(\alpha-(1+\alpha\beta))}\right] + \frac{c^2\alpha^2(1+\beta)-(1+\alpha\beta)}{(c^2-1)(c^2\alpha^2-(1+\alpha\beta)^2)}.$$

A pulse solution is shown in Figure 2.4.

We cannot derive explicit expressions for (c, Δ) from (2.34) and (2.35), but we can solve them numerically using a root finding algorithm. Notice that adaptation parameters do enter into this system as they play a role in how quickly activity tails back down to subthreshold levels. We plot existence curves for traveling pulses as a function of β in Figure 2.5. Stable traveling pulses exist for small enough depression strength β. As in the case of linear adaptation [136], there coexists a stable branch of fast/wide pulses and an unstable branch of slow/narrow pulses. We show similar existence curves as functions of the time constant α in Figure 2.6. Here, stable traveling pulses exist for slow enough

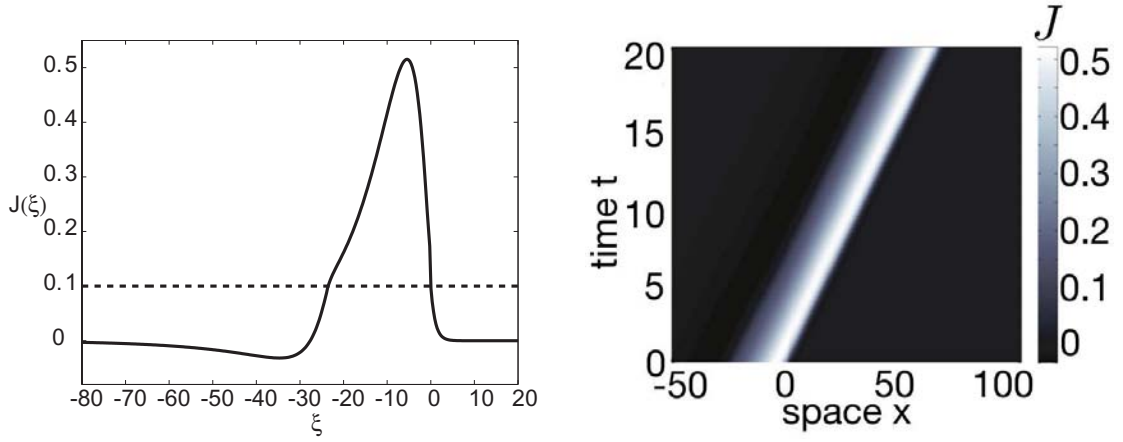

Figure 2.4. Traveling pulse solution in neuronal network with synaptic depression and adaptation. (Left): Profile of a pulse solution $J(\xi) = U(\xi) - A(\xi)$. Note that the solution remains above threshold within the region $\xi \in (-\Delta, 0)$. (Right) Corresponding space–time plot of a traveling pulse obtained by numerically solving (2.1) with the analytical solution as the initial condition. Parameters are $\alpha = 20$, $\beta = 0.4$, $\epsilon = 5$, and $\gamma = 0.1$. Compare with Figure 1.1, which pictures a traveling pulse of neural activity in actual cortical tissue [139].

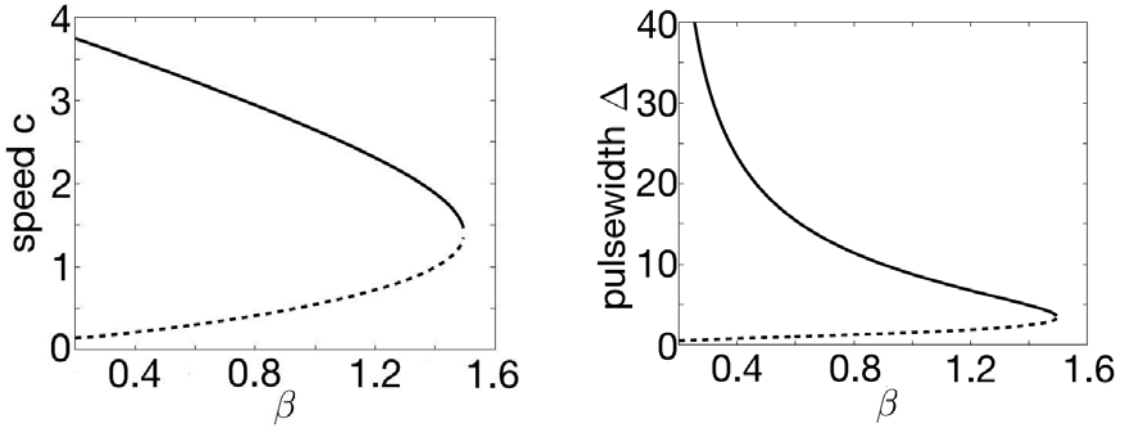

Figure 2.5. Bifurcation curves for the existence of traveling pulses for the system (2.1) in (Left) the (β,c) and (Right) the (β,Δ) plane. There exists a stable branch of fast/wide pulses (solid curves) and an unstable branch of slow/narrow pulses (dashed curves), which annihilate in a saddle–node bifurcation. Parameter values are $\theta = 0.1$, $\alpha = 20$, $\epsilon = 5$, and $\gamma = 0.1$.

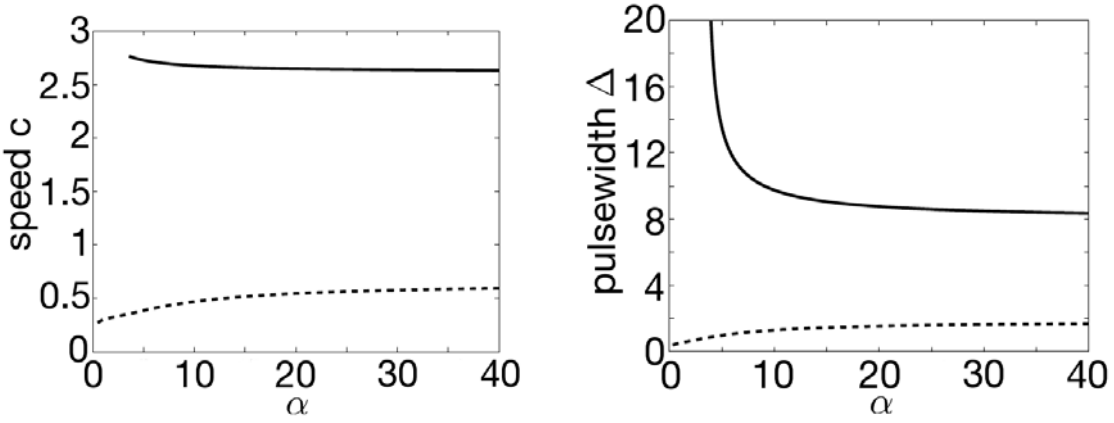

Figure 2.6. Corresponding bifurcation curves for the existence of traveling pulses for the system (2.1) in (Left) the (α,c) and (Right) the (α,Δ) plane. Stable (unstable) branches are indicated by solid (dashed) curves. Parameter values are $\theta = 0.1$, $\beta = 0.9$, $\epsilon = 5$, and $\gamma = 0.1$.

synaptic depression. In general, the wavespeed c and pulsewidth Δ are fairly insensitive to changes in γ or the time constant of adaptation ϵ despite their appearance in the dispersion relation. As in the case of traveling fronts (section 2.1.1), it appears that adaptation has little influence on the character of traveling waves, aside from slightly modifying existence regions.

2.2 Stationary pulses or bumps

Stationary bumps of persistent neural activity have been implicated as neural substrates of several memory, sensory, and motor tasks (see section 1.2.1 for a discussion of such experimental findings). In this section, we analyze the existence and stability of stationary bumps in a one–dimensional neural field model with only synaptic depression given by

$$\frac{\partial u(x,t)}{\partial t} = -u(x,t) + \int_{-\infty}^{\infty} q(x',t) w(x-x') \Theta(u(x',t)-\theta) \mathrm{d}x', \tag{2.36a}$$

$$\frac{\partial q(x,t)}{\partial t} = \frac{1-q(x,t)}{\alpha} - \beta q(x,t) \Theta(u(x,t)-\theta), \tag{2.36b}$$

where we have set $f \equiv \Theta$, the Heaviside activation function. Note that one may reduce the system (2.1) to the above system (2.36) by merely setting the strength of adaptation $\gamma = 0$. The choice of removing adaptation from the model is motivated by two factors. First, we found in our study of traveling waves in section 2.1 and will show in our study on synchronous oscillations in section 2.3 that adaptation has very little effect on the

qualitative dynamics of the system. Synaptic depression dominates. Second, in studying bumps we examine stationary solutions that have a countable number of threshold crossing points. Since adaptation is activated by a discontinuous function, any threshold crossing would lead to a discontinuous change in the stationary variable $a(x,t) = A(x)$, driving part of the interior back below threshold. We found that stable stationary bumps are disrupted in numerical simulations by arbitrarily small amounts of adaptation. In essence, no stationary solutions can exist in the network with adaptation. This issue is circumvented in a study of the system (1.8) by Coombes and Owen [42] by taking different thresholds for the activation of the activity and adaptation variables. We shall revisit their analysis in Appendix B.

Consistent with previous continuum neural field models, negative feedback in the form of synaptic depression cannot generate stable stationary pulses or bumps in a homogeneous excitatory network. Thus some form of lateral inhibition [3, 137, 42] or external input [55, 57] is required to stabilize the bump. Therefore, we will employ the Mexican hat (2.6) as our weight function. (Rubin and Bose have shown that for a discrete network of type I oscillators with synaptic depression, stationary bumps could also be stabilized, but they did not explore the continuum case [144]).

The essential result of our analysis of bumps in the system (2.36) is that its piecewise smooth nature no longer allows for stability to be determined by directly linearizing the equations about a bump solution, as in previous studies [3, 137, 55]. Previous studies have thus constructed an Evans function for bump stability by linearizing neural field equations with a smooth sigmoid (2.4) and then taking the high gain limit [42, 43]. However, such an approach will likely be an incomplete characterization of stability. This is due to the fact that the effects of a Heaviside function's discontinuities in nonlinear equations describing a network are not always captured by taking the high gain limit of the sigmoid. For example, intersections in the continuous system may vanish in the discontinuous system (see section 2.2.1). Therefore, a more careful approach to studying stability must be taken where one considers the piecewise smooth nature of the network equations. The operators that result from studying perturbations to bumps in such networks can be piecewise linear themselves [27, 81].

We indicate some of the effects piecewise smoothness can have on the stability of stationary solutions by first examining linear stability of equilibria in the space–clamped version of (2.36) in section 2.2.1. Following this, we calculate the dependence of a stationary

bump's width on the full system's parameters, when the weight function includes lateral inhibition in the form of equation (2.6) in section 2.2.2. Then, we analyze the stability of these bumps. We proceed by first demonstrating that an Evans function approach, where we take the limit of a steep sigmoid, will break down in the singular limit (section 2.2.3). Thus, we resort to a more careful treatment of the piecewise smooth nature of the system (section 2.2.4). We can then calculate sufficient conditions for the instability of bumps, due to synaptic depression. Our analysis shows that as synaptic depression becomes stronger, bumps certainly destabilize with respect to perturbations that shift their boundary. We are able to study all possible perturbations associated with real eigenvalues, due to making a change of variables in the system describing the evolution of perturbation. We conclude by presenting examples of the destabilization of bumps by different perturbations as predicted by our appropriate stability analysis in section 2.2.5.

2.2.1 Phase–plane analysis

Let us first consider the corresponding space–clamped system in which solutions are restricted to be spatially uniform:

$$\begin{aligned} \dot{u}(t) &= -u(t) + q(t)\Theta(u(t)-\theta), \\ \alpha\dot{q}(t) &= 1 - q(t) - \alpha\beta q(t)\Theta(u(t)-\theta). \end{aligned} \tag{2.37}$$

In order to calculate equilibria of (2.37), we consider the possible solutions on the two domains of the step function $\Theta(u-\theta)$. We find that there is always a low activity or Down state on the lower domain ($u<\theta$) for $\theta>0$ such that $(u,q)=(0,1)$. The stability of this Down state is determined by the eigenvalues of the Jacobian

$$\mathcal{J}(0,1) = \begin{pmatrix} -1 & 0 \\ 0 & -1/\alpha \end{pmatrix} \tag{2.38}$$

and is therefore stable since $\alpha>0$. In the upper domain ($u>\theta$), an equilibrium is given by the system

$$0 = -u + q, \tag{2.39}$$

$$0 = (1-q)/\alpha - \beta q, \tag{2.40}$$

implying a fixed point $(u,q) = (1/(1+\alpha\beta),\ 1/(1+\alpha\beta))$ will exist, provided $\theta < 1/(1+\alpha\beta)$. Its stability is determined by the eigenvalues of the Jacobian

$$\mathcal{J}(u,q) = \begin{pmatrix} -1 & 1 \\ 0 & -(1/\alpha+\beta) \end{pmatrix}, \tag{2.41}$$

which guarantees that such an Up state is always stable. Therefore, we have a bistable system as long as $\theta < 1/(1+\alpha\beta)$, as pictured in Figure 2.7. However, if $\theta > 1/(1+\alpha\beta)$, only the Down state exists, which physically means that in this case synaptic depression curtails recurrent excitation to the point that no sustained activity is possible. In the special case $\theta = 1/(1+\alpha\beta)$, an equilibrium exists at $u = q = \theta$, provided that we take $\Theta(0) = 1$. However, the piecewise smooth nature of the dynamics needs to be taken into account in order to determine the stability of the fixed point. That is, the fixed point is stable with respect to perturbations $\delta u > 0$ but unstable with respect to perturbations $\delta u < 0$. Thus, there does not exists a unique linear operator whose spectrum determines local stability. While this special case is nongeneric in the space–clamped system, it foreshadows potential problems in the study of the stability of spatially structured solutions of the full system (2.36). This is due to the fact that one has to consider perturbations at threshold crossing points x where $u(x,t) = \theta$.

2.2.2 Existence

In the case of a stationary (time–independent) bump solution, we look for solutions to the system (2.36) of the form $u(x,t) = U(x)$ and $q(x,t) = Q(x)$. The activity variable U crosses threshold θ twice for a single bump solution. We then let $R[U] = \{x|U(x) > \theta\}$ be the region over which the network is excited or superthreshold. Exploiting the fact that

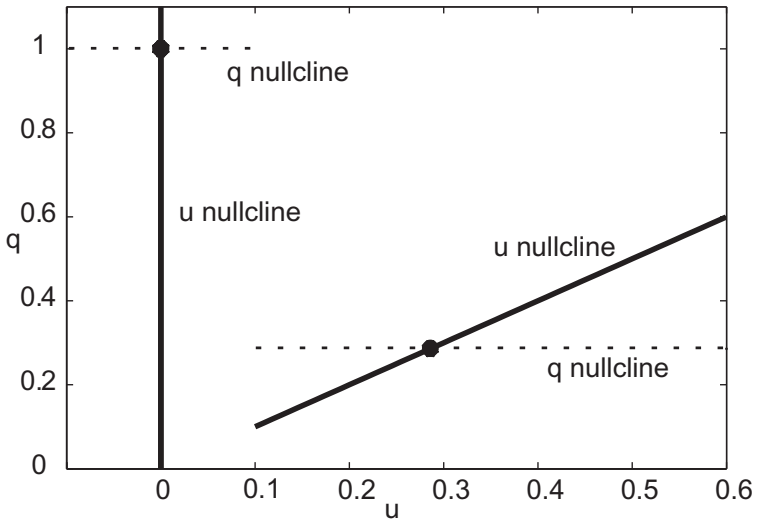

Figure 2.7. Phase plane plot of the space–clamped system (2.37) in the case $\theta < 1/(1+\alpha\beta)$ for which there exist two stable fixed points. Parameters are $\alpha = 50$, $\beta = 0.05$, and $\theta = 0.1$.

any solution can be arbitrarily translated along the x–axis, we define a stationary bump solution of half–width $\mathfrak{a}$ to be one for which $R[U] = (-\mathfrak{a}, \mathfrak{a})$. Thus, our conditions for a bump solution are as follows:

$$\begin{aligned}
U(x) &= \theta, && \text{at } x = -\mathfrak{a}, \mathfrak{a}, \\
U(x) &> \theta, && \text{for } x \in (-\mathfrak{a}, \mathfrak{a}), \\
U(x) &< \theta, && \text{for } x \in (-\infty, -\mathfrak{a}) \cup (\mathfrak{a}, \infty) \\
U(x) &\to 0, && \text{as } x \to \pm\infty, \\
Q(x) &\to 1, && \text{as } x \to \pm\infty.
\end{aligned}$$

The time independent version of system (2.36) then reduces to the pair of equations

$$U(x) = \int_{-\mathfrak{a}}^{\mathfrak{a}} Q(x')w(x - x')\mathrm{d}x', \tag{2.42}$$

$$Q(x) = 1 - \frac{\alpha\beta}{1 + \alpha\beta}\Theta(U(x) - \theta). \tag{2.43}$$

Substituting equation (2.43) into (2.42) yields

$$U(x) = \frac{1}{1 + \alpha\beta}[W(x + \mathfrak{a}) + W(x - \mathfrak{a})], \quad W(x) = \int_0^x w(y)\mathrm{d}y,$$

which is identical to the scalar case modulo a constant scale factor (see Appendix A).

As lateral inhibition is commonly requisite in neuronal network models to stabilize bumps we consider the Mexican hat distribution given by the difference–of–exponentials (2.6). Substituting the specific weight function (2.6) into the steady state solution for $U(x)$ and evaluating the integral yields

$$U(x) = \frac{1}{(1 + \alpha\beta)} \begin{cases} 2\sinh\mathfrak{a}\mathrm{e}^{-x} - 2A_i\sigma_i\sinh(\mathfrak{a}/\sigma_i)\mathrm{e}^{-x/\sigma_i}, & x > \mathfrak{a}, \\ 2 - 2\mathrm{e}^{-\mathfrak{a}}\cosh x - 2A_i\sigma_i[1 - \mathrm{e}^{-\mathfrak{a}/\sigma_i}\cosh(x/\sigma_i)], & |x| < \mathfrak{a}, \\ 2\sinh\mathfrak{a}\mathrm{e}^{x} - 2A_i\sigma_i\sinh(\mathfrak{a}/\sigma_i)\mathrm{e}^{x/\sigma_i}, & x < -\mathfrak{a}. \end{cases}$$

Applying the threshold conditions $U(\pm\mathfrak{a}) = \theta$, we arrive at an implicit expression relating the bump half–width $\mathfrak{a}$ to all other parameters:[1]

$$\frac{1}{(1 + \alpha\beta)}\left[1 - \mathrm{e}^{-2\mathfrak{a}} - A_i\sigma_i(1 - \mathrm{e}^{-2\mathfrak{a}/\sigma_i})\right] = \theta. \tag{2.44}$$

The transcendental equation (2.44) can be solved numerically using a root finding algorithm. Since $0 < A_i < 1$ and $\sigma_i > 1$, it is straightforward to show that $\mathrm{e}^{-2\mathfrak{a}} - A_i\sigma_i\mathrm{e}^{-2\mathfrak{a}/\sigma_i}$

[1]These threshold–crossing conditions are necessary but not sufficient for existence of a bump. A rigorous proof of existence, which establishes that activity is superthreshold everywhere within the domain $|x| < \mathfrak{a}$ and subthreshold for all $|x| > \mathfrak{a}$, has not been obtained except in special cases [3]. However, it is straightforward to check numerically that these conditions are satisfied.

is a unimodal function of $\mathfrak{a}$ and, hence, the maximum number of bump solutions is two. The variation of the bump half–width $\mathfrak{a}$ with the parameters θ and β is shown in Figure 2.8; the stability of the bumps is calculated below.

2.2.3 Stability: High gain limit approach

A popular approach to analyzing the stability of standing bumps in neural field models is to linearize about the bump and derive an Evans function, whose roots represent the spectrum of the associated linear system [41]. Thus, it is tempting to try to calculate the Evans function of the bump solutions (2.44), find its roots, and use these to make statements about the linear stability of the bump. However, the steps necessary to linearize the system (2.36) are not well defined, due to the exposed Heaviside function in equation (2.36b). This suggests that one way to proceed is to take f to be the sigmoid function (2.4) with high gain ($\sigma \gg 1$), formally construct the associated Evans function by Taylor expanding about the bump solution and then take the high–gain limit $\sigma \to \infty$ to recover the Evans function in the case of the Heaviside (One cannot evaluate the Evans function analytically for a smooth sigmoid, since one does not have an explicit expression for the bump solution). However, in the high–gain limit, the region of phase space in which the linear stability theory is valid becomes vanishingly small, due to the ever steepening slope of the sigmoid right at the threshold crossing points. Thus, it is not clear that the resulting

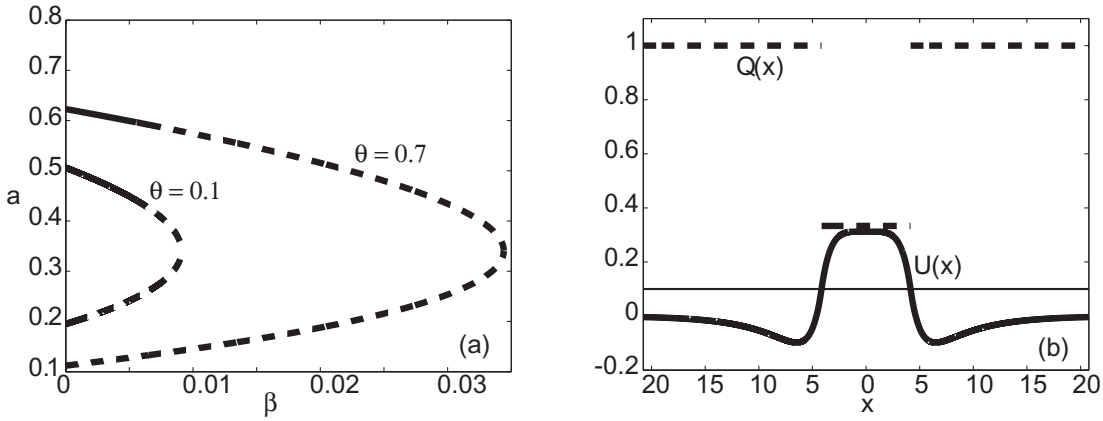

Figure 2.8. One–dimensional bumps. (a) Plots relating bump half–width $\mathfrak{a}$ to amplitude of synaptic depression β for different values of θ using equation (2.44). Stable (unstable) bumps lie on the solid (broken) curve. Beyond each curve's vertical asymptote β value, no bumps exist for that particular value of θ. Other parameter values are $A_i = 0.6$, $\sigma_i = 4$, $\alpha = 20$. (b) Bump profile when $\theta = 0.1$.

Evans function will correctly characterize the linear stability of the bump. Nonetheless, it is useful to present such a construction here and to point out how it breaks down in the high–gain limit, leading to erroneous stability results.

We begin by letting $u(x,t) = U_\sigma(x) + \varepsilon\psi(x,t)$ and $q(x,t) = Q_\sigma(x) + \varepsilon\varphi(x,t)$, where ψ, φ are smooth perturbations, $\varepsilon \ll 1$, and the pair (U_σ, Q_σ) denotes a stationary bump solution of equation (2.36) for a smooth sigmoid function f (2.4) with gain σ. Substituting into the full system (2.36), expanding to first order in ε, and imposing the stationary bump solutions yields

$$\begin{aligned}\frac{\partial\psi(x,t)}{\partial t} &= -\psi(x,t) \qquad (2.45)\\ &\quad + \int_{-\infty}^{\infty} w(x-x')\left\{Q_\sigma(x')f'(U_\sigma(x')-\theta)\psi(x',t) + \varphi(x',t)f(U_\sigma(x')-\theta)\right\}\mathrm{d}x',\\ \frac{\partial\varphi(x,t)}{\partial t} &= -\frac{\varphi(x,t)}{\alpha} - \beta[Q_\sigma(x)f'(U_\sigma(x)-\theta)\psi(x,t) + \varphi(x,t)f(U_\sigma(x)-\theta)]. \qquad (2.46)\end{aligned}$$

We have used the Taylor series approximation to $f(U_\sigma + \psi - \theta)$, which is

$$f(U_\sigma + \psi - \theta) = f(U_\sigma - \theta) + f'(U_\sigma - \theta)\psi + \cdots \qquad (2.47)$$

Notice that

$$f'(U_\sigma(x) - \theta) = \frac{\sigma\exp(-\sigma(U_\sigma(x)-\theta))}{(1+\exp(-\sigma(U_\sigma(x)-\theta)))^2}. \qquad (2.48)$$

is well defined when $U_\sigma(x) \neq \theta$ as $\sigma \to \infty$. However, when $U_\sigma(x) = \theta$, which in fact is where we define threshold crossings in the high gain limit, (2.48) scales linearly with σ. This will invalidate any linear approximation to f in the vicinity of a threshold crossing. Along these lines, as the high gain limit is approached, for steeper and steeper sigmoids, the linear approximation at the threshold crossing becomes progressively worse. Thus, there is a vanishingly small region of the phase space $(\psi(x,t), \varphi(x,t))$ in which this stability analysis will be valid. Therefore, although one can formally analyze the high–gain limit of the spectrum of the smooth linear operator defined by the right hand side of equations (2.45) and (2.46), this does not yield valid conditions for linear stability of a bump in a network with Heaviside nonlinearities. Nevertheless, it is instructive to carry out the spectral analysis of equations (2.45) and (2.46). That is, set $\psi(x,t) = \mathrm{e}^{\lambda t}\psi(x)$ and $\varphi(x,t) = \mathrm{e}^{\lambda t}\varphi(x)$

with $(\psi(x), \varphi(x))$ bounded continuous functions on $\mathbb{R}$ that decay to zero exponentially as $x \to \infty$. This gives

$$(\lambda+1)\psi(x) = \int_{-\infty}^{\infty} w(x-x')\left\{Q_\sigma(x')\psi(x')f'(U_\sigma(x')-\theta)+\varphi(x')f(U_\sigma(x')-\theta)\right\}\mathrm{d}x', \tag{2.49}$$

$$(\lambda+\alpha^{-1})\varphi(x) = -\beta\left[Q_\sigma(x)\psi(x)f'(U_\sigma(x)-\theta)+\varphi(x)f(U_\sigma(x)-\theta)\right]. \tag{2.50}$$

The resulting spectral problem is nontrivial since we have a non–compact linear operator on $\mathbb{R}$, However, we can obtain a simpler spectral problem by formally taking the high–gain limit $\sigma \to \infty$. First, solving equation (2.50) for $\varphi(x)$ yields

$$\varphi(x) = -\beta(\lambda+\alpha^{-1}+\beta f(U_\sigma(x)-\theta)))^{-1}Q_\sigma(x)\psi(x)f'(U_\sigma(x)-\theta). \tag{2.51}$$

Assuming that $\varphi(x)$ is non–singular, we may substitute back into equation (2.49) to give a closed equation for the eigenfunction $\psi(x)$

$$\begin{aligned}(\lambda+1)\psi(x) = \int_{-\infty}^{\infty} w(x-x')Q_\sigma(x')\psi(x')\Big\{&f'(U_\sigma(x')-\theta) \\ &-\beta\left(\lambda+\alpha^{-1}+\beta f(U_\sigma(x')-\theta)\right)^{-1}f(U_\sigma(x')-\theta)f'(U_\sigma(x')-\theta)\Big\}\mathrm{d}x'.\end{aligned} \tag{2.52}$$

We now take the high–gain limit using

$$\lim_{\sigma\to\infty} f(U_\sigma(x)-\theta) = \Theta(U_\sigma(x)-\theta) = \Theta(x+\mathfrak{a})-\Theta(x-\mathfrak{a}), \tag{2.53}$$

$$\lim_{\sigma\to\infty} f'(U_\sigma(x)-\theta) = \Theta'(U_\sigma(x)-\theta) = \frac{\delta(x+\mathfrak{a})}{|U'(\mathfrak{a})|}+\frac{\delta(x-\mathfrak{a})}{|U'(\mathfrak{a})|}, \tag{2.54}$$

$$\lim_{\sigma\to\infty} f(0) = 1/2, \tag{2.55}$$

$$\lim_{\sigma\to\infty} Q_\sigma(\pm\mathfrak{a}) = \frac{1+\alpha\beta/2}{1+\alpha\beta} \tag{2.56}$$

so that equation (2.52) becomes

$$\left(\lambda+\frac{1}{\alpha}+\frac{\beta}{2}\right)(\lambda+1)\psi(x) = \frac{(\lambda+\alpha^{-1})(1+\alpha\beta/2)}{(1+\alpha\beta)|U'(\mathfrak{a})|}\left[w(x+\mathfrak{a})\psi(-\mathfrak{a})+w(x-\mathfrak{a})\psi(\mathfrak{a})\right]. \tag{2.57}$$

Equation (2.57) may appear to be a perfectly reasonable spectral equation for characterizing stability of the bump, due to its similarity to previous studies of the scalar equation (1.3), as shown in Appendix A. Indeed, one can determine λ in terms of the spectrum of the linear opertator $\mathcal{L}\psi(x) = w(x+\mathfrak{a})\psi(-\mathfrak{a})+w(x-\mathfrak{a})\psi(\mathfrak{a})$ acting on the space of continuous bounded functions on $[-\mathfrak{a},\mathfrak{a}]$; it can then be shown that the linear operator is compact in

the case of standard norms such as L^1 [62]. It then follows that the essential spectrum is located at $\lambda = -1$ and the discrete spectrum is determined by setting $x = \pm\mathfrak{a}$ in equation (2.57). This yields two classes of eigenfunctions $\psi_\pm(x) = w(x+\mathfrak{a}) - w(x-\mathfrak{a})$ with associated characteristic equations

$$\left(\lambda + \alpha^{-1} + \frac{\beta}{2}\right)(\lambda + 1) \quad = \quad \Omega_\pm(\lambda + \alpha^{-1})(1 + \alpha\beta/2),$$

where $\Omega_+ = \Omega$ and $\Omega_- = 1$ with

$$\Omega \quad = \quad \frac{w(0) + w(2a)}{w(0) - w(2a)}. \tag{2.58}$$

It is straightforward to show that the characteristic equation for $\psi_-(x)$ has a simple root $\lambda_- = 0$; one expects a zero eigenvalue, since this is an indication of the full system of equations (2.36) being invariant with respect to spatial translations. However, although one can formally take the high–gain limit of the linear equation (2.57), this does not properly take into account the breakdown in the Taylor expansion of the full equations due to the singularity arising on the steepest part of the sigmoid. Consequently, the Evans function approach misses instabilities arising from the piecewise smooth nature of the full system (2.36). Indeed, the Evans function approach implies that the upper branch of the existence curve shown in Figure 2.8 is linearly stable. That is, all non–zero solutions of (2.58) have negative real part along this branch, whereas at least some of this branch is unstable according to the piecewise smooth approach and according to numerical simulations (see sections 2.2.4 and 2.2.5).

2.2.4 Stability: Piecewise smooth approach

In the case of the scalar equation (1.3) it is possible to determine the local stability of a stationary bump by differentiating the Heaviside firing rate function inside the convolution integral, which is equivalent to differentiating with respect to the locations of the bump boundary (see Appendix A). This is no longer possible for the neural field system (2.36), since the steady–state depression variable $Q(x)$ is a discontinuous function of x, reflecting the piecewise smooth nature of the depression dynamics. Therefore, one has to carry out the stability analysis more carefully by taking into account the sign of the perturbations of the bump boundary along analogous lines to the space–clamped system.

Let us set $u(x,t) = U(x) + \varepsilon\psi(x,t)$ and $q(x,t) = Q(x) + \varepsilon\varphi(x,t)$. Substituting into the full system (2.36) and imposing the stationary bump solutions (2.42) and (2.43), and dividing through by ε gives

$$\begin{aligned}\frac{\partial\psi(x,t)}{\partial t} &= -\psi(x,t) \\ &\quad +\frac{1}{\varepsilon}\int_{-\infty}^{\infty} w(x-x')Q(x')\left[\Theta(U(x')+\varepsilon\psi(x',t)-\theta)-\Theta(U(x')-\theta)\right]\mathrm{d}x' \\ &\quad +\frac{1}{\varepsilon}\int_{-\infty}^{\infty} w(x-x')\varphi(x',t)\Theta(U(x')+\varepsilon\psi(x',t)-\theta)\mathrm{d}x' \qquad (2.59)\end{aligned}$$

$$\begin{aligned}\frac{\partial\varphi(x,t)}{\partial t} &= -\frac{\varphi(x,t)}{\alpha}-\frac{\beta}{\varepsilon}Q(x)\left[\Theta(U(x)+\varepsilon\psi(x,t)-\theta)-\Theta(U(x)-\theta)\right] \\ &\quad -\beta\varphi(x,t)\Theta(U(x)+\varepsilon\psi(x,t)-\theta). \qquad (2.60)\end{aligned}$$

Denote the perturbations of the bump boundary by $\varepsilon\Delta_{\pm}(t)$ such that

$$u(\mathfrak{a}+\varepsilon\Delta_{+}(t),t)=u(-\mathfrak{a}+\varepsilon\Delta_{-}(t),t)=\theta$$

for all $t>0$. Therefore, we can relate perturbations $\Delta_{\pm}(t)$ to $\psi(\pm\mathfrak{a},t)$ as

$$\begin{aligned}U(\pm\mathfrak{a})+\varepsilon\Delta_{\pm}(t)U'(\pm\mathfrak{a})+\varepsilon\psi(\pm\mathfrak{a},t)+\mathcal{O}(\varepsilon^2) &= \theta \\ \Delta_{\pm}(t) &\approx \pm\frac{\psi(\pm\mathfrak{a},t)}{|U'(\mathfrak{a})|}, \qquad (2.61)\end{aligned}$$

where we have used $U(\pm\mathfrak{a})=\theta$. We can then smooth out the discontinuities in equation (2.60) by introducing the modified field

$$\Phi(x,t) = \int_{-\mathfrak{a}+\varepsilon\Delta_{-}(t)}^{\mathfrak{a}+\varepsilon\Delta_{+}(t)} w(x-x')\varphi(x',t)\mathrm{d}x'. \qquad (2.62)$$

(Such a change of variables cannot always be invoked in the stability analysis of bumps in piecewise smooth neural fields, as is the case in the network with spike frequency adaptation (1.8), which we analyze in Appendix B). The motivation for this is that a perturbation of the bump boundary means that in a small neighborhood of the bump boundary, the synaptic depression variable will start to switch its steady–state value from $q=1$ to $q=(1+\alpha\beta)^{-1}$ or vice–versa according to equation (2.37). That is, it will undergo $\mathcal{O}(1)$ changes over a time–scale of α^{-1}. However, this does not necessarily imply that the bump solution is unstable, since the region over which the growth or decay of q occurs may shrink to zero. This is captured by the dynamics of the auxiliary field $\Phi(x,t)$, which will remain $\mathcal{O}(1)$ even when $\varphi(x,t)$ is $\mathcal{O}(1/\varepsilon)$ over infinitesimal domains, as in the case of shift perturbations (see case (iii) of analysis that follows).

Differentiating equation (2.62) with respect to time shows that

$$\begin{aligned}\frac{\partial\Phi(x,t)}{\partial t} &= \int_{-\mathfrak{a}+\varepsilon\Delta_-(t)}^{\mathfrak{a}+\varepsilon\Delta_+(t)} w(x-x')\frac{\partial\varphi(x',t)}{\partial t}\mathrm{d}x \\ &\quad +\varepsilon w(x-\mathfrak{a}-\varepsilon\Delta_+(t))\varphi(a+\varepsilon\Delta_+(t),t)\dot{\Delta}_+(t) \\ &\quad -\varepsilon w(x+\mathfrak{a}-\varepsilon\Delta_-(t))\varphi(-\mathfrak{a}+\varepsilon\Delta_-(t),t)\dot{\Delta}_-(t).\end{aligned}$$

Substituting for $\partial\varphi/\partial t$ using equation (2.60) and replacing the second term on the right–hand side of equation (2.59) by Φ lead to the pair of equations

$$\begin{aligned}\frac{\partial\psi(x,t)}{\partial t} &= -\psi(x,t)+\Phi(x,t) \\ &\quad +\frac{1}{\varepsilon}\int_{-\mathfrak{a}+\varepsilon\Delta_-(t)}^{\mathfrak{a}+\varepsilon\Delta_+(t)} w(x-x')Q(x')\mathrm{d}x' - \frac{1}{\varepsilon}\int_{-\mathfrak{a}}^{\mathfrak{a}} w(x-x')Q(x')\mathrm{d}x' \qquad (2.63)\\ \frac{\partial\Phi(x,t)}{\partial t} &= -\left(\alpha^{-1}+\beta\right)\Phi(x,t) \\ &\quad -\frac{\beta}{\varepsilon}\int_{-\mathfrak{a}+\varepsilon\Delta_-(t)}^{\mathfrak{a}+\varepsilon\Delta_+(t)} w(x-x')Q(x')\Theta(U(x')+\varepsilon\psi(x',t)-\theta)\mathrm{d}x' \\ &\quad +\frac{\beta}{\varepsilon}\int_{-\mathfrak{a}+\varepsilon\Delta_-(t)}^{\mathfrak{a}+\varepsilon\Delta_+(t)} w(x-x')Q(x')\Theta(U(x')-\theta)\mathrm{d}x' \qquad (2.64)\\ &\quad +\varepsilon w(x-\mathfrak{a}-\varepsilon\Delta_+(t))\varphi(\mathfrak{a}+\varepsilon\Delta_+(t),t)\dot{\Delta}_+(t) \\ &\quad -\varepsilon w(x+\mathfrak{a}-\varepsilon\Delta_-(t))\varphi(-\mathfrak{a}+\varepsilon\Delta_-(t),t)\dot{\Delta}_-(t).\end{aligned}$$

We now "linearize" equations (2.63) and (2.64) by expanding in powers of ε and collecting all $\mathcal{O}(1)$ terms. Note that it is important to keep track of the signs of $\Delta_\pm$ when approximating the various integrals, since the stationary solution $Q(x)$ is discontinuous at the bump boundary. For example,

$$\begin{aligned}\int_{\mathfrak{a}}^{\mathfrak{a}+\varepsilon\Delta_+} w(x-x')Q(x')\mathrm{d}x' &\approx \varepsilon\Delta_+ \lim_{\varepsilon\to 0} w(x-\mathfrak{a}-\varepsilon\Delta_+)Q(\mathfrak{a}+\varepsilon\Delta_+) \\ &= \varepsilon\Delta_+\, w(x-\mathfrak{a})G(\Delta_+) \qquad (2.65)\end{aligned}$$

and

$$\begin{aligned}\int_{-\mathfrak{a}+\varepsilon\Delta_-}^{-\mathfrak{a}} w(x-x')Q(x')\mathrm{d}x' &\approx -\varepsilon\Delta_- \lim_{\varepsilon\to 0} w(x+\mathfrak{a}-\varepsilon\Delta_-)Q(-\mathfrak{a}+\varepsilon\Delta_-) \\ &= -\varepsilon\Delta_-\, w(x+\mathfrak{a})G(-\Delta_-), \qquad (2.66)\end{aligned}$$

where G is the step function

$$G(\Delta) = \begin{cases} 1 & \text{if } \Delta > 0 \\ (1+\alpha\beta)^{-1} & \text{if } \Delta < 0 \end{cases}. \qquad (2.67)$$

Similarly, the integral on the right–hand side of equation (2.64) can be approximated by the expression

$$\varepsilon\Delta_+(t)w(x-\mathfrak{a})G(\Delta_+)\Theta(\Delta_+) - \varepsilon\Delta_-(t)w(x+\mathfrak{a})G(-\Delta_-)\Theta(-\Delta_-). \tag{2.68}$$

Finally, collecting all $\mathcal{O}(1)$ terms and using equation (2.61), we obtain the following piecewise–linear system of equations:

$$\begin{aligned}\frac{\partial\psi(x,t)}{\partial t} &= -\psi(x,t) + \Phi(x,t) + \gamma_a w(x+\mathfrak{a})\psi(-\mathfrak{a},t)G(\psi(-\mathfrak{a},t)) \\ &\quad +\gamma_a w(x-a)\psi(\mathfrak{a},t)G(\psi(\mathfrak{a},t))\end{aligned} \tag{2.69}$$

$$\begin{aligned}\frac{\partial\Phi(x,t)}{\partial t} &= -\left(\alpha^{-1}+\beta\right)\Phi(x,t) \\ &\quad -\beta\gamma_a w(x+\mathfrak{a})\psi(-\mathfrak{a},t)G(\psi(-\mathfrak{a},t))\Theta(\psi(-\mathfrak{a},t)) \\ &\quad -\beta\gamma_a w(x-\mathfrak{a})\psi(\mathfrak{a},t)G(\psi(\mathfrak{a},t))\Theta(\psi(\mathfrak{a},t)).\end{aligned} \tag{2.70}$$

Here

$$\gamma_a^{-1} = U'(-\mathfrak{a}) = -U'(a) = \frac{w(0)-w(2\mathfrak{a})}{1+\alpha\beta}. \tag{2.71}$$

Equations (2.69) and (2.70) imply that the local stability of a stationary bump solution depends on the spectral properties of a piecewise linear operator. However, we can obtain a simpler eigenvalue problem under the ansatz that the perturbations $\psi(\pm\mathfrak{a},t)$ (or equivalently $\Delta_\pm(t)$) do not switch sign for any time t. In other words, we assume that equations (2.69) and (2.70) have separable solutions of the form $(\psi(x,t),\Phi(x,t)) = \mathrm{e}^{\lambda t}(\psi(x),\Phi(x))$, where λ is real and $\psi(x)$ and $\Phi(x)$ are bounded continuous functions on $\mathbb{R}$ that decay to zero exponentially as $x\to\pm\infty$. Under the assumption that λ is real, the step functions Θ, G are time–independent so that there is a common factor $\mathrm{e}^{\lambda t}$ that cancels everywhere. We thus obtain an eigenvalue problem specified by the pair of equations

$$(\lambda+1)\psi(x) - \Phi(x) = \gamma_a w(x+\mathfrak{a})\psi(-\mathfrak{a})G(\psi(-\mathfrak{a})) + \gamma_a w(x-\mathfrak{a})\psi(\mathfrak{a})G(\psi(\mathfrak{a})) \tag{2.72}$$

$$\begin{aligned}(\lambda+\alpha^{-1}+\beta)\Phi(x) &= -\beta\gamma_a w(x+\mathfrak{a})\psi(-\mathfrak{a})G(\psi(-\mathfrak{a}))\Theta(\psi(-\mathfrak{a})) \\ &\quad -\beta\gamma_a w(x-\mathfrak{a})\psi(\mathfrak{a})G(\psi(\mathfrak{a}))\Theta(\psi(\mathfrak{a})).\end{aligned} \tag{2.73}$$

One class of solution to equation (2.73) is given by $\lambda = -(\alpha^{-1}+\beta)$ and $\psi(\mathfrak{a})\le 0, \psi(-\mathfrak{a})\le 0$. The functions $\psi(x)$ and $\Phi(x)$ are then related according to equation (2.72). However, such solutions do not contribute to any instabilities. Therefore, we will assume that $\lambda \neq$

$-(\alpha^{-1}+\beta)$. We can then algebraically eliminate $\Phi(x)$ to obtain the nonlinear eigenvalue problem

$$\begin{aligned}(\lambda+1)\psi(x) &= \gamma_a w(x-\mathfrak{a})\psi(\mathfrak{a})G(\psi(\mathfrak{a}))\left[1-\frac{\beta}{\lambda+\alpha^{-1}+\beta}\Theta(\psi(\mathfrak{a}))\right] \\ &\quad +\gamma_a w(x+\mathfrak{a})\psi(-\mathfrak{a})G(\psi(-\mathfrak{a}))\left[1-\frac{\beta}{\lambda+\alpha^{-1}+\beta}\Theta(\psi(-\mathfrak{a}))\right].\end{aligned} \tag{2.74}$$

Hence, in the case of a neural field with synaptic depression, the piecewise smooth nature of the full system persists in the piecewise linear system characterizing the stability of bumps. This is an indication that the discontinuities arising in the stationary bump solution are manageable by linear stability analysis under the appropriate change of variables (2.62). By generalizing the analysis of Guo and Chow [62], it is possible to show how the solutions for λ can be identified with the spectra of a set of compact linear operators acting in the space of bounded continuous functions on the interval $[-\mathfrak{a},\mathfrak{a}]$. However, here it will suffice to calculate λ directly from equation (2.74). One particular class of solutions to equation (2.74) consists of functions $\psi(x)$ that vanish on the boundary, $\psi(\pm\mathfrak{a})=0$, such that $\lambda=-1$. This determines the essential spectrum, since $\lambda=-1$ has infinite multiplicity, and does not contribute to any instabilities. There are then four other classes of solution to equation (2.74): (i) $\psi(-\mathfrak{a})>0$ and $\psi(-\mathfrak{a})<0$; (ii) $\psi(-\mathfrak{a})<0$ and $\psi(\mathfrak{a})>0$; (iii) $\psi(-\mathfrak{a})>0$ and $\psi(\mathfrak{a})>0$; (iv) $\psi(-\mathfrak{a})<0$ and $\psi(\mathfrak{a})<0$. In the special case $|\psi(\mathfrak{a})|=|\psi(-\mathfrak{a})|$, the four types of perturbation correspond, respectively to a leftward shift, a rightward shift, an expansion, and a contraction of the stationary bump solution. If $|\psi(\mathfrak{a})|\neq|\psi(-\mathfrak{a})|$ then we have a mixture of these basic transformations. For example if $|\psi(-\mathfrak{a})|>|\psi(\mathfrak{a})$ in case (i), then the perturbation is a mixture of a leftward shift and a bump expansion. Figure 2.9 visualizes these cases for $\psi(x)$, along with the piecewise continuous function $Q(x)$, elucidating why different quantities are considered depending on the shape of the perturbation.

(i) $\psi(\pm\mathfrak{a})>0$: When we apply this assumption and rearrange equation (2.74), we have

$$\begin{aligned}\left(\lambda+\alpha^{-1}+\beta\right)(\lambda+1)\psi(x) &= \gamma_a w(x+\mathfrak{a})\psi(-\mathfrak{a})\left(\lambda+\alpha^{-1}\right) \\ &\quad +\gamma_a w(x-\mathfrak{a})\psi(\mathfrak{a})\left(\lambda+\alpha^{-1}\right).\end{aligned} \tag{2.75}$$

Setting $x=\pm\mathfrak{a}$ and noting that $\psi(\pm\mathfrak{a})$ have the same sign, we have $\psi(\mathfrak{a})=\psi(-\mathfrak{a})>0$ with λ satisfying the quadratic equation

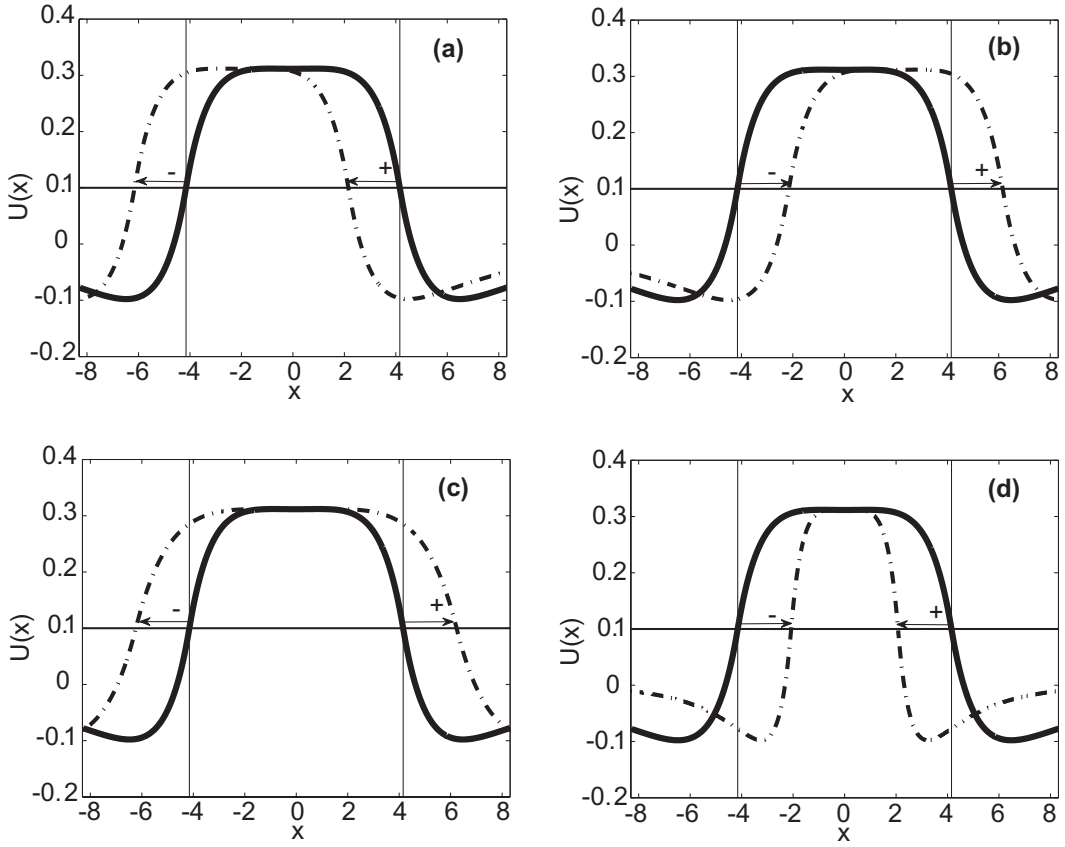

Figure 2.9. Illustration of different types of perturbation of stationary one–dimensional bump solution: (a) leftward shift; (b) rightward shift; (c) expansion; (d) contraction.

$$\left(\lambda + \alpha^{-1} + \beta\right)(\lambda + 1) \;=\; \left(\lambda + \alpha^{-1}\right)(1 + \alpha\beta)\Omega, \tag{2.76}$$

where

$$\Omega \;=\; \frac{w(0) + w(2\mathfrak{a})}{w(0) - w(2\mathfrak{a})}.$$

We have substituted for γ_a using equation (2.71). It follows that $\lambda = \lambda_\pm$ with

$$\begin{aligned}\lambda_\pm \;&=\; \frac{1}{2}\left[\Omega(1+\alpha\beta) - \left(1 + \alpha^{-1} + \beta\right)\right] \\ &\quad \pm \frac{1}{2}\sqrt{\left[\Omega(1+\alpha\beta) - (1 + \alpha^{-1} + \beta)\right]^2 + 4(\Omega - 1)\,(\alpha^{-1} + \beta)}.\end{aligned} \tag{2.77}$$

The corresponding eigenfunctions represent expansions of the bump and take the form

$$\begin{pmatrix} \psi(x) \\ \Phi(x) \end{pmatrix} \;=\; [w(x + \mathfrak{a}) + w(x - \mathfrak{a})] \begin{pmatrix} 1 \\ -\dfrac{\lambda_\pm + 1}{\lambda_\pm + \alpha^{-1}} \end{pmatrix}. \tag{2.78}$$

As we illustrate below, for certain ranges of parameters the eigenvalues $\lambda_\pm$ form a complex conjugate pair and thus must be excluded from our analysis, since they violate the separability assumption.

(ii) $\psi(\pm\mathfrak{a}) < 0$: In this case equation (2.74) becomes

$$(\lambda+1)\psi(x) \;=\; \gamma_a w(x+\mathfrak{a})\psi(-\mathfrak{a})\frac{1}{1+\alpha\beta} + \gamma_a w(x-\mathfrak{a})\psi(\mathfrak{a})\frac{1}{1+\alpha\beta}. \tag{2.79}$$

Setting $x = \pm\mathfrak{a}$ and noting that $\psi(\pm\mathfrak{a})$ must have the same sign shows that $\psi(\mathfrak{a}) = \psi(-\mathfrak{a})$ and $\lambda = \lambda_0$ with

$$\lambda_0 = \Omega - 1. \tag{2.80}$$

Hence, there is a single eigenfunction corresponding to a contraction of the bump given by

$$\begin{pmatrix} \psi(x) \\ \Phi(x) \end{pmatrix} \;=\; -\begin{pmatrix} w(x+\mathfrak{a}) + w(x-\mathfrak{a}) \\ 0 \end{pmatrix}. \tag{2.81}$$

(iii) $\psi(\mathfrak{a}) \le 0, \psi(-\mathfrak{a}) \ge 0$: In this case equation (2.74) becomes

$$\begin{aligned}\left(\lambda+\alpha^{-1}+\beta\right)(\lambda+1)\psi(x) \;&=\; \gamma_a w(x+\mathfrak{a})\psi(-\mathfrak{a})\left(\lambda+\alpha^{-1}\right) \\ &\quad +\gamma_a w(x-\mathfrak{a})\psi(\mathfrak{a})\frac{\lambda+\alpha^{-1}+\beta}{1+\alpha\beta}.\end{aligned} \tag{2.82}$$

Setting $x = \pm\mathfrak{a}$ then yields the matrix equation

$$\begin{pmatrix} \Gamma_\beta(\lambda) - \gamma_a w(0)\left(\lambda+\alpha^{-1}\right) & -\gamma_a\left(\lambda+\alpha^{-1}\right)w(2\mathfrak{a}) \\ -\gamma_a\left(\lambda+\alpha^{-1}\right)w(2\mathfrak{a}) & \Gamma_\beta(\lambda) - \gamma w(0)\left(\lambda+\alpha^{-1}\right) \end{pmatrix}\begin{pmatrix} \psi(-\mathfrak{a}) \\ \psi(\mathfrak{a}) \end{pmatrix}$$

$$= -\frac{\gamma_a\alpha\beta\lambda}{1+\alpha\beta}\begin{pmatrix} w(2\mathfrak{a})\psi(\mathfrak{a}) \\ w(0)\psi(\mathfrak{a}) \end{pmatrix}, \tag{2.83}$$

where

$$\Gamma_\beta(\lambda) \;=\; \left(\lambda+\alpha^{-1}+\beta\right)(\lambda+1).$$

This yields a quartic equation for λ. It is straightforward to show that there always exists a zero eigenvalue $\lambda = 0$ with corresponding eigenmode $\psi(-\mathfrak{a}) = -\psi(\mathfrak{a})$. The existence of a zero eigenvalue reflects the translation invariance of the full system (2.36).[2] In order to calculate the other eigenvalues, we assume that $\beta \ll 1$ (which is consistent with

[2]Although a small uniform shift of the bump corresponds to $\mathcal{O}(1)$ pointwise changes in the depression variable q, these occur over an infinitesimal spatial domain so that the auxiliary variable Φ is still small. Hence, the response to small uniform shifts is covered by our linear stability analysis.

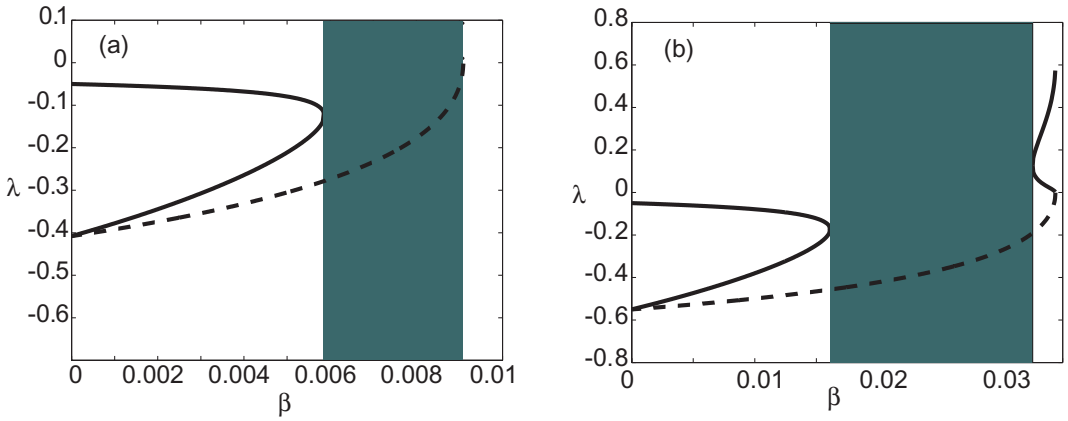

Figure 2.10. Stability with respect to expansion and contraction perturbations (cases (i) and (ii)). (a) Eigenvalues of the expansion (solid curves) and contraction (dashed curve) perturbations when (a) $\theta = 0.1$ and (b) $\theta = 0.07$. In the grey regions, the roots of equation (2.77) are complex thus violating the ansatz that λ is real. Other parameters are $A_i = 0.6$, $\sigma_i = 4$, and $\alpha = 20$.

physiological values for the depletion rate of synaptic depression [169, 164]) and carry out a perturbation expansion in β with $\lambda = \lambda_0 + \beta\lambda_1 + \cdots$ (Using the implicit function theorem it can be shown that λ is a continuous function of β around the origin). First, setting $\beta = 0$ in equation (2.83) we find that there are three eigenvalues $\lambda_0 = \Omega - 1, 0, -\alpha^{-1}$. The first eigenvalue is $\lambda_0 = \Omega - 1$, which can be excluded since the corresponding eigenmode violates the assumption that $\psi(\pm\mathfrak{a})$ have opposite sign. The second eigenvalue is $\lambda_0 = 0$, which persists when $\beta > 0$. Finally, the third eigenvalue $\lambda_0 = -\alpha^{-1}$ is doubly degenerate so that one needs top use degenerate perturbation theory in order to determine the splitting of the eigenvalue into two branches as β increases from zero. Again, one of the branches is excluded by requiring that $\psi(\pm\mathfrak{a})$ have opposite sign. We conclude that for sufficiently small β, shift perturbations do not lead to instabilities.

(iv) $\psi(\mathfrak{a}) \geq 0, \psi(-\mathfrak{a}) \leq 0$: As expected from the reflection symmetry of the original system (2.36) when $w(x)$ is an even function, the spectrum associated with rightward shifts is identical to that of leftward shifts.

We illustrate the above analysis by considering stationary bumps in a network with the Mexican hat weight function (2.6). Specifically, we plot the eigenvalues for each type of perturbation in the case of the wider bump shown in Figure 2.8, which is stable as $\beta \to 0$. In Figure 2.10, we plot the real eigenvalues associated with expansions and contractions (cases (i) and (ii)) as functions of β. In the case of contractions, there is a single negative

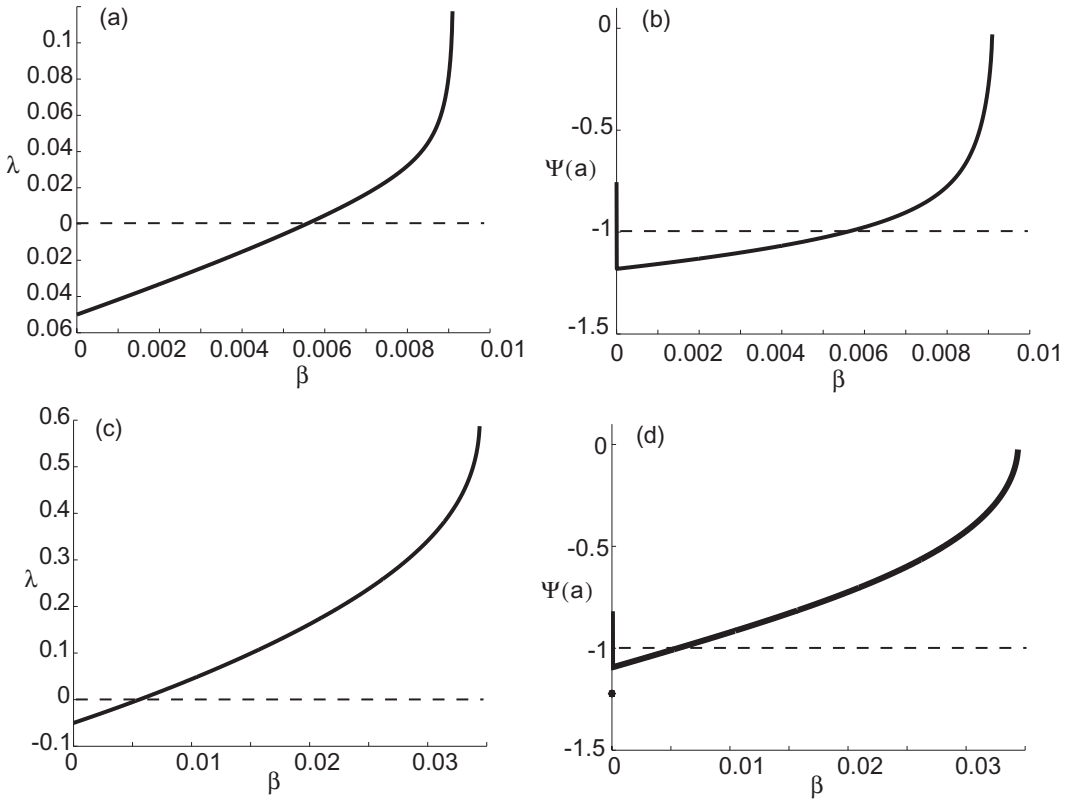

Figure 2.11. Stability of a stationary bump with respect to shift perturbations (cases (iii) and (iv)). (a) Nonzero eigenvalue when $\theta = 0.1$ for various β. Bump destabilizes under shifts for sufficiently large β. (b) Corresponding plot of the ratio $\Psi(\mathfrak{a}) = \psi(\mathfrak{a})/\psi(-\mathfrak{a})$ for a leftward shift and $\theta = 0.1$. As β increases, the ratio approaches zero, implying the perturbation is a combination of a pure shift and an expansion. (c) Nonzero eigenvalue when $\theta = 0.07$ for various β. (d) Corresponding plot of the ratio $\Psi(\mathfrak{a}) = \psi(\mathfrak{a})/\psi(-\mathfrak{a})$ for a leftward shift and $\theta = 0.07$. Other parameters are $A_i = 0.6$, $\sigma_i = 4$, $\alpha = 20$. Results are the same for a rightward shift on exchanging $x = -\mathfrak{a}$ and $x = \mathfrak{a}$.

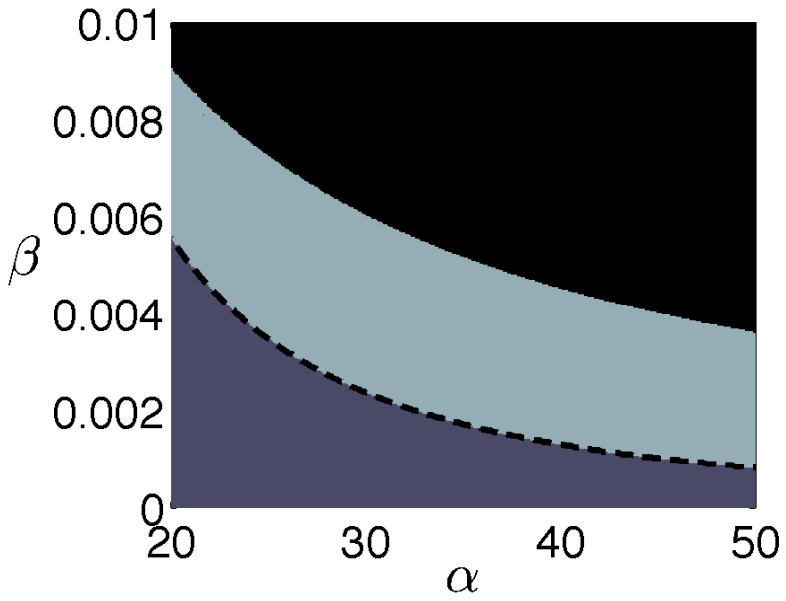

Figure 2.12. Stability map in (α,β) parameter space. Black denotes nonexistence of bumps; light grey denotes unstable bumps; dark grey denotes stable bumps. Dashed black line denotes location of a saddle bifurcation, where stable bumps transition to traveling pulses. Other parameters are $A_i = 0.6$, $\sigma_i = 4$, and $\theta = 0.1$.

branch that approaches zero at a critical value $\beta = \beta_c$. Equations (2.80) and (2.77) imply that the variation in λ is due to the β–dependence of the bump half–width $\mathfrak{a}$ such that $\Omega \to 1$ as $\beta \to \beta_c$. Hence $\mathfrak{a} \to \mathfrak{a}_c$ as $\beta \to \beta_c$ where $\mathfrak{a}_c$ is the width at which the upper and lower existence curves meet in Figure 2.8, that is, $w(2\mathfrak{a}_c) = 0$ (see also Appendix A). In the case of expansions, there are two negative branches for sufficiently small β, which annihilate at the left–hand end of a forbidden region in which the eigenvalues $\lambda_\pm$ given by equation (2.77) are complex, so the stability of expanding perturbations cannot be determined. At the other end of this forbidden region, a pair of positive branches emerges with $\lambda_- \to 0$ as $\beta \to \beta_c$. The latter follows from setting $\Omega = 1$ in equation (2.77). When real roots appear again, there is a jump in their value. In Figure 2.11 we plot the nonzero eigenvalue λ for shift perturbations; the other two nonzero solutions to the characteristic equation (2.83) violate the condition that $\psi(\pm\mathfrak{a})$ have opposite sign. As β increases, the eigenvalue becomes positive, representing destabilization of the bump with respect to shift perturbations. Moreover, Figure 2.11 shows that beyond the point of instability we have $0 > \Psi(\mathfrak{a}) \equiv \psi(\mathfrak{a})/\psi(-\mathfrak{a}) > -1$, so that the width of the bump also increases. Since the shift instability occurs at smaller values of β that expansion perturbations, the former dominate bump instabilities in the case of the given Mexican hat weight function.

We summarize stability results in Figure 2.12, which shows the parameter space (α, β) divided into separability regions where either: no bumps exist (black); bumps are stable with respect to perturbations associated with real eigenvalues (dark grey); bumps are unstable (light grey). Even when the stability analysis of the expansion mode breaks down, bumps destabilize under shift perturbations. We conclude that strong enough synaptic depression can destabilize as stationary bump, which would be stable in the absence of depression.

2.2.5 Numerical simulations

We now study instabilities of bumps in the full system (2.36) using a numerical approximation scheme. To evolve the system in time, we use a fourth order Runge–Kutta method with 2000–4000 spatial grid points and a time–step of $dt = 0.01$. The integral term in equation (2.36a) is approximated using Simpson's rule. We systematically examined whether taking finer grids changed stability results, and it does not. This is important because too coarse a grid can drastically alter numerical results, since discreteness can stabilize bumps that are not stable in the continuous system [62]. For all of our numerical

simulations, we begin with an initial condition specified by an associated bump solution (2.44) that lies on the unstable part of the upper branch of the existence curves shown in Figure 2.8. After a brief period, we stimulate the system by adding an input perturbation to the variable $u(x,t)$ defined as

$$\psi_{\pm}(x,t) = \chi(t)(w(x+\mathfrak{a}) \pm w(x-\mathfrak{a})), \tag{2.84}$$

which is motivated by eigenmodes of the linearized Amari equation (1.3), which we calculate in Appendix A. Leftward shifts (rightward shifts) correspond to $\psi_{-}(x,t)$ when $\chi(t) \geq 0$ ($\chi(t) \leq 0$), while expansions (contractions) correspond to $\psi_{+}(x,t)$ when $\chi(t) \geq 0$ ($\chi(t) \leq 0$). The resulting dynamics depends specifically on the type of perturbation applied to the bump.

When shift perturbations destabilize a bump, the resulting dynamics evolves to a traveling pulse solution. As we showed in section 2.1.2, synaptic depression is a reliable mechanism for generating traveling pulses in excitatory neural fields [79, 80]. As illustrated in Figure 2.13, following a perturbation by a leftward shift, the bump initially expands and then starts to propagate. Eventually, the traveling pulse's width stabilizes to a constant value, larger than the initial bump width. The initial linear growth in the bump's width is consistent with our linear stability calculations. In other simulations, we found that as synaptic depression strength β is increased, the rate of linear growth in the width increases as well, which is also predicted by our stability analysis. In Figure 2.14, we show an example of how expansions destabilize the bump to result in two counter–propagating pulses. A closer look at the solution as a function of time immediately after the perturbation shows a transient phase, where the superthreshold region is still a connected domain, prior to the splitting into two pulses. As also predicted by our stability analysis, we found that contraction perturbations did not drive the system to the homogeneous zero state, unless their amplitude was large enough to drive the system to the other side of the separatrix given by the smaller unstable bump (see Figures 2.8 and A.1c). Finally, we found that, as predicted by our analysis, numerical simulations of bumps in a purely excitatory network ($A_i = 0$) always destabilize to two counter–propagating fronts that spread across the domain (see [79]).

In summary, our mathematical and numerical analysis of stationary bumps in the one–dimensional piecewise smooth neural field model (2.36) reveals several novel features compared to previous neural field models [3, 136, 39]. These are a consequence of the piecewise nature of the linear operator obtained by expanding about the stationary solution.

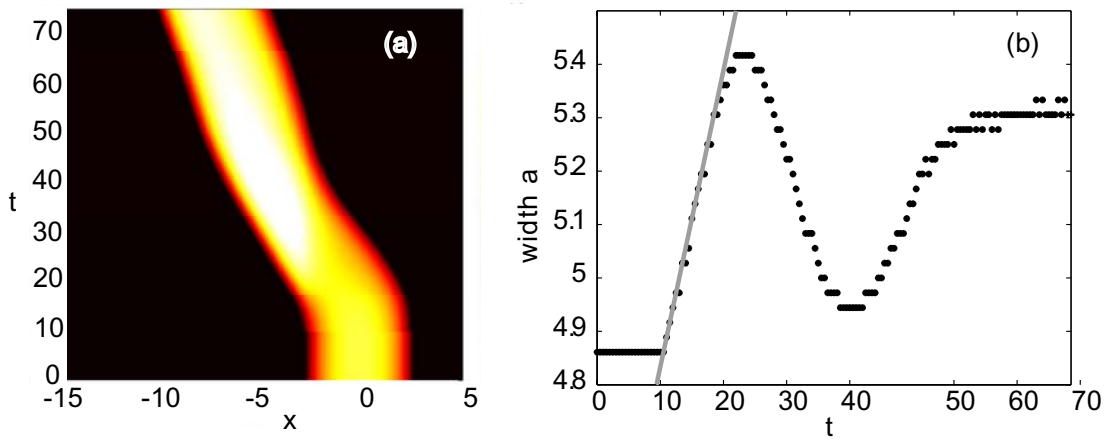

Figure 2.13. Numerical simulation of a bump destabilized by a leftward shift perturbation. (a) Plot of $u(x,t)$ for an initial condition taken to be a stationary bump specified by equation (2.44). Solution is perturbed at $t = 10$ by a leftward shift $\psi_-(x,t)$, such that $\chi(t) = -0.1$ for $t \in [10, 10.1]$ and zero otherwise. (b) Bump width plotted versus time. Bump width increases linearly following the perturbation, but eventually relaxes back to a constant value as the solution evolves to a traveling pulse. Parameters are $A_i = 0.3$, $\sigma_i = 4$, $\alpha = 50$, $\beta = 0.01$, $\theta = 0.1$.

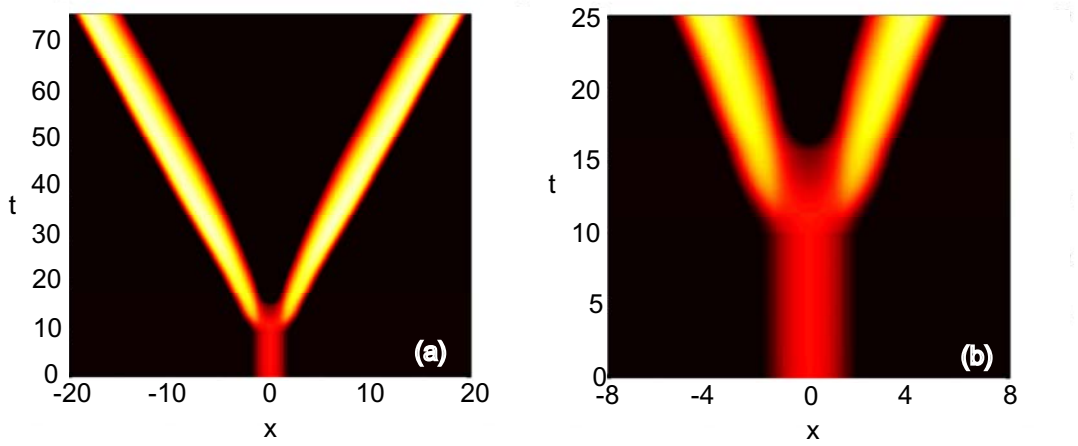

Figure 2.14. Numerical simulation of a bump destabilized by an expanding perturbation. (a) Plot of $u(x,t)$ for an initial condition taken to be stationary bump specified by (2.44). Solution is perturbed at $t = 10$ by an expansion $\psi_+(x,t)$, such that $\chi(t) = 0.1$ for $t \in [10, 10.1]$ and zero otherwise. (b) Plot of $u(x,t)$ for $t = 0$ to $t = 25$, showing initial expansion of the bump prior to splitting into two counter–propagating pulses. Parameters are $A_i = 0.3$, $\sigma_i = 4$, $\alpha = 50$, $\beta = 0.05$, $\theta = 0.1$.

First, shift perturbations that destabilize the bump are a combination of a pure shift and an expansion, rather than a pure shift, leading to an initial increase in the width of the bump prior to propagation as a traveling pulse. Second, there is an asymmetry between expansion and contraction modes, which have different spectra. Physically, this can be understood from the fact that neural populations just outside of the initial bump have maximal synaptic resources so they can recruit their nearest neighbors to continue spreading activity brought about by an initial expansion. On the other hand, neural populations within the interior of the bump do not possess the resources to continue the damping of activity via lateral inhibition brought about by an initial contraction. Finally, note that analyzing stability by formally Taylor expanding equation (2.36) about a bump solution for smooth sigmoidal f (2.4) and then taking the high–gain limit generates stability conditions that underestimate the effectiveness of synaptic depression in destabilizing the bump (see section 2.2.3), since they do not take proper account of the piecewise–smooth nature of the dynamics in the high–gain limit.

In Appendix B, we extend the work in this section to a neuronal network with spike frequency adaptation. In particular, we analyze the existence and stability of bumps in the system (1.8), developed by Coombes and Owen [42], noting the piecewise smooth nature of the system. However, in our stability calculations, we are not able to use the same trick we use here, of introducing a smoothed auxiliary variable (see equation (2.62)) in place of the negative feedback variable. We do show that, for a wide class of perturbations, the activity and adaptation variables decouple in the linear regime, allowing us to calculate stability in terms of a smooth linear operator. Bumps are always unstable with respect to this class of perturbations, and destabilization of the bump can result in either a traveling pulse or a spatially localized breather.

2.3 Synchronous oscillations

Shusterman and Troy [155] have recently shown that rhythmic activity can occur in the Pinto–Ermentrout model with linear adaptation and a Heaviside firing rate function provided that the strength of negative feedback β_p is sufficiently high, see system (1.7). In such a parameter regime, the space–clamped version of these equations exhibits bistability in which a stable rest state coexists with a stable limit cycle. A local stimulation of the corresponding spatially extended network can then lead to the emergence of synchronous oscillations that expand outwards, ultimately leading to synchronization of the whole net-

work. However, since the linear form of adaptation assumed in the Pinto–Ermentrout model is not directly related to physiological models of adaptation, it is difficult to determine whether or not a large value of β_p is reasonable. Indeed, the analysis of Benda and Herz [9] suggests that the negative feedback should be proportional to the firing rate which would be nonlinear in the case of a Heaviside firing rate function. It is also possible to generate oscillations when nonlinear adaptation is included, although it appears necessary to introduce different activation thresholds for the adaptation current and spiking [42] (see also Appendix B). Here we show how synaptic depression with or without spike frequency adaptation can generate oscillations in the system given by equation (2.1). Such oscillations arise when the firing rate function is taken to be the piecewise linear activation function (2.3) rather than a Heaviside function.

2.3.1 Phase space analysis

As a means of determining the oscillatory behavior of the system, we examine the equilibria of the space–clamped system [164, 7, 175]

$$\begin{aligned} \dot{u}(t) &= -u(t) + q(t)f(u(t) - a(t)), \\ \alpha\dot{q}(t) &= 1 - q(t) - \alpha\beta q(t)f(u(t) - a(t)), \\ \epsilon\dot{a}(t) &= -a(t) + \gamma f(u(t) - a(t)), \end{aligned} \tag{2.85}$$

where f is now taken to be the piecewise linear activation function (2.3) shown in Figure 2.1. To calculate equilibria of (2.85), we consider the possible solutions on the three domains of the piecewise function $f(J)$. We find that there is a low activity or Down state on the lower domain ($u-a<\theta$) for $\theta>0$ such that $(u,q,a)=(0,1,0)$. The stability of this Down state is determined by the eigenvalues of the Jacobian

$$\mathcal{J}(0,1,0) = \begin{pmatrix} -1 & 0 & 0 \\ 0 & -1/\alpha & 0 \\ 0 & 0 & -1/\epsilon \end{pmatrix} \tag{2.86}$$

and is therefore stable for all realistic parameters. We find additional equilibria by solving (2.85) on the middle and upper domains of f. On the middle domain ($\theta \le u-a \le \theta+\sigma^{-1}$), where $f(J)=\sigma(J-\theta)$, we have

$$
\begin{aligned}
u &= \sigma(u-a-\theta)q, && (2.87)\\
q &= 1/(1+\sigma\alpha\beta(u-a-\theta)), && (2.88)\\
a &= \sigma\gamma(u-a-\theta), && (2.89)\\
\theta &\leq u-a \leq \theta+\sigma^{-1}, && (2.90)
\end{aligned}
$$

which has solutions

$$
\begin{aligned}
u &= \frac{\phi-(1+\phi)\gamma-\phi\theta\alpha\beta\pm\sqrt{\mathcal{D}_p}}{\alpha\beta(\phi+(1+\phi)\gamma-\phi\theta\alpha\beta\pm\sqrt{\mathcal{D}_p})} && (2.91)\\
q &= \frac{2(1+\phi)\gamma}{\phi+(1+\phi)\gamma-\phi\theta\alpha\beta\pm\sqrt{\mathcal{D}_p}} && (2.92)\\
a &= \frac{\phi-(1+\phi)\gamma-\phi\theta\alpha\beta\pm\sqrt{\mathcal{D}_p}}{2(1+\phi)\alpha\beta} && (2.93)\\
\mathcal{D}_p &= (\phi-(1+\phi)\gamma-\phi\theta\alpha\beta)^2-4\phi\gamma\theta(1+\phi)\alpha\beta, \quad \phi=\sigma\gamma, && (2.94)
\end{aligned}
$$

provided $\mathcal{D}_p \geq 0$ and condition (2.90) is satisfied. Stability is determined by the eigenvalues of the Jacobian

$$
\mathcal{J}(u,q,a) = \begin{pmatrix} -1+\sigma q & \sigma(u-a-\theta) & -\sigma q \\ -\beta\sigma q & -(1/\alpha+\beta\sigma(u-a-\theta)) & \beta\sigma q \\ \gamma\sigma/\epsilon & 0 & -(1+\gamma\sigma)/\epsilon \end{pmatrix}. \qquad (2.95)
$$

We find that for a wide range of parameters, the middle domain contains two equilibria, one of which is a saddle and the other is a stable or unstable spiral. The latter corresponds to a high activity or Up state. For sufficiently fast depression and/or adaptation, destabilization of the Up state can lead to the formation of a stable limit cycle via a Hopf bifurcation, see Figures 2.15 and 2.16. In parameter regimes where the spiral equilibrium does not exist, the Up state occurs on the upper domain ($u-a > \theta+\sigma^{-1}$), where $f(J)=1$, and is given by

$$
\begin{aligned}
u &= 1/(1+\alpha\beta), && (2.96)\\
q &= 1/(1+\alpha\beta), && (2.97)\\
a &= \gamma. && (2.98)
\end{aligned}
$$

Its stability is determined by the eigenvalues of the Jacobian

$$
\mathcal{J}(u,q,a) = \begin{pmatrix} -1 & 1 & 0 \\ 0 & -(1/\alpha+\beta) & 0 \\ 0 & 0 & -1/\epsilon \end{pmatrix}, \qquad (2.99)
$$

which guarantees that such an Up state is always stable.

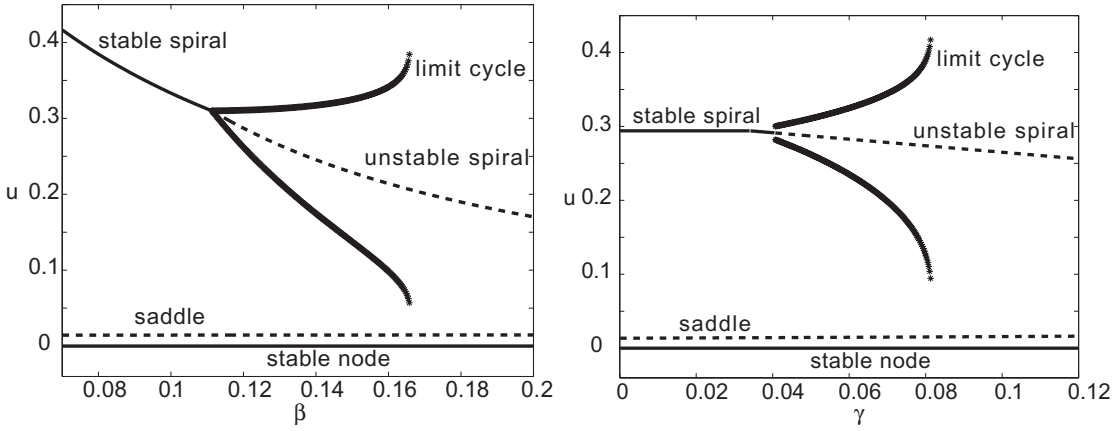

Figure 2.15. Equilibria of space–clamped neuronal network with synaptic depression and adaptation and piecewise–linear firing rate. (Left) Bifurcation diagram showing fixed points u of the system (2.85) as a function of β for piecewise–linear firing rate (2.3). Other parameters are $\gamma = 0.05$, $\epsilon = 5$, $\alpha = 20$, $\theta = 0.01$ and $\sigma = 4$. Linear stability is determined using the eigenvalues of the Jacobian given by (2.95). Stable (unstable) branches are shown as solid (dashed) curves, whereas the stable limit cycle is shown as a thick solid curve. (Right) Corresponding bifurcation diagram showing u as a function of γ for $\beta = 0.12$.

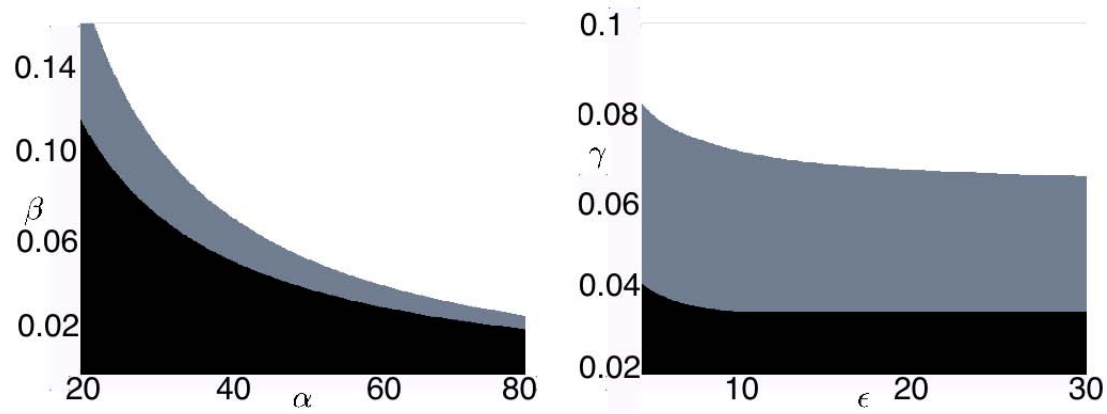

Figure 2.16. Stability maps of space–clamped neuronal network with synaptic depression and adaptation. (Left) Stability diagram in the (α,β)–plane showing where the Up state is a stable spiral (black) , an unstable spiral surrounded by a stable limit cycle (grey), or an unstable spiral without a limit cycle (white). (Right) Corresponding stability diagram in the (ϵ,γ)–plane. Other parameters are as in Figure 2.15

In Figure 2.17 we show a simulation of the space–clamped network for a choice of parameters that supports a limit cycle. The parameter values are consistent with physiological measurements and previous models, for which the synaptic depression time constant α is in the range 200–800ms [2, 170] and the adaptation time constant ϵ is in the range 20–80ms [9, 109, 162]. Notice that all variables oscillate at a period of roughly 30 time units or 300ms, which correlates nicely with the timescale of epileptiform events in slice and *in vivo* [183, 67, 155, 126] (see section 1.2.2 for a discussion of other experimentally observed neural activity oscillations). It also indicates that the synaptic depression timescale sets the period of oscillations in our model. Indeed, spike frequency adaptation as realized in this model does not play a major role in generating oscillations. The network can also support self–sustained oscillations in the absence of adaptation ($\gamma = 0$), which we will discuss more in section 3.1. One major difference from the Pinto–Ermentrout model with large negative feedback is that the equilibrium spiral in our model is associated with an Up state rather than a Down or rest state [168].

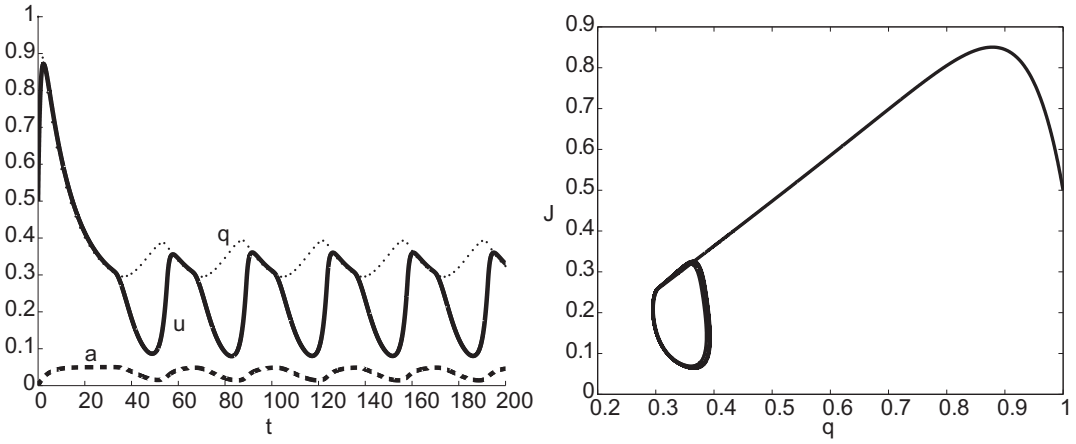

Figure 2.17. Numerical simulation of the space–clamped system (3.4) using the parameters $\theta = 0.01$, $\sigma = 4$, $\alpha = 50$, $\beta = 0.06$, $\epsilon = 4$, and $\gamma = 0.05$. (Left) Plot of u, q, and a trajectories in time. As predicted by linear stability analysis, the solution settles into a limit cycle about the Up state. (Right) A plot in the (q,J) phase plane, where $J = u - a$ is the total current input to the firing rate function $f(J)$. Notice that at its lowest point, J dips below the value corresponding to the mean value of f: $(J,f(J))$=(0.135,0.5).

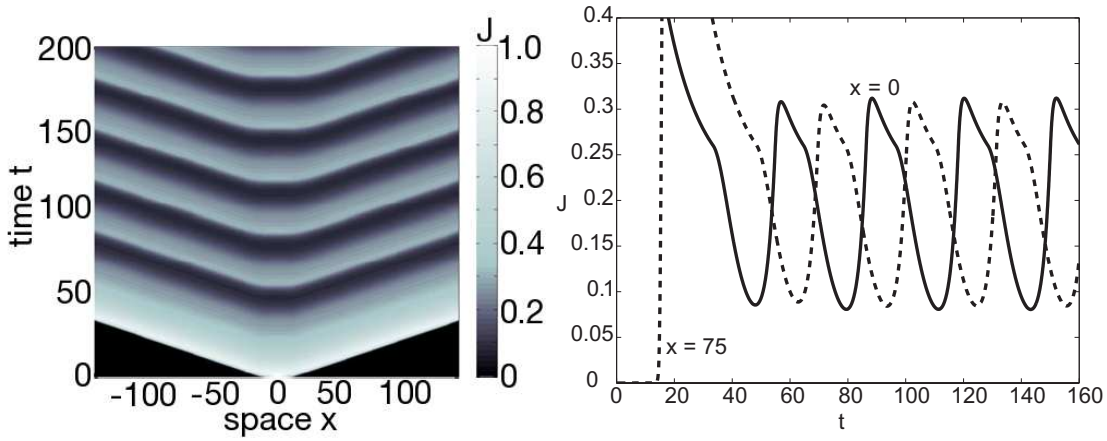

Figure 2.18. Self–sustained oscillations in space. (Left) Numerical simulation of the system (2.1) when the firing rate is the piecewise linear function (2.3). An initial Gaussian activity profile evolves into a core of oscillatory activity that emits outward propagating pulses. These pulses of activity arise due to neighboring cells oscillating with a spatially–dependent phase shift. Although the baseline current is not subthreshold in the sense of causing no firing rate, it is relatively small compared to the pulse amplitude. We plot the evolution of input current J in pseudocolor as a function of space x and time t. Notice that the oscillating core is relatively confined in this long time interval and hardly expands outward at all. Parameters are $\theta = 0.01$, $\alpha = 50$, $\beta = 0.05$, $\epsilon = 4$, and $\gamma = 0.05$. (Right) Corresponding trajectories of current J at two spatial locations.

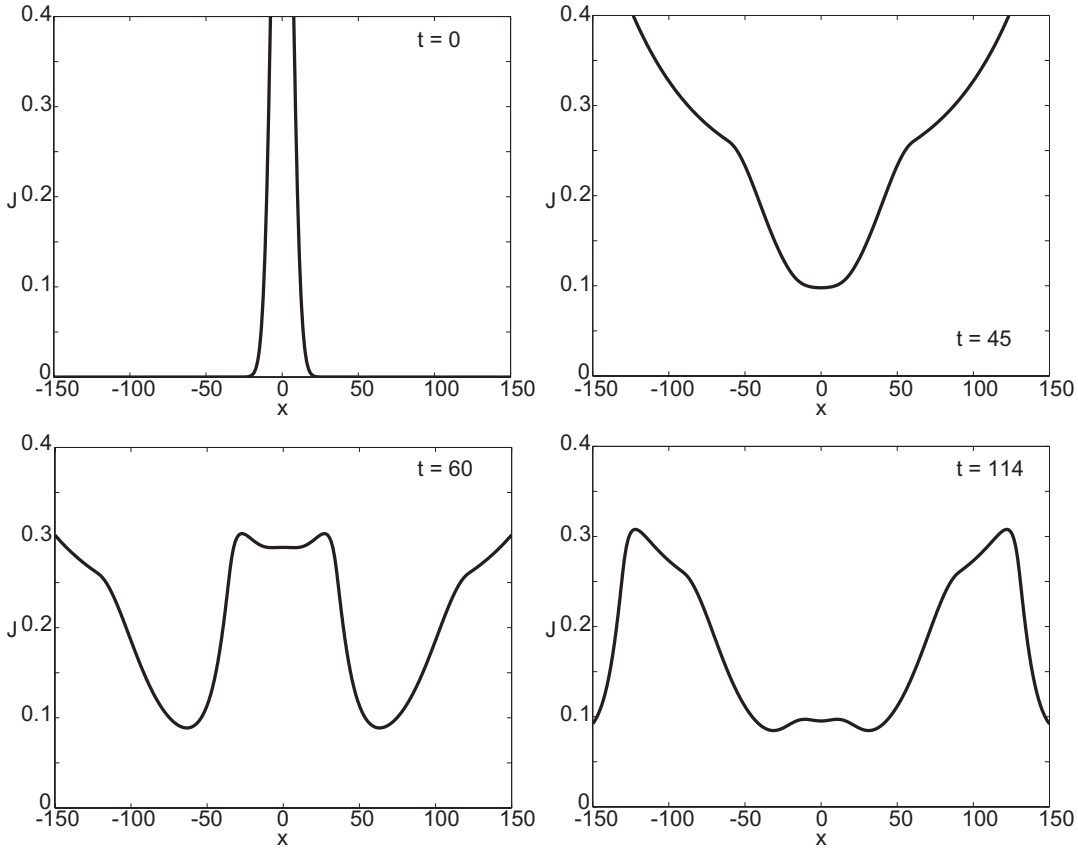

Figure 2.19. Snapshots of total input current $J(x,t)$ as a function of space x for times (Top left) $t = 0$; (Top right) $t = 45$; (Bottom left) $t = 65$; and (Bottom right) $t = 139$. Oscillating core is centered at $x = 0$ and periodically emits pulses of activity after an initial traveling front.

2.3.2 Spatially extended model

A number of previous studies have shown how a space–clamped system with synaptic depression can support oscillations in population activity [164, 7]. However, as far as we are aware, the evolution of self–sustained oscillations in space and time has not been explored before in such a system. Therefore, we extend the results of section 2.3.1 by examining the behavior of the full system (2.1) in the case of the piecewise linear activation function (2.3) and for the same range of parameter values for depression and adaptation as the space–clamped case. We take an initial condition in the form of a Gaussian

$$(u(x,0),q(x,0),a(x,0)) \quad = \quad (\mathcal{I}\mathrm{e}^{-x^2/\zeta^2},1,0), \tag{2.100}$$

where $\mathcal{I}=0.5$ and $\zeta=15$ are the amplitude and width of the Gaussian. We numerically solve (2.1) using fourth–order Runge–Kutta with timestep $\Delta t=0.01$ and Riemann integration on 4000 gridpoints for the convolution term, verifying that the time and space steps were small enough so that they did not to affect the qualitative behavior. Boundary points evolve freely, and the domain is chosen to be large enough that the oscillating core is unaffected by boundaries. In Figure 2.18 we show a simulation wherein an oscillating core of activity generates outward propagating pulses. Note that this self–sustaining activity does not require continuous input [55] nor does the nondimensionalized synaptic input current go below zero [155, 168, 167]. As seen in the snapshots of Figure 2.19, the oscillating core expands extremely slowly, remaining localized to the area of initial input on the timescale of several seconds. As mentioned above, the network supports similar behavior in the absence of spike frequency adaptation ($\gamma=0$), as illustrated in Figure 2.20.

Note that the system (2.1) also supports solitary traveling pulses in the case of the piecewise linear activation function (2.3). However, such pulses do not exist in the same parameter range as synchronous oscillations. Although we cannot derive rigorous conditions for the existence of traveling pulses, as we did in section 2.1.2 for a Heaviside firing rate function, we can numerically simulate traveling pulses as illustrated in Figure 2.20 for a pair of counter–propagating waves. Similar to the traveling pulse shown in Figure 2.4, a pulse is defined by the region where $J(\xi)\geq\theta$, and $J(\xi)<\theta$ otherwise. Hence, although the Heaviside firing rate function is very useful for carrying out a detailed analysis of spatiotemporal dynamics in neural field models, it cannot capture all solutions that arise when a more realistic firing rate function is considered.

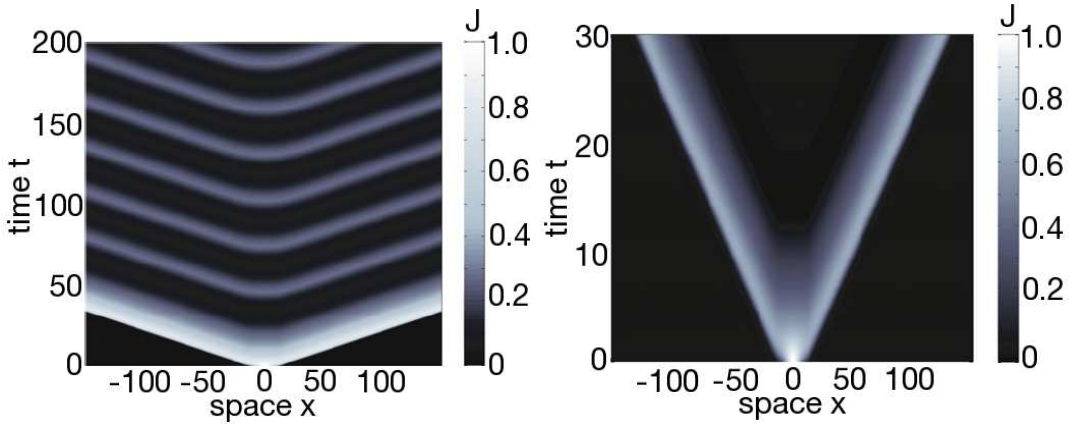

Figure 2.20. (Left) Self–sustained oscillations with no adaptation. As in Figure 2.18, we find a pulse–emitting core that oscillates synchronously, and in this case adaptation is not necessary to sustain these dynamics. We plot the evolution of input current J in pseudocolor as a function of space x and time t. Parameters are $\theta = 0.01$, $\alpha = 50$, $\beta = 0.1$, and $\gamma = 0$. (Right) Two counter–propagating pulses supported by the system (2.1) in the case where the activation function f is piecewise linear as defined in (2.3). Initial condition is taken to be the Gaussian defined in (2.100). Parameters are $\alpha = 20$, $\beta = 0.2$, $\gamma = 0.1$, $\epsilon = 5$, $\theta = 0.01$, and $\sigma = 4$.

2.4 Discussion

In this chapter, we analyzed the spatiotemporal dynamics of a neuronal network with two physiologically based forms of nonlinear negative feedback – synaptic depression and spike frequency adaptation. Both depression and adaptation were introduced as dynamically evolving variables that depend on the output firing rate. We showed that traveling fronts and pulses exist over a reasonable range of parameters, and that adaptation plays little or no role in determining the wavespeed and pulsewidth. Stationary pulses or bumps also exist if adaptation is removed. In analyzing their stability, we found that we had to address the piecewise smooth nature of the system by keeping track of the sign of perturbations. Thus, we find sufficient conditions for the destabilization of bumps for sufficiently strong depression. Finally, when the firing rate function is taken to be piecewise linear, self–sustained oscillations exist in the spatially extended network. A localized region of synchronous activity repetitively emits traveling pulses with each oscillation. Self–sustained oscillations and stationary superthreshold activity have been observed in real neural tissue, both in slice [183, 126] and *in vivo* [126, 155]. While the frequency of oscillations seems to match nicely with that observed in experiments (1–10 Hz), the spatial

scale of emitted traveling pulses seems to be much longer. That is, assuming that synaptic connections have a range of 1mm, the width of pulses ranges between 5–30mm, whereas those in slice tend to be roughly 1mm [136, 184, 182].

In the next chapter, we will examine the behavior of self–sustained oscillatory solutions as well as stationary bumps in two dimensions. In previous work, Fourier analysis has been used to predict how the symmetry of circular bumps is broken when they are perturbed [56, 133, 98]. Troy and Shusterman have shown that the Pinto–Ermentrout model supports self–sustained oscillations in two dimensions when the symmetry of a ring wave is broken [168]. In the space–clamped model with only synaptic depression, noise provides a means of transitioning between the Up and Down states [7]. Including noise of the appropriate form in our model will lead to interesting behavior in the spatially extended case.

CHAPTER 3

TWO–DIMENSIONAL NEURONAL NETWORK WITH SYNAPTIC DEPRESSION

In this chapter, we show how various forms of spatially structured oscillations, including spiral waves and pulse emitters, can occur in a two–dimensional neuronal network with a physiologically based form of nonlinear negative feedback, namely, synaptic depression. In the previous chapter, we considered the combined effects of synaptic depression and spike frequency adaptation on the spatiotemporal dynamics of a one–dimensional excitatory network. We showed that synaptic depression tends to dominate the dynamics, providing a mechanism for generating spatially localized oscillations. Here we extend our analysis to two dimensions and to the case of noisy networks. For simplicity, we ignore the effects of spike frequency adaptation since they tend to be relatively weak.

Thus, we consider a neuronal network model that includes negative feedback only in the form of synaptic depression [2, 7, 116, 164, 169, 189]

$$\tau \frac{\partial u(\mathbf{r},t)}{\partial t} = -u(\mathbf{r},t) + \int_{\mathbb{R}^2} w(|\mathbf{r}-\mathbf{r}'|) q(\mathbf{r}',t) f(u(\mathbf{r}',t)) \mathrm{d}\mathbf{r}' \tag{3.1a}$$

$$\frac{\partial q(\mathbf{r},t)}{\partial t} = \frac{1-q(\mathbf{r},t)}{\alpha} - \beta q(\mathbf{r},t) f(u(\mathbf{r},t)), \tag{3.1b}$$

where $\mathbf{r}$ and $\mathbf{r}'$ are spatial positions in the two–dimensional plane $\mathbb{R}^2$. Equation (3.1a) describes the evolution of the synaptic current or drive $u(\mathbf{r},t)$ in the presence of synaptic depression, which takes the form of a synaptic scaling factor $q(\mathbf{r},t)$ evolving according to equation (3.1b). The factor $q(\mathbf{r},t)$ can be interpreted as a measure of available presynaptic resources, which are depleted at a rate βf [169, 7, 164], and are recovered on a timescale specified by the constant α (experimentally shown to be 200–1500ms [2, 170, 169, 161]). In the previous chapter, we considered a one–dimensional model with synaptic depression and adaptation and showed that adaptation has a relatively small effect on the dynamics. Therefore, we focus on synaptic depression here. It will be convenient in the following to

fix parameters so that f is interpreted as the fraction of the maximum firing rate, that is $0 \leq f \leq 1$. We fix the temporal scale of the network by setting $\tau = 1$. The membrane time constant is typically around 10 ms.

Most of our analysis and numerics are carried out for a general piecewise linear firing rate function (2.3) that attains saturation. We use this continuous function to study existence and stability of oscillatory solution in the network with depression (sections 3.1 and 3.2). In the high gain limit ($\sigma \to \infty$), we recover a Heaviside firing rate function (2.2). We will use such a function in order to study target waves and stationary bumps (see section 3.3). We compare the piecewise linear (2.3), sigmoid (2.4), and Heaviside (2.2) functions in Figure 2.1 (see beginning of Chapter 2).

The homogeneous weight distribution $w(|\mathbf{r} - \mathbf{r}'|)$ defines the strength of the synaptic connections between neurons at $\mathbf{r}$ and $\mathbf{r}'$, depending only on the distance between two cells. As in the case of the one–dimensional system in the previous chapter, we consider two different forms for the weight function w of the two–dimensional network in this chapter. To represent a homogeneous excitatory network, we will take w to be given by a difference of modified Bessel functions of the second kind: [55, 93, 133]

$$w(r) \quad = \quad \frac{2w_0}{3\pi d} \left(K_0(r/d) - K_0(2r/d) \right), \tag{3.2}$$

where w_0 determines the strength of the synaptic connections. The use of the weight function (3.2) is motivated by studies of traveling waves, oscillations, and spiral waves (sections 3.1, 3.2, and 3.3.1) of activity in epileptiform tissue or cortical slice, where inhibition is mostly absent [126, 67]. The factor $2/3\pi$ ensures that equation (3.2) is a very good fit to the exponential weight function

$$w(r) = \frac{w_0}{2\pi d} \mathrm{e}^{-r/d}.$$

The expansion in terms of Bessel functions is particularly convenient because it allows us to transform the system (3.1) into a fourth order PDE, which is computationally less expensive to simulate [98, 93, 168, 133] (see section 3.2). In our studies employing the excitatory weight function (3.2), we fix the spatial scale by setting $d = 1$, noting the length scale of synaptic connections within cortex is typically of the order 1mm. We also fix synaptic strength by setting $w_0 = 1$. The effects of varying w_0 are briefly discussed at the end of section 3.1. We represent a homogeneous network with lateral inhibition

by taking w to be a Mexican hat weight distribution given by a combination of modified Bessel functions of the second kind

$$w(r) = \frac{2}{3\pi}\left(K_0(r) - K_0(2r) - A_i(K_0(r/\sigma) - K_0(2r/\sigma_i))\right), \tag{3.3}$$

where A_i is the relative strength of inhibition, σ_i is the relative scale of inhibition, and the spatial scale of excitation is taken to be 1mm. Use of this Mexican hat weight function (3.3) is motivated by experimental studies of standing pulses (or bumps) of activity in prefrontal cortex, where lateral inhibition is present and required for stabilization of the bumps (see sections 3.3.2 and 3.3.3). Such a weight function is qualitatively similar to a difference of exponential weight functions

$$w(r) = (2\pi)^{-1}(\mathrm{e}^{-r} - A_i\mathrm{e}^{-r/\sigma_i}).$$

With this model of a two–dimensional slice of cortical tissue, we study the spatiotemporal dynamics of activity it supports that relate to experiments of tangential slices, epileptiform tissue, and prefrontal cortex. We begin by analyzing the space–clamped version of the model, and show that it supports a stable limit cycle in the absence of noise (section 3.1). However, in the presence of additive white noise, the parameter regime over which oscillations can occur can be significantly widened. In section 3.2 we present a number of numerical simulations illustrating various two–dimensional spatiotemporal activity patterns supported by the full network model. Depending on the initial conditions, we show that in the absence of noise, network activity can evolve as a pulse–emitting oscillating core or as a spiral wave. Furthermore, addition of a small amount of spatially uncorrelated noise to a quiescent network can drive pockets of the system superthreshold and lead to discrete locations of pulse–emitting cores. On the other hand, large amounts of noise lead to bulk oscillations which can disrupt any spatially structured activity. We also show that when a radially symmetric stimulus is applied to the network in the presence of noise, spiral waves can be generated due to symmetry breaking, similar to the organized activity found in mammalian cortical slice [67, 148]. Finally, we study the system in the high gain limit (section 3.3). In this case, oscillations do not exist in the deterministic system, but depression is a sufficient mechanism for generating outward propagating target waves following a brief stimulus. We can also extend our piecewise smooth analysis of bumps to the two–dimensional case for symmetric perturbations, revealing qualitatively similar results to the one–dimensional case regarding their destabilization.

3.1 Oscillations in the space–clamped system

Previous modeling studies of space–clamped neuronal networks with synaptic depression showed the existence of oscillations in the case of excitatory/inhibitory networks [169] or for a purely excitatory network with noise [7]. Tabak and colleagues showed that an excitatory network with depression could support regular oscillations and bursting, using an alternative form for the neural field equation as well as different gains and thresholds for each variable's activation function [164]. In our study, we find that saturation of the activation function is sufficient to stabilize limit cycles using the same activation function for both the activity and depression variables.

3.1.1 Phase plane for piecewise linear firing rate

As a means of determining the oscillatory behavior of the system, we examine the equilibria of the space–clamped system [7, 164, 169]

$$\begin{aligned} \dot{u}(t) &= -u(t) + q(t)f(u(t)), \\ \alpha\dot{q}(t) &= 1 - q(t) - \alpha\beta q(t)f(u(t)), \end{aligned} \tag{3.4}$$

where f is the piecewise linear activation function (2.3) shown in Figure 2.1. We carry out the stability analysis of phase space using the piecewise linear function because explicit analytical expressions can be derived for the fixed points. However, these results extend to the case where there is a smooth transition from the linear to the saturated portion of the firing rate.

To calculate equilibria of (3.4), we consider the possible solutions on the three domains of the piecewise function $f(u)$. We find that there is a low activity or Down state on the lower domain ($u < \theta$) for $\theta > 0$ such that $(u, q) = (0, 1)$. The stability of this Down state is determined by the eigenvalues of the Jacobian

$$\mathcal{J}(0,1) = \begin{pmatrix} -1 & 0 \\ 0 & -1/\alpha \end{pmatrix} \tag{3.5}$$

and is therefore stable for all realistic parameters. A stable Down state exists in the network for any f with a hard threshold, that is $f(u) = 0$ for $u < \theta$. Without this condition, it is possible that the Down may destabilize or vanish due to a nonzero firing rate existing for zero synaptic drive.

We find additional equilibria by solving (3.4) on the middle and upper domains of f. On the middle domain ($\theta \leq u \leq \theta + \sigma^{-1}$), where $f(u) = \sigma(u - \theta)$, we have

$$
\begin{aligned}
u &= \sigma(u-\theta)q, && (3.6)\\
q &= 1/(1+\sigma\alpha\beta(u-\theta)), && (3.7)\\
\theta &\leq u \leq \theta+\sigma^{-1}, && (3.8)
\end{aligned}
$$

which has solutions

$$
\begin{aligned}
u &= \frac{\sigma+\sigma\alpha\beta\theta-1\pm\sqrt{\mathcal{D}}}{2\sigma\alpha\beta} && (3.9)\\
q &= \frac{2}{1+\sigma-\sigma\alpha\beta\theta\pm\sqrt{\mathcal{D}}} && (3.10)\\
\mathcal{D} &= (\sigma+\sigma\alpha\beta\theta-1)^2-4\sigma^2\alpha\beta\theta
\end{aligned}
$$

provided $\mathcal{D}\geq 0$ and condition (3.8) is satisfied. Stability is determined by the eigenvalues of the Jacobian

$$
\mathcal{J}(u,q) = \begin{pmatrix} -1+\sigma q & \sigma(u-\theta) \\ -\beta\sigma q & -(1/\alpha+\beta\sigma(u-\theta)) \end{pmatrix}. \qquad (3.11)
$$

We find that for a wide range of parameters, the middle domain contains two equilibria, one of which is a saddle and the other is a stable or unstable focus. The latter corresponds to a high activity or Up state. For sufficiently fast depression, destabilization of the Up state can lead to the formation of a stable limit cycle via a subcritical Hopf bifurcation as pictured in Figure 3.1. In parameter regimes where the focus equilibrium does not exist, the Up state occurs on the upper domain ($u>\theta+\sigma^{-1}$), where $f(u)=1$, and is given by

$$
\begin{aligned}
u &= 1/(1+\alpha\beta), && (3.12)\\
q &= 1/(1+\alpha\beta). && (3.13)
\end{aligned}
$$

Its stability is determined by the eigenvalues of the Jacobian

$$
\mathcal{J}(u,q,a) = \begin{pmatrix} -1 & 1 \\ 0 & -(1/\alpha+\beta) \end{pmatrix}, \qquad (3.14)
$$

which guarantees that such an Up state is always stable.

In Figure 3.2 we show a simulation of the space–clamped network for a choice of parameters that supports a limit cycle. The parameter value for synaptic depression time constant α is taken to be within the physiological range 200–1500ms [2, 169]. Notice that both variables oscillate at a period of roughly 40 time units or 400ms, which correlates well with the scale of epileptiform events [31, 119, 126, 155]. This also implies that the timescale

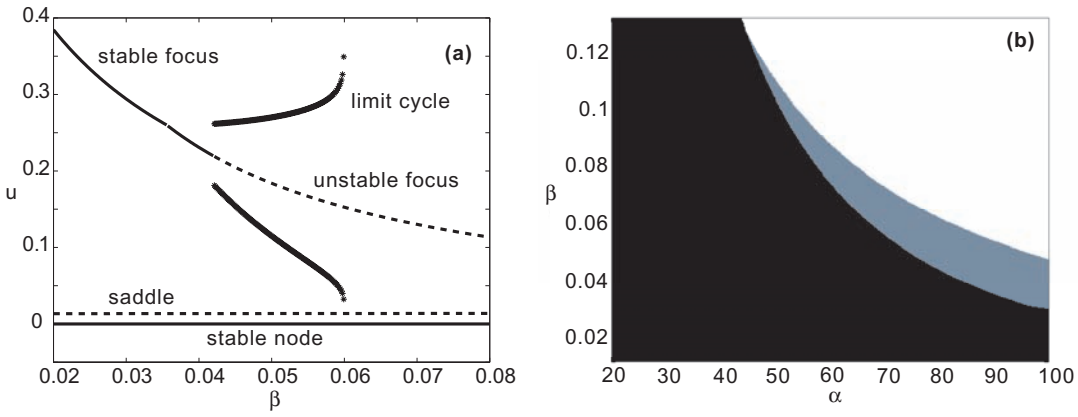

Figure 3.1. Equilibria of space–clamped neuronal network with synaptic depression and piecewise–linear firing rate. (a) Bifurcation diagram showing fixed points u of the system (3.4) as a function of β for $\alpha = 80$. (b) Stability diagram for the space–clamped system (3.4) showing regions in parameter space where the Up state is a stable focus (black), an unstable focus surrounded by a stable limit cycle (grey), or an unstable focus without a limit cycle (white) . Other parameters are $\theta = 0.01$, and $\sigma = 4$.

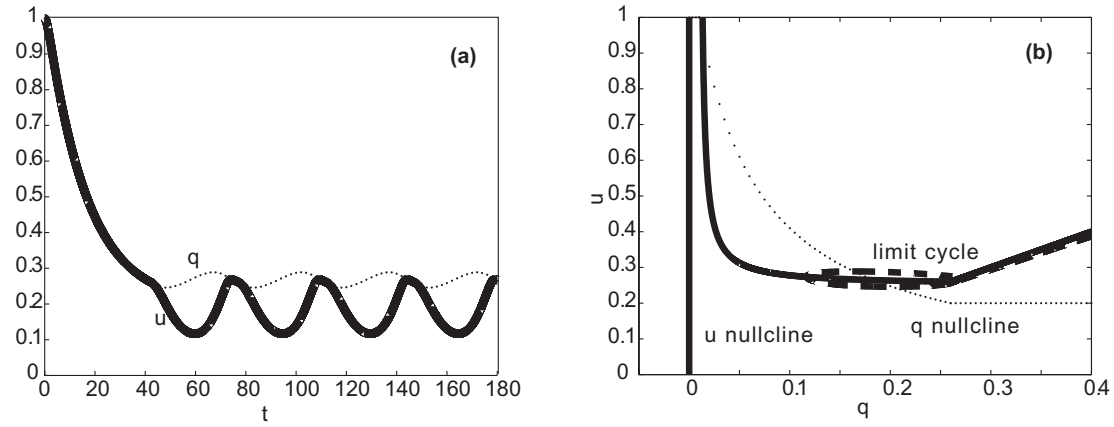

Figure 3.2. Limit cycles in space–clamped neuronal network with synaptic depression. (a) Numerical simulation of (3.4) using the parameters $\theta = 0.01$, $\sigma = 4$, $\alpha = 80$, and $\beta = 0.05$ given the initial condition $(u,q) = (1,1)$. The synaptic input u and fraction of available resources q are plotted as a function of time t. Oscillations lock to a period roughly determined by the time constant α. (b) Corresponding phase–plane plot of q versus u (dashed line) showing that the system supports a stable limit cycle.

of oscillations is roughly set by the time constant of synaptic depression. Notice that as opposed to self sustained oscillations in the Pinto–Ermentrout model [155], the equilibrium focus in our model is associated with the Up rather than the Down or rest state. As stated, these results easily extend to the case where f is a smooth, saturating function above the threshold value $u = \theta$. In particular, since limit cycles are structurally stable solutions in continuous systems, oscillations persist when $f(u)$ is modified by smoothing out the corner at $u = \theta + 1/\sigma$. However, without a hard threshold at $u = \theta$, we have not witnessed the same types of dynamics as presented here for the piecewise linear f. If oscillations exist, a stable Down state does not, which we show in an analysis of the system with a sigmoidal firing rate function (2.4).

3.1.2 Phase plane for sigmoidal firing rate

We use a numerical root finding algorithm to identify the equilibria of the system (3.4) in the case where f is the sigmoidal function (2.4). It is possible to find parameter regimes where limit cycles exist, but they do not coincide with a stable Down state, as in the piecewise linear f case. We show an example of one such limit cycle in Figure 3.3, showing the limit cycle employs the lower knee of the u–nullcline as a turing point from the Down to the Up state. There is no such mechanism in the limit cycle present in the piecewise linear system. This distinction points out that the loss of a hard threshold may in fact change the overall topology of dynamics within the network. Rather than finding an excitable regime with limit cycles about the Up state, we find either a purely oscillatory regime, or an excitable regime with no limit cycles.

3.1.3 Space–clamped system with noise

A previous study of the space–clamped system (3.4) with f given by (2.3) considered parameter regimes in which the subcritical Hopf bifurcation of the Up state only produced an unstable limit cycle [7]. In this case the authors showed that oscillations could be generated in the presence of additive noise, which switched the system between the Up and Down states (see also [66]). It follows that noise enlarges the parameter regime over which self–sustained oscillations can occur. We illustrate the effects of additive noise by simulating the system

$$\begin{aligned} \dot{u}(t) &= -u(t) + q(t)f(u(t)) + \gamma\nu(t), \\ \alpha\dot{q}(t) &= 1 - q(t) - \alpha\beta q(t)f(u(t)), \end{aligned} \tag{3.15}$$

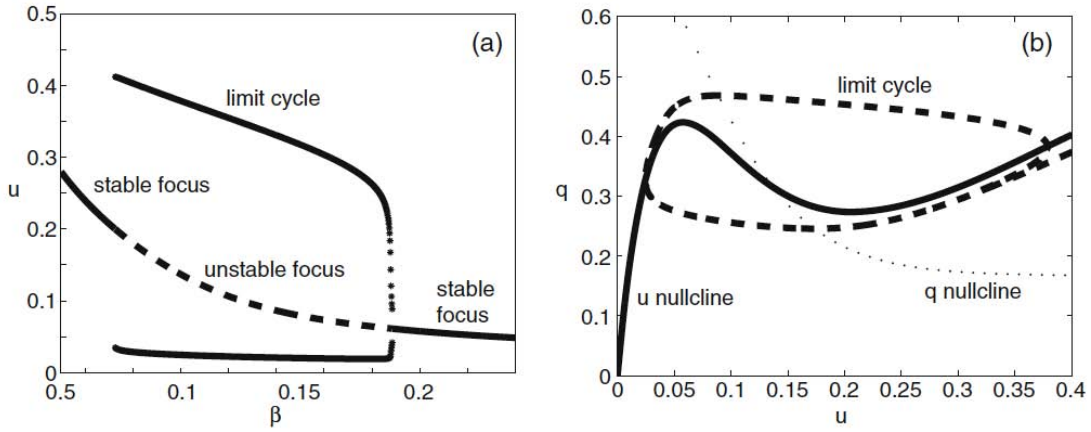

Figure 3.3. Limit cycle in space–clamped neuronal network with synaptic depression and sigmoid firing rate. (a) Bifurcation diagram showing fixed points u of the system (3.4) as a function of β for $\alpha = 50$. (b) Phase–plane plot of q versus u (dashed line) showing the system supports a limit cycle. Other parameters are $\theta_s = 0.15$, and $\sigma = 20$.

where f is the piecewise linear function (2.3), $\nu(t)$ is a Gaussian white noise process such that $\langle \nu(t) \rangle = 0$, and $\langle \nu(s)\nu(t) \rangle = 2\delta(t-s)$; γ is the noise strength. We simulated the system (3.15) using an Euler–Maruyama scheme for stochastic differentiation with a timestep $\Delta t = 10^{-6}$. The nature of the noise–induced oscillations depends upon whether the Up state is a stable or unstable focus. In the case of a stable focus, even though oscillations are damped out eventually in the deterministic system, noise is sufficient to repeatedly drive the system between the Up and Down states, along analogous lines to [7]. However, the oscillations tend to be rather irregular as illustrated in Figure 3.4.

More regular noise–induced oscillations occur in the case of an unstable focus. Equations (3.15) now represent an excitable system with only a stable Down state, in which noise periodically drives the system above threshold, leading to an elevated firing rate that then relaxes back down as synaptic depression is activated. An example simulation is shown in Figure 3.5, which neatly illustrates the regularity of the noise–induced oscillations. This is an example of a well known stochastic property of excitable systems, namely, coherence resonance [107]. That is, there exists an optimal level of noise with respect to the degree of regularity of the induced oscillations; if the level of noise is too high then this completely washes out any oscillations. We conclude that noise extends the parameter range over which the space–clamped system supports oscillations to include regions where the underlying deterministic system supports a stable or unstable focus without a stable limit cycle. This

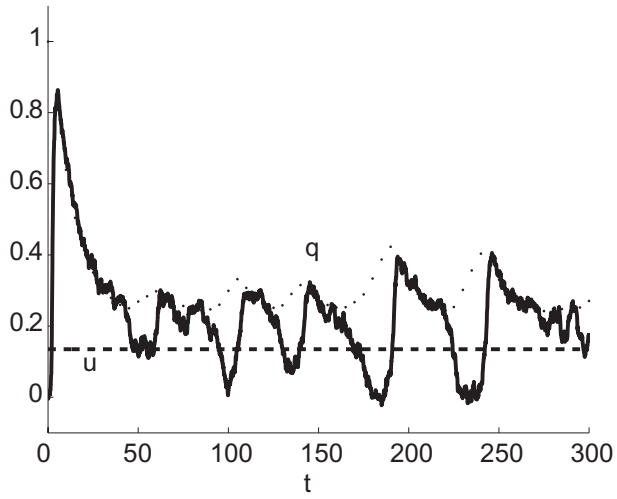

Figure 3.4. Numerical simulation of the space–clamped system (3.15) in which background noise drives the system between Up and Down states. The horizontal dashed line denotes the input current value at which activity is half of its maximal value ($\theta_s = 0.135$). Firing rate is taken to be piecewise linear function (2.3). Parameters are $\alpha = 60$, $\beta = 0.06$, $\gamma = 0.02$, $\theta = 0.01$, and $\sigma = 4$. In the absence of noise, the Up state is a stable focus.

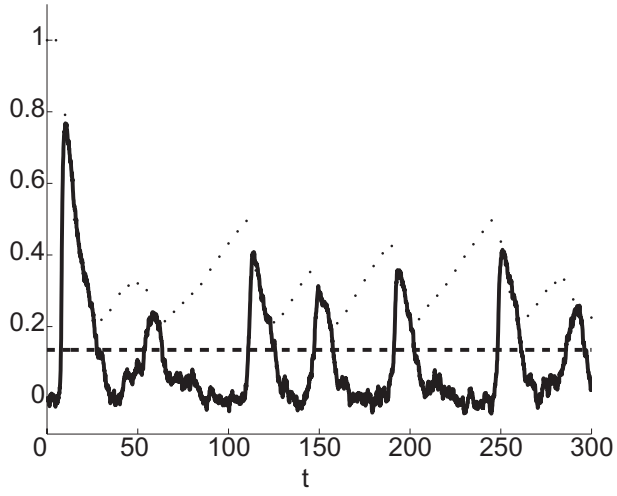

Figure 3.5. Numerical simulation of the space–clamped system (3.15) in which noise initiates superthreshold portion of Up and Down state oscillations. The horizontal dashed line denotes the input current value at which activity is half of its maximal value ($\theta_s = 0.135$). Firing rate is taken to be piecewise linear function (2.3). Parameters are $\alpha = 80$, $\beta = 0.06$, $\gamma = 0.02$, $\theta = 0.01$, and $\sigma = 4$. In the absence of noise, the Up state is an unstable focus.

also has important implications for the effects of noise in the spatially extended system (see section 3.2).

Bart and colleagues [7] showed that changing the synaptic strength w_0 can also alter the stability of the Up state of the system (3.4), whilst keeping all other parameters fixed. Stronger synapses (higher w_0) stabilize the Up state, while weaker synapses (lower w_0) destabilize it. Consistent with these observations, we found that changing w_0 alters the parameter ranges of α and β over which a stable limit cycle exists. That is, increasing w_0 shifts the region in which limit cycles exist to higher values of α. On the other hand, decreasing w_0 allows for limit cycles to exist for lower values of α, but the range of β values over which they exist is much narrower. Thus, superthreshold activity in a network with weak synapses is much more easily overridden by synaptic depression. In our simulations we take $w_0 = 1$.

3.2 Oscillations in the spatially extended model

We now consider the implications of the existence of deterministic and noise–induced oscillations in the space–clamped model for spatially structured oscillations in the full model (3.1) with the excitatory weight function (3.2). Using numerical simulations, we demonstrate that the two–dimensional network supports a spatially localized oscillating core that emits target waves each cycle, as well as spiral waves. The results presented can also be generated for a system with smoother forms for f. However, as the simulations are qualitatively similar, we merely illustrate dynamics in the case of a piecewise linear f here. As in previous studies of two–dimensional neural field models, we carry out a transformation of our system for more efficient computation [98, 93, 168, 133]. That is, we convert the integro–differential equation system (3.1) to a fourth order PDE using two–dimensional Fourier transforms. This is possible due to the fact that the Fourier transform of the weight distribution $w(\mathbf{r}, \mathbf{r}')$ given by equation (3.2) is a rational function. Discretizing the resulting differential operators leads to sparse matrices, as opposed to full matrices arising from an integral operator.

Numerical simulations are thus performed on the following system, which is equivalent to equations (3.1) and (3.2):

$$\begin{aligned} \left[\nabla^4 - A\nabla^2 + B\right](u_t + u) &= Mqf(u), \\ q_t &= \frac{1-q}{\alpha} - \beta q f(u), \end{aligned} \tag{3.16}$$

over the domain $\Omega \subset \mathbb{R}^2$. Here, the fourth order operator, $\mathcal{L} = \nabla^4 - A\nabla^2 + B$, arises as the denominator of the two–dimensional Fourier transform of our modified Bessel weight function (3.2), which is given by

$$\begin{aligned} \widehat{w}(\rho) &= \frac{2}{3\pi}\left(\frac{1}{\rho^2+1} - \frac{1}{\rho^2+2^2}\right) \\ &= \frac{2/\pi}{\rho^4+5\rho^2+4}, \end{aligned} \tag{3.17}$$

where $\widehat{\cdot}$ denotes the two–dimensional Fourier transform. In this case, $A = 5$, $B = 4$, and $M = 2/\pi$, but we may adjust these parameters by considering a rescaling of w. We solve the system (3.16) numerically on a Cartesian grid of 1000×1000, applying homogeneous Dirichlet and Neumann boundary conditions. For the fourth order operator, we employed a second order finite difference method to construct a matrix version of $\mathcal{L}$. The time derivative was approximated using forward Euler with a timestep of $\Delta t = 0.01$, which was small enough so that shrinking it further did not change results.

3.2.1 Pulse emitter

Similar to our study of the one–dimensional network in the previous chapter, we find that in parameter regimes where a stable limit cycle exists in the space–clamped system, the corresponding two–dimensional network supports a spatially localized oscillating core that periodically emits traveling pulses. All that is necessary to induce such behavior is an initial condition of the form

$$(u(\mathbf{r},0), q(\mathbf{r},0)) = (\chi \mathrm{e}^{-(x^2+y^2)/\zeta^2}, 1), \tag{3.18}$$

where χ and ζ parameterize the amplitude and spatial constant of the initial state. We seek to characterize the evolving activity in the limit cycle regime, especially the period of oscillation and the speed of emitted pulses. In Figure 3.6, we show an example of a pulse–emitting core, which oscillates at a frequency of roughly 3Hz. Pulses are emitted each cycle, and travel at a speed of roughly 30cm/s, which is determined by the period of the oscillations; the latter is set by the time constant of synaptic depression. The initial emission of spreading activity appears as a traveling front which propagates from the region activated by the input current into the surrounding region of zero activity; it travels at the same speed as the subsequent target waves. The front converts each region of the network into an oscillatory state that is phase–shifted relative to the core, resulting in the appearance of a radially symmetric target pattern. Since our network has solely excitatory

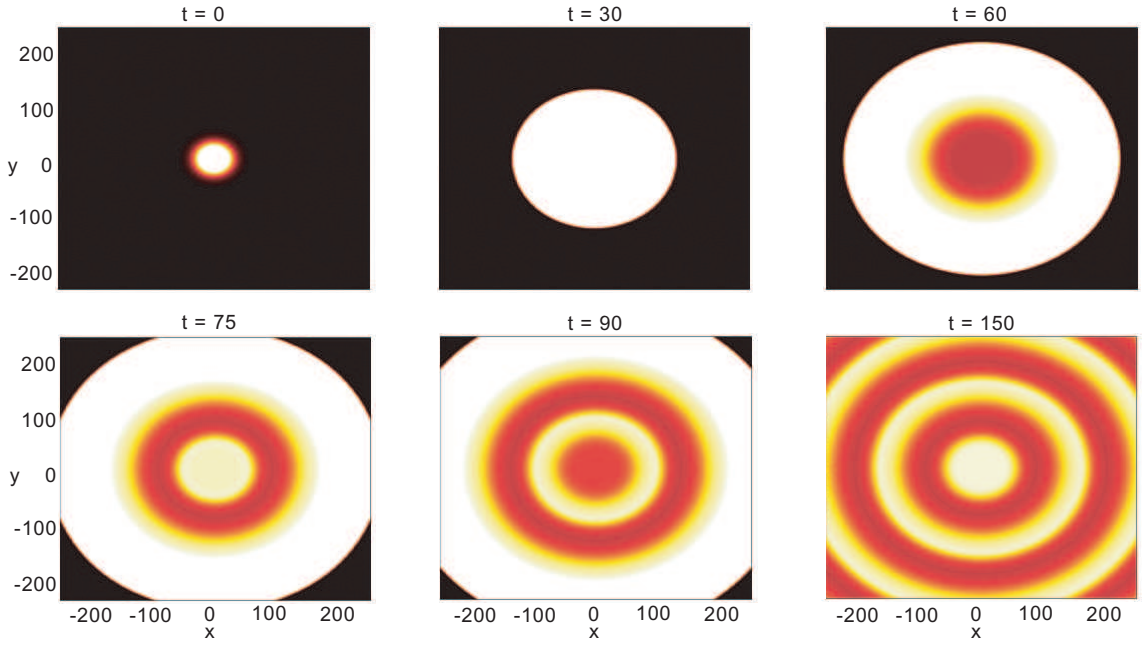

Figure 3.6. Snapshots of the solution $u(x, y, t)$ to the fourth order PDE (3.16), following a stimulus specified by equation (3.18) at $t = 0$, where $\chi = 1$ and $\zeta = 25$. Initially, an activated state spreads radially outward, across the entire medium as a traveling front. Then, the localized oscillating core of activity emits a target wave with each oscillation cycle. Eventually, these target waves fill the domain. Each target wave can be considered as a phase shift in space of the oscillation throughout the medium; they travel with the same speed as the initial front. Parameters are $\alpha = 80$, $\beta = 0.05$, $\sigma = 4$.

connections, we can consider it to be akin to disinhibited neocortical or hippocampal slices [37, 183, 182] or regions of cortex or hippocampus where excitatory circuitry dominates due to some pathology [31, 48]. Interestingly, the speed of the simulated waves matches the time–scale of fast seizure spread in cortex [126].

3.2.2 Spiral waves

Several experimental and modeling studies of two–dimensional cortex reveal the existence of spiral waves [67, 93, 126, 149, 148] (see also section 1.2.4 for discussion of spiral waves in cortical slice). Such self–sustained activity can often be classified by a constant angular velocity [67, 149]. When identified using voltage sensitive dye, one finds such activity patterns have true phase singularities about which the spiral organizes. One may think of such spatially structured activity as a network property manifesting the recovery period necessary for groups of neurons. Therefore, sections of cortex about the phase

singularity alternate between Down and Up states, giving ample time for sections to recover during the Down state.

Spiral waves have been generated in previous studies of neural field models with linear adaptation, in which the neuronal network acts like an excitable medium [93, 168]. The oscillations necessary for the generation of spiral waves arise from the Down state of the network being a stable focus. Laing used the rotational symmetry of the spiral waves to generate equations for the activity profile and angular velocity of a spiral on a disc domain [93]. Troy and Shusterman generated spiral waves by continually breaking the symmetry of target waves in the network [168]. In our model, we find that spiral wave patterns can be induced by breaking the rotational symmetry of pulse emitter solutions. More specifically, we chose an initial condition where the target pattern produced by the emitter has the top and bottom halves of its domain phase shifted. The network then evolves into two counter–rotating spirals on the left and right halves of the domain as shown in Figure 3.7. Closer inspection of one of these spirals reveals that it has a fixed center about which activity rotates indefinitely as shown in Figure 3.8.

Huang and colleagues showed that spiral waves generated in cortical slices are a way for oscillating activity to organize spatially in a smooth and isotropic medium [67]. They found the waves persisted for up to 30 cycles and rotated at a rate of roughly 10 cycles per second. Also, the phase singularity at the center of a spiral wave experiences a reduction in

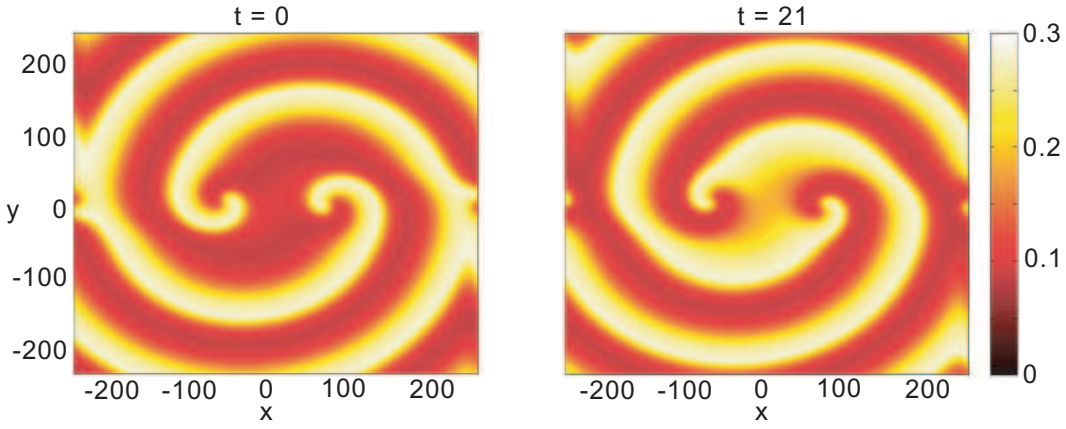

Figure 3.7. Snapshots of a solution $u(x, y, t)$ to the fourth order PDE (3.16) revealing the counter–rotation of two spiral waves on either side of the domain. These were generated with an initial condition where the target pattern of Figure 3.6 had the top and bottom halves of the domain phase shifted. Parameters are $\alpha = 80$, $\beta = 0.05$, $\sigma = 4$, and $\theta = 0.01$.

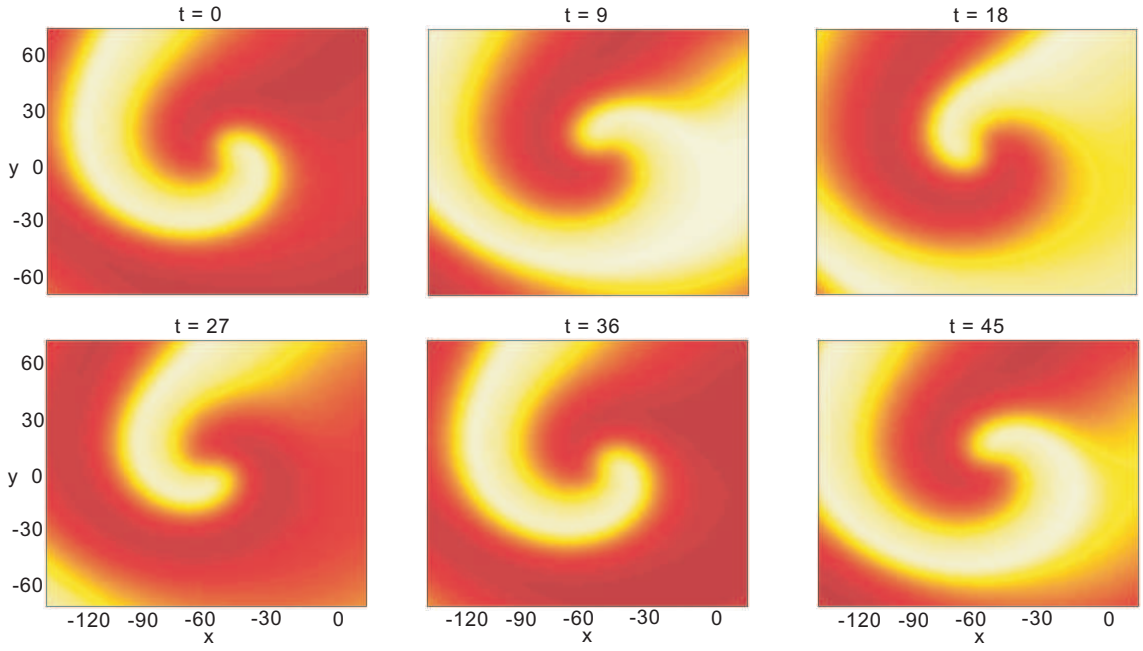

Figure 3.8. A zoomed in version of the rotating left spiral wave pictured in Figure 3.7. The period of the spiral wave oscillation is roughly the same as the period of the oscillation in the space–clamped system. All patches of neurons are oscillating at the same frequency, but phase–shifted as coordinates are rotated about the central phase singularity. Parameters are $\alpha = 80$, $\beta = 0.05$, $\sigma = 4$, and $\theta = 0.01$.

oscillation amplitude due to the mixing of all phases in a small region. Certainly, the spiral waves we have found in our system persist for a long time, but it seems that the rotation rate is slightly slower at roughly 2Hz. Of course this is due in part to the time constant of synaptic depression. As we showed in Chapter 2, including spike frequency adaptation can increase the frequency of oscillations.

3.2.3 Noise–induced oscillations

As in the space–clamped system, it is interesting to consider the effects of noise on the two–dimensional spatially extended network. In a recent study of the role of additive Gaussian noise on Turing instabilities in neural field equations, Hutt and colleagues found that noise delays the onset of pattern formation [72]. Also, Laing and colleagues have shown that in a neural field model with linear adaptation, moving bumps are slowed by the introduction of an additive noise term [97]. Here we show that in addition to modulating spatiotemporal activity patterns that exist in the deterministic system, noise also gives rise

to new dynamics.

Following a previous neural field studies with additive noise [97], we introduce a Gaussian white noise term to each equation of a discretized version of the fourth order PDE (3.16):

$$\begin{aligned} \mathcal{L}_h\left(\frac{u_{ij}^{k+1}-u_{ij}^{k}}{\Delta t}+u_{ij}+\eta\mu_{ij}(t)\right) &= Mq_{ij}f(u_{ij}), \\ \frac{q_{ij}^{k+1}-q_{ij}^{k}}{\Delta t} &= \frac{1-q_{ij}}{\alpha}-\beta q_{ij}f(u_{ij}), \end{aligned} \tag{3.19}$$

where $i = 1, ..., N_x$ and $j = 1, ..., N_y$, $\mathcal{L}_h$ is the finite difference version of the linear operator given in equation (3.16) , u_{ij} and q_{ij} are discrete values of u and q at $(x, y) = (x_i, y_j)$, each μ_{ij} evolves independently as $\langle\mu_{ij}(t)\rangle = 0$ and $\langle\mu_{ij}(t)\mu_{ij}(s)\rangle = \delta(t-s)$, and η is the variance of our white noise term.

In the case of low levels of spatially incoherent Gaussian noise, we find that small pockets of the network spontaneously form spatially localized oscillators which then interact with one another via the target waves that propagate from their cores. We picture this in Figure 3.9 for $\eta = 0.005$. Therefore, as in the space–clamped case, noise provides a mechanism for generating oscillations in a situation where the deterministic system would remain quiescent. If the noise level is increased then it tends to disrupt these oscillating cores, which provides a symmetry breaking mechanism for the generation of spiral waves as illustrated in Figure 3.10. Following induction of a spatially localized oscillation using a Gaussian stimulus of the form (3.18), we find that the oscillating core begins to be broken up by the noise such that the two halves of the core oscillate antisynchronously. A semi–ring wave then propagates from the bottom to the top of the domain (first three snapshots in Figure 3.10), and breaks up into two spiral waves as it reaches the boundary of the core (fourth snapshot). Background oscillations absorb the two spiral waves and the ring–wave is reinitiated (final two snapshots). At even higher levels of noise any spatially structured activity in the network is disrupted and the entire network exhibits bulk oscillations. Note that an alternative mechanism to noise for generating spiral waves is to introduce random network inhomogeneities (quenched disorder), as shown in the case of a two–dimensional integrate–and–fire network [127].

3.3 High gain limit

To study the existence and stability of spatially structured solutions in neuronal networks, the high gain limit of continuous firing rate functions is often considered [3, 40,

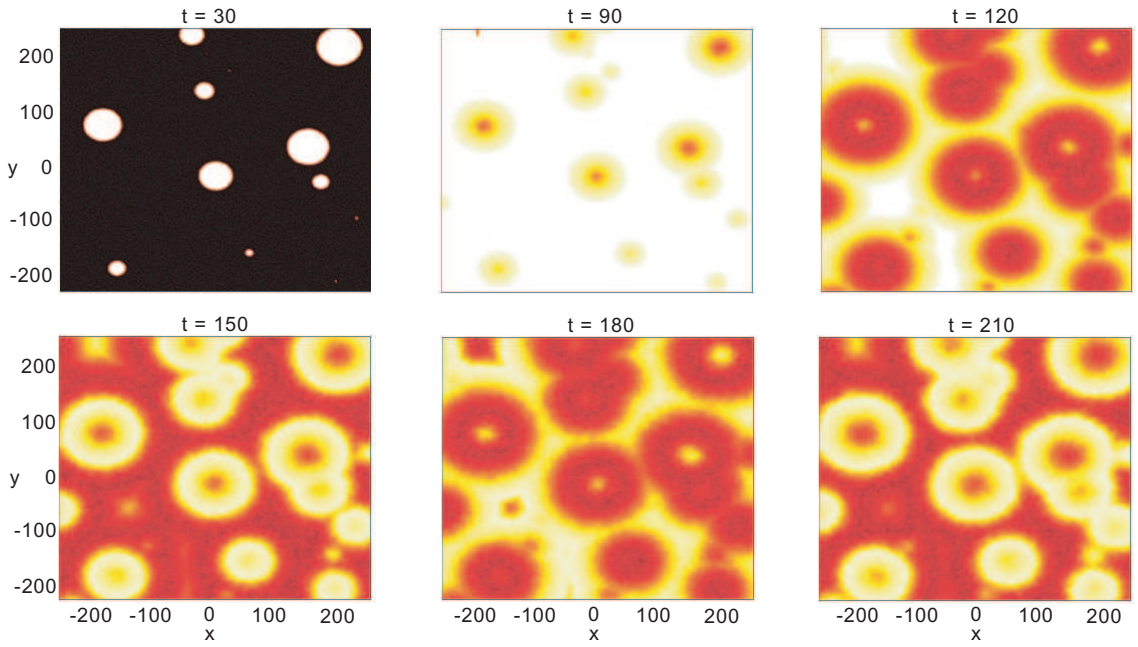

Figure 3.9. Snapshots of a solution $u(x, y, t)$ to the noisy system (3.19) in the absence of stimulation. Background noise initiates spatially localized oscillating cores at discrete sites in the medium. Target waves emitted by the various oscillating regions collide, disrupting the spatial structure of the oscillations. Parameters are $\alpha = 80$, $\beta = 0.05$, $\eta = 0.005$, $\sigma = 4$, and $\theta = 0.01$.

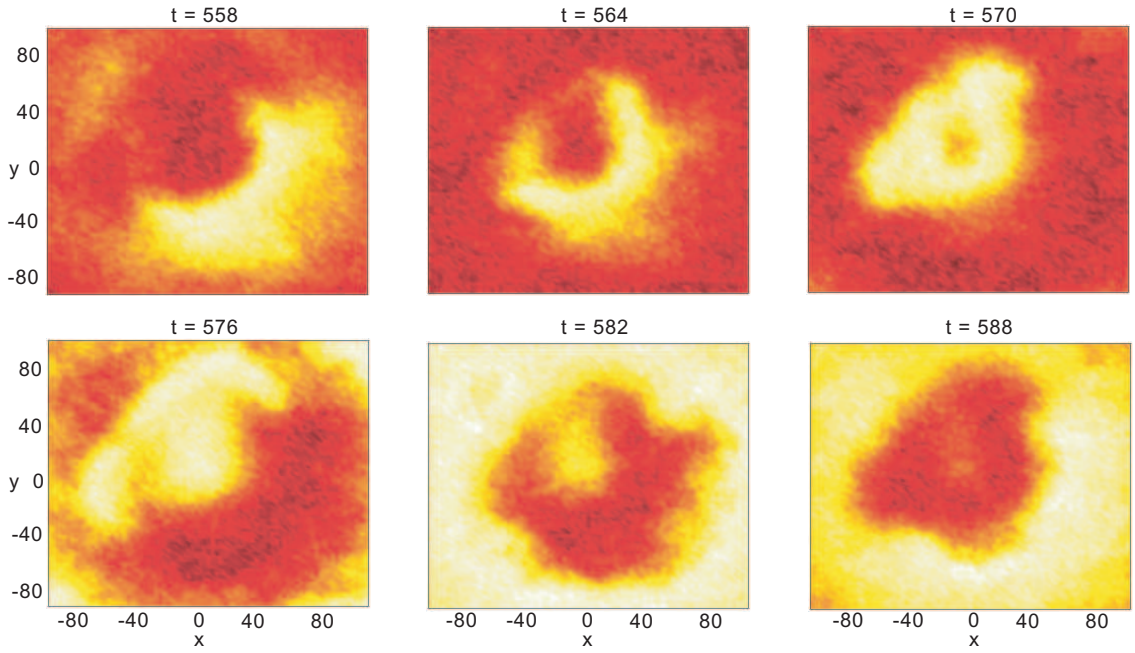

Figure 3.10. Snapshots of a solution $u(x, y, t)$ to the noisy system (3.19), following a stimulus specified by equation (3.18) at $t = 90$, where $\chi = 1$ and $\zeta = 60$. As activity develops, the background noise starts to break the symmetry of an oscillating central core. Rather than a contiguous oscillation, two halves of the core oscillate antisynchronously. A semi–ring wave propagates from the bottom to the top of the medium, and breaks into two spiral waves as it collides with the boundary of the core. This exemplifies noise induced spiral waves, which are sustained for relatively long time intervals. Parameters are $\alpha = 80$, $\beta = 0.05$, $\eta = 0.01$, $\sigma = 4$, and $\theta = 0.01$.

55, 168]. Instead of f being a continuous function, it becomes the Heaviside step function (2.2) with a discontinuity at the threshold $u = \theta$. Oscillatory solutions do not exist for the neuronal network (3.1) in the high gain limit. However, there are subtle and interesting consequences of employing a firing rate function with a discontinuity that arise in the space–clamped system as well as the spatially extended system. In this section, we show that stable target wave solutions exist, derive equations for the existence of stationary bumps, and analyze some of the bump instabilities using piecewise smooth analysis.

3.3.1 Target waves

As shown by numerical simulations in the case of a piecewise linear firing rate, spatially structured oscillations can generate expanding target waves via propagating phase shifts in an oscillatory medium. Here, we show that in the high gain limit of continuous firing rate functions, target waves arise in the context of an excitable medium. We studied the existence of traveling pulses in a one–dimensional excitatory network with synaptic depression in the previous chapter (see section 2.1.2). Traveling pulses of this type represent a homoclinic orbit in the projected space of the traveling wave coordinate, rather than phase shifts of an existing limit cycle, as in an oscillatory medium. Implications of these two different dynamical systems scenarios may be useful in determining the mechanism that generates traveling waves in experiment. For example, in studies of disinhibited cortical slice, localized stimuli may lead to either traveling plane waves, which are transient, or spiral waves, which are persistent [67].

We found that by simulating the two–dimensional spatially extended system with the Heaviside step firing rate function, a localized stimulus could lead to outwardly propagating target waves. In Figure 3.11, we show snapshots of such a simulation where the initial condition is taken to be a Gaussian stimulus of the synaptic drive, as specified by equation (3.18). In the case of a piecewise linear firing rate function, symmetric stimuli lead to an oscillating core that recurrently generated target waves. Here, a single target wave is generated, after which, the system returns to a quiescent state. The system is radially symmetric, due to the radially symmetric weight function (3.2), so symmetric stimuli lead to a symmetric solution. Numerical simulations suggest that these target waves are indeed stable.

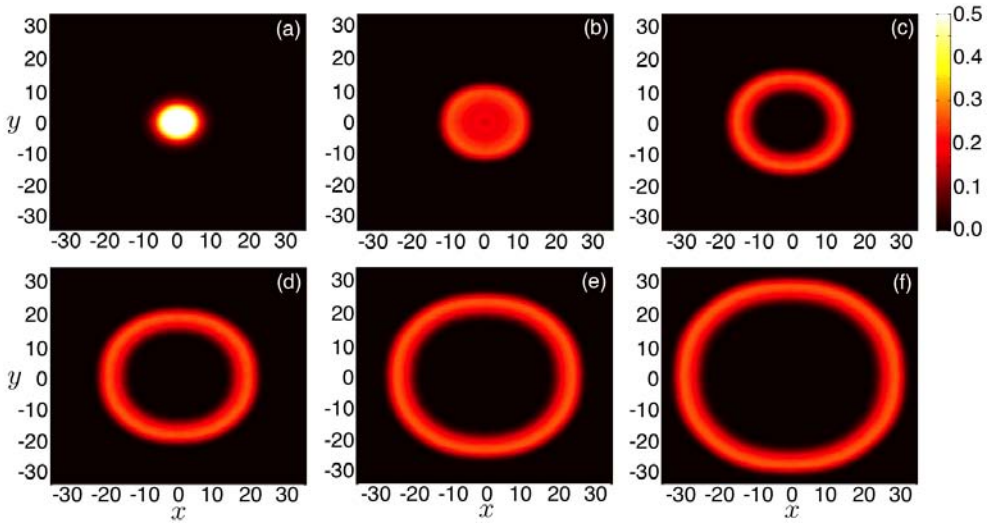

Figure 3.11. Snapshots of a solution $u(x, y, t)$ to the fourth order PDE (3.16) showing a single outward propagating target wave, following a stimulus specified by equation (3.18) at $t = 0$, where $\chi = 1$ and $\zeta = 25$. The firing rate function $f(u) = H(u-\theta)$ is the piecewise constant Heaviside step function. Parameters are $\alpha = 50$, $\beta = 0.4$, and $\theta = 0.1$.

3.3.2 Existence of standing bumps

We now extend our analysis of stationary bumps in a one–dimensional network, shown in section 2.2, to derive conditions for the existence and stability of radially symmetric stationary bump solutions of the corresponding two–dimensional piecewise smooth neural field model.

Consider a circularly symmetric bump solution of radius a such that $u(\mathbf{r}, t) = U(r)$, $q(\mathbf{r}, t) = Q(r)$ with $U(a) = \theta$ and

$$U(r) \gtrless \theta, \qquad \text{for } r \lessgtr a, \tag{3.20}$$

$$\{U(r), Q(r))\} \to \{0, 1\}, \qquad \text{as } r \to \infty. \tag{3.21}$$

Imposing such constraints on a stationary solution of equation (3.1) gives

$$U(r) = \int_{\mathcal{U}} Q(r')w(|\mathbf{r} - \mathbf{r}'|)\mathrm{d}\mathbf{r}', \tag{3.22}$$

$$Q(r) = (1 + \alpha\beta\Theta(a - r))^{-1}, \tag{3.23}$$

where $\mathcal{U} = \{\mathbf{r} = (r, \phi) : r \leq a\}$ is the domain on which the bump is superthreshold. Substituting equation (3.23) back into (3.22) yields

$$(1 + \alpha\beta)U(r) = \Pi(a, r), \tag{3.24}$$

where

$$\Pi(a,r) \;=\; \int_0^{2\pi}\int_0^a w(|\mathbf{r}-\mathbf{r}'|)r'\mathrm{d}r'\mathrm{d}\phi'. \tag{3.25}$$

We can calculate the double integral in (3.25) using the Hankel transform and Bessel function identities, as in [55, 133]. Thus, we find that

$$\Pi(a,r) \;=\; 2\pi a\int_0^\infty \hat{w}(\rho)J_0(r\rho)J_1(a\rho)\mathrm{d}\rho, \tag{3.26}$$

where $\hat{w}(\rho)$ is the Hankel transform of w.

For the sake of illustration consider the Mexican hat weight distribution (3.3) given by a combination of modified Bessel functions of the second kind [55, 93, 133]. Using the fact that the corresponding Hankel transform of $K_0(sr)$ is $\mathcal{H}(\rho,s)=(\rho^2+s^2)^{-1}$, we have

$$\widehat{w}(\rho)=\frac{2}{3\pi}(\mathcal{H}(\rho,1)-\mathcal{H}(\rho,2)-A_i(\mathcal{H}(\rho,1/\sigma_i)-\mathcal{H}(\rho,2/\sigma_i))). \tag{3.27}$$

Thus, the integral (3.26) can be evaluated explicitly by substituting (3.27) into (3.26), and using the identity

$$\int_0^\infty \frac{1}{\rho^2+s^2}J_0(r\rho)J_1(a\rho)\mathrm{d}\rho \;\equiv\; \mathcal{I}(a,r,s)=\begin{cases}\frac{1}{s}I_1(sa)K_0(sr), & r>a,\\ \frac{1}{as^2}-\frac{1}{s}I_0(sr)K_1(sa), & r<a,\end{cases}$$

where I_ν is the modified Bessel function of the first kind of order ν. Thus, the stationary bump $U(r)$ given by equation (3.24) has the form

$$U(r) \;=\; \frac{4a}{3(1+\alpha\beta)}\left(\mathcal{I}(a,r,1)-\mathcal{I}(a,r,2)-A_i(\mathcal{I}(a,r,1/\sigma_i)-\mathcal{I}(a,r,2/\sigma_i))\right). \tag{3.28}$$

The bump radius may then be computed by finding the roots a of the equation

$$(1+\alpha\beta)\theta \;=\; \mathbf{\Pi}(a), \tag{3.29}$$

with

$$\begin{aligned}\mathbf{\Pi}(a)\equiv\Pi(a,a) \;=\; &\frac{4a}{3}\Big(I_1(a)K_0(a)-\frac{1}{2}I_1(2a)K_0(2a)\\ &-A_i(\sigma_i I_1(a/\sigma_i)K_0(a/\sigma_i)-\frac{\sigma_i}{2}I_1(2a/\sigma_i)K_0(2a/\sigma_i))\Big).\end{aligned} \tag{3.30}$$

Relations between bump radius a and depression strength β are shown in Figure 3.12 for different thresholds θ.

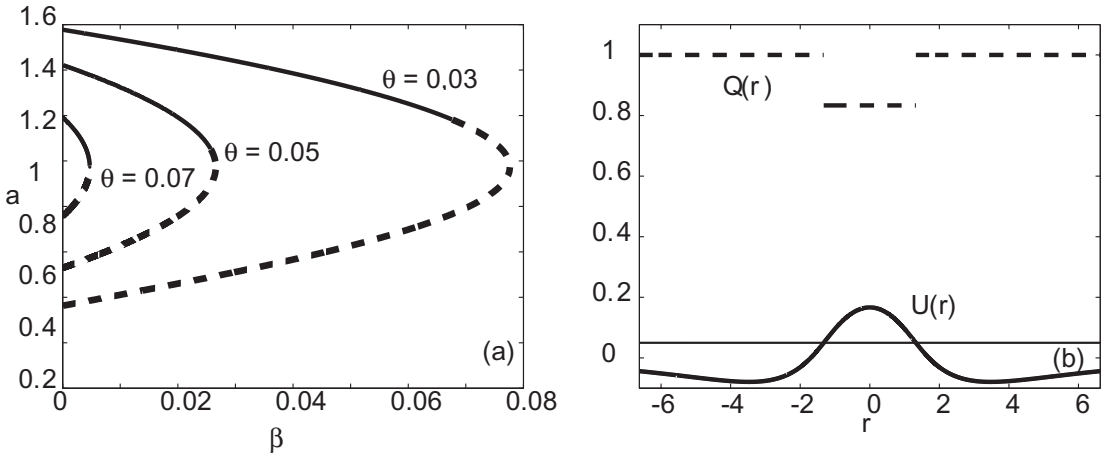

Figure 3.12. Two–dimensional bumps. (a) Plots relating bump radius a to amplitude of synaptic depression β for various values of threshold θ based on equation (3.29). Solid (dashed) curves indicate bumps that are unstable with respect to radially symmetric perturbations. Other parameters are $A_i = 0.3$, $\sigma_i = 4$, $\alpha = 20$. (b) Bump profile when $\theta = 0.05$, $\alpha = 20$, $\beta = 0.01$.

3.3.3 Stability of standing bumps

We now analyze the stability of radially symmetric two–dimensional bump solutions. As in the case of one–dimensional bumps (see section 2.2.4), we must consider the sign of the perturbations of the bump boundary. However, there are now an infinite number of cases to consider with regard to how perturbations subdivide the continuum boundary of a two–dimensional bump. For this initial exposition, we explicitly compute stability with respect to radially symmetric perturbations only. We also formulate the spectral problem associated with radially nonsymmetric perturbations, but due to its complexity, leave its analysis for future work.

Let us set $u(\mathbf{r},t) = U(r) + \varepsilon\psi(\mathbf{r},t)$ and $q(\mathbf{r},t) = Q(r) + \varepsilon\varphi(\mathbf{r},t)$, where ψ, φ are smooth perturbations and $\varepsilon \ll 1$. Substituting into the full two–dimensional system (3.1) and imposing the stationary bump solutions (3.22) and (3.23) gives

$$\begin{aligned}\frac{\partial\psi(\mathbf{r},t)}{\partial t} &= -\psi(\mathbf{r},t) \\ &\quad + \frac{1}{\varepsilon}\int_{\mathbf{R}^2} w(|\mathbf{r}-\mathbf{r}'|)Q(r')[\Theta(U(r')+\varepsilon\psi(\mathbf{r}',t)-\theta)-\Theta(U(r')-\theta)]\mathrm{d}\mathbf{r}' \\ &\quad + \frac{1}{\varepsilon}\int_{\mathbf{R}^2} w(|\mathbf{r}-\mathbf{r}'|)\varphi(\mathbf{r}',t)\Theta(U(r')+\varepsilon\psi(\mathbf{r}',t)-\theta)\mathrm{d}\mathbf{r}' \qquad (3.31)\end{aligned}$$

$$\begin{aligned}\frac{\partial\varphi(\mathbf{r},t)}{\partial t} &= -\frac{\varphi(\mathbf{r},t)}{\alpha} - \beta Q(r)[\Theta(U(r)+\varepsilon\psi(\mathbf{r},t)-\theta)-\Theta(U(r)-\theta)] \\ &- \beta\varphi(\mathbf{r},t)H(U(r)+\varepsilon\psi(\mathbf{r},t)-\theta). \end{aligned} \tag{3.32}$$

If $\varepsilon\Delta(\phi,t)$ denote perturbations to the bump boundary at polar coordinate (a,ϕ), then the ensuing threshold equation will be

$$u(a+\varepsilon\Delta(\phi,t),\phi,t)=\theta$$

for $\phi\in[0,2\pi)$ and all $t>0$. Following our analysis of the one–dimensional case (section 2.2), we introduce the auxiliary field

$$\Phi(\mathbf{r},t) = \int_0^{2\pi}\int_0^{a+\varepsilon\Delta(\phi',t)} w(|\mathbf{r}-\mathbf{r}'|)\varphi(\mathbf{r}',t)\mathrm{d}r'\mathrm{d}\phi'. \tag{3.33}$$

Differentiating $\Phi(\mathbf{r},t)$ with respect to t and combining this with equations (3.31) and (3.32) leads to the pair of equations

$$\begin{aligned}\frac{\partial\psi(\mathbf{r},t)}{\partial t} &= -\psi(\mathbf{r},t)+\Phi(\mathbf{r},t)+\frac{1}{\varepsilon}\int_0^{2\pi}\int_0^{a+\varepsilon\Delta(\phi',t)} w(|\mathbf{r}-\mathbf{r}'|)Q(r')r\mathrm{d}r'\mathrm{d}\phi' \\ &\quad -\frac{1}{\varepsilon}\int_0^{2\pi}\int_0^{a} w(|\mathbf{r}-\mathbf{r}'|)Q(r')r'\mathrm{d}r'\mathrm{d}\phi' \end{aligned} \tag{3.34}$$

$$\begin{aligned}\frac{\partial\Phi(\mathbf{r},t)}{\partial t} &= -(\alpha^{-1}+\beta)\Phi(\mathbf{r},t)-\frac{\beta}{\varepsilon}\int_0^{2\pi}\int_0^{a+\Delta(\phi',t)} w(|\mathbf{r}-\mathbf{r}'|)Q(r') \\ &\quad\times[\Theta(U(\mathbf{r}',t)+\varepsilon\phi(\mathbf{r}',t)-\theta)-\Theta(U(\mathbf{r}',t)-\theta)]r'\mathrm{d}r'\mathrm{d}\phi' \\ &\quad+\varepsilon\int_0^{2\pi} w(|\mathbf{r}-\mathbf{r}'|)\varphi(\mathbf{r}',t)\dot{\Delta}(\phi',t)\mathrm{d}r'\mathrm{d}\phi'. \end{aligned} \tag{3.35}$$

We now expand these equations in powers of ε and collect all $\mathcal{O}(1)$ terms. It is important to keep track of the sign of $\Delta(\phi,t)$ at all values of ϕ when approximating the integrals, since $Q(r)$ is discontinuous on the boundary. For example

$$\begin{aligned}\int_0^{2\pi}\int_a^{a+\varepsilon\Delta(\phi',t)} w(|\mathbf{r}-\mathbf{r}'|)Q(r')r'\mathrm{d}r'\mathrm{d}\phi' &\approx \varepsilon a\int_{\mathcal{A}_+(t)}\Delta(\phi',t)w(|\mathbf{r}-\mathbf{a}|)\mathrm{d}\phi' \\ &\quad+\varepsilon\frac{a}{1+\alpha\beta}\int_{\mathcal{A}_-(t)}\Delta(\phi',t)w(|\mathbf{r}-\mathbf{a}|)\mathrm{d}\phi', \end{aligned} \tag{3.36}$$

where the domain $\mathcal{A}_+(t)$ ($\mathcal{A}_-(t)$) defines the region in ϕ over which the perturbation $\Delta(\phi,t)>0$ ($\Delta(\phi,t)<0$) at time $t>0$ and $\mathbf{a}=(a,\phi')$. We have used the fact in the region $\mathcal{A}_+(t)$ ($\mathcal{A}_-(t)$), we approach the stationary bump boundary from the exterior (interior) of

the bump in the limit $\varepsilon \to 0^+$ so that $Q = 1$ ($Q = 1/(1+\alpha\beta)$). Likewise, the first integral on the right hand side of (3.35) can be approximated by

$$\varepsilon a \int_{\mathcal{A}_+(t)} \Delta(\phi', t) w(|\mathbf{r} - \mathbf{a}|) \mathrm{d}\phi'.$$

Finally, we use the approximation

$$\begin{aligned} \theta &= u(a + \varepsilon\Delta(\phi,t), \phi, t) = U(a + \varepsilon\Delta(\phi,t)) + \varepsilon\psi(a + \varepsilon\Delta(\phi,t), \phi, t), \\ &\approx U(a) + \varepsilon U'(a)\Delta(\phi,t) + \varepsilon\psi(a,\phi), \end{aligned}$$

and $U(a) = \theta$ so that

$$\Delta(\phi,t) \approx \frac{\psi(a,\phi,t)}{|U'(a)|}$$

to lowest order in ε. This leads to the following set of equations

$$\begin{aligned} \frac{\partial\psi(\mathbf{r},t)}{\partial t} &= -\psi(\mathbf{r},t) + \Phi(\mathbf{r},t) + a\gamma \int_{\mathcal{A}_+(t)} \psi(a,\phi',t) w(|\mathbf{r} - \mathbf{a}|) \mathrm{d}\phi' \\ &\quad + \frac{a\gamma}{1+\alpha\beta} \int_{\mathcal{A}_-(t)} \psi(a,\phi',t) w(|\mathbf{r} - \mathbf{a}|) \mathrm{d}\phi', \qquad (3.37) \\ \frac{\partial\Phi(\mathbf{r},t)}{\partial t} &= -(\alpha^{-1} + \beta)\Phi(\mathbf{r},t) - a\gamma\beta \int_{\mathcal{A}_+(t)} \psi(a,\phi',t) w(|\mathbf{r} - \mathbf{a}|) \mathrm{d}\phi'. \qquad (3.38) \end{aligned}$$

Here

$$\gamma^{-1} = |U'(a)| = \frac{2\pi a}{1+\alpha\beta} \int_0^\infty \rho \widehat{w}(\rho) J_1(a\rho) J_1(a\rho) \mathrm{d}\rho, \qquad (3.39)$$

which for the Mexican hat weight function (3.2) can be explicitly computed as

$$\begin{aligned} |U'(a)| &= \frac{4a}{3(1+\alpha\beta)} \left(I_1(a)K_1(a) - I_1(2a)K_1(2a) \right. \qquad (3.40) \\ &\quad \left. - A_i(I_1(a/\sigma_i)K_1(a/\sigma_i) - I_1(2a/\sigma_i)K_1(2a/\sigma_i)) \right). \end{aligned}$$

Equations (3.37) and (3.38) imply that the local stability of a stationary bump solution depends on the spectral properties of a piecewise linear operator. As in the one–dimensional case (section 2.2.4), we can obtain a simpler spectral problem under the ansatz that the perturbation $\psi(a,\phi,t)$ (equivalently $\Delta(\phi,t)$) does not switch sign at each ϕ for any time t. Thus, we assume (3.37) and (3.38) have separable solutions $(\psi(\mathbf{r},t), \Phi(\mathbf{r},t)) = \mathrm{e}^{\lambda t}(\psi(\mathbf{r}), \Phi(\mathbf{r}))$, where λ is real and $(\psi(\mathbf{r}), \Phi(\mathbf{r}))$ are bounded continuous functions that decay to zero exponentially as $|\mathbf{r}| \to \infty$. Under this assumption, the domains $\mathcal{A}_\pm(t)$ are constant in time, so there is a common factor $\mathrm{e}^{\lambda t}$ that cancels everywhere. In a similar

fashion to the analysis of one–dimensional bumps, one class of solution of the resulting eigenvalue problem is given by $\lambda = -(\alpha^{-1} + \beta)$ and $\psi(a, \phi) \leq 0$ for all ϕ. However, this does not contribute to any instabilities. Therefore, suppose that $\lambda \neq -(\alpha^{-1} + \beta)$. We can then eliminate $\Phi(\mathbf{r})$ to obtain a nonlinear eigenvalue equation for λ of the form

$$\begin{aligned}(\lambda+1)\psi(\mathbf{r}) &= \frac{a\gamma(\lambda+\alpha^{-1})}{\lambda+\alpha^{-1}+\beta}\int_{\mathcal{A}_+}\psi(a,\phi')w(|\mathbf{r}-\mathbf{a}|)\mathrm{d}\phi' \\ &\quad +\frac{a\gamma}{1+\alpha\beta}\int_{\mathcal{A}_-}\psi(a,\phi')w(|\mathbf{r}-\mathbf{a}|)\mathrm{d}\phi'.\end{aligned} \tag{3.41}$$

Now, it would be possible to formulate the spectral problem in terms of compact linear operators acting on continuous bounded functions $\psi(r, \phi)$ defined on the disc of radius a centered at the origin with the sign of $\psi(a, \phi)$, $\phi \in [0, 2\pi)$ prescribed. However, here we simply summarize the results. First, one class of solution to equation (3.41) consists of functions $\psi(\mathbf{r})$ that vanish on the boundary, $\psi(a, \phi) = 0$, such that $\lambda = -1$. (It also follows that $\Phi(\mathbf{r}) \equiv 0$). This belongs to the essential spectrum, which does not contribute to any instabilities. The discrete spectrum for given $\mathcal{A}_\pm$ is then determined by setting $r = a$ in equation (3.41):

$$\begin{aligned}(\lambda+1)\psi(a,\phi) &= \frac{a\gamma(\lambda+\alpha^{-1})}{\lambda+\alpha^{-1}+\beta}\int_{\mathcal{A}_+}\psi(a,\phi')w\left(2a\sin\frac{\phi-\phi'}{2}\right)\mathrm{d}\phi' \\ &\quad +\frac{a\gamma}{1+\alpha\beta}\int_{\mathcal{A}_-}\psi(a,\phi')w\left(2a\sin\frac{\phi-\phi'}{2}\right)\mathrm{d}\phi',\end{aligned} \tag{3.42}$$

where we have simplified the argument of $w(r)$ using

$$|(a,\phi)-(a,\phi')| = \sqrt{(a\sin\phi - a\sin\phi')^2 + (a\cos\phi - a\cos\phi')^2} = 2a\sin\frac{\phi-\phi'}{2}.$$

There are then three other classes of solution to equation (3.42): (i) radially symmetric expansions, such that $\psi(a, \phi) = \psi(a) > 0$ for $\phi \in [0, 2\pi)$; (ii) radially symmetric contractions, such that $\psi(a, \phi) = \psi(a) < 0$ for $\phi \in [0, 2\pi)$; and (iii) radially nonsymmetric perturbations for which $\psi(a, \phi)$ changes sign as a function of ϕ. In the limit $\beta \to 0$, equation (3.42) reduces to the simpler form

$$(\lambda+1)\psi(a,\phi) = a\gamma\int_0^{2\pi}\psi(a,\phi')w\left(2a\sin\frac{\phi-\phi'}{2}\right)\mathrm{d}\phi'. \tag{3.43}$$

The eigenmodes are then given by pure Fourier modes $\psi(a, \phi) = \Delta_n(\phi) \equiv c_n \mathrm{e}^{in\phi} + \text{c.c.}$, integer n, with corresponding real eigenvalues $\lambda_n = -1 + \gamma\mu_n$,

$$\mu_n = 2a\int_0^{2\pi} w(2a\sin\phi)\mathrm{e}^{-2in\phi}d\phi. \tag{3.44}$$

Some examples of low–order Fourier eigenmodes $\Delta_n(\phi)$ are shown in Figure 3.13, together with the associated boundary domains $\mathcal{A}_\pm$. As β is increased from zero only the

zeroth–order eigenmodes persist (expansions and contractions), whereas the non–radially symmetric eigenmodes become a mixture of Fourier modes:

$$\psi(a,\phi) = \sum_{n=-\infty}^{\infty} c_n(a)\mathrm{e}^{in\phi}.$$

This is analogous to the mixing between shift and expansion perturbations in the one–dimensional case.

(i) $\psi(a,\phi) = \psi(a) > 0$: In this case, equation (3.42) becomes

$$(\lambda+1)\psi(a) \quad = \quad \frac{a\gamma(\lambda+\alpha^{-1})\psi(a)}{\lambda+\alpha^{-1}+\beta}\int_0^{2\pi} w\left(2a\sin\frac{\phi-\phi'}{2}\right)\mathrm{d}\phi', \tag{3.45}$$

where we have used the facts that $\mathcal{A}_+ = [0,2\pi)$, $\mathcal{A}_-$ is empty, and $\psi(a,\phi)$ is constant in ϕ. Therefore, equation (3.45) should be equivalent for all ϕ, so $\psi(a) > 0$ and λ satisfies the

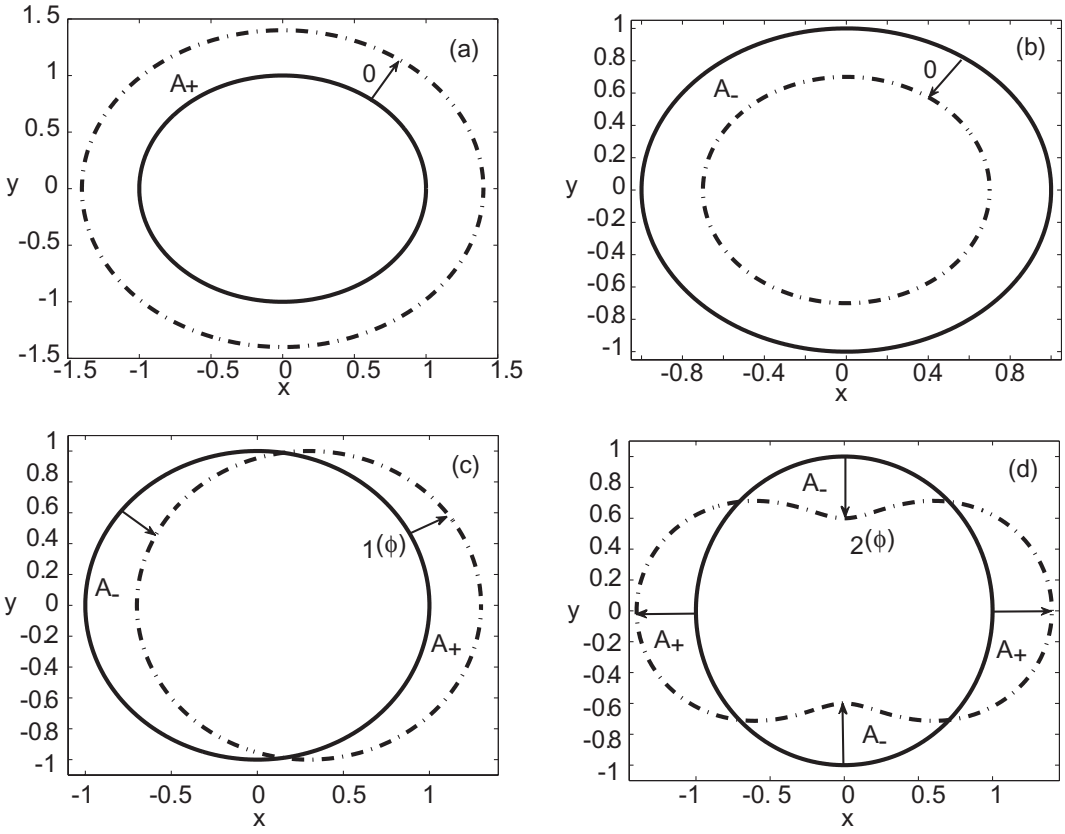

Figure 3.13. Low–order perturbations of a radially symmetric two–dimensional bump: (a) expansion ($\Delta_0 > 0$); (b) contraction ($\Delta_0 < 0$); (c) D_1–symmetric shift $\Delta_1(\phi)$; (d) D_2–symmetric perturbation $\Delta_2(\phi)$.

quadratic

$$(\lambda + \alpha^{-1} + \beta)(\lambda + 1) \quad = \quad (\lambda + \alpha^{-1})(1 + \alpha\beta)\Omega_0, \tag{3.46}$$

where

$$\Omega_0 = \frac{\mu_0(a)}{(1 + \alpha\beta)|U'(a)|}, \qquad \mu_0(a) = 2a \int_0^\pi w(2a \sin\phi) \mathrm{d}\phi. \tag{3.47}$$

For the Mexican hat weight function (3.2), we can use

$$\int_0^\pi K_0(2b \sin\phi) \mathrm{d}\phi \quad = \quad \pi I_0(b) K_0(b)$$

to calculate

$$\begin{aligned} \mu_0(a) \quad = \quad & \frac{4a}{3}(I_0(a)K_0(a) - I_0(2a)K_0(2a) \\ & -A_i(I_0(a/\sigma_i)K_0(a/\sigma_i) - I_0(2a/\sigma_i)K_0(2a/\sigma_i))). \end{aligned} \tag{3.48}$$

It follows that $\lambda = \lambda_0^{\pm}$ with

$$\begin{aligned} \lambda_0^{\pm} \quad = \quad & \frac{1}{2}\left[\Omega_0(1 + \alpha\beta) - (1 + \alpha^{-1} + \beta)\right] \\ & \pm \frac{1}{2}\sqrt{[\Omega_0(1 + \alpha\beta) - (1 + \alpha^{-1} + \beta)]^2 + 4(\Omega_0 - 1)(\alpha^{-1} + \beta)}. \end{aligned} \tag{3.49}$$

The associated eigenmode corresponds to an expansion of the bump.

(ii) $\psi(a, \phi) = \psi(a) < 0$: In this case, equation (3.42) becomes

$$(\lambda + 1)\psi(a) \quad = \quad \frac{a\gamma\psi(a)}{1 + \alpha\beta} \int_0^{2\pi} w\left(2a \sin\frac{\phi - \phi'}{2}\right) \mathrm{d}\phi', \tag{3.50}$$

where we have used the facts that $\mathcal{A}_+$ is empty, $\mathcal{A}_- = [0, 2\pi)$, and $\psi(a, \phi)$ is constant in ϕ. Therefore, equation (3.50) should be equivalent for all ϕ, so $\psi(a) < 0$ and $\lambda = \lambda_0$ with

$$\lambda_0 \quad = \quad \Omega_0 - 1. \tag{3.51}$$

The associated eigenmode corresponds to a contraction of the bump.

(iii) $\psi(a, \phi)$ radially nonsymmetric : In this final case for $\beta > 0$, the characteristic equation (3.42) involves integrals over subdomains of $[0, 2\pi)$, and is no longer a standard Fredholm integral equation. Hence, as we have already indicated, eigenmodes will be more complicated than the pure Fourier modes $\mathrm{e}^{in\phi}$ found in previous studies of bump instabilities in two–dimensions [98, 55, 56, 133]. This is due to the faster growth of the lobes of the perturbation $\psi(a, \phi)$ that are superthreshold versus those that are subthreshold. We leave the explicit analysis of general solutions to equation (3.42) to future work.

We illustrate the stability properties of two–dimensional bumps with respect to radially symmetric perturbations by plotting the spectrum of expansions and contractions in the case of the Mexican hat weight function (3.2), see Figure 3.14. We consider the upper branches of the existence curves shown in Figure 3.12, since these are stable in the limit $\beta \to 0$. As in the one–dimensional case (section 2.2.4), the expansion mode dominates over contraction, due to more resources existing outside of the bump. As β increases, the two roots of the characteristic equation (3.49) meet and they become complex, violating our ansatz. When the eigenvalues become real again, they are both greater than zero, implying the bump will certainly be unstable. Contraction perturbations are always stable. By analogy with one–dimensional bumps, we expect that bump instabilities in two dimensions are dominated by higher–order perturbations of the bump boundary that include shifts, see Figure 3.13.

3.4 Discussion

In this chapter, we analyzed the spatiotemporal dynamics of a two–dimensional excitatory neuronal network with synaptic depression. We showed that there is an extensive parameter range over which spatially structured oscillations are supported. With the inclusion of noise in the model this range is widened even further. We found that application

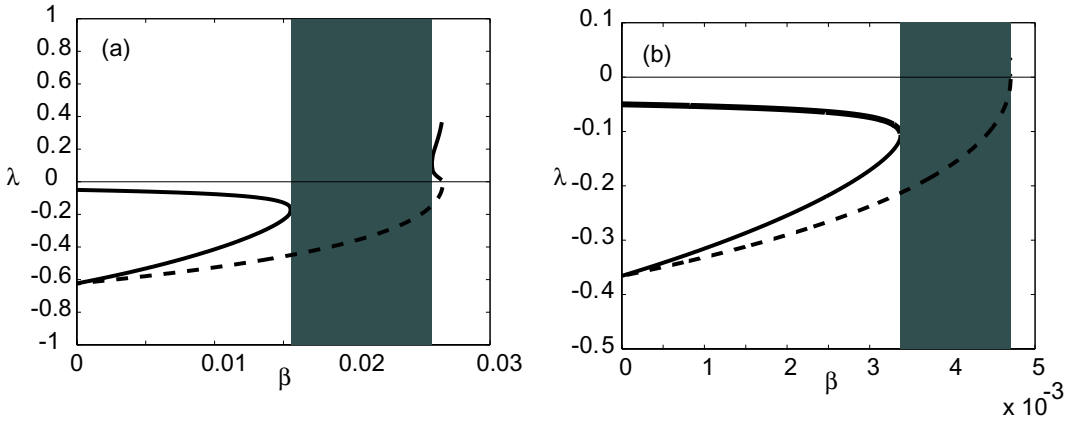

Figure 3.14. Stability of a two–dimensional bump with respect to radially symmetric perturbations. Eigenvalues of the expansion (solid curves) and contraction (dashed curve) perturbations are plotted for (a) $\theta = 0.05$ and (b) $\theta = 0.07$. Stability analysis of expansion perturbations breaks down in the grey region due to the roots (3.49) being complex. Other parameters are $A_i = 0.3$, $\sigma_i = 4$, and $\alpha = 20$.

of a localized current input as an initial condition to the network leads to a localized region of synchronous activity repeatedly emitting target waves. This type of activity has been linked to epileptic seizures [31, 126], memory [86], and sensory input [100, 101, 142, 158]. Additionally, breaking the symmetry of target wave emitting solutions either using external stimulation or noise generated spiral waves. Disinhibited mammalian cortical slices also support spiral waves, and it has been postulated that such activity allows periodic activity to be organized in spatially extended populations of neurons [67, 148]. Finally, we studied the dynamics that result the high gain limit, where in the case of an excitatory network the only spatially structured solutions are transient, such single target waves. In the case of a network with lateral inhibition, we studied existence and some of the instabilities of standing bump solutions using analysis that accounts for the piecewise smooth nature of the system.

In the next chapter, we will continue our study of neuronal networks with synaptic depression by considering its effects in a competitive neuronal network. Rather than only considering a single neural field, we shall model two populations, where each population represents a group of cells responding to inputs to either the left or right eye. Both local and cross connections are modified by synaptic depression. In this way, we can study the onset of oscillations in the network indicative of binocular rivalry.

CHAPTER 4

DYNAMICS OF BINOCULAR RIVALRY IN A COMPETITIVE NEURONAL NETWORK WITH SYNAPTIC DEPRESSION

In this chapter, we study binocular rivalry in a competitive neuronal network model with synaptic depression. In particular, we consider two coupled hypercolums within primary visual cortex (V1), representing orientation selective cells responding either to left or right eye inputs, respectively. Coupling between hypercolumns is dominated by inhibition, especially for neurons with dissimilar orientation preferences. Within hypercolumns, recurrent connectivity is excitatory for similar orientations and inhibitory for different orientations. All synaptic connections are modifiable by local synaptic depression. In Chapters 2 and 3, we studied single populations either on the infinite domain, or on a finite domain with nonperiodic boundary conditions. Here, we study the interaction of two populations, each with period boundary conditions. This alteration in network topology leads to novel dynamics thusfar unobserved the previous chapters. When the hypercolumns are driven by orthogonal oriented stimuli, it is possible to induce oscillations that are representative of binocular rivalry.

Binocular rivalry concerns the phenomenon whereby perception switches back and forth between different images presented to either eye. Due to the supposed link to activity in visual cortex, binocular rivalry continues to be an excellent way to obtain information about the human visual system. Psychophysical experiments are noninvasive and can provide a great deal of data about the response of the visual system to different characteristics of binocular stimuli. Although binocular rivalry has been studied for centuries, only recently have experimentalists clarified some of its specific statistical properties [13]. In 1965, Levelt proposed four characteristics of binocular rivalry, which he had ascertained empirically: (i) increasing the contrast of the stimulus in one eye increases the predominance of the stimulus

in that eye; (ii) increasing the contrast in one eye does not affect average dominance time of that eye; (iii) increasing contrast in one eye increases the rivalry alternation rate; and (iv) increasing the contrast in both eyes increases the rivalry alternation rate [104]. Propositions (i), (iii), and (iv) have been verified independently by other experimental studies, but proposition (ii) remains suspect [19].

Physiological recordings from primates as well as psychophysical data suggest that simple binocular stimuli invoke rivalry in the activity of neurons in the primary visual cortex (V1) [13]. Thus, it is important to understand some essential features of the functional architecture of V1 in order to study binocular rivalry. First, each neuron in V1 has a particular patch of the visual scene to which it responds, known as its *receptive field* [68, 69]. Stimuli outside a neuron's receptive field do not directly affect its activity. Second, most neurons in V1 respond preferentially to stimuli of a particular eye, right or left, which assigns their *ocular dominance* [68, 14, 124]. It has been suggested that neurons with different ocular dominance (one right, one left) may inhibit one another if they have nearby receptive fields [76]. As signals are relayed to higher areas of visual cortex, these two pathways are combined to process more complex stimuli. Third, most neurons in V1 are tuned to respond maximally when a stimulus of a particular orientation is in their receptive field [68, 36, 14]. This is known as a neuron's *orientation preference*, and the neuron will not be directly affected if a stimulus is sufficiently different from its preferred orientation. Finally, there is a great deal of evidence that suggests that, for a discrete patch of visual space, there exists a corresponding collection of neurons spanning the entire spectrum of orientation preferences that are packed together as a unit in V1, known as a *hypercolumn*. Within this hypercolumn, neurons with sufficiently similar orientations will excite each other and those with sufficiently different orientations will inhibit each other, which serves to sharpen a particular neuron's orientation preference [8, 54]. Anatomical evidence suggests that inter–hypercolumn connections excite similar orientations [157, 4]. The combination of these neurons' stimulus preference and connections suggests that V1 is most likely the seat of many simple examples of binocular rivalry.

With knowledge of the neurophysiology of V1, we can consider the following example of binocular rivalry. A horizontally oriented grating is presented to the left eye and a vertically oriented grating is presented to the right eye. This triggers rivalry due to the combination of orientation specific and ocular dominant cross–inhibition in V1 [8, 157, 13]. During the dominance of the left eye stimulus, it is proposed that a group of the left eye neurons

that respond to horizontal orientations are firing persistently, while right eye neurons are suppressed by cross–inhibitory connections. During right eye dominance, right eye, vertical orientation neurons fire persistently, suppressing the left eye neurons (see Figure 4.1). The process can continue indefinitely. While other types of stimuli may actually employ higher areas of visual cortex as neural substrates of binocular rivalry, we restrict our attention to V1 here to study spatiotemporal properties of the oscillations due to grating stimuli.

It remains an open question as to what slow adaptive process is most responsible for the eventual switching of one stimulus dominance to the other. The mechanism of spike frequency adaptation has been suggested, since it can curtail excitatory activity in a single neuron. Spike frequency adaptation is the process by which a hyperpolarizing current is switched on due to a build–up of a certain ion, like calcium, within the cell due to repetitive firing [162]. The maximal firing rate of a neuron is lowered as a result. In the

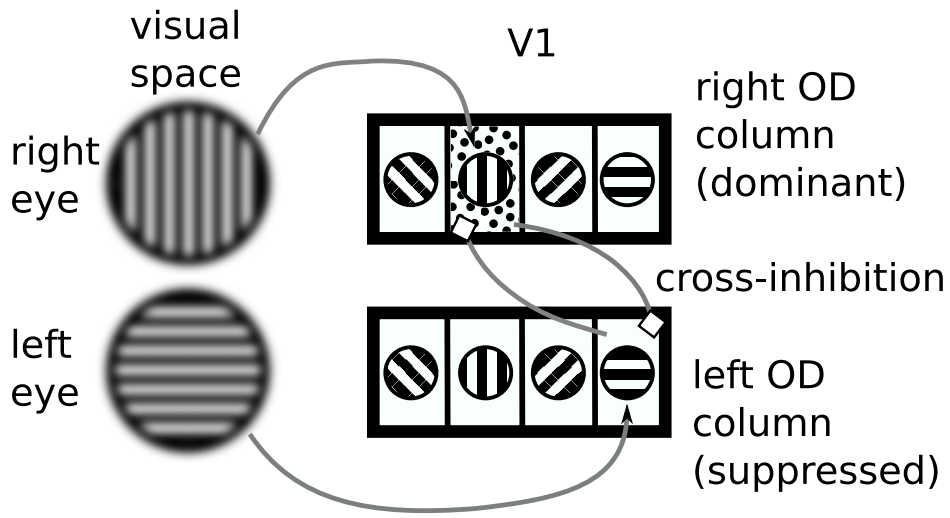

Figure 4.1. Primary visual cortex (V1) response to rival grating stimuli. In V1, neurons with the orientation preference of the stimulus presented to each eye will fire persistently in the dominant eye's ocular dominance (OD) column. Here, we see a snapshot in time, where the vertical orientation preference neurons fire persistently (polka dots) in the right OD column, while the horizontal orientation preference neurons of the left OD column are quiescent, even though they are receiving input. This is due to cross–inhibitory connections (white diamonds) between the two populations. In a winner–take–all (WTA) scenario, the picture would remain unchanged as time evolves, but in a binocular rivalry situation, a slow adaptive process would eventually release the left OD column's horizontal orientation preference neurons from suppression.

case of binocular rivalry, this may cause the dominant population to eventually drop its firing rate so that cross–inhibition suppressing the other population in then low enough for the suppressed populations to rekindle its firing rate into dominance. Since the recently released population is not adapted, it can then remain in dominance and suppress the other population for a period of time roughly equal to the time constant of spike frequency adaptation [179, 96, 108]. Another proposed switching mechanism is that the inhibitory synapses from one eye's neurons to the other's undergo synaptic depression.[1] This is the process by which synaptic resources such as neurotransmitters, vesicles, and scaffolding proteins are exhausted due to their continuous use [174, 34]. If inhibitory synapses remain repeatedly active, due to one eye's neurons suppressing the others, eventually most of those synapses' resources will be used up, the effect of inhibition will be weakened and the suppressed population will be released [96, 154].

In this chapter, we explore the hypothesis that synaptic depression is responsible for binocular rivalry in the primary visual cortex. While there has been some previous work studying depression as the sole mechanism for rivalry [165, 154], none has studied the onset of rivalry oscillations by analyzing bifurcations of stationary bump solutions in a spatially extended system. Thus, we consider a competitive neuronal network model of binocular rivalry in which a pair of hypercolumns for the left and right eyes, respectively, are coupled together with depressing local and cross–inhibitory synapses [8, 24]. In order to make the analysis analytically tractable, we take the mean firing rate of the neurons to be a Heaviside function of local activity, following along similar lines to previous studies of continuum neural fields [3, 39]. We introduce the model in section 4.1 and analyze a space clamped version of the model in section 4.2. Similar to a previous study with both adaptation and depression, we derive explicit formulae for the relation between dominance times and the parameters of the model [96]. Thus, we are able to compare the results of our model with the Levelt propositions given above. In section 4.3, we analyze binocular rivalry in the full spatially extended model by considering dynamical instabilities of stationary bump solutions. We consider the existence of both winner–take–all (WTA) solutions, represented by a single bump of activity persisting in a single population, and solutions where both populations support persistent bumps. We then analyze the linear stability

[1] More precisely, synaptic depression tends to be associated only with excitatory synapses, so that in our simplified model depressing inhibitory connections would have to be mediated by excitatory connections innervating local interneurons, for example.

of these solutions by taking into account the piecewise smooth nature of the neural field equations arising from the use of a Heaviside firing rate function. As in sections 2.2.4 and 3.3.3, it is necessary to keep track of the sign of perturbations of the bump boundary in order to characterize instabilities accurately. Finally, in section 4.4 we simulate the spatially extended system using a numerical approximation scheme, and compare with the results of our stability analysis.

4.1 Coupled hypercolumn model

We consider a neuronal network subdivided into two distinct populations (hypercolumns), one responding to the left eye and the other to the right eye. Each eye's local and cross–population synapses experience synaptic depression [174, 169]. This is an extension of the analysis presented in Chapters 2 and 3, which considered synaptic depression in a single population. Thus, the network in the most general form is described by the system of equations

$$\tau\frac{\partial u_L(\theta,t)}{\partial t} = -u_L(\theta,t) + w_l * (q_L f(u_L)) + w_c * (q_R f(u_R)) + I_L(\theta), \tag{4.1a}$$

$$\tau\frac{\partial u_R(\theta,t)}{\partial t} = -u_R(\theta,t) + w_l * (q_R f(u_R)) + w_c * (q_L f(u_L)) + I_R(\theta), \tag{4.1b}$$

$$\frac{\partial q_j(\theta,t)}{\partial t} = \frac{1-q_j(\theta,t)}{\alpha} - \beta q_j(\theta,t) f(u_j(\theta,t)), \quad j = L, R, \tag{4.1c}$$

where

$$w_i * (q_j f(u_j)) \quad = \quad \int_{-\pi/2}^{\pi/2} w_i(\theta,\theta') q_j(\theta',t) f(u_j(\theta',t)) \mathrm{d}\theta', \quad j = L, R.$$

Equations (4.1a) and (4.1b) describe the evolution of the synaptic current or drive $u_L(\theta,t)$ and $u_R(\theta,t)$ of neurons with orientation preference $\theta \in [-\pi/2, \pi/2]$ responding either to left (L) or right (R) eye inputs $I_j(\theta)$, $j = L, R$.[2] The nonlinear function f represents the mean firing rate of a local population and is usually taken to be a smooth, bounded monotonic function such as a sigmoid [180, 53]

$$f(u) = \frac{1}{1+\mathrm{e}^{-\eta(u-\kappa)}}, \tag{4.2}$$

[2]In this chapter, we shall use θ to represent a neuron's orientation preference. This does not change the fact that in the previous Chapters 2 and 3, θ represents firing threshold.

with gain η and threshold κ.[3] However, in order to explicitly compute solutions of interest, it will be convenient to consider the high gain limit $\eta \to \infty$ of the sigmoid (4.2), such that f becomes a Heaviside function [3, 39]

$$f(u) \quad = \quad \Theta(u-\kappa) = \begin{cases} 0 & \text{if } u > \kappa \\ 1 & \text{if } u < \kappa. \end{cases} \tag{4.3}$$

The strength of connections between neurons within a single eye's population (local) and from one population to another (cross) are specified by the weight function $w_l(\theta, \theta')$ and $w_c(\theta, \theta')$ respectively. A typical weight distribution within the hypercolumn or "ring" model is a harmonic function dependent on the difference in orientations [8, 24, 185]. Thus, for our studies of simple grating based binocular rivalry, we will employ the functions

$$w_j(\theta, \theta') = w(\theta - \theta') \quad = \quad w_0^j + w_2^j \cos(2(\theta - \theta')/d), \quad j = l, c, \tag{4.4}$$

where w_0^j is the mean strength of connectivity and w_2^j is the orientation specific strength. Depressing synapses are incorporated into the model in the form of a presynaptic scaling factor $q_j(\theta, t)$ evolving according to equation (4.1c). The factor $q_j(\theta, t)$ can be interpreted as a measure of available presynaptic resources, which are depleted at a rate βf [169, 164, 7], and are recovered on a timescale specified by the constant α. Specifically, we will study the effect of slow short–term synaptic depression (experimentally shown to recover over 5–10s [174, 34]). Slow short–term synaptic depression has been implicated as a mechanism for contrast adaptation in V1, due to its comparable recovery timescale of 5–10s [174]. Thus, there is evidence for participation of this slower depression in processes of V1 in addition to faster short–term synaptic depression, which recovers on timescales of roughly 200–800ms [2, 174]. Finally, we fix the temporal and spatial scales of the network by setting $\tau = 1$ and $d = 1$. The membrane time constant is typically around 10ms, while the range of synaptic connections and specifically the size of a hypercolumn within the visual cortex is on the order of 1mm.

Several previous studies have examined the phenomenon of binocular rivalry in the presence of adaptation, sometimes paired with synaptic depression [179, 96, 165, 129, 154]. These studies combine numerical simulations of spatially extended networks with numerical and analytical studies of reduced space–clamped networks. For example, Laing and Chow

[3] As stated, we use θ in this chapter to represent orientation preference, so we take κ to represent firing threshold.

have considered a similar coupled hypercolumn model to ours, which includes both adaptation and depression [96]. However, they carry out a rigorous analysis on only a reduced system with adaptation. More recently, Moreno–Bote and colleagues [129] have studied a neurally plausible attractor network model, where noise can be instrumental in switching dominance from one eye to the other. Finally, Shpiro and colleagues [154] have explored the commonalities and differences of several models of binocular rivalry that lead to oscillations on the appropriate timescale of physiological observation. In particular, they have looked at the Laing–Chow model in the case where adaptation–only or depression–only is present, and find that a space–clamped model with only synaptic depression satisfies Levelt Propositions (i) and (iii), while a model with only adaptation does not [154]. Rivalry effects in a spatially extended model with spike frequency adaptation have also been examined in a prior study by Loxley and Robinson [108].

4.2 Oscillations in the space–clamped system

In this section we analyze oscillations in a space–clamped (θ–independent) version of our model. That is, we take the inputs I_L and I_R from both eyes to be homogeneous in the variable θ. While stimuli used in binocular rivalry experiments often have a preferred orientation to either eye, it is indeed possible to evoke the rivalry percept without such a specification [12]. Taking the weight functions to be given by the simple sum of harmonics (4.4) and specifying that solutions be homogeneous in θ, the system (4.1) becomes

$$\begin{aligned} \dot{u}_L(t) &= -u_L(t) + \bar{w}_l q_L(t) f(u_L(t)) + \bar{w}_c q_R(t) f(u_R(t)) + I_L, \\ \dot{u}_R(t) &= -u_R(t) + \bar{w}_l q_R(t) f(u_R(t)) + \bar{w}_c q_L(t) f(u_L(t)) + I_R, \\ \dot{q}_j(t) &= (1 - q_j(t))/\alpha - \beta q_j(t) f(u_j(t)), \quad j = L, R, \end{aligned} \tag{4.5}$$

where

$$\bar{w}_j = \int_{-\pi/2}^{\pi/2} w_j(\theta') \mathrm{d}\theta', \quad j = l, c \tag{4.6}$$

denotes the average strength of connectivity for either weight function. We will prescribe that $\bar{w}_c < 0$ so the cross connections are "inhibition–dominated," as this has been a suggested mechanism of binocular rivalry [76]. As an extensive numerical study of equilibria of a system similar to (4.5) has been carried out when f is sigmoidal [154], we will proceed analytically by examining the behavior of the system (4.5) in the case that f is the Heaviside function (4.3). In the latter case, we can compute any equilibria explicitly. Moreover, a

fast–slow analysis can be used to determine the residence times spent with either the left or right eye being dominant. We will follow along similar lines to Laing and Chow [96], who used Heaviside functions to analyze binocular rivalry in a coupled hypercolumn model with spike frequency adaptation rather than synaptic depression. The dynamics of the system (4.5) can be characterized in terms of some simple parametric inequalities, specifying whether the system oscillates or settles into a steady state. Of course, we are interested in the parameter regimes in which the system oscillates, since this is indicative of binocular rivalry.

There are several different possible steady states, whose existence mainly depends on the strength of the input to either population. First, the off–state given by $(u_L, u_R, q_L, q_R) = (I_1, I_2, 1, 1)$ occurs when $I_L, I_R < \kappa$, which implies that the input is not strong enough to activate either population. Second, the both–on or fusion state

$$u_j = \frac{\bar{w}_l + \bar{w}_c}{1+\alpha\beta} + I_j, \quad q_j = \frac{1}{1+\alpha\beta}, \quad j = L, R, \tag{4.7}$$

occurs when $I_L, I_R > \kappa - (\bar{w}_l + \bar{w}_c)/(1+\alpha\beta)$. This case is more likely for very strong depression (β large), since cross inhibition will be weak, or when the local connections are strong and excitation–dominated,. The third type of equilibrium is the winner–take–all (WTA), where one population dominates the other. For example, if the left eye population is dominant then

$$\begin{aligned} u_L &= \frac{\bar{w}_l}{1+\alpha\beta} + I_L, \quad u_R = \frac{\bar{w}_c}{1+\alpha\beta} + I_R, \\ q_L &= \frac{1}{1+\alpha\beta}, \qquad\qquad q_R = 1, \end{aligned} \tag{4.8}$$

which can be transformed to the right eye dominant case by interchanging L and R For the steady state (4.8) to exist, we require

$$I_L > \kappa - \frac{\bar{w}_l}{1+\alpha\beta}, \quad I_R < \kappa - \frac{\bar{w}_c}{1+\alpha\beta},$$

This will occur in the presence of weak depression (β small) and strong cross–inhibition such that depression cannot exhaust the dominant hold one population has on the other.

The local stability of each equilibrium can be determined by calculating the general Jacobian for the system (4.5) in the case that $f(u) \equiv \Theta(u-\kappa)$ and $u_L, u_R \neq \kappa$:

$$\mathcal{J}(u_L, u_R, q_L, q_R) = \begin{pmatrix} -1 & 0 & \bar{w}_l\Theta(u_L-\kappa) & \bar{w}_c\Theta(u_R-\kappa) \\ 0 & -1 & \bar{w}_c\Theta(u_L-\kappa) & \bar{w}_l\Theta(u_R-\kappa) \\ 0 & 0 & -(\alpha^{-1}+\beta\Theta(u_L-\kappa)) & 0 \\ 0 & 0 & 0 & -(\alpha^{-1}+\beta\Theta(u_R-\kappa)) \end{pmatrix}. \tag{4.9}$$

It is straightforward to show that the eigenvalues of this Jacobian for a general equilibrium (excluding cases where $u_L = \kappa$ or $u_R = \kappa$) are

$$\lambda = -1, \quad -(\alpha^{-1} + \beta\Theta(u_L - \kappa)), \quad -(\alpha^{-1} + \beta\Theta(u_R - \kappa)), \tag{4.10}$$

which are all negative, regardless of the values u_L and u_R. Therefore, all steady states of the system (4.5) are stable. It follows that a limit cycle corresponding to a binocular rivalry state cannot arise from the destabilization of an equilibrium via a standard Hopf bifurcation. Indeed, due to the piecewise smooth nature of the dynamics, we find that a limit cycle corresponding to an oscillating rivalrous state surrounds a stable fusion state as illustrated in Figure 4.2. In can be seen that as the amplitude of the inputs $I_L = I_R$ is varied, the system (4.5) exhibits bistability between fusion/rivalry states, between off/WTA states, and between WTA/fusion states (when $\bar{w}_l \neq 0$). Such bistability has seldom been observed in other models of binocular rivalry. However, in [154], it was shown that Wilson's model [178] of binocular rivalry supports a WTA/rivalry bistable state. Bifurcation analysis of the Laing and Chow model in [154] did not exhibit bistability, perhaps owing to the fact that it included no recurrent excitation. Since the occurrence of oscillations cannot be studied using standard bifurcation theory, we will follow Laing and Chow [96] by assuming that we are in a regime where oscillations exist and characterize the dominance times by

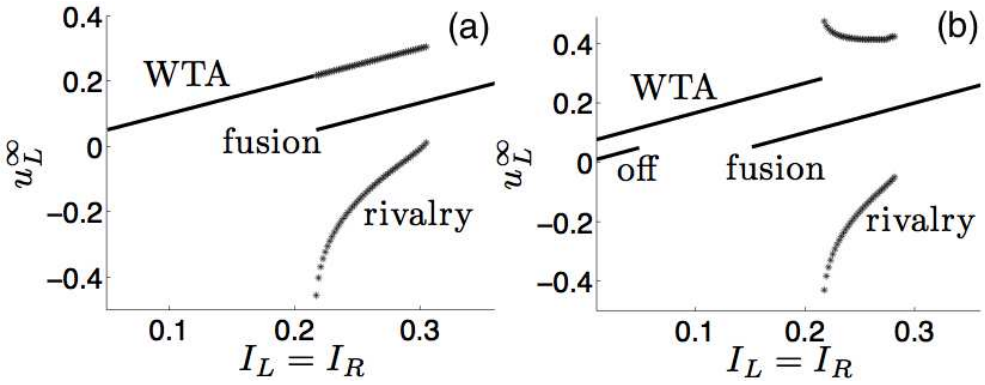

Figure 4.2. Equilibria of the left population u_L as a function of the input amplitude $I_L = I_R$ to both populations . Solid lines represent stable states, whereas stars represent maximum and minimum of rivalry oscillations. (a) For no local connections, $\bar{w}_l = 0$, we find a bistable region, where rivalry coexists with a stable fusion state. (b) When local connections are non–zero, $\bar{w}_l = 0.4$, there are regions of off/WTA bistability, WTA/fusion bistability, and fusion/rivalry bistability. Other parameters are $\kappa = 0.05$, $\alpha = 500$, $\beta = 0.01$, and $\bar{w}_c = -1$.

exploiting the separation in timescales between synaptic depression and neural activity, that is, $\alpha \gg 1$.

Suppose that the system has settled onto a limit cycle as pictured in Figure 4.3, and that it is at the point where u_L has just been released from suppression by u_R. Since both u_L and u_R equilibrate quickly compared with q_L and q_R, it follows that

$$u_L(t) = \bar{w}_l q_L(t) + I_L, \qquad u_R(t) = \bar{w}_c q_L(t) + I_R. \tag{4.11}$$

We can also solve explicitly for $q_L(t)$ and $q_R(t)$ using the equations

$$\dot{q}_L = (1 - q_L)/\alpha - \beta q_L, \qquad \dot{q}_R = (1 - q_R)/\alpha, \tag{4.12}$$

Assuming the initial conditions $q_L(0) = q_L^s$ and $q_R(0) = q_R^d$, we have

$$q_L(t) = \frac{1}{1+\alpha\beta} + \left(q_L^s - \frac{1}{1+\alpha\beta} \right) \mathrm{e}^{-(1+\alpha\beta)t/\alpha}, \tag{4.13}$$

$$q_R(t) = 1 - (1 - q_R^d)\mathrm{e}^{-t/\alpha}, \tag{4.14}$$

for $t \in (0, T_L)$, where T_L is the dominance time of the left eye. Therefore, when the left eye population is suppressing the right eye population, the dynamics of the input currents

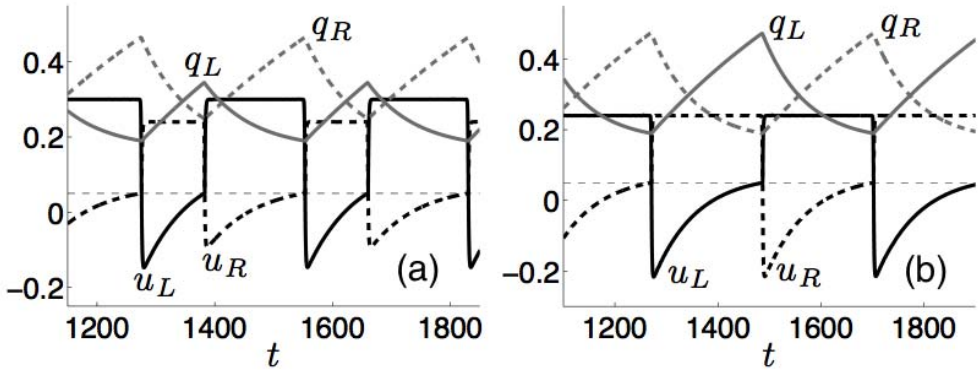

Figure 4.3. Oscillatory solutions of the space–clamped system (4.5) for a Heaviside activation function (4.3). (a) Plot against time of the activities u_L (solid black) and u_R (dashed black) with the depression variables q_L (solid grey) and q_R (dashed grey) when inputs are the same to both populations so that $I_L = I_R = 0.24$. This leads to an oscillation wherein the dominance times ($T_L = T_R \approx 210$) are equivalent for each percept. (b) Plot against time of the activities u_L, u_R and depression variables q_L, q_R when inputs are different so that $I_L = 0.30$ and $I_R = 0.24$. This leads to an oscillation wherein the dominance times ($T_L \approx 170$, $T_R \approx 105$) are different for each percept. Other parameters are $\bar{w}_l = 0$, $\bar{w}_c = -1$, $\kappa = 0.05$, $\alpha = 500$, and $\beta = 0.01$.

is explicitly

$$u_L(t) = \bar{w}_l \left(\frac{1}{1+\alpha\beta} + \left(q_L^s - \frac{1}{1+\alpha\beta} \right) \mathrm{e}^{-(1+\alpha\beta)t/\alpha} \right) + I_L, \tag{4.15}$$

$$u_R(t) = \bar{w}_c \left(\frac{1}{1+\alpha\beta} + \left(q_1^s - \frac{1}{1+\alpha\beta} \right) \mathrm{e}^{-(1+\alpha\beta)t/\alpha} \right) + I_R. \tag{4.16}$$

At the time $t = T_L$, the synaptic drive u_R will be released from u_L's dominance by reaching threshold, that is, $u_R(T_L) = \kappa$. This generates the equation

$$\kappa = \bar{w}_c \left(\frac{1}{1+\alpha\beta} + \left(q_L^s - \frac{1}{1+\alpha\beta} \right) \mathrm{e}^{-(1+\alpha\beta)T_L/\alpha} \right) + I_R. \tag{4.17}$$

Note that although $u_L(T_L) > \kappa$, u_L will drop below threshold much more rapidly than the timescale of the q_j's due to cross inhibition. Hence, we can make the approximation $T_L^* \approx T_L$ where $u_L(T_L^*) = \kappa$. In the next phase of the oscillation

$$u_L(t) = \bar{w}_c q_R(t) + I_L, \qquad u_R(t) = \bar{w}_l q_R(t) + I_R, \tag{4.18}$$

with

$$\dot{q}_L = (1 - q_L)/\alpha, \qquad \dot{q}_R = (1 - q_R)/\alpha - \beta q_R. \tag{4.19}$$

Assuming the new set of initial conditions $q_L(T_L) = q_L^d$ and $q_R(T_L) = q_R^s$, we now have

$$q_L(t) = 1 - (1 - q_L^d)\mathrm{e}^{(T_L - t)/\alpha}, \tag{4.20}$$

$$q_R(t) = \frac{1}{1+\alpha\beta} + \left(q_R^s - \frac{1}{1+\alpha\beta} \right) \mathrm{e}^{-(1+\alpha\beta)(T_L - t)/\alpha}, \tag{4.21}$$

for $t \in (T_L, T_L + T_R)$, where T_R is the dominance time of the right eye. Therefore, when the right eye population is suppressing the left eye population, the dynamics of the input currents is approximately described by

$$u_L(t) = \bar{w}_c \left(\frac{1}{1+\alpha\beta} + \left(q_R^s - \frac{1}{1+\alpha\beta} \right) \mathrm{e}^{-(1+\alpha\beta)(T_L - t)/\alpha} \right) + I_L, \tag{4.22}$$

$$u_R(t) = \bar{w}_l \left(\frac{1}{1+\alpha\beta} + \left(q_R^s - \frac{1}{1+\alpha\beta} \right) \mathrm{e}^{-(1+\alpha\beta)(T_L - t)/\alpha} \right) + I_R. \tag{4.23}$$

Finally, at $t = T_L + T_R$, u_L will be released from u_R's dominance such that $u_L(T_L + T_R) = \kappa$. This generates the equation

$$\kappa = \bar{w}_c \left(\frac{1}{1+\alpha\beta} \left(q_R^s - \frac{1}{1+\alpha\beta} \right) \mathrm{e}^{-(1+\alpha\beta)T_R/\alpha} \right) + I_L, \tag{4.24}$$

At this point, $u_R > \kappa$, but u_R will rapidly drop below threshold so that $u_R(T_R^*) = \kappa$ with $T_R^* \approx T_R$.

Equations (4.13), (4.14), (4.20) and (4.21) generate four equations for the four unknown initial conditions of the depression variables:

$$q_L^s = 1-(1-q_L^d)\mathrm{e}^{-T_R/\alpha}, \tag{4.25}$$

$$q_R^s = 1-(1-q_R^d)\mathrm{e}^{-T_L/\alpha}, \tag{4.26}$$

$$q_L^d = \frac{1}{1+\alpha\beta}+\left(q_L^s-\frac{1}{1+\alpha\beta}\right)\mathrm{e}^{-(1+\alpha\beta)T_L/\alpha}, \tag{4.27}$$

$$q_R^d = \frac{1}{1+\alpha\beta}+\left(q_R^s-\frac{1}{1+\alpha\beta}\right)\mathrm{e}^{-(1+\alpha\beta)T_R/\alpha}. \tag{4.28}$$

We can solve these explicitly for q_L^s and q_R^s in terms of the parameters α, β and the dominance times T_L, T_R as

$$q_L^s = \frac{\left(1-\mathrm{e}^{-T_R/\alpha}+\frac{1}{1+\alpha\beta}\left(1-\mathrm{e}^{-(1+\alpha\beta)T_L/\alpha}\right)\mathrm{e}^{-T_R/\alpha}\right)}{\left(1-\mathrm{e}^{-(1+\alpha\beta)T_L/\alpha}\mathrm{e}^{-T_R/\alpha}\right)} \tag{4.29}$$

$$q_R^s = \frac{\left(1-\mathrm{e}^{-T_L/\alpha}+\frac{1}{1+\alpha\beta}\left(1-\mathrm{e}^{-(1+\alpha\beta)T_R/\alpha}\right)\mathrm{e}^{-T_L/\alpha}\right)}{\left(1-\mathrm{e}^{-(1+\alpha\beta)T_R/\alpha}\mathrm{e}^{-T_L/\alpha}\right)}. \tag{4.30}$$

Substituting equations (4.29) and (4.30) into equations (4.17) and (4.24) then gives

$$\begin{aligned}\kappa = \bar{w}_c\Bigg(\frac{1}{1+\alpha\beta}+\Bigg(\Bigg(1-\mathrm{e}^{-T_R/\alpha}+\frac{1}{1+\alpha\beta}\left(1-\mathrm{e}^{-(1+\alpha\beta)T_L/\alpha}\right)\mathrm{e}^{-T_R/\alpha}\Bigg)\times \\ \left(1-\mathrm{e}^{-(1+\alpha\beta)T_L/\alpha}\mathrm{e}^{-T_R/\alpha}\right)^{-1}-\frac{1}{1+\alpha\beta}\Bigg)\mathrm{e}^{-(1+\alpha\beta)T_L/\alpha}\Bigg)+I_R,\end{aligned} \tag{4.31}$$

$$\begin{aligned}\kappa = \bar{w}_c\Bigg(\frac{1}{1+\alpha\beta}+\Bigg(\Bigg(1-\mathrm{e}^{-T_L/\alpha}+\frac{1}{1+\alpha\beta}\left(1-\mathrm{e}^{-(1+\alpha\beta)T_R/\alpha}\right)\mathrm{e}^{-T_L/\alpha}\Bigg)\times \\ \left(1-\mathrm{e}^{-(1+\alpha\beta)T_R/\alpha}\mathrm{e}^{-T_L/\alpha}\right)^{-1}-\frac{1}{1+\alpha\beta}\Bigg)\mathrm{e}^{-(1+\alpha\beta)T_R/\alpha}\Bigg)+I_L.\end{aligned} \tag{4.32}$$

A numerical root finding algorithm can be used to solve for the dominance times T_L and T_R in terms of the parameters $\alpha, \beta, \kappa, \bar{w}_c$. We show examples of the dependence of these dominance times on a common drive strength to both populations $I_L = I_R = I_B$ and a modulation of input I_L, while keeping I_R constant in Figure 4.4. Recall that Levelt proposition (iv) states increasing contrast (stimulus strength) to both eyes increases alternation rate, which is corroborated by $T_L = T_R = T_B$ being a decreasing function of I_B in Figure 4.4a. Also, both propositions (i) and (iii) are in agreement with Figure 4.4b, since increasing I_L leads to lower values of both T_L and T_R and the ratio $T_L/(T_L+T_R)$ increases as well. However, the Levelt proposition (ii) states increasing input to one eye

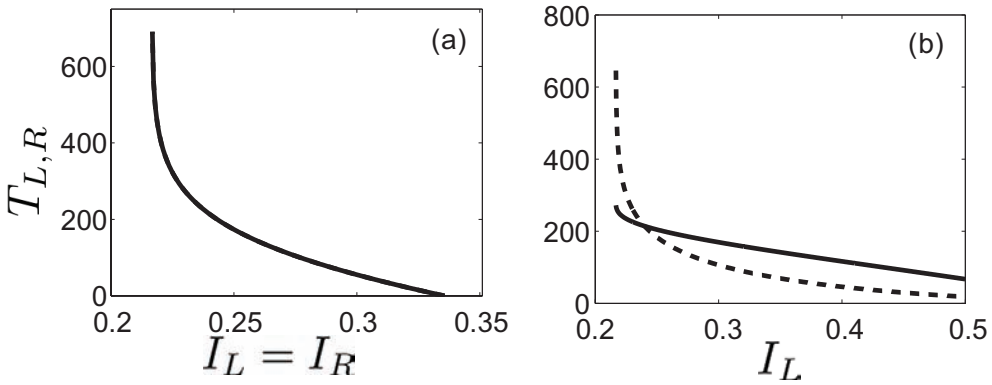

Figure 4.4. Dominance times calculated from equations (4.31) and (4.32) plotted against input amplitude. (a) Effect of changing the amplitude of both inputs $I_L = I_R = I$ on the dominance times of both percepts. In this case, dominance times are identical. (b) Effect of changing input to left eye (I_L) on dominance times of left population u_L (dashed curve) and right population (solid curve) when $I_R = 0.24$. Other parameters are as in Figure 4.3.

does not change that eye's average dominance, but we find in Figure 4.4b that T_L decreases slightly. Indeed, previous experiments have produced results at odds with proposition (ii), finding the statement may depend on specific contrast ranges of stimuli [19]. Interestingly, the dominance times do not depend at all on the strength of local connections $\bar{w}_l$. In a recent study, it was shown that recurrent connections are not needed at all in order to produce the competition dynamics of rivalry in a network with synaptic depression [154].

4.3 Oscillations and bumps in the coupled hypercolumn model

Let us now return to the full spatially extended coupled hypercolumn model (4.1). In section 2.2, we showed that stable stationary bumps of activity can exist in a scalar neural field model with lateral inhibition for sufficiently weak synaptic depression. Additionally, it has been shown that a single ring (or hypercolumn) model with synaptic depression can support stable stationary bumps as well as a rotating bumps [185]. We extend these results here by considering two coupled rings (hypercolumns) with synaptic depression driven by stimuli with different orientations. A related study based on networks with spike frequency adaptation is considered elsewhere [108]. We consider the system (4.1) in the case of the Heaviside firing rate function (4.3) and inputs $I_L(\theta)$ and $I_R(\theta)$ given by functions peaked at a specific orientation, which are meant to represent stationary grating stimuli [12, 178]. For concreteness, we take

$$I_L(\theta) = I_L^0 \cos^p(\theta - \pi/4), \qquad I_R(\theta) = I_R^0 \cos^p(\theta + \pi/4), \tag{4.33}$$

where $\pi/4$ and $-\pi/4$ are the stimulus orientations and p is an even integer power that determines the sharpness of the inputs with respect to orientation. (We set $p = 6$). As a simplification, we take the left and right input strengths to be the same, $I_L^0 = I_R^0 = I_0$. The particular choice of stimulus orientations and strengths simplifies our calculations, since the associated neural field equations are reflection symmetric. That is they are equivariant with respect to the transformation $L \to R$ and $\theta \to -\theta$. Note, however, that our analysis can be extended to take into account more general stimulus orientations and asymmetric input strengths $I_L^0 \neq I_R^0$. Finally, we take both the local and cross populations' weight functions w_l, w_c to be the harmonic weight function (4.4). Our analysis then proceeds by studying the existence and linear stability of nontrivial stationary solutions corresponding to either single bump or double bump solutions. A stationary solution $(u_L, u_R, q_L, q_R) = (U_L(\theta), U_R(\theta), Q_L(\theta), Q_R(\theta))$ of equations ((4.1) satisfies the system of equations (for $f \equiv \Theta$)

$$\begin{aligned} U_L(\theta) &= w_l * (Q_L \Theta(U_L - \kappa)) + w_c * (Q_R \Theta(U_R - \kappa)) \\ U_R(\theta) &= w_l * (Q_R \Theta(U_R - \kappa)) + w_c * (Q_L \Theta(U_L - \kappa)) \\ Q_j(\theta) &= 1 - \frac{\alpha\beta}{1 + \alpha\beta} \Theta(U_j(\theta) - \kappa), \quad j = L, R. \end{aligned} \tag{4.34}$$

Introduce the excited or superthreshold regions $R[U_j] = \{\theta | U_j(\theta) > \theta\}$ of the left ($j = L$) and right ($j = R$) populations. These will vary, depending on whether we study a single or double bump. A single bump solution is equivalent to a winner–take–all (WTA) scenario where only a single hypercolumn contains superthreshold bump activity, for example, $R[U_L] = (\theta_1, \theta_2)$ and $R[U_R] = \emptyset$. On the other hand, in the case of a double bump solution both hypercolumns exhibit superthreshold bump activity. Exploiting the reflection symmetry, this means that $R[U_L] = (\theta_1, \theta_2)$ and $R[U_R] = (-\theta_1, -\theta_2)$.

4.3.1 Existence of single bump

For a single bump or winner–take–all (WTA) solution, only one neural activity variable will have an associated nonempty excited region, so we pick the left population such that $R[U_L] = (\theta_1, \theta_2)$, whereas the right input U_R will always remain below threshold so that $R[U_R] = \emptyset$. Threshold crossing points are then defined as $U_L(\theta_1) = U_L(\theta_2) = \kappa$. We could

just as easily have picked the right population due to reflection symmetry of the network. As we have prescribed, the system (4.34) becomes

$$U_L(\theta) = \int_{\theta_1}^{\theta_2} w_l(\theta-\theta')Q_L(\theta')\mathrm{d}\theta' + I_L(\theta), \tag{4.35}$$

$$U_R(\theta) = \int_{\theta_1}^{\theta_2} w_c(\theta-\theta')Q_L(\theta')\mathrm{d}\theta' + I_R(\theta), \tag{4.36}$$

$$Q_j(\theta) = 1 - \frac{\alpha\beta}{1+\alpha\beta}\Theta(U_j(\theta)-\kappa), \quad j = L, R. \tag{4.37}$$

Substituting equations (4.37) into (4.35) and (4.36) yields

$$U_L(\theta) = \frac{1}{1+\alpha\beta}\int_{\theta_1}^{\theta_2} w_l(\theta-\theta')Q_L(\theta')\mathrm{d}\theta' + I_L(\theta), \tag{4.38}$$

$$U_R(\theta) = \frac{1}{1+\alpha\beta}\int_{\theta_1}^{\theta_2} w_c(\theta-\theta')Q_L(\theta')\mathrm{d}\theta' + I_R(\theta). \tag{4.39}$$

Plugging in the sum of harmonics weight function (4.4) for w_l and w_c, we analytically calculate the single bump solution

$$U_L(\theta) = \frac{1}{1+\alpha\beta}\left[w_0^l(\theta_2-\theta_1) + \frac{w_2^l}{2}(\sin(2(\theta-\theta_1)) - \sin(2(\theta-\theta_2)))\right] + I_L(\theta) \tag{4.40}$$

$$U_R(\theta) = \frac{1}{1+\alpha\beta}\left[w_0^c(\theta_2-\theta_1) + \frac{w_2^c}{2}(\sin(2(\theta-\theta_1)) - \sin(2(\theta-\theta_2)))\right] + I_R(\theta). \tag{4.41}$$

Applying the threshold conditions $U_L(\theta_1) = U_L(\theta_2) = \kappa$ and noting the symmetry of the system,

$$\kappa = \frac{1}{1+\alpha\beta}\left[w_0^l\Delta\theta + \frac{w_2^l}{2}\sin(2\Delta\theta)\right] + I_0\cos^p(\Delta\theta/2), \tag{4.42}$$

which provides us with an implicit equation relating the bump width $\Delta\theta = \theta_2 - \theta_1$ to all other parameters. One additional constraint on the solution (4.41) is that it always remain below threshold. For sufficiently strong inputs, the maximum of U_R will occur at the peak of the input I_R, so that we need only check if $U_R(-\pi/4) < \kappa$ which we compute as

$$\begin{aligned} U_R(-\pi/4) &= \frac{1}{1+\alpha\beta}\left[w_0^c(\Delta\theta) + \frac{w_2^c}{2}(\sin(2\theta_2+\pi/2) - \sin(2\theta_1+\pi/2))\right] + I_0 \\ &= \frac{1}{1+\alpha\beta}\left[w_0^c(\Delta\theta) - w_2^c\sin(\Delta\theta)\right] + I_0, \end{aligned} \tag{4.43}$$

where we have used $\theta_1 = \pi/4 - \Delta\theta/2$ and $\theta_2 = \pi/4 + \Delta\theta/2$. This yields

$$w_0^c(\Delta\theta) - w_2^c\sin(\Delta\theta) < (1+\alpha\beta)(\kappa - I_0) \tag{4.44}$$

for the subthreshold condition. Thus, for a single bump solution to exist, the threshold condition (4.42) and the subthreshold condition (4.44) must be satisfied. Equation (4.42)

can be solved numerically using a root finding algorithm. Following this, we can find whether the inequality (4.44) is satisfied by direct computation. The variation of the width of the bump $\Delta\theta$ with the input strength I_0 and depression strength β is shown in Figure 4.5; the stability of the bump is calculated below.

4.3.2 Stability of single bump

To study the stability of the single bump solution, we begin by letting $u_j(\theta,t) = U_j(\theta) + \varepsilon\psi_j(\theta,t)$ and $q_j(\theta,t) = Q_j(\theta) + \varepsilon\varphi_j(\theta,t)$ for $j = L, R$, where ψ_j and φ_j denote smooth perturbations and $\varepsilon \ll 1$. Substituting into the full system (4.1), imposing the single bump solutions (4.35), (4.36), and (4.37), and dividing through by ε gives

$$\begin{aligned}\frac{\partial\psi_L(\theta,t)}{\partial t} &= -\psi_L(\theta,t) + w_l * (Q_L[\Theta(U_L+\psi_L-\kappa) - \Theta(U_L-\kappa)]) \\ &\quad + w_l * (\varphi_L\Theta(U_L+\psi_L-\kappa)), \qquad (4.45)\end{aligned}$$

$$\begin{aligned}\frac{\partial\psi_R(\theta,t)}{\partial t} &= -\psi_R(\theta,t) + w_c * (Q_L[\Theta(U_L+\psi_L-\kappa) - \Theta(U_L-\kappa)]) \\ &\quad + w_c * (\varphi_L\Theta(U_L+\psi_L-\kappa)), \qquad (4.46)\\ \frac{\partial\varphi_j(\theta,t)}{\partial t} &= -\frac{\varphi_j(\theta,t)}{\alpha} - \beta Q_j[\Theta(U_j+\psi_L-\kappa) - \Theta(U_j-\kappa)] - \beta\varphi_j\Theta(U_j+\psi_L-\kappa), \\ &\qquad (4.47)\end{aligned}$$

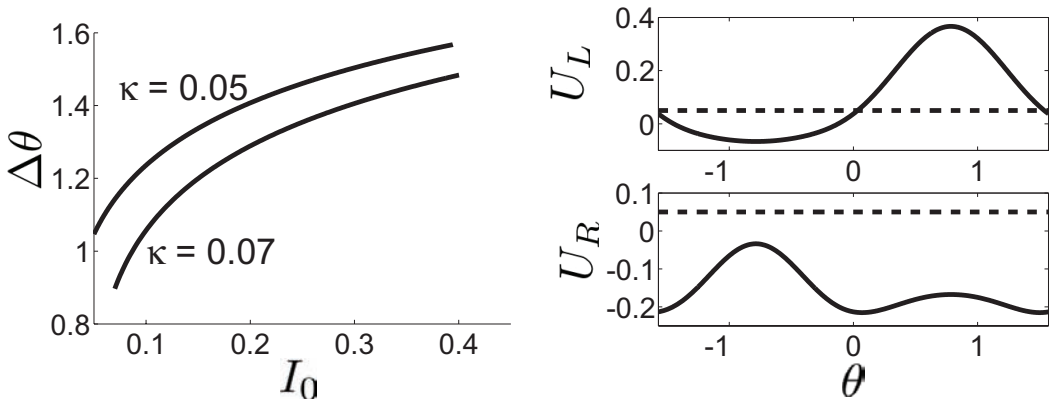

Figure 4.5. Single bumps in coupled hypercolumns. (Left) Plots relating single bump width $\Delta\theta$ to the amplitude of input I_0 for different values of κ using equation (4.42) and constrained by inequality (4.44). Bumps do not exist for a particular value of κ to the right of the associated curve. Other parameters are $w_0^l = 0$, $w_2^l = 0.4$, $w_0^e = -1$, $w_2^e = 0.5$, $\alpha = 500$, $\beta = 0.01$. (Right) Bump profile when $\kappa = 0.05$ and $I_0 = 0.3$.

for $j = L, R$. Denote the perturbations of the bump boundaries by $\varepsilon\Delta_{\pm}^{L}(t)$ such that

$$u_L(\theta_1 + \varepsilon\Delta_{-}^{L}(t), t) = u_L(\theta_2 + \varepsilon\Delta_{+}^{L}(t), t) \quad = \quad \kappa. \tag{4.48}$$

Taylor expanding these threshold conditions to first order in perturbations, we find that

$$\Delta_{-}^{L}(t) \approx -\frac{\psi_L(\theta_1, t)}{|U_L'(\theta_1)|}, \quad \Delta_{+}^{L}(t) \approx \frac{\psi_L(\theta_2, t)}{|U_L'(\theta_2)|}. \tag{4.49}$$

Following our analysis of stationary bumps in sections 2.2.4 and 3.3.3, we can smooth out discontinuities in equations (4.47) by introducing the infinitesimal fields

$$\Phi_{Lm}(\theta, t) \quad = \quad \int_{\theta_1 + \varepsilon\Delta_{-}^{L}}^{\theta_2 + \varepsilon\Delta_{+}^{L}} w_m(\theta - \theta')\varphi_L(\theta', t)\mathrm{d}\theta', \tag{4.50}$$

for $m = l, c$. Differentiating equation (4.50) with respect to t and combining this with equations (4.45), (4.46), and (4.47) gives

$$\begin{aligned} \frac{\partial\psi_L(\theta,t)}{\partial t} &= -\psi_L(\theta,t) + \Phi_{Ll}(\theta,t) \\ &\quad + \frac{1}{\varepsilon}\int_{\theta_1+\varepsilon\Delta_{-}^{L}(t)}^{\theta_2+\varepsilon\Delta_{+}^{L}(t)} w_l(\theta-\theta')Q_L(\theta')\mathrm{d}\theta' - \frac{1}{\varepsilon}\int_{\theta_1}^{\theta_2} w_l(\theta-\theta')Q_L(\theta')\mathrm{d}\theta', \end{aligned} \tag{4.51}$$

$$\begin{aligned} \frac{\partial\psi_R(\theta,t)}{\partial t} &= -\psi_R(\theta,t) + \Phi_{Lc}(\theta,t) \\ &\quad + \frac{1}{\varepsilon}\int_{\theta_1+\varepsilon\Delta_{-}^{L}(t)}^{\theta_2+\varepsilon\Delta_{+}^{L}(t)} w_c(\theta-\theta')Q_L(\theta')\mathrm{d}\theta' - \frac{1}{\varepsilon}\int_{\theta_1}^{\theta_2} w_c(\theta-\theta')Q_L(\theta')\mathrm{d}\theta', \end{aligned} \tag{4.52}$$

$$\begin{aligned} \frac{\partial\Phi_{Lm}(\theta,t)}{\partial t} &= -(\alpha^{-1}+\beta)\Phi_{Lm}(\theta,t) \\ &\quad - \frac{\beta}{\varepsilon}\int_{\theta_1+\varepsilon\Delta_{-}^{L}(t)}^{\theta_2+\varepsilon\Delta_{+}^{L}(t)} w_m(\theta-\theta')Q_L(\theta')[\Theta(U_L+\varepsilon\psi_L-\kappa)-\Theta(U_L-\kappa)]\mathrm{d}\theta, \\ &\quad + \varepsilon w_m(\theta-\theta_2-\varepsilon\Delta_{+}^{L}(t))\varphi_{Lm}(\theta_2+\varepsilon\Delta_{+}^{L}(t),t)\dot{\Delta}_{+}^{L}(t) \\ &\quad - \varepsilon w_m(\theta-\theta_1-\varepsilon\Delta_{-}^{L}(t))\varphi_{Lm}(\theta_1+\varepsilon\Delta_{-}^{L}(t),t)\dot{\Delta}_{-}^{L}(t), \qquad m = l, c. \end{aligned} \tag{4.53}$$

We can now linearize the system of equations (4.51), (4.52), and (4.53) by expanding in powers of ε and collecting all $\mathcal{O}(1)$ terms. Note that it is important to keep track of the

signs of $\Delta_{\pm}^{L}$ when approximating the various integrals due to the discontinuous nature of $Q_L(\theta)$. We thus obtain the piecewise linear system of equations:

$$\begin{aligned}
\frac{\partial \psi_L(\theta,t)}{\partial t} &= -\psi_L(\theta,t) + \Phi_{Ll}(\theta,t) + \gamma_S w_l(\theta-\theta_1)\psi_L(\theta_1,t)G(\psi_L(\theta_1,t)) \\
&\quad +\gamma_S w_l(\theta-\theta_2)\psi_L(\theta_2,t)G(\psi_L(\theta_2,t)), \qquad (4.54)\\
\frac{\partial \psi_R(\theta,t)}{\partial t} &= -\psi_R(\theta,t) + \Phi_{Lc}(\theta,t) + \gamma_S w_c(\theta-\theta_1)\psi_L(\theta_1,t)G(\psi_L(\theta_1,t)), \\
&\quad +\gamma_S w_c(\theta-\theta_2)\psi_L(\theta_2,t)G(\psi_L(\theta_2,t)) \qquad (4.55)\\
\frac{\partial \Phi_{Lm}(\theta,t)}{\partial t} &= -(\alpha^{-1}+\beta)\Phi_{Lm}(\theta,t) \qquad (4.56)\\
&\quad -\beta(\gamma_S w_m(\theta-\theta_1)\psi_L(\theta_1,t)G(\psi_L(\theta_1,t))\Theta(\psi_L(\theta_1,t)), \\
&\quad +\gamma_S w_m(\theta-\theta_2)\psi_L(\theta_2,t)G(\psi_L(\theta_2,t))\Theta(\psi_L(\theta_2,t))), \quad m=l,c,
\end{aligned}$$

where G is the step function

$$G(\Delta) = \begin{cases} 1 & \text{if } \Delta > 0 \\ (1+\alpha\beta)^{-1} & \text{if } \Delta < 0 \end{cases}, \qquad (4.57)$$

and

$$(\gamma_S)^{-1} = |U_L'(\theta_k)| = \Big|\frac{1}{1+\alpha\beta}\Big[w_l(\theta_k-\theta_1) - w_l(\theta_k-\theta_2)\Big] + I_L'(\theta_k)\Big|. \qquad (4.58)$$

Equations (4.54)–(4.56) imply that the local stability of the stationary bump solution depends upon the spectral properties of a piecewise linear operator. In section 2.2.4, we solved a similar spectral problem by assuming that solutions were nonoscillatory, which generated a simpler eigenvalue problem dependent on the sign of perturbations. Here, we make a similar assumption, namely, that the perturbations $\psi_L(\theta_1,t)$ and $\psi_L(\theta_2,t)$ (equivalently Δ_{-}^{L} and Δ_{+}^{L}) do not switch sign. In other words, we assume equations (4.54)–(4.56) have separable solutions of the form

$$(\psi_L(\theta,t), \psi_R(\theta,t), \Phi_{Ll}(\theta,t), \Phi_{Lc}(\theta,t)) = \mathrm{e}^{\lambda t}(\psi_L(\theta), \psi_R(\theta), \Phi_{Ll}(\theta), \Phi_{Lc}(\theta)),$$

where λ is real.[4] The step functions Θ, G are then time–independent so there is a common factor $\mathrm{e}^{\lambda t}$ that cancels everywhere. We thus obtain an eigenvalue problem of the form

[4]Restricting our stability analysis to real eigenvalues means that we can only derive sufficient conditions for the instability rather than stability of a single or double bump solution. Moreover, we cannot establish the existence of limit cycle oscillations in terms of standard Hopf bifurcation theory. Nevertheless, numerical simulations will establish that destabilization of a (double) bump solution can lead to oscillatory solutions suggestive of binocular rivalry, see section 4.4.

$$
\begin{aligned}
(\lambda+1)\psi_L(\theta) &= \gamma_S w_l(\theta-\theta_1)\psi_L(\theta_1)G(\psi_L(\theta_1))\left(1-\frac{\beta\Theta(\psi_L(\theta_1))}{\lambda+\alpha^{-1}+\beta}\right) \\
&\quad +\gamma_S w_l(\theta-\theta_2)\psi_L(\theta_2)G(\psi_L(\theta_2))\left(1-\frac{\beta\Theta(\psi_L(\theta_2))}{\lambda+\alpha^{-1}+\beta}\right) \qquad (4.59) \\
(\lambda+1)\psi_R(\theta) &= \gamma_S w_c(\theta-\theta_1)\psi_L(\theta_1)G(\psi_L(\theta_1))\left(1-\frac{\beta\Theta(\psi_L(\theta_1))}{\lambda+\alpha^{-1}+\beta}\right) \\
&\quad +\gamma_S w_c(\theta-\theta_2)\psi_L(\theta_2)G(\psi_L(\theta_2))\left(1-\frac{\beta\Theta(\psi_L(\theta_2))}{\lambda+\alpha^{-1}+\beta}\right). \qquad (4.60)
\end{aligned}
$$

Note that we have assumed $\lambda \neq -(\alpha^{-1}+\beta)$ so that we can use equation (4.56) to solve for $\Phi_{Ll}(\theta)$ and $\Phi_{Lc}(\theta)$ in terms of $\psi_L(\theta_1)$ and $\psi_L(\theta_2)$; the case $\lambda = -(\alpha^{-1}+\beta)$ does not contribute to any instabilities.

It is possible to show that the solutions for λ can be identified with the spectra of a set of compact linear operators acting in the space of bounded continuous functions on the interval $[\theta_1, \theta_2]$, along the lines of Guo and Chow [62]. However, here we will simply calculate λ directly from the set of equations (4.59) and (4.60). In one class of solutions, we need only restrict the function $\psi_L(\theta)$ to vanish on the boundary, $\psi_L(\theta_1) = \psi_L(\theta_2) = 0$, so that $\psi_R(\theta)$ is unrestricted and $\lambda = -1$. This determines the essential spectrum, since $\lambda = -1$ has infinite multiplicity, and does not contribute to any instabilities. The discrete spectrum is then obtained by setting $\theta = \theta_1$ and $\theta = \theta_2$ in equation (4.59), which determines both the eigenvalues λ and the pair $\psi_L(\theta_1), \psi_L(\theta_2)$ (up to a scale factor). Once these are known, the eigensolutions $\psi_L(\theta)$ and $\psi_R(\theta)$ on $\theta \in [-\pi/2, \pi/2)$ are fully determined by equations (4.59) and (4.60). Note that the resulting eigenvalue equation is qualitatively similar to one derived in the linearization of a single bump in a single network with synaptic depression in section 2.2.4. One major difference here is that the input to the network is inhomogeneous so that translation invariance is lost. Hence, we no longer expect a zero eigenvalue associated with uniform shifts. We distinguish four classes of eigensolution to equations (4.59) and (4.60): (i) $\psi_L(\theta_1) > 0$ and $\psi_L(\theta_2) < 0$; (ii) $\psi_L(\theta_1) < 0$ and $\psi_L(\theta_2) > 0$; (iii) $\psi_L(\theta_1) > 0$ and $\psi_L(\theta_2) > 0$; (iv) $\psi_L(\theta_1) < 0$ and $\psi_L(\theta_2) < 0$. The four types of perturbation correspond, respectively, to a leftward shift, a rightward shift, an expansion, and a contraction of the bump in the left eye hypercolumn. As the eigenvalue problem is qualitatively similar to our previous work, we merely summarize the stability properties for each class of perturbation.

(i) $\psi_L(\theta_1) > 0; \psi_L(\theta_2) < 0$: As has been shown in the spatially extended network with synaptic depression and no input, increasing the strength of synaptic depression β will lead to a destabilization of standing bumps through the shift perturbation. In fact, in

all parameter regimes we have studied, this is the particular perturbation that destabilizes first.[5] In the case that the system is driven by an input, we find that inputs serve to move the onset of destabilization to a higher value of β. As before, we can study stability merely on the bump boundaries by setting $\theta = \theta_1, \theta_2$, along with our perturbation sign assumptions yields

$$\begin{pmatrix} \Gamma_\beta(\lambda) - \gamma_S w_l(0)\left(\lambda + \alpha^{-1}\right) & -\gamma_S\left(\lambda + \alpha^{-1}\right) w_l(\Delta\theta) \\ -\gamma_S\left(\lambda + \alpha^{-1}\right) w_l(\Delta\theta) & \Gamma_\beta(\lambda) - \gamma_S w_l(0)\left(\lambda + \alpha^{-1}\right) \end{pmatrix} \begin{pmatrix} \psi_L(\theta_1) \\ \psi(\theta_2) \end{pmatrix}$$

$$= -\frac{\gamma_S \alpha\beta\lambda}{1+\alpha\beta} \begin{pmatrix} w_l(\Delta\theta)\psi_L(\theta_2) \\ w_l(0)\psi_L(\theta_2) \end{pmatrix}. \tag{4.61}$$

As in the case without inputs, we assume $\beta \ll 1$ and carry out a perturbation expansion in β. First, we set $\beta = 0$ in equation (4.61) shows that the lowest order solution is $\psi_0^- = -\psi_0^+$ with $\lambda_0 = -\alpha^{-1}$ as a degenerate eigenvalue and $\lambda_0 = -1 + \gamma_S(w_l(0) - w_l(\Delta\theta))$, which will always be negative, since $\gamma_S^{-1} > w_l(0) - w_l(\Delta\theta)$. All eigensolutions pickup $\mathcal{O}(\beta)$ corrections as β is then increased from zero, but we will show that the valid eigenvalue originating from $-\alpha^{-1}$ eventually becomes positive, signifying traveling pulse solutions. See [185] for a recent study of traveling pulse solutions in a ring model with synaptic depression.

(ii) $\psi_L(\theta_1) < 0; \psi_L(\theta_2) > 0$: Due to reflection symmetry of the original system, when w_l is an even function, the spectrum of rightward shifts is identical to that of leftward shifts.

(iii) $\psi_L(\theta_1) > 0; \psi_L(\theta_2) > 0$: In this case, if we set $\theta = \theta_1, \theta_2$, we have $\psi_L(\theta_1) = \psi_L(\theta_2) > 0$, so equations (4.59) and (4.60) become

$$(\lambda + \alpha^{-1} + \beta)(\lambda + 1) \;=\; (\lambda + \alpha^{-1})(1 + \alpha\beta)\Omega_I, \tag{4.62}$$

where

$$\Omega_I \;=\; \frac{w_l(0) + w_l(\Delta\theta)}{w_l(0) - w_l(\Delta\theta) + (1+\alpha\beta)I_L'(\theta_1)} \tag{4.63}$$

and we have substituted for γ_S using equation (4.58). It then follows that $\lambda = \lambda_\pm$ with

$$\begin{aligned} \lambda_\pm \;=\; & \frac{1}{2}\left[\Omega_I(1+\alpha\beta) - \left(1 + \alpha^{-1} + \beta\right)\right] \\ & \pm \frac{1}{2}\sqrt{\left[\Omega_I(1+\alpha\beta) - (1 + \alpha^{-1} + \beta)\right]^2 + 4(\Omega_I - 1)\left(\alpha^{-1} + \beta\right)}. \end{aligned} \tag{4.64}$$

The associated eigenmode corresponds to a pure expansion of the bump.

[5] More precisely, shift perturbations are the dominant instability associated with real eigenvalues. Our analysis cannot determine possible instabilities associated with complex eigenvalues. However, numerical simulations suggest that single bump solutions are stable for sufficiently small β and destabilize at the point where an eigenvalue associated with shift perturbations crosses the origin, see section 4.4.

(iv) $\boldsymbol{\psi_L(\theta_1) < 0; \psi_L(\theta_2) < 0}$ **:** In this final case, if we set $\theta = \theta_1, \theta_2$ and note $\psi_L(\theta_1) = \psi_L(\theta_2)$ then equations (4.59) and (4.60) implies $\lambda = \lambda_0$ with

$$\lambda_0 = \Omega_I - 1. \tag{4.65}$$

The associated eigenmode corresponds to a pure contraction of the bump.

We illustrate the above analysis by considering stationary single bumps in the coupled hypercolumn network with a harmonic weight function (4.4). In particular, we plot eigenvalues for the destabilizing perturbations for the stimulus driven bump, which is stable as $\beta \to 0$. In Figure 4.6, we plot the maximal real eigenvalue associated with the shift perturbation (cases (i) and (ii)) as a function of β and as a function of I_0. The bump destabilizes to shift perturbations for sufficiently strong depression β. However, large inputs I_0 can keep the bump stable for larger values of β. In Figure 4.7, we plot the eigenvalues of the expansion and contraction perturbations as a function of β and I_0. In the case of contractions, there is a single negative branch of eigenvalues. In the case of expansions, there are two negative branches for fixed I_0 and sufficiently small β, which annihilate at the left edge of a forbidden region in which eigenvalues given by equation (4.64) are complex so that stability cannot be determined. At the other end of the forbidden region, a pair of positive branches emerges for sufficiently large β. By fixing β and varying I_0, we see that

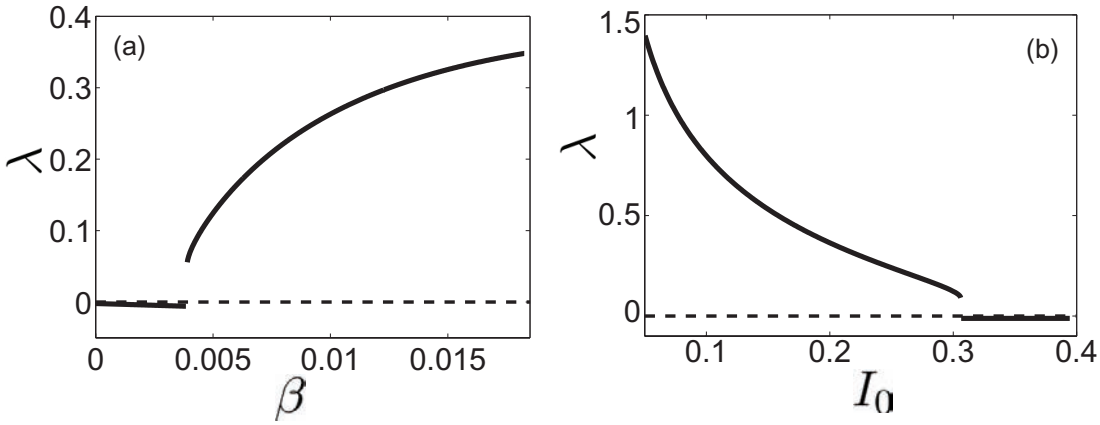

Figure 4.6. Eigenvalues associated with shift perturbations of single bump (cases (i) and (ii)). (a) Maximal nonzero real eigenvalues plotted as a function of β for $I_0 = 0.24$. Bump is unstable with respect to shifts for sufficiently large β. (b) Maximal nonzero real eigenvalue plotted as a function of I_0 for $\beta = 0.01$. Bump is unstable with respect to shifts for an intermediate range of I_0. Other parameters are $\kappa = 0.05$, $w_0^l = 0$, $w_2^l = 0.4$, $w_0^c = -1$, $w_2^c = 0.5$, $\alpha = 500$.

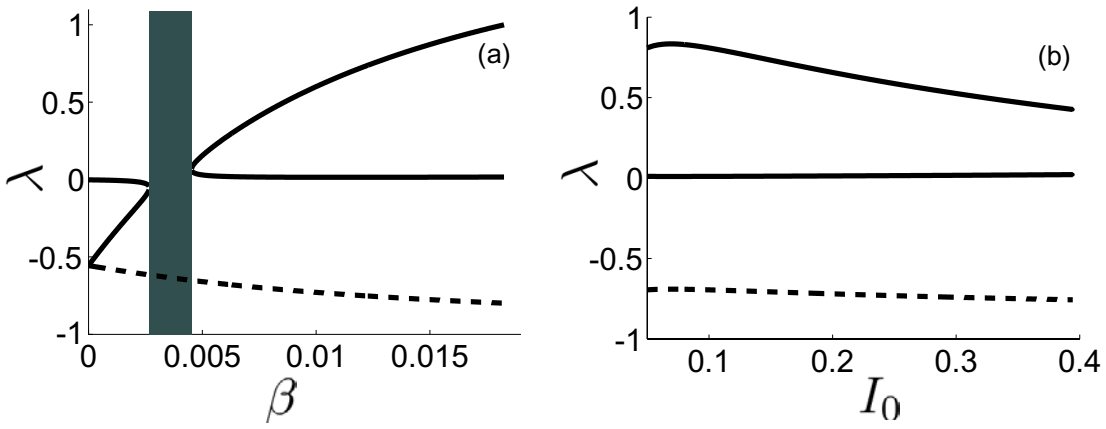

Figure 4.7. Eigenvalues associated with expansion and contraction perturbations (cases (iii) and (iv)). (a) Eigenvalues of the expansion (solid) and contraction (dashed) perturbations as a function of β when $I_0 = 0.24$. In the grey regions, the roots of equation (4.64) are complex violating the ansatz that λ is real. (b) Eigenvalues of the expansion (solid) and contraction (dashed) perturbations as a function of I_0 for $\beta = 0.01$. Other parameters are $\kappa = 0.05$, $w_0^l = 0$, $w_2^l = 0.4$, $w_0^c = -1$, $w_2^c = 0.5$, $\alpha = 500$.

eigenvalues are slightly less sensitive to the input strength and remain the same sign over wide range. We find that the lower branch of the expansion mode and the branch of the contraction mode never meet, as opposed to our study of a network without inhomogeneous input in section 2.2.

4.3.3 Existence of double bump

For a double bump or fusion solution, neural activity variables will both have associated non–empty excited regions $R[U_L] = (\theta_1, \theta_2)$ and $R[U_R] = (-\theta_2, -\theta_1)$ and thus threshold crossing points $U_L(\theta_1) = U_R(\theta_2) = \kappa$ and $U_R(-\theta_2) = U_R(-\theta_1) = \kappa$. Therefore, by prescribing the double bump solution in both populations, equations (4.34) become

$$U_L(\theta) = \int_{\theta_1}^{\theta_2} w_l(\theta - \theta')Q_L(\theta')\mathrm{d}\theta' + \int_{-\theta_2}^{-\theta_1} w_c(\theta - \theta')Q_R(\theta')\mathrm{d}\theta' + I_L(\theta), \quad (4.66)$$

$$U_R(\theta) = \int_{-\theta_2}^{-\theta_1} w_l(\theta - \theta')Q_R(\theta')\mathrm{d}\theta' + \int_{\theta_1}^{\theta_2} w_c(\theta - \theta')Q_L(\theta')\mathrm{d}\theta' + I_R(\theta), \quad (4.67)$$

$$Q_j(\theta) = 1 - \frac{\alpha\beta}{1+\alpha\beta}\Theta(U_j(\theta) - \kappa), \quad j = L, R. \quad (4.68)$$

Substituting equations (4.68) into (4.66) and (4.67) yields

$$U_L(\theta) = \frac{1}{1+\alpha\beta}\left[\int_{\theta_1}^{\theta_2} w_l(\theta-\theta')\mathrm{d}\theta' + \int_{-\theta_2}^{-\theta_1} w_c(\theta-\theta')\mathrm{d}\theta'\right] + I_L(\theta), \quad (4.69)$$

$$U_R(\theta) = \frac{1}{1+\alpha\beta}\left[\int_{-\theta_2}^{-\theta_1} w_l(\theta-\theta')\mathrm{d}\theta' + \int_{\theta_1}^{\theta_2} w_c(\theta-\theta')\mathrm{d}\theta'\right] + I_R(\theta). \quad (4.70)$$

Employing the sum of harmonics weight function (4.4), we can analytically calculate the double bump solutions

$$\begin{aligned} U_L(\theta) &= \frac{1}{1+\alpha\beta}\left[(w_0^l+w_0^c)(\theta_2-\theta_1) + \frac{w_2^l}{2}(\sin(2(\theta-\theta_1)) - \sin(2(\theta-\theta_2))) \right. \\ &\left. + \frac{w_2^c}{2}(\sin(2(\theta+\theta_2)) - \sin(2(\theta+\theta_1)))\right] + I_L(\theta), \quad (4.71) \\ U_R(\theta) &= \frac{1}{1+\alpha\beta}\left[(w_0^l+w_0^c)(\theta_2-\theta_1) + \frac{w_2^l}{2}(\sin(2(\theta+\theta_2)) - \sin(2(\theta+\theta_1))) \right. \\ &\left. + \frac{w_2^c}{2}(\sin(2(\theta-\theta_1)) - \sin(2(\theta-\theta_2)))\right] + I_R(\theta). \quad (4.72) \end{aligned}$$

Applying the threshold conditions

$$\begin{aligned} \kappa &= \frac{1}{1+\alpha\beta}\left[(w_0^l+w_0^c)(\theta_2-\theta_1) + \frac{w_2^l}{2}\sin(2(\theta_2-\theta_1)) + \frac{w_2^c}{2}(\sin(2(\theta_2+\theta_1)) - \sin(4\theta_1))\right] \\ &\quad + I_0\cos^p(\theta_1+\theta_I), \quad (4.73) \\ \kappa &= \frac{1}{1+\alpha\beta}\left[(w_0^l+w_0^c)(\theta_2-\theta_1) + \frac{w_2^l}{2}\sin(2(\theta_2-\theta_1)) + \frac{w_2^c}{2}(\sin(4\theta_2) - \sin(2(\theta_2+\theta_1)))\right] \\ &\quad + I_0\cos^p(\theta_2+\theta_I), \quad (4.74) \end{aligned}$$

provides us with a system of implicit expressions that relate the threshold crossing points θ_1, θ_2 to all other parameters. The system prescribed by (4.73) and (4.74) can be solved numerically using a root finding algorithm. The variation of the width of each bump $\Delta\theta = \theta_2 - \theta_1$ with the input strength I_0 and depression strength β is shown in Figure 4.8; the stability of these bumps is calculated below.

4.3.4 Stability of the double bump

We begin by letting $u_j(\theta,t) = U_j(\theta) + \varepsilon\psi_j(\theta,t)$ and $q_j(\theta,t) = Q_j(\theta) + \varepsilon\varphi_j(\theta,t)$ for $j = L, R$, where ψ_j and φ_j denote smooth perturbations and $\varepsilon \ll 1$. Substituting into the full system (4.1), imposing the stationary solutions (4.66), (4.67), and (4.68), and dividing through by ε then gives

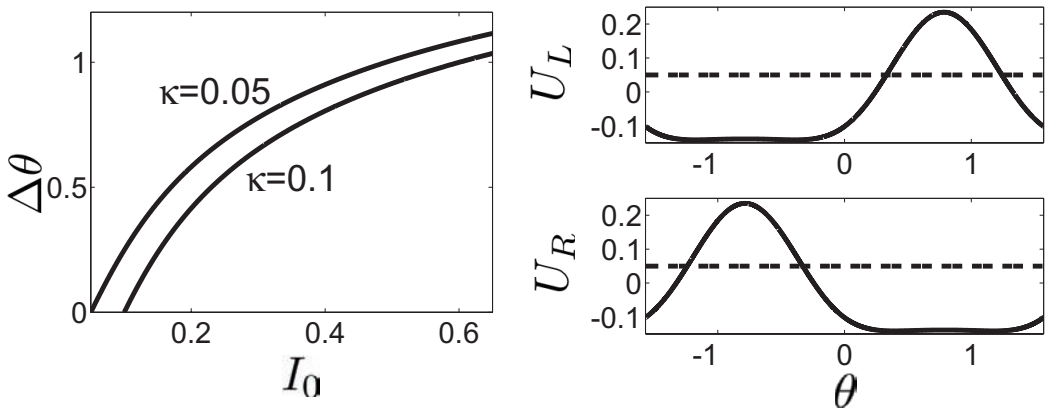

Figure 4.8. Double bumps in coupled hypercolumns. (Left) Plots relating bump width $\Delta\theta$ to the amplitude of input strength I_0 for different values of κ using equations (4.73) and (4.74). Other parameters are $\kappa = 0.05$, $\alpha = 500$, $\beta = 0.01$, $p = 6$. (Right) Double bump profile when $\kappa = 0.05$ and $I_0 = 0.4$.

$$\begin{aligned}
\frac{\partial\psi_L(\theta,t)}{\partial t} &= -\psi_L(\theta,t) + \frac{1}{\varepsilon}w_l * (Q_L[\Theta(U_L + \varepsilon\psi_L - \kappa) - \Theta(U_L - \kappa)]) \\
&\quad + w_l * (\varphi_L\Theta(U_L + \varepsilon\psi_L - \kappa)) + w_c * (\varphi_R\Theta(U_R + \varepsilon\psi_R - \kappa)) \\
&\quad + \frac{1}{\varepsilon}w_c * (Q_R[\Theta(U_R + \varepsilon\psi_R - \kappa) - \Theta(U_R - \kappa)]), \qquad (4.75) \\
\frac{\partial\psi_R(\theta,t)}{\partial t} &= -\psi_R(\theta,t) + \frac{1}{\varepsilon}w_l * (Q_R[\Theta(U_R + \varepsilon\psi_R - \kappa) - \Theta(U_R - \kappa)]) \\
&\quad + w_l * (\varphi_R\Theta(U_R + \varepsilon\psi_R - \kappa)) + w_c * (\varphi_L\Theta(U_L + \varepsilon\psi_L - \kappa)) \\
&\quad + \frac{1}{\varepsilon}w_c * (Q_L[\Theta(U_L + \varepsilon\psi_L - \kappa) - \Theta(U_L - \kappa)]), \qquad (4.76) \\
\frac{\partial\varphi_j(\theta,t)}{\partial t} &= -\frac{\varphi_j(\theta,t)}{\alpha} - \frac{\beta}{\varepsilon}Q_j[\Theta(U_j + \varepsilon\psi_j - \kappa) - \Theta(U_j - \kappa)] - \beta\varphi_j\Theta(U_j + \varepsilon\psi_j - \kappa) \\
& \qquad (4.77)
\end{aligned}$$

for $j = L, R$. Denote the perturbations of the bump boundaries by $\varepsilon\Delta_\pm^L(t)$ and $\varepsilon\Delta_\pm^R$ such that

$$\begin{aligned}
u_L(\theta_1 + \varepsilon\Delta_-^L(t), t) = u_L(\theta_2 + \varepsilon\Delta_+^L(t), t) &= \kappa, \qquad (4.78) \\
u_R(-\theta_1 + \varepsilon\Delta_-^R(t), t) = u_R(-\theta_2 + \varepsilon\Delta_+^R(t), t) &= \kappa, \qquad (4.79)
\end{aligned}$$

for an initial time interval $t \in [0, T)$. We are especially interested in perturbations that violate these threshold conditions eventually (after time T), since this is precisely what occurs in the case of rivalry oscillations. Taylor expanding these threshold conditions to first order in perturbations, we find that

$$\begin{aligned}
\Delta^L_-(t) &\approx -\frac{\psi_L(\theta_1,t)}{|U'_L(\theta_1)|}, \quad \Delta^L_+(t) \approx \frac{\psi_L(\theta_2,t)}{|U'_L(\theta_2)|}, \\
\Delta^R_-(t) &\approx \frac{\psi_R(-\theta_1,t)}{|U'_R(-\theta_1)|}, \quad \Delta^R_+(t) \approx -\frac{\psi_R(-\theta_2,t)}{|U'_R(-\theta_2)|}.
\end{aligned} \tag{4.80}$$

As in the single bump case, we can smooth out discontinuities in equations (4.77) by introducing the fields

$$\Phi_{Lm}(\theta,t) = \int_{\theta_1+\varepsilon\Delta^L_-}^{\theta_2+\varepsilon\Delta^L_+} w_m(\theta-\theta')\varphi_L(\theta',t)\mathrm{d}\theta', \tag{4.81}$$

$$\Phi_{Rm}(\theta,t) = \int_{-\theta_2+\varepsilon\Delta^R_+}^{-\theta_1+\varepsilon\Delta^R_-} w_m(\theta-\theta')\varphi_R(\theta',t)\mathrm{d}\theta', \tag{4.82}$$

for $m = l, c$. Differentiating equations (4.81) and (4.82) with respect to t and combining this with equations (4.75), (4.76), and (4.77) gives

$$\begin{aligned}
\frac{\partial\psi_L(\theta,t)}{\partial t} &= -\psi_L(\theta,t) + \Phi_{Ll}(\theta,t) + \Phi_{Rc}(\theta,t) \\
&+\frac{1}{\varepsilon}\int_{\theta_1+\varepsilon\Delta^L_-(t)}^{\theta_2+\varepsilon\Delta^L_+(t)} w_l(\theta-\theta')Q_L(\theta')\mathrm{d}\theta' - \frac{1}{\varepsilon}\int_{\theta_1}^{\theta_2} w_l(\theta-\theta')Q_L(\theta')\mathrm{d}\theta' \\
&+\frac{1}{\varepsilon}\int_{-\theta_2+\varepsilon\Delta^R_+(t)}^{-\theta_1+\varepsilon\Delta^R_-(t)} w_c(\theta-\theta')Q_R(\theta')\mathrm{d}\theta' - \frac{1}{\varepsilon}\int_{-\theta_2}^{-\theta_1} w_c(\theta-\theta')Q_R(\theta')\mathrm{d}\theta',
\end{aligned} \tag{4.83}$$

$$\begin{aligned}
\frac{\partial\psi_L(\theta,t)}{\partial t} &= -\psi_R(\theta,t) + \Phi_{Rl}(\theta,t) + \Phi_{Lc}(\theta,t) \\
&+\frac{1}{\varepsilon}\int_{-\theta_2+\varepsilon\Delta^R_-(t)}^{-\theta_1+\varepsilon\Delta^R_+(t)} w_l(\theta-\theta')Q_R(\theta')\mathrm{d}\theta' - \frac{1}{\varepsilon}\int_{-\theta_2}^{-\theta_1} w_l(\theta-\theta')Q_R(\theta')\mathrm{d}\theta' \\
&+\frac{1}{\varepsilon}\int_{\theta_1+\varepsilon\Delta^L_-(t)}^{\theta_2+\varepsilon\Delta^L_+(t)} w_c(\theta-\theta')Q_L(\theta')\mathrm{d}\theta' - \frac{1}{\varepsilon}\int_{\theta_1}^{\theta_2} w_c(\theta-\theta')Q_L(\theta')\mathrm{d}\theta',
\end{aligned} \tag{4.84}$$

$$\begin{aligned}
\frac{\partial\Phi_{Lm}(\theta,t)}{\partial t} &= -(\alpha^{-1}+\beta)\Phi_{Lm}(\theta,t) \\
&-\frac{\beta}{\varepsilon}\int_{\theta_1+\varepsilon\Delta^L_-(t)}^{\theta_2+\varepsilon\Delta^L_+(t)} w_m(\theta-\theta')Q_L(\theta')[\Theta(U_L+\varepsilon\psi_L-\kappa)-\Theta(U_L-\kappa)]\mathrm{d}\theta, \\
&+\varepsilon w_m(\theta-\theta_2-\varepsilon\Delta^L_+(t))\varphi_{Lm}(\theta_2+\varepsilon\Delta^L_+(t),t)\dot{\Delta}^L_+(t) \\
&-\varepsilon w_m(\theta-\theta_1-\varepsilon\Delta^L_-(t))\varphi_{Lm}(\theta_1+\varepsilon\Delta^L_-(t),t)\dot{\Delta}^L_-(t), \quad m=l,c,
\end{aligned} \tag{4.85}$$

$$\begin{aligned}
\frac{\partial\Phi_{Rm}(\theta,t)}{\partial t} &= -(\alpha^{-1}+\beta)\Phi_{Rm}(\theta,t) \\
&-\frac{\beta}{\varepsilon}\int_{-\theta_2+\varepsilon\Delta^R_+(t)}^{-\theta_1+\varepsilon\Delta^R_-(t)} w_m(\theta-\theta')Q_R(\theta')[\Theta(U_R+\varepsilon\psi_R-\kappa)-\Theta(U_R-\kappa)]\mathrm{d}\theta, \\
&-\varepsilon w_m(\theta+\theta_2-\varepsilon\Delta^R_+(t))\varphi_{Lm}(-\theta_2+\varepsilon\Delta^R_+(t),t)\dot{\Delta}^R_+(t) \\
&+\varepsilon w_m(\theta+\theta_1-\varepsilon\Delta^R_-(t))\varphi_{Lm}(-\theta_1+\varepsilon\Delta^R_-(t),t)\dot{\Delta}^R_-(t), \quad m=l,c.
\end{aligned} \tag{4.86}$$

We can now linearize the system of equations (4.83), (4.84), (4.85), and (4.86) by expanding in powers of ε and collecting all $\mathcal{O}(1)$ terms. Again it is important to keep track of the signs of $\Delta_{\pm}^{L}$ and $\Delta_{\pm}^{R}$ when approximating the various integrals due to the discontinuous nature of $Q_L(\theta)$ and $Q_R(\theta)$. We thus obtain the following piecewise linear system:

$$\begin{aligned}
\frac{\partial \psi_L(\theta,t)}{\partial t} &= -\psi_L(\theta,t) + \Phi_{Ll}(\theta,t) + \Phi_{Rc}(\theta,t) + \gamma_D w_l(\theta-\theta_1)\psi_L(\theta_1,t)G_{L,1}(t) \\
&\quad +\gamma_D w_l(\theta-\theta_2)\psi_L(\theta_2,t)G_{L,2}(t) + \gamma_D w_c(\theta+\theta_1)\psi_R(-\theta_1,t)G_{R,1}(t) \\
&\quad +\gamma_D w_c(\theta+\theta_2)\psi_R(-\theta_2,t)G_{R,2}(t) \qquad (4.87) \\
\frac{\partial \psi_R(\theta,t)}{\partial t} &= -\psi_R(\theta,t) + \Phi_{Rl}(\theta,t) + \Phi_{Lc}(\theta,t) + \gamma_D w_l(\theta+\theta_1)\psi_R(-\theta_1,t)G_{R,1}(t) \\
&\quad +\gamma_D w_l(\theta+\theta_2)\psi_R(-\theta_2,t)G_{R,2}(t) + \gamma_D w_c(\theta-\theta_1)\psi_1(\theta_1,t)G_{L,1}(t) \\
&\quad +\gamma_D w_c(\theta-\theta_2)\psi_L(\theta_2,t)G_{L,2}(t) \qquad (4.88)
\end{aligned}$$

and

$$\begin{aligned}
\frac{\partial \Phi_{Lm}(\theta,t)}{\partial t} &= -(\alpha^{-1}+\beta)\Phi_{Lm}(\theta,t) \\
&\quad -\beta(\gamma_D w_m(\theta-\theta_1)\psi_L(\theta_1,t)G_{L,1}(t)\Theta(\psi_L(\theta_1,t)) \\
&\quad +\gamma_D w_m(\theta-\theta_2)\psi_L(\theta_2,t)G_{L,2}(t)\Theta(\psi_L(\theta_2,t))), \qquad (4.89) \\
\frac{\partial \Phi_{Rm}(\theta,t)}{\partial t} &= -(\alpha^{-1}+\beta)\Phi_{Rm}(\theta,t) \\
&\quad -\beta(\gamma_D w_m(\theta+\theta_1)\psi_R(-\theta_1,t)G_{R,1}(t)\Theta(\psi_R(-\theta_1,t)) \\
&\quad +\gamma_D w_m(\theta+\theta_2)\psi_R(-\theta_2,t)G_{R,2}(t)\Theta(\psi_R(-\theta_2,t))), \qquad (4.90)
\end{aligned}$$

where $G_{L,j}(t) = G(\psi_L(\theta_j,t)), G_{R,j}(t) = G(\psi_R(-\theta_j,t))$ and

$$\begin{aligned}
(\gamma_D)^{-1} &= |U_L'(\theta_k)| \\
&= \frac{1}{1+\alpha\beta}\Big| w_l(\theta_k-\theta_1) - w_l(\theta_k-\theta_2) + w_c(\theta_k+\theta_2) - w_c(\theta_k+\theta_1) + I_L'(\theta_k)\Big| \\
&= |U_R'(-\theta_k)| \qquad (4.91) \\
&= \frac{1}{1+\alpha\beta}\Big| w_l(\theta_k-\theta_2) - w_l(\theta_k-\theta_1) + w_c(\theta_k+\theta_1) - w_c(\theta_k+\theta_2) + I_R'(-\theta_k)\Big|.
\end{aligned}$$

Equations (4.87)–(4.90) imply that the local stability of the stationary bump solution depends upon the spectral properties of a piecewise–linear operator. As in section 4.3.2, we assume that equations (4.87)–(4.90) have separable solutions of the form

$$(\psi_L, \psi_R, \Phi_{1l}, \Phi_{2l}, \Phi_{Lc}, \Phi_{Rc})(\theta,t) = \mathrm{e}^{\lambda t}(\psi_L, \psi_R, \Phi_{Ll}, \Phi_{Rl}, \Phi_{Lc}, \Phi_{Rc})(\theta),$$

where λ is real. Under this assumption, the step functions Θ, G are time–independent so that $\mathrm{e}^{\lambda t}$ cancels everywhere. Further simplification can be achieved by assuming that

$\lambda \neq -(\alpha^{-1}+\beta)$ so that we can eliminate the auxiliary fields $\Phi_{Ll}, \Phi_{Rl}, \Phi_{Lc}, \Phi_{Rc}$. The resulting eigenvalue problem can be analyzed along similar lines to single bumps. That is, one particular class of solutions consists of functions $\psi_L(\theta)$ and $\psi_R(\theta)$ that vanish on the bump boundaries so that $\psi_L(\theta_1) = \psi_L(\theta_2) = \psi_R(-\theta_2) = \psi_R(-\theta_1) = 0$ and $\lambda = -1$. This determines the essential spectrum. The discrete spectrum is then found by setting $\theta = \pm\theta_1, \pm\theta_2$, which yields a four–dimensional matrix equation for the quantities $\psi_L(\theta_j), \psi_R(-\theta_j),\ j = 1, 2$. Specifying the sign of these quantities thus yields sixteen classes of perturbation corresponding to all possible combinations of the perturbations for each individual bump: expansion, contraction, left–shift, and right–shift. However, there are only in fact seven qualitatively different cases due to symmetry considerations. We summarize these in Figure 4.9: (i) expand and contract (rivalry); (ii) same–shift; (iii) different–shift; (iv) expand both; (v) contract both; (vi) expand and shift; (vii) contract and shift. It is straightforward to numerically compute the eigenvalues associated with each perturbation after assigning the values for G and Θ due to the signs each of the four points $\psi_L(\theta_1)$, $\psi_L(\theta_2)$, $\psi_R(-\theta_1)$, and $\psi_R(-\theta_2)$. We shall briefly summarize our findings for the eigenvalues associated with each perturbation followed by some specific examples.

(i) Expand and contract (rivalry): e.g. $\psi_L(\theta_{1,2}) > 0$ and $\psi_R(-\theta_{1,2}) < 0$. In the study of binocular rivalry, we are most interested in this perturbation, which expands one bump and contracts the other. For sufficiently small inputs I_0, we find that the double bump is unstable with respect to this class of perturbation as $\beta \to 0$. There are then three possibilities which we have found numerically: it destabilizes to the winner take all solution (single bump), which occurs for weak synaptic depression; destabilizes to damped oscillations which eventually return to the double bump solution; or it destabilizes to persistent oscillations, which occurs for sufficiently strong depression. Finally, if the input strength I_0 is large enough, we find that this is sufficient to stabilize the double bump solution with respect to rivalry perturbations, as expected. We have found that, in the case that the double bump is linearly stable to rivalry perturbations, there can coexist a state where the system persistently oscillates between either population possessing superthreshold activity. However, the initial conditions of the system must be sufficiently far away from the double bump solution.

(ii) Same–shift: e.g. $\psi_L(\theta_1) < 0, \psi_L(\theta_2) > 0,\ \psi_R(-\theta_2) < 0, \psi_R(-\theta_1) > 0$. We find that eigenvalues associated with this perturbation are always negative for sufficiently strong cross inhibition ($w_0^c < 0$). However, as the amplitudes of the parameters w_0^c

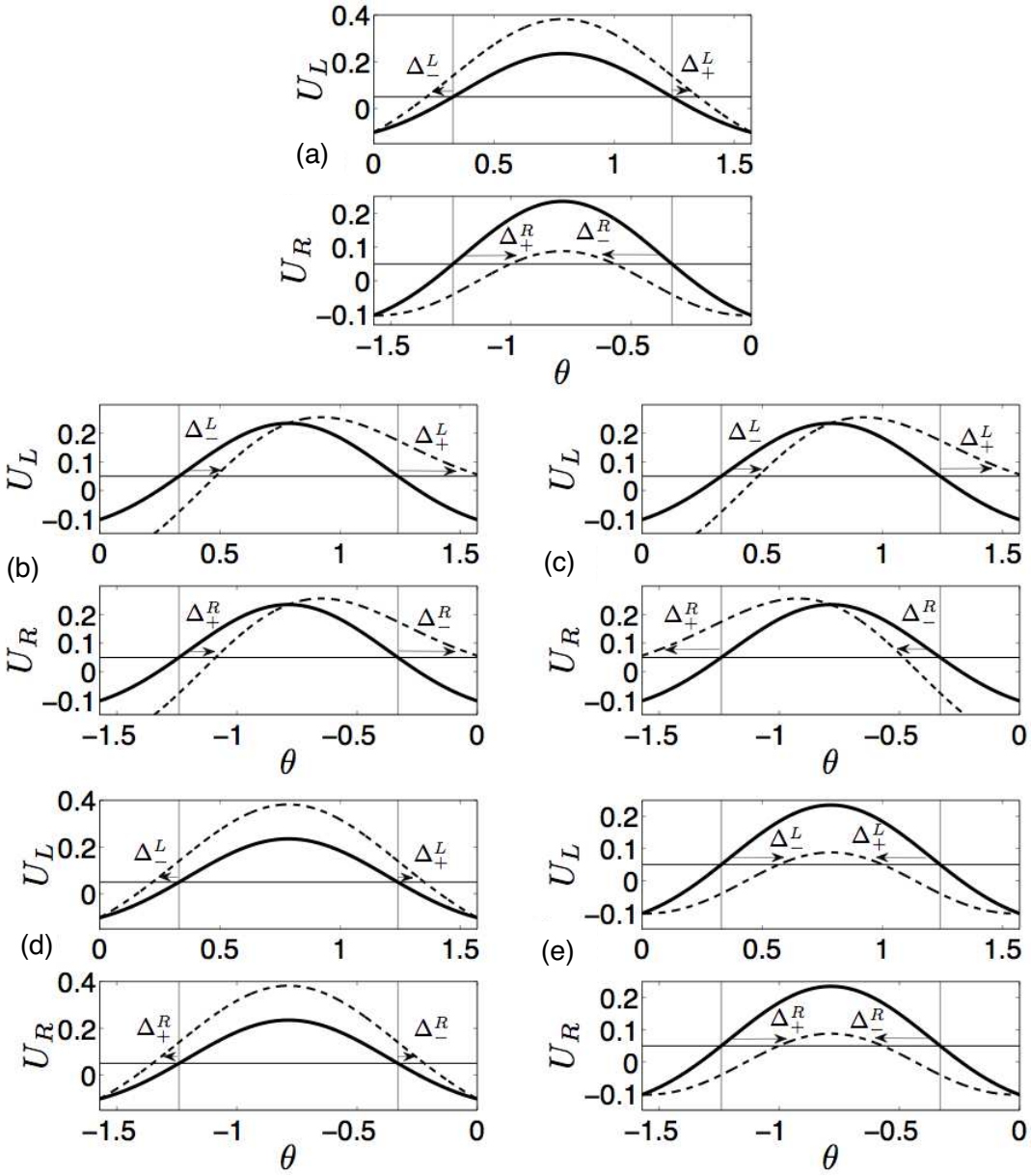

Figure 4.9. Illustration of different types of perturbation of a stationary double–bump solution: (a) expand and contract; (b) right–shift both; (c) left–shift and right–shift; (d) expand both; (e) contract both.

and w_2^c are reduced, it is possible to destabilize the double bump solution with respect to this perturbation, which numerically results in traveling pulse–like solutions in both hypercolumns that eventually settle back into the double bump solution.

(iii) Different–shift: e.g. $\psi_L(\theta_1) < 0, \psi_L(\theta_2) > 0$, $\psi_R(-\theta_2) > 0, \psi_R(-\theta_1) < 0$. We find that eigenvalues associated with this perturbation are always negative for sufficiently strong cross inhibition ($w_0^c < 0$). However, as with case (ii), when the amplitude of the parameters w_0^c and w_2^c are reduced, it is possible to destabilize the double bump solution, resulting in traveling pulse–like solutions in both hypercolumns that eventually settle back into the double bump solution.

(iv) Expand–both: e.g. $\psi_L(\theta_1) > 0, \psi_L(\theta_2) > 0$, $\psi_R(-\theta_2) > 0, \psi_R(-\theta_1) > 0$. Similar to cases (ii) and (iii), we find that this perturbation is stabilized by strong cross-inhibition, but can lead to instability when w_0^c and w_2^c are sufficiently small in amplitude. However, due to periodicity, the spread of activity eventually settles back into the double bump solution.

(v) Contract–both: e.g. $\psi_L(\theta_1) < 0, \psi_L(\theta_2) < 0$, $\psi_R(-\theta_2) < 0, \psi_R(-\theta_1) < 0$. Due to the underlying symmetry of the system, we can in fact compute the eigenvalue associated with this perturbation explicitly. Noting the sign restrictions and the fact that we must have $\psi_L(\theta_1) = \psi_L(\theta_2) = \psi_R(-\theta_2) = \psi_R(-\theta_1) < 0$ then

$$\lambda = -1 + \frac{\gamma_D}{1+\alpha\beta}(w_l(0) + w_l^- + w_c(2\theta_1) + w_c^+), \tag{4.92}$$

which we find to always be negative, so long as $w_0^c \leq 0$. Thus, the bump will always be stable with respect to contractions. In fact, this seems to be what allows the system to settle back into the double bump solution after a long excursion due to a destabilizing perturbation, since there are flows that treat the double bump as an attractor.

(vi) Expand–shift: e.g. $\psi_L(\theta_1) > 0, \psi_L(\theta_2) > 0$, $\psi_R(-\theta_2) < 0, \psi_R(-\theta_1) > 0$. We find no eigensolutions of this form for any parameters.

(vii) Contract–shift: e.g. $\psi_L(\theta_1) < 0, \psi_L(\theta_2) < 0$, $\psi_R(-\theta_2) < 0, \psi_R(-\theta_1) > 0$. We find no eigensolutions of this form for any parameters.

We illustrate the stability analysis of the stationary double bump solution by plotting eigenvalues calculated for each perturbation to bumps in a network with the harmonic weight function (4.4). Specifically, we plot the eigenvalues for each perturbation for a stimulus driven double bump that is unstable to rivalry perturbations as $\beta \to 0$. In Figure 4.10, we plot the maximal nonzero real eigenvalue for rivalry perturbation as a function of β and I_0. For fixed I_0, as β increases from zero the positive real eigenvalue

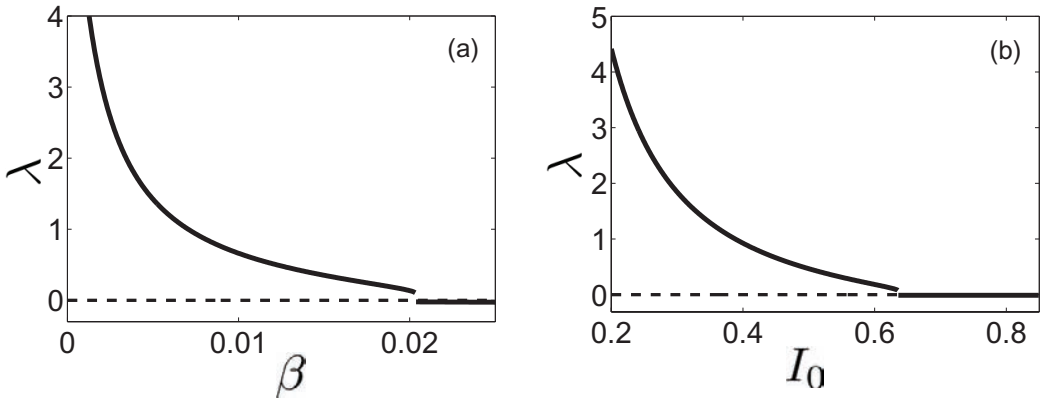

Figure 4.10. Eigenvalues associated with expand and contract (rivalry) perturbation. (a) Maximal nonzero eigenvalue plotted as a function of β for fixed $I_0 = 0.45$. (b) Maximal nonzero real eigenvalues plotted as a function of I_0 for $\beta = 0.01$. Other parameters are $\kappa = 0.05$, $w_0^l = 0$, $w_2^l = 0.4$, $w_0^e = -1$, $w_2^e = 0.5$, $\alpha = 500$.

decreases as a function of β. For sufficiently large β, this positive eigenvalue vanishes, and the double bump solution is predicted to be stable to rivalry perturbations. For fixed β, double bumps are unstable to rivalry perturbations for sufficiently weak inputs, but stabilize beyond a critical value of I_0. In Figure 4.11, we plot the maximal eigenvalues of all other perturbations to the bump, showing they are negative for a wide range of input strengths I_0 and depression strengths β. They are all quite insensitive to variations in these parameters.

4.4 Numerical simulations

We now study the full system (4.1) using a numerical approximation scheme. To evolve the system in time, we use a fourth order Runge–Kutta method with 1000–2000 spatial grid points and a time step of $dt = 0.01$. The integral terms in equations (4.1a) and (4.1b) are approximated using Simpson's rule. We systematically checked whether taking finer grids changed stability results, and it does not. Such checks are essential to studying stability of bumps as grids that are too coarse can drastically alter stability results [62].

In much of parameter space, we find that our existence and stability analysis characterizes very well the type of solutions that the system (4.1) will relax to over long times as well as the nature of various local instabilities. Thus, if we take as an initial condition a stationary bump solution that is stable with respect to perturbations associated with

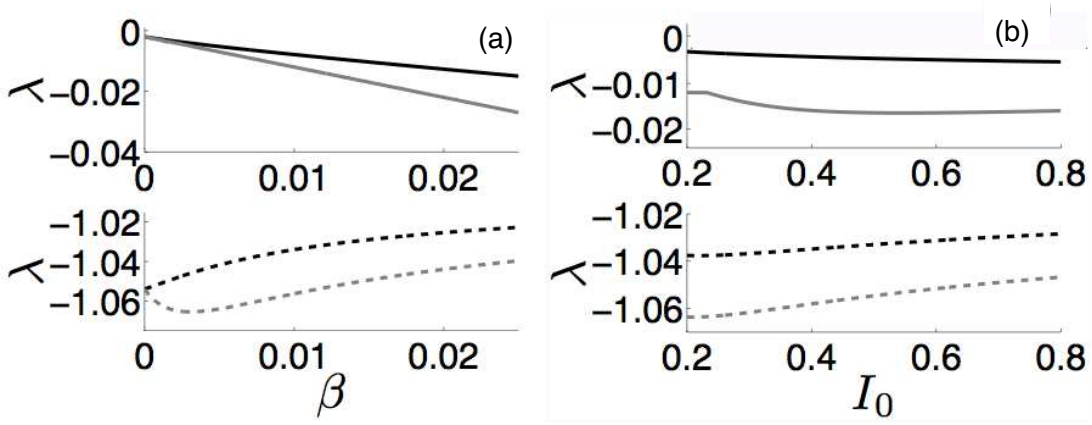

Figure 4.11. Eigenvalues associated with nonrivalry perturbations. (a) Maximal real eigenvalues of the expand–both (solid black), contract–both (dashed black), same–shift (solid grey), and different–shift (dashed grey) perturbations plotted as a function of β for fixed $I_0 = 0.45$. (b) Maximal real eigenvalues of each perturbation plotted as a function of I_0 for $\beta = 0.01$. Other parameters are $\kappa = 0.05$, $w_0^l = 0$, $w_2^l = 0.4$, $w_0^c = -1$, $w_2^c = 0.5$, $\alpha = 500$.

real eigenvalues, and then vary a bifurcation parameter such as β or I_0, we find that the dominant instability, as predicted by our piecewise smooth analysis, corresponds well with the numerical solution seen initially to evolve away from the stationary solution. However, one interesting feature we find in numerical simulations of the network is that solutions that destabilize initially can eventually return to a stationary solution in the absence of noise. This is due to two features of the underlying system and associated stationary solution. First, the bump is stable with respect to certain perturbations in our piecewise linear stability analysis. Therefore, even though the solution may move away from a stationary bump when one perturbation is applied, it may follow a trajectory in phase space which is eventually close to the stationary bump solution again. This phenomenon is aided by the second effect, which is that the variables $q_j(\theta, t)$ as defined by equation (4.1c) reduce their value at a location quite quickly when superthreshold activity of $u_j(\theta, t)$ sweeps over that location in the network. Thus, $q_j(\theta, t)$ will be lower than the value prescribed by the stationary solutions on the regions immediately exterior to the original bump location following the bump. This effect will last for long periods of time since α is large. Therefore, in some situations, there will not be enough resources in the regions about the bump's original location to reignite the instability once the activity profile returns to the general

proximity of the bump. We shall witness this phenomenon in both single and double bump instabilities.

For our first numerical example, we take the initial condition to be a single bump solution specified by (4.40) which is predicted to be unstable to shift perturbations. After a brief period, we perturb the system by adding a rightward shift perturbation of $u_L(\theta,t)$ defined as

$$\psi_L^{shift}(\theta,t) \quad = \quad \chi(t)(w_l(\theta-\theta_2)-w_l(\theta-\theta_1)). \tag{4.93}$$

As shown in Figure 4.12, the resulting dynamics initially evolves to a propagating solution similar to a traveling pulse. However, due to the input and periodic boundaries of the system, the profile does not settle to be invariant as in our studies of traveling pulses in a network with synaptic depression in sections 2.1.2 and 2.2.5. In fact, activity then changes direction, sloshing to the other side of the input region. Following its excursion, the activity profile eventually settles back into the stationary single bump solution. As mentioned, the trajectory of the variable $u_L(\theta,t)$ is such that it relaxes back to the bump solution through a stable flow. Since the piecewise smooth boundary of the variables $q_j(\theta,t)$ have been

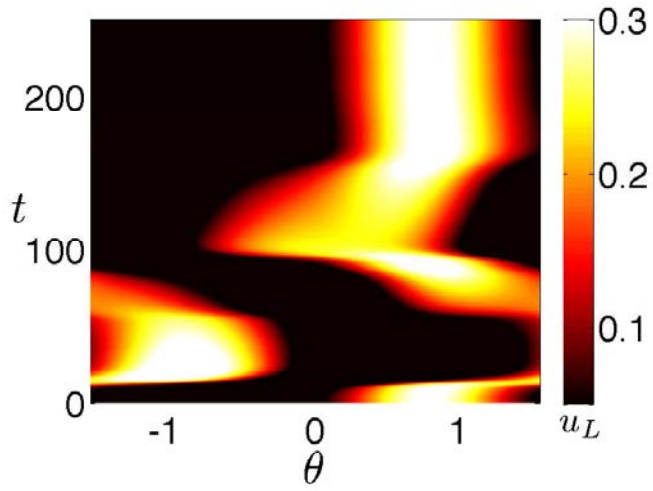

Figure 4.12. Numerical simulation of a single bump destabilized by a rightward shift perturbation. Plot of $u_L(\theta,t)$ for an initial condition taken to be a stationary bump specified by equation (4.40). Solution is perturbed at $t=5$ by a rightward shift $\psi_L^{shift}(\theta,t)$ such that $\chi(t)=0.02$ for $t\in[5,5.1)$ and zero otherwise. Activity initially propagates rightward and then back leftward until settling back into the single bump profile. Parameters are $\kappa=0.05$, $w_0^l=0$, $w_2^l=0.4$, $w_0^e=-1$, $w_2^e=0.5$, $\alpha=500$, $\beta=0.01$, $I_0=0.24$.

disrupted by nonlinear effects of the evolving solution, the bump will be an attracting state for virtually all reasonable flows over long time. Thus, even though the bump is unstable to shift perturbations, it always restabilizes in the long time limit.

For our next numerical example, we take the initial condition to be a double bump solution specified by (4.71) and (4.72), which is predicted to be unstable to rivalry perturbations. After a brief period, we perturb the system by adding a rivalry perturbation of $u_L(\theta,t)$ and $u_R(\theta,t)$ defined as

$$\psi_L^{riv}(\theta,t) = \chi(t)(w_l(\theta-\theta_2)+w_l(\theta-\theta_1)), \tag{4.94}$$

$$\psi_R^{riv}(\theta,t) = -\chi(t)(w_l(\theta+\theta_2)+w_l(\theta+\theta_1)). \tag{4.95}$$

As shown in Figure 4.13, the resulting dynamics can evolve to a slow oscillation in the activity of both populations for sufficiently weak inputs I_0. First the right population's

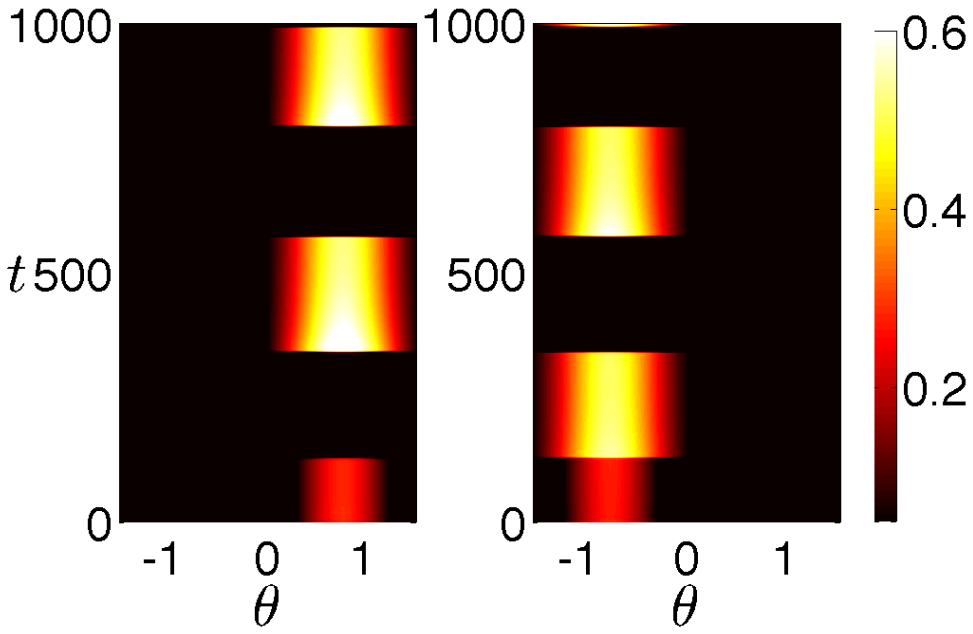

Figure 4.13. Numerical simulation of a double bump destabilized by a rivalry perturbation. Plot of $u_L(\theta,t)$ (left) and $u_R(\theta,t)$ (right) for an initial condition taken to be a double bump specified by equations (4.71) and (4.72). Solution is perturbed at $t=5$ by a rivalry shift $\psi_L^{riv}(\theta,t)$ and $\psi_R^{riv}(\theta,t)$ respectively such that $\chi(t)=0.02$ for $t\in[5,5.1)$ and zero otherwise. Activity settles into a slow oscillation where dominance switches between either population roughly every two seconds. Parameters are $\kappa=0.05$, $w_0^l=0$, $w_2^l=0.4$, $w_0^c=-1$, $w_2^c=0.5$, $\alpha=500$, $\beta=0.01$, $I_0=0.45$.

activity $u_R(\theta, t)$ exhibits a relatively invariant bump of activity until synaptic depression exhausts the inhibitory synapses and the left population's activity $u_L(\theta, t)$ is released from suppression. Then the left population's activity dominates for a period until the right population is released. This cycle continues indefinitely. Thus, even though the linear stability analysis predicts the rivalry perturbation having an associated positive real eigenvalue (see Figure 4.10), nonlinear effects of the system take over in long time and the system oscillates. As we alluded to in section 4.3.4, the spatially extended system supports a fusion/rivalry bistable state, just as the space–clamped system did in section 4.2. Thus, even in cases where the double bump solution is linearly stable, some initial conditions evolve to a rivalry solution similar to that pictured in Figure 4.13. Buckthought and colleagues recently showed that such bistability can exist in psychophysical experiments [28]. By showing subjects binocular stimuli with increasingly dissimilar orientations, they found a region of hysteresis, wherein the subject could perceive either rivalry or fusion, depending on their initial perception. Admittedly, the stimuli used to induce the effect never differed more than 30 degrees whereas ours differ by 90 degrees, but they observed bistability nonetheless.

In Figure 4.14, we show an example of a perturbation evolving to a damped oscillation. Even though our stability analysis predicts the double bump is unstable to the rivalry oscillation, the solution eventually returns to the stationary double bump. As we have mentioned double bumps can be stable to all other perturbations aside from the rivalry perturbation. Therefore, nonlinear effects can dominate the system in the long time limit and the solution may flow along a trajectory which has the double bump as an attractor. As mentioned, resources as defined by $q_j(\theta, t)$ in the periphery of the original bump locations are exhausted so that there is not sufficient excitation to continue the oscillation. In addition, we cannot trust the stability analysis we have carried out beyond the point that the original threshold conditions are violated. To our knowledge, no studies have addressed these types of nonlinear effects at work in restabilizing bumps in spatially extended systems. It remains an open problem as to how best to characterize the onset of such an oscillation.

Finally, in Figure 4.15, we show an example of a coupled hypercolumn network driven by stimuli of two different strengths so that $I_L \neq I_R$. We take our initial condition to be the quiescent state $u_L(\theta, 0) = u_R(\theta, 0) = 0$ and $q_L(\theta, t) = q_R(\theta, 0) = 1$. In this case, we see that the dominance times are different for the left and right populations, just as we found in the space–clamped system (see Figures 4.3 and 4.4). Since the right population

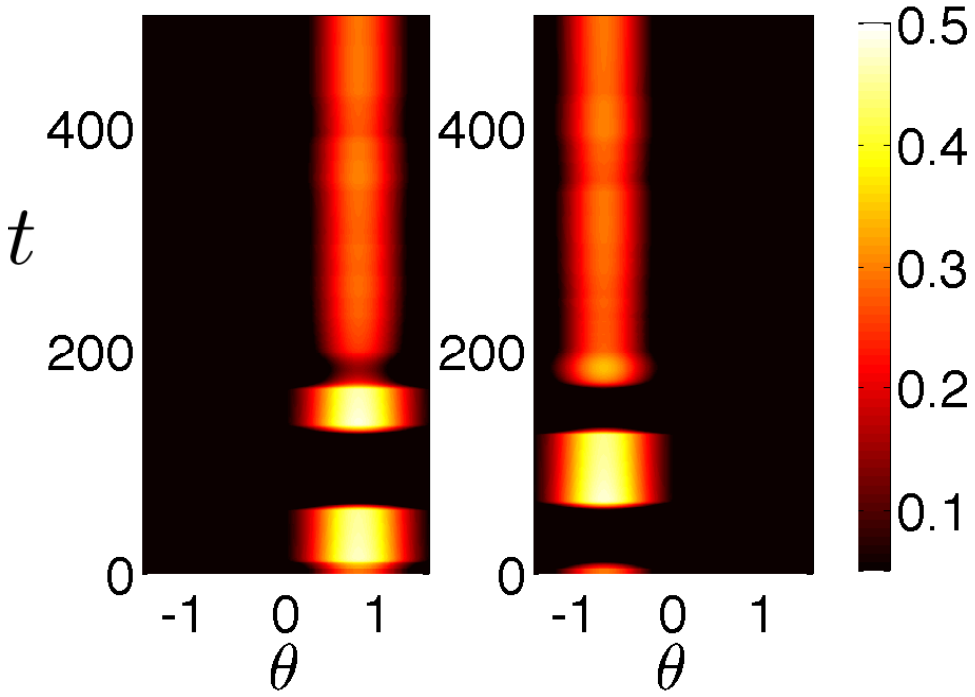

Figure 4.14. Numerical simulation of a double bump destabilized by a rivalry perturbation. Plot of $u_L(\theta, t)$ (left) and $u_R(\theta, t)$ (right) for an initial condition taken to be a double bump specified by equation (4.71) and (4.72). Solution is perturbed at $t = 5$ by a rivalry shift $\psi_L^{riv}(\theta, t)$ and $\psi_R^{riv}(\theta, t)$ respectively such that $\chi(t) = 0.02$ for $t \in [5, 5.1)$ and zero otherwise. Activity evolves to a damped oscillation temporarily and then settles back into the stationary double bump. Parameters are $\kappa = 0.05$, $w_0^l = 0$, $w_2^l = 0.4$, $w_0^c = -1$, $w_2^c = 0.5$, $\alpha = 500$, $\beta = 0.02$, $I_0 = 0.4$.

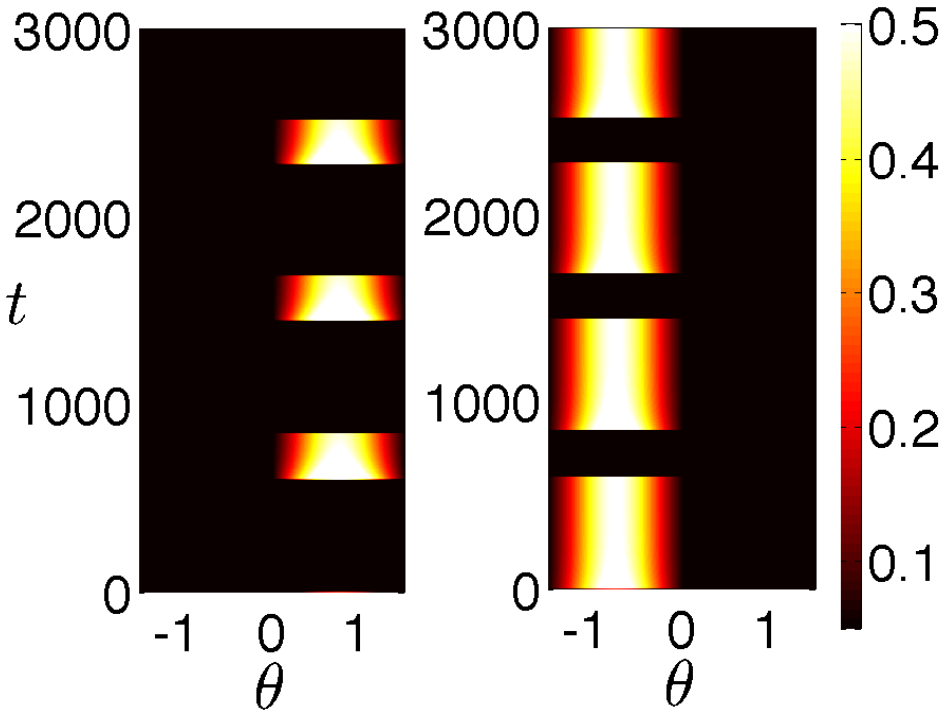

Figure 4.15. Numerical simulation of an asymmetric rivalry solution. Plot of $u_L(\theta,t)$ (left) and $u_R(\theta,t)$ (right) for an initial condition taken to be the quiescent state $u_L(\theta,0) = u_R(\theta,0) = 0$ and $q_L(\theta,t) = q_R(\theta,0) = 1$. Activity evolves to a damped oscillation temporarily and then settles back into the stationary double bump. Parameters are $\kappa = 0.05$, $w_0^l = 0$, $w_2^l = 0.4$, $w_0^c = -1$, $w_2^c = 0.5$, $\alpha = 500$, $\beta = 0.01$, $I_L^0 = 0.4$, $I_R^0 = 0.45$.

receives a stronger input ($I_R = 0.45$) than the left population ($I_L = 0.4$), superthreshold bump–like activity exists in the right population for a longer period than the left. Also, note that the transient bump in the right population is wider than that in the left.

4.5 Discussion

In this chapter, we analyzed the onset of binocular rivalry oscillations in a coupled hypercolumn model with synaptic depression. In order to facilitate our analysis we took the firing rate function to be a Heaviside (4.3). However, it was then necessary to take the piecewise nature of the system into account when analyzing the stability of stationary solutions. We first calculated the period of rivalry oscillations arising in the space–clamped version of our model. When the input to the left and right eye populations were varied, we found that the corresponding changes in dominance times matched very well with

some of the observations of binocular rivalry made by Levelt [104]. In the spatially extended version of our model, we analyzed the onset of oscillations in neural activity due to orientation biased stimuli using local stability determined by the spectrum of a piecewise linear operator. For winner–take–all or single bump solutions, we found that the dominant instability was usually a shifting of the bump boundary, which in numerical simulations led to traveling pulse type solutions. For fusion or double bump solutions, we found that the dominant instability was an expansion of one bump and a contraction of the other, which in simulations often led to rivalry type oscillations. In numerical simulations, we found that the local stability analysis predicted the point at which bump solutions destabilized, but the long time behavior of the simulation is beyond the scope of our analysis.

In future work, it would be interesting to develop tools to analyze the long time behavior of oscillations in the spatially extended system so we could compute the dominance times of each population. In addition, the fact that piecewise smooth analysis predicts that a bump can be stable to one sign of perturbation and unstable to another sign of perturbation was borne out in the results of our numerical simulations. It appears this behavior allows the bump to be a starting and stopping point for homoclinic trajectories in the infinite dimensional system (4.1). In a sense, the bump is marginally stable. This was not an issue when we studied instabilities of bumps in a network with synaptic depression without periodic boundaries in section 2.2. We would like to explore this notion more exactly using tools developed for the study of piecewise smooth dynamical systems [47].

CHAPTER 5

TRAVELING PULSES AND WAVE PROPAGATION FAILURE IN AN INHOMOGENEOUS NEURONAL NETWORK

Mathematical analyses of cortical wave propagation typically consider reduced one–dimensional network models. Under the additional assumption that the synaptic interactions are homogeneous, it has been shown that an excitatory neuronal network supports the propagation of a traveling front [52, 73, 22] or, in the presence of slow adaptation, a traveling pulse [3, 136, 187, 188, 39, 57, 168] (See section 1.3 for a review of such studies and section 2.1 for a traveling wave study in a homogeneous network with depression and adaptation.). However, the patchy nature of long–range horizontal connections in superficial layers of certain cortical areas suggests that the cortex is more realistically modeled as an inhomogeneous neural medium. For example, in primary visual cortex the horizontal connections tend to link cells with similar stimulus feature preferences such as orientation and ocular dominance [111, 186, 18] (See also Chapter 4 for a description of the architecture of primary visual cortex.). Moreover, these patchy connections tend to be anisotropic, with the direction of anisotropy correlated with the underlying orientation preference map. Hence the anisotropic pattern of connections rotates approximately periodically across cortex resulting in a periodic inhomogeneous medium [20, 21]. Another example of inhomogeneous horizontal connections is found in the prefrontal cortex [105, 122], where pyramidal cells are segregated into stripes that are mutually connected via horizontally projecting axon collaterals; neurons within the gaps between stripes do not have such projections.

In this chapter we investigate how a spatially periodic modulation of long–range synaptic weights affects the propagation of traveling pulses in a one–dimensional excitatory neuronal network, extending previous work on traveling fronts in neuronal network models

[20] and reaction–diffusion systems [77, 78]. Our network contains local linear negative feedback, developed by Pinto and Ermentrout, meant to heuristically model either spike frequency adaptation or synaptic depression [136, 137]. We briefly introduced this model in section 1.3, but here we further modify the equations by considering a periodically modulated weight function. Our analysis of the model then proceeds by studying how the periodic modulation in the weight function affects its traveling wave solutions. We proceed then in section 5.2 by introducing a slowly varying phase into the traveling wave solution of the unperturbed homogeneous network and then use perturbation theory to derive a dynamical equation for the phase, from which the mean speed of the wave can be calculated. When we take our firing rate to be a Heaviside function (1.4), we can explicitly calculate a first order approximation to the wave speed in section 5.3. We show that a periodic modulation of the long–range connections slows down the wave and if the amplitude and wavelength of the periodic modulation is sufficiently large, then wave propagation failure can occur. We can even derive a formula for the wavespeed in the case of a smooth firing rate function. A particularly interesting result is that in the case of large amplitude modulations, the traveling pulse is no longer superthreshold everywhere within its interior, even though it still propagates as a coherent solitary wave. As verified by numerical simulations in section 5.4, we find that the pulse now corresponds to the envelope of a multibump solution, in which individual bumps are nonpropagating and transient. The appearance (disappearance) of bumps at the leading (trailing) edge of the pulse generates the propagation of activity; propagation failure occurs when activity is insufficient to create new bumps at the leading edge.[1]

5.1 Inhomogeneous network model

Consider a one–dimensional neuronal network model of the form [136]

$$\begin{aligned} \tau_m \frac{\partial u(x,t)}{\partial t} &= -u(x,t) + \int_{-\infty}^{\infty} w(x,x') f(u(x',t)) dx' - \beta_p v(x,t) \\ \frac{1}{\alpha_p} \frac{\partial v(x,t)}{\partial t} &= -v(x,t) + u(x,t) \end{aligned} \tag{5.1}$$

where $u(x,t)$ is the population activity at position $x \in \mathbb{R}$, τ_m is a membrane time constant, $f(u)$ is the output firing rate function, $w(x,x')$ is the excitatory connection strength from

[1] Please note that throughout this chapter, we shall be using variable and parameter names, such as A and q, which have been used in previous chapters. We shall define what each variable represents in the confines of this chapter, which does not change what those variables represented in the previous chapters.

neurons at x' to neurons at x, and $v(x,t)$ is a local negative feedback mechanism, with β_p and α_p determining the relative strength and rate of feedback. This type of feedback, which could be spike frequency adaptation or synaptic depression, favors traveling waves [136, 57, 168]. The nonlinearity f is a smooth monotonic increasing function, the sigmoid (1.2). As the gain $\eta \to \infty$, $f \to \Theta(u-\kappa)$, the Heaviside nonlinearity (1.4).[2]

The periodic microstructure of the cortex is incorporated by taking the weight distribution to be of the form [20, 21]

$$w(x,x') \quad = \quad W(|x-x'|)[1+\mathcal{D}_c'(\frac{x'}{\varepsilon})] \tag{5.2}$$

where $\mathcal{D}_c$ is a 2π–periodic function and ε determines the microscopic length–scale. (We consider the first–order derivative of $\mathcal{D}_c$ so that the zeroth order harmonic is explicitly excluded). It is important to note that equation (5.2) is a one–dimensional abstraction of the detailed anatomical structure found in the two–dimensional layers of real cortex. (See [22] for a more detailed discussion of cortical models). However, it captures both the periodic–like nature of long–range connections and possible inhomogeneities arising from the fact that this periodicity is correlated with a fixed set of cortical feature maps.

For concreteness, we take the homogeneous weight function W to be an exponential,

$$W(x) = \frac{W_0}{2d} e^{-|x|/d}, \tag{5.3}$$

where d is the effective range of the excitatory weight distribution, and set

$$\mathcal{D}_c\,(x) \quad = \quad \rho \sin\,(x)\,, \quad 0 \leq \rho < 1, \tag{5.4}$$

where ρ is the amplitude of the periodic modulation. We require $0 \leq \rho < 1$ so that the weight distribution remains nonnegative everywhere. Example plots of the resulting weight function $w(x,y)$ of equation (5.2) are shown in Figure 5.1 for fixed x. This illustrates both the periodic modulation and the associated network inhomogeneity, since the shape of the weight distribution varies periodically as the location x of the postsynaptic neuron shifts. Plotting $w(x,x')$ for fixed x' simply gives an exponential distribution whose maximum depends on x'. Finally, the temporal and spatial scales of the network are fixed by setting $\tau_m = 1, d = 1$ and the scale of the synaptic weights is fixed by setting $W_0 = 1$. The membrane time constant is typically around 10 ms and the length scale of synaptic

[2] As in the previous chapter, we take the liberty of making a change of notation, so that κ corresponds to the firing threshold here.

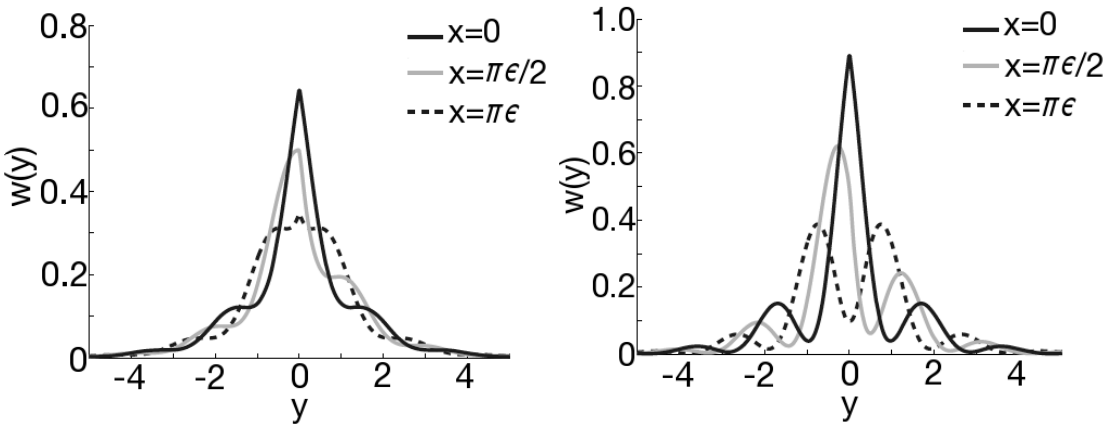

Figure 5.1. Weight kernel with periodic inhomogeneities. (Left): Weight kernel $w(y) = w(x, y)$ for a neuron centered at $x = 0, \pi\varepsilon/2, \pi\varepsilon$ when $\rho = 0.3$, and $\varepsilon = 0.3$. (Right): Corresponding weight kernel when $\rho = 0.8$ and $\varepsilon = 0.3$.

connections is typically 1 mm. Thus, in dimensionless units the speed of an experimentally measured wave will be $c = \mathcal{O}(1)$.

5.2 Averaging theory and homogenization

Our goal in this chapter is to determine how the periodic modulation of the weight function affects properties of traveling pulses in the one–dimensional system obtained by substituting equation (5.2) into equation (5.1):

$$\begin{aligned} \frac{\partial u(x,t)}{\partial t} &= -u(x,t) + \int_{-\infty}^{\infty} W(|x-x'|)[1 + \mathcal{D}_c'(\frac{x'}{\varepsilon})]f(u(x',t))dx' - \beta_p v(x,t) \\ \frac{1}{\alpha_p}\frac{\partial v(x,t)}{\partial t} &= -v(x,t) + u(x,t). \end{aligned} \tag{5.5}$$

Assuming ε is a small parameter (in units of the space constant d), a zeroth–order approximation to (5.5) can be generated by performing spatial averaging with respect to the periodic weight modulation, leading to the homogeneous system given by equation (5.1) with weight distribution $w(x, x') = W(|x - x'|)$. Suppose that the homogeneous network supports the propagation of a traveling pulse of constant speed c. That is, $u(x,t) = U(\xi), v(x,t) = V(\xi)$, where $\xi = x - ct$ is the traveling wave coordinate, and $U(\xi), V(\xi) \to 0$ as $\xi \to \pm\infty$. Substituting such a solution into equation (5.1) with $w(x, x') = W(|x - x'|)$ gives

$$-cU'(\xi) = -U(\xi) + \int_{-\infty}^{\infty} W(\xi - \xi') f(U(\xi'))d\xi' - \beta V(\xi),$$
$$-\frac{c}{\alpha_p} V'(\xi) = -V(\xi) + U(\xi). \tag{5.6}$$

Assuming the existence of a solution $(U(\xi), V(\xi))$ to system (5.6), we would like to determine whether or not a traveling wave persists in the presence of the periodic weight modulation. A crucial requirement for trajectories of the averaged homogeneous system to remain sufficiently close to trajectories of the exact inhomogeneous system for sufficiently small ε is that solutions of the averaged system be structurally stable [60]. However, traveling pulses correspond to homoclinic trajectories within a dynamical systems framework and are thus not structurally stable. Therefore, one must go beyond lowest order averaging to resolve differences between the homogeneous and inhomogeneous systems. We will proceed by carrying out a perturbation expansion in ε, extending previous work on traveling fronts in reaction diffusion systems [77, 78] and excitable neuronal networks [20].

We begin by performing an integration by parts on the first equation in the system (5.5) so that

$$\begin{aligned}
\frac{\partial u(x,t)}{\partial t} &= -u(x,t) - \beta_p v(x,t) + \int_{-\infty}^{\infty} W(x-x') f(u(x',t)) \mathrm{d}x' \\
&\quad + \varepsilon \int_{-\infty}^{\infty} \mathcal{D}_c\left(\frac{x'}{\varepsilon}\right) \left[W'(x-x') f(u(x',t)) - W(x-x') \frac{\partial f(u(x',t))}{\partial x'} \right] \mathrm{d}x', \\
\frac{1}{\alpha_p} \frac{\partial v(x,t)}{\partial t} &= -v(x,t) + u(x,t).
\end{aligned} \tag{5.7}$$

Although the inhomogeneous system is not translationally invariant, we can assume that perturbations about the homogeneous system will provide us with nearly translationally invariant solutions [77]. Thus, we perform the change of variables $\xi = x - \phi(t)$ and $\tau = t$, so that equation (5.7) becomes

$$\begin{aligned}
\frac{\partial u(\xi,\tau)}{\partial \tau} &= -u(\xi,\tau) - \beta_p v(\xi,\tau) + \int_{-\infty}^{\infty} W(\xi-\xi') f(u(\xi',\tau)) \mathrm{d}\xi' + \phi' \frac{\partial u(\xi,\tau)}{\partial \xi} \\
&+ \varepsilon \int_{-\infty}^{\infty} \mathcal{D}_c\left(\frac{\xi'+\phi}{\varepsilon}\right) \left[W'(\xi-\xi') f(u(\xi',\tau)) - W(\xi-\xi') \frac{\partial f(u(\xi',\tau))}{\partial \xi'} \right] \mathrm{d}\xi', \\
\frac{1}{\alpha_p} \frac{\partial v(\xi,\tau)}{\partial \tau} &= -v(\xi,\tau) + u(\xi,\tau) + \frac{\phi'}{\alpha_p} \frac{\partial v(\xi,\tau)}{\partial \xi}.
\end{aligned} \tag{5.8}$$

Next perform the perturbation expansions

$$u(\xi,\tau) = U(\xi) + \varepsilon u_1(\xi,\tau) + \varepsilon^2 u_2(\xi,\tau) + \cdots, \tag{5.9}$$
$$v(\xi,\tau) = V(\xi) + \varepsilon v_1(\xi,\tau) + \varepsilon^2 v_2(\xi,\tau) + \cdots, \tag{5.10}$$
$$\phi'(\tau) = c + \varepsilon \phi_1'(\tau) + \varepsilon^2 \phi_2'(\tau) + \cdots, \tag{5.11}$$

where $(U(\xi), V(\xi))^{\mathrm{T}}$ is a traveling pulse solution of the corresponding homogeneous system, see equation (5.6), and c is the speed of the unperturbed pulse. The first order terms u_1, v_1 satisfy

$$-\frac{\partial}{\partial\tau}\begin{pmatrix} u_1(\xi,\tau) \\ v_1(\xi,\tau)/\alpha_p \end{pmatrix} + \mathcal{L}\begin{pmatrix} u_1(\xi,\tau) \\ v_1(\xi,\tau) \end{pmatrix} = -\phi_1'(\tau)\begin{pmatrix} U'(\xi) \\ V'(\xi)/\alpha_p \end{pmatrix} + \begin{pmatrix} h_1\left(\xi, \frac{\phi}{\varepsilon}\right) \\ 0 \end{pmatrix} \tag{5.12}$$

where

$$\mathcal{L}\begin{pmatrix} u \\ v \end{pmatrix} = \begin{pmatrix} c\frac{\mathrm{d}u}{\mathrm{d}\xi} - u + \int_{-\infty}^{\infty} W(\xi-\xi')f'(U(\xi'))u(\xi')d\xi' - \beta_p v \\ \frac{c}{\alpha_p}\frac{\mathrm{d}v}{\mathrm{d}\xi} - v + u \end{pmatrix}, \tag{5.13}$$

for $u, v \in \mathcal{C}^1(\mathbb{R}, \mathbb{C})$ and

$$h_1\left(\xi, \frac{\phi}{\varepsilon}\right) = -\int_{-\infty}^{\infty} \mathcal{D}\left(\frac{\xi'+\phi}{\varepsilon}\right)\left[W'(\xi-\xi')f(U(\xi')) - W(\xi-\xi')\frac{\mathrm{d}f(U(\xi'))}{\mathrm{d}\xi'}\right]\mathrm{d}\xi'. \tag{5.14}$$

The linear operator $\mathcal{L}$ has a one–dimensional null–space spanned by $(U'(\xi), V'(\xi))^{\mathrm{T}}$. The existence of $(U'(\xi), V'(\xi))^{\mathrm{T}}$ as a null vector follows immediately from differentiating the homogeneous equation (5.6), and is a consequence of the translation invariance of the homogeneous system. Uniqueness can be shown using properties of positive linear operators. A bounded solution to equation (5.12) then exists if and only if the right hand side is orthogonal to all elements of the null space of the adjoint operator $\mathcal{L}^*$. The latter is defined according to the inner product relation

$$\int_{-\infty}^{\infty} (\mathsf{a}(\xi) \;\; \mathsf{b}(\xi))\mathcal{L}\begin{pmatrix} u(\xi) \\ v(\xi) \end{pmatrix} d\xi = \int_{-\infty}^{\infty} (u(\xi) \;\; v(\xi))\mathcal{L}^*\begin{pmatrix} \mathsf{a}(\xi) \\ \mathsf{b}(\xi) \end{pmatrix} \tag{5.15}$$

where $u(\xi)$, $v(\xi)$, $\mathsf{a}(\xi)$, and $\mathsf{b}(\xi)$ are arbitrary integrable functions. It follows that

$$\mathcal{L}^*\begin{pmatrix} \mathsf{a} \\ \mathsf{b} \end{pmatrix} = \begin{pmatrix} -c\frac{\mathrm{d}\mathsf{a}}{\mathrm{d}\xi} - \mathsf{a} + \mathsf{b} + f'(U(\xi))\int_{-\infty}^{\infty} W(\xi-\xi')\mathsf{a}(\xi')d\xi' \\ -\frac{c}{\alpha_p}\frac{\mathrm{d}\mathsf{b}}{\mathrm{d}\xi} - \beta_p\mathsf{a} - \mathsf{b} \end{pmatrix}. \tag{5.16}$$

The adjoint operator also has a one–dimensional null–space spanned by some vector $(A, B)^T$. (An explicit construction of this null vector in the case of a Heaviside nonlinearity will be

presented in section 5.3.1). Therefore, for equation (5.12) to have a solution, it is necessary that

$$K\phi_1'(\tau) = \int_{-\infty}^{\infty} A(\xi) h_1\left(\xi, \frac{\phi}{\varepsilon}\right) d\xi, \tag{5.17}$$

where

$$K = \int_{-\infty}^{\infty} [A(\xi)U'(\xi) + \alpha_p^{-1} B(\xi)V'(\xi)] d\xi. \tag{5.18}$$

Substituting for h_1 using equation (5.14) leads to a first–order differential equation for the phase ϕ:

$$\frac{d\phi}{d\tau} = c - \varepsilon \Phi_1\left(\frac{\phi}{\varepsilon}\right) \tag{5.19}$$

where

$$\begin{aligned} \Phi_1\left(\frac{\phi}{\varepsilon}\right) &= \frac{1}{K}\int_{-\infty}^{\infty}\int_{-\infty}^{\infty} A(\xi)\mathcal{D}_c\left(\frac{\xi' + \phi}{\varepsilon}\right) \\ &\quad \times \left[W'(\xi - \xi')f(U(\xi')) - W(\xi - \xi')\frac{df(U(\xi'))}{d\xi'}\right] d\xi' d\xi. \end{aligned} \tag{5.20}$$

If the right hand side of equation (5.19) is strictly positive, then there exists a traveling pulse of the approximate form $U(x - \phi(t))$, and average speed $\bar{c} = 2\pi\varepsilon/T$ with

$$T = \int_0^{2\pi\varepsilon} \frac{d\phi}{c - \varepsilon\Phi_1(\phi/\varepsilon)}. \tag{5.21}$$

However, if the right hand side of equation (5.19) vanishes for some ϕ, then the first–order analysis predicts wave propagation failure.

5.3 Calculation of average wave speed

In this section we use equation (5.21) to calculate the average wave speed $\bar{c}$ as a function of ε in the limiting case of a Heaviside nonlinearity. Note that since derivatives of f always appear inside integral terms, the high gain limit $\eta \to \infty$ is well defined. One advantage of using a Heaviside nonlinearity is that all calculations can be carried out explicitly. Moreover, as previously shown for traveling fronts [20], in the case of smooth nonlinearities it is necessary to develop the perturbation analysis to $\mathcal{O}(\varepsilon^2)$ since the $\mathcal{O}(\varepsilon)$ terms may be exponentially small, see also section 5.3.3.

5.3.1 Homogeneous network with Heaviside nonlinearity

The existence (and stability) of single bump traveling pulse solutions in the homogeneous network obtained by setting $f = H$ and $w(x, x') = W(|x - x'|)$ in equation (5.1) has been studied by a number of authors [136, 138, 187, 41, 57, 168]. A single bump solution $(U(\xi), V(\xi))$ is one for which U is above threshold over a domain of length a, corresponding to the width of the bump, and subthreshold everywhere else. In other words, the activity U crosses threshold at only two points, which by translation invariance can be taken to be $\xi = -a, 0$:

$$\begin{aligned} U(-a) = U(0) = \kappa; \qquad & U(\xi) \longrightarrow 0 \text{ as } \xi \longrightarrow \pm\infty; \\ U(\xi) > \kappa, \ -a < \xi < 0; \qquad & U(\xi) < \kappa, \qquad \text{otherwise.} \end{aligned}$$

It follows from equation (5.6) with $f = \Theta$ that

$$\begin{aligned} -c\, U_\xi &= -U - \beta_p V + \int_{-a}^{0} W(\xi - \eta) d\eta, \\ -\frac{c}{\alpha_p} V_\xi &= -V + U. \end{aligned} \tag{5.22}$$

One way to solve this pair of equations is to use variation of parameters [187, 57]. For completeness, we present the details of this calculation here, since some of the results will be used in our subsequent analysis.

Let $\mathbf{s} = (U, V)^T$ and rewrite the system as

$$\mathcal{L}\mathbf{s} \equiv \begin{pmatrix} cU'(\xi) - U(\xi) - \beta_p V(\xi) \\ cV'(\xi) + \alpha_p U(\xi) - \alpha_p V(\xi) \end{pmatrix} = -\begin{pmatrix} N_e(\xi) \\ 0 \end{pmatrix}, \tag{5.23}$$

where

$$N_e(\xi) = \Omega_p(\xi + a) - \Omega_p(\xi), \quad \Omega_p(\xi) = \int_{-\infty}^{\xi} W(\xi') d\xi'. \tag{5.24}$$

We solve equation (5.23) using variation of parameters. The homogeneous problem $\mathcal{L}\mathbf{s} = \mathbf{0}$ has two linearly independent solutions,

$$\mathbf{S}_+(\xi) = \begin{pmatrix} \beta_p \\ m_+ - 1 \end{pmatrix} \exp(\mu_+ \xi), \qquad \mathbf{S}_-(\xi) = \begin{pmatrix} \beta_p \\ m_- - 1 \end{pmatrix} \exp(\mu_- \xi),$$

where

$$\mu_\pm = \frac{m_\pm}{c}, \qquad m_\pm = \frac{1}{2}(1 + \alpha_p \pm \sqrt{(1 - \alpha_p)^2 - 4\alpha_p\beta_p}). \tag{5.25}$$

We shall work in the parameter regime where $\mu_\pm$ are real, though interesting behavior can arise when $\mu_\pm$ is complex [168]. Thus, set

$$\mathbf{s}(\xi) = [\mathbf{S}_+|\mathbf{S}_-] \begin{pmatrix} \mathfrak{a}(\xi) \\ \mathfrak{b}(\xi) \end{pmatrix},$$

where $\mathfrak{a}, \mathfrak{b} \in \mathcal{C}^1(\mathbb{R}, \mathbb{R})$ and $[A|B]$ denotes the matrix whose first column is A and whose second column is B. Since $\mathcal{L}\mathbf{S}_\pm = 0$, equation (5.23) becomes

$$[\mathbf{S}_+|\mathbf{S}_-] \frac{\partial}{\partial \xi} \begin{pmatrix} \mathfrak{a}(\xi) \\ \mathfrak{b}(\xi) \end{pmatrix} = -\frac{1}{c} \begin{pmatrix} N_e(\xi) \\ 0 \end{pmatrix}. \tag{5.26}$$

Since $[\mathbf{S}_+|\mathbf{S}_-]$ is invertible, we find that

$$\frac{\partial}{\partial \xi} \begin{pmatrix} \mathfrak{a}(\xi) \\ \mathfrak{b}(\xi) \end{pmatrix} = -\frac{1}{c\beta(m_+ - m_-)} [\mathbf{Z}_+|\mathbf{Z}_-]^T \begin{pmatrix} N_e(\xi) \\ 0 \end{pmatrix},$$

where

$$\mathbf{Z}_+(\xi) = \begin{pmatrix} 1 - m_- \\ \beta \end{pmatrix} \exp(-\mu_+ \xi), \qquad \mathbf{Z}_-(\xi) = -\begin{pmatrix} 1 - m_+ \\ \beta_p \end{pmatrix} \exp(-\mu_- \xi).$$

For $c > 0$, we can integrate from ξ to ∞ and find

$$\begin{pmatrix} \mathfrak{a}(\xi) \\ \mathfrak{b}(\xi) \end{pmatrix} = \begin{pmatrix} \mathfrak{a}_\infty \\ \mathfrak{b}_\infty \end{pmatrix} + \frac{1}{c\beta_p(m_+ - m_-)} \int_\xi^\infty [\mathbf{Z}_+|\mathbf{Z}_-]^T \begin{pmatrix} N_e(\xi') \\ 0 \end{pmatrix} d\xi',$$

where $\mathfrak{a}_\infty, \mathfrak{b}_\infty$ are the values of $\mathfrak{a}(\xi), \mathfrak{b}(\xi)$ as $\xi \to \infty$. Thus

$$\mathbf{s}(\xi) = [\mathbf{S}_+|\mathbf{S}_-] \begin{pmatrix} \mathfrak{a}_\infty \\ \mathfrak{b}_\infty \end{pmatrix} + \frac{1}{c\beta_p(m_+ - m_-)} [\mathbf{S}_+|\mathbf{S}_-] \int_\xi^\infty [\mathbf{Z}_+|\mathbf{Z}_-]^T \begin{pmatrix} N_e(\xi') \\ 0 \end{pmatrix} d\xi'. \tag{5.27}$$

Using Hölder's inequality and that $N_e \in \mathcal{C}^0(\mathbb{R}, \mathbb{R})$, we can show that the integral in (5.27) is bounded for all $\xi \in \mathbb{R}$. Thus, a bounded solution $\mathbf{s}$ exists if $\mathfrak{a}_\infty = \mathfrak{b}_\infty = 0$. Our general traveling pulse solution is given by

$$\mathbf{s}(\xi) = \frac{1}{c\beta_p(m_+ - m_-)} [\mathbf{S}_+|\mathbf{S}_-] \int_\xi^\infty [\mathbf{Z}_+|\mathbf{Z}_-]^T \begin{pmatrix} N_e(\xi') \\ 0 \end{pmatrix} d\xi'.$$

Furthermore, if we define

$$\mathcal{M}_\pm(\xi) = \frac{1}{c(m_+ - m_-)} \int_\xi^\infty \mathrm{e}^{\mu_\pm(\xi - \xi')} N_e(\xi') d\xi',$$

we can express our solution (U, V) as:

$$U(\xi) = (1 - m_-)\mathcal{M}_+(\xi) - (1 - m_+)\mathcal{M}_-(\xi), \tag{5.28}$$

$$V(\xi) = \beta_p^{-1}(m_+ - 1)(1 - m_-)\left[\mathcal{M}_+(\xi) - \mathcal{M}_-(\xi)\right]. \tag{5.29}$$

Since $N_e(\xi)$ is dependent upon the pulse width a, the threshold conditions $U(-a) = U(0) = \kappa$ lead to the following consistency conditions for the existence of a traveling pulse:

$$\kappa = (1 - m_-)\mathcal{M}_+(-a) - (1 - m_+)\mathcal{M}_-(-a), \tag{5.30}$$

$$\kappa = (1 - m_-)\mathcal{M}_+(0) - (1 - m_+)\mathcal{M}_-(0). \tag{5.31}$$

This pair of nonlinear equations determines the pulse width a and wave speed c of a single bump traveling wave solution as a function of the various parameters of the network. For a given weight distribution $W(x)$, existence of such a solution is established if a solution for a, c can be found, and provided that U does not cross threshold at any other points besides $\xi = -a, 0$. Recently the existence (and stability) of single bump traveling waves has been examined for quite a general class of weight distributions [139], which includes both exponential and Gaussian distributions. For concreteness, we consider the exponential weight function (5.3) with $W_0 = d = 1$. Numerically solving equations (5.30) and (5.31) for a and c as a function of the adaptation rate α_p yields the existence curves shown in Figure 5.2. This figure illustrates the well known result that for sufficiently slow adaptation (small α_p) there exists a pair of traveling pulses with the fast/wide pulse stable and the

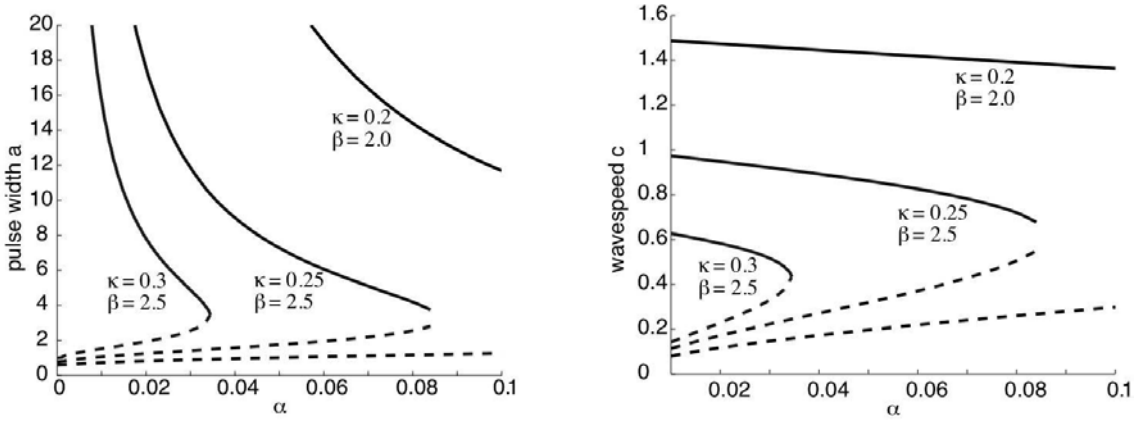

Figure 5.2. Existence curves for a single bump traveling pulse solution of equation (5.1) in the case of a homogeneous network with an exponential weight distribution $W(x) = \mathrm{e}^{-|x|/2}$. (Left): Existence curves in the (α_p,a) plane. (Right) Existence curves in the (α_p,c) plane. Pulses only exist for small enough α_p (sufficiently slow adaptation). For each parameter set, there exists a stable branch (solid) of wide/fast pulses and an unstable branch (dashed) of narrow/slow pulses. In the case $\kappa = 0.3$ the branches annihilate at a saddle–node bifurcation at a critical value α_c. In the other two cases, the branches end abruptly due to the fact that the eigenvalues $\mu_\pm$ become complex–valued [168].

slow/narrow pulse unstable [136]. Also shown in the figure is the stability of the various solution branches, which can be determined analytically using an Evans function approach [187, 41, 57, 139].

The analysis of existence in a homogeneous network also provides some insights into what happens when we include a periodic modulation of the weights according to equations (5.2) and (5.4). Such a modulation induces a periodic variation in the amplitude W_0 of the exponential weight distribution (5.3) between the limiting values $W_\pm = (1 \pm \rho)W_0$. This suggests that the speed of a wave in the inhomogeneous network will be bounded by the speeds $c_\pm$ of a traveling wave in the corresponding homogeneous network obtained by taking $W_0 \to W_\pm$. Note that rescaling the weight distribution in equations (5.30) and (5.31) is equivalent to rescaling the threshold according to $\kappa \to \kappa/(1 \pm \rho)$. In Figure 5.3 we plot the speeds $c_\pm$ and the corresponding pulse widths $a_\pm$ as a function of ρ. For sufficiently small ρ, the wave speed c_+ increases with ρ at approximately the same rate as c_- decreases so that their arithmetic mean remains constant. Therefore, one might expect that a periodic variation in weights would lead to a corresponding periodic variation in wave speed such that the mean wave speed is approximately independent of ρ. However, when a pulse enters a region of enhanced synaptic weights, the resulting increase in wave speed

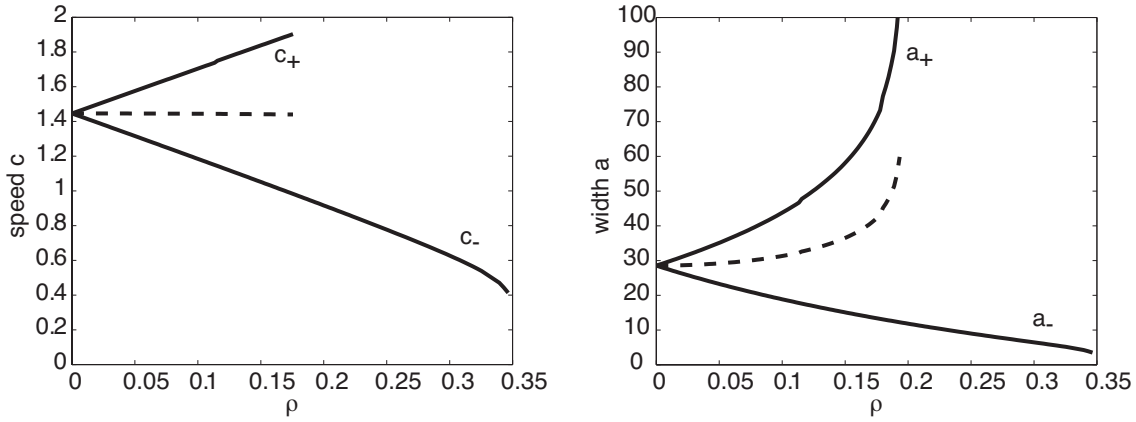

Figure 5.3. Existence curves for a single bump traveling pulse solution of equation (5.1) in the case of a homogeneous network with an exponential weight distribution $W(x) = W_\pm e^{-|x|/2}$ with $W_\pm = 1 \pm \rho$. (Left): Plot of wave speed $c_\pm$ as a function of ρ for weight amplitudes $W_\pm$. Dashed curve indicates arithmetic mean of pair $c_\pm$. The slower branch terminates at around $\rho = 0.35$ due to a saddle–node bifurcation. The faster branch terminates due to a blow–up of the pulse width. (Right): Plot of pulse width $a_\pm$ as a function of ρ for weight amplitudes $W_\pm$.

coincides with a rapid increase in pulse width as a function of ρ. Thus, the pulse will tend to extend into neighboring regions of reduced synaptic weights and the resulting spatial averaging will counteract the speeding up of the wave. On the other hand, when a pulse enters a region of reduced synaptic weights, the reduction in wave speed coincides with a reduction in pulse width so that spatial averaging can no longer be carried out as effectively. (The effectiveness of spatial averaging will depend on the ratio of the pulse width a to the periodicity $2\pi\varepsilon$ of the weight modulation). Hence, we expect regions where the weights are reduced to have more effect on wave propagation than regions where the weights are enhanced, suggesting that a periodic weight modulation leads to slower, narrower waves. This is indeed found to be the case, both in our perturbation analysis (see section 5.3.2) and our numerical simulations (see section 5.4). Interestingly, we also find that traveling waves persist for larger values of ρ than predicted by our analysis of single bumps in homogeneous networks, although such waves tend to consist of multiple bumps (see section 5.4).

5.3.2 Inhomogeneous network with Heaviside nonlinearity

Suppose that the homogeneous network with a Heaviside nonlinearity supports a stable traveling wave solution $(U(\xi), V(\xi))^T$ of wave speed c. As shown in section 5.3.1, a stable/unstable pair of traveling waves exists for sufficiently slow adaptation. In order to calculate the average wave speed $\bar{c}$ for nonzero ε and ρ, see equation (5.21), we first need to compute the null–vector $(A(\xi), B(\xi))^T$ of the adjoint operator $\mathcal{L}^*$ defined by equation (5.16). In the case of a Heaviside nonlinearity,

$$\begin{aligned} -c\frac{\mathrm{d}A(\xi)}{\mathrm{d}\xi} - A(\xi) + B(\xi) + \frac{\delta(\xi)}{|U'(0)|}\int_{-\infty}^{\infty} W(\xi-\xi')A(\xi')d\xi' & \\ + \frac{\delta(\xi+a)}{|U'(-a)|}\int_{-\infty}^{\infty} W(\xi-\xi')A(\xi')d\xi' &= 0 \\ -\frac{c}{\alpha_p}\frac{\mathrm{d}B(\xi)}{\mathrm{d}\xi} - \beta_p A(\xi) - B(\xi) &= 0. \end{aligned} \tag{5.32}$$

For $\xi \neq 0, -a$, this has solutions of the form $(A(\xi), B(\xi)^T) = \mathbf{u}e^{-\lambda\xi}$ with associated characteristic equation $\mathbf{M}\mathbf{u} = c\lambda\mathbf{u}$ and

$$\mathbf{M} = \begin{pmatrix} 1 & -1 \\ \beta_p\alpha_p & \alpha_p \end{pmatrix}. \tag{5.33}$$

The eigenvalues are $\lambda = \mu_\pm = m_\pm/c$ with $m_\pm$ given by equation (5.25). The corresponding eigenvectors are

$$\mathbf{u}_\pm = \begin{pmatrix} 1 \\ 1-m_\pm \end{pmatrix}. \tag{5.34}$$

The presence of the Dirac delta functions at $\xi = 0, -a$ then suggests that we take the null solution to be of the form

$$\begin{aligned}\mathbf{V}^*(\xi) &= \varsigma_+\mathbf{u}_+\left[e^{-\mu_+\xi}\Theta(\xi) + \chi e^{-\mu_+(\xi+a)}\Theta(\xi+a)\right] \\ &\quad +\varsigma_-\mathbf{u}_-\left[e^{-\mu_-\xi}\Theta(\xi) + \chi e^{-\mu_-(\xi+a)}\Theta(\xi+a)\right] \end{aligned} \tag{5.35}$$

with the coefficients $\varsigma_\pm$ chosen such that the Dirac delta function terms that come from differentiating the null vector only appear in the $A(\xi)$ term,

$$\varsigma_+\mathbf{u}_+ + \varsigma_-\mathbf{u}_- = \begin{pmatrix} \Gamma \\ 0 \end{pmatrix}, \tag{5.36}$$

and χ is a constant yet to be determined. Taking

$$\varsigma_\pm = \pm(1 - m_\mp) \tag{5.37}$$

we have $\Gamma = m_+ - m_-$.

In order to determine χ, substitute equation (5.35) into equation (5.32) to obtain the pair of equations

$$c(m_+ - m_-) = \frac{1}{|U'(0)|}(\Lambda(0) + \chi\Lambda(-a)) \tag{5.38}$$

and

$$\chi c(m_+ - m_-) = \frac{1}{|U'(-a)|}(\Lambda(a) + \chi\Lambda(0)) \tag{5.39}$$

with

$$\Lambda(\zeta) = \int_0^\infty [(1-m_-)W(\xi+\zeta)e^{-\mu_+\xi} - (1-m_+)W(\xi+\zeta)e^{-\mu_-\xi}]d\xi. \tag{5.40}$$

We require that equations (5.38) and (5.39) are consistent with the formula for $U'(\xi)$ obtained by differentiating equation (5.28) with respect to ξ:

$$\begin{aligned} U'(\xi) &= \frac{1-m_-}{c(m_+-m_-)}\int_\xi^\infty e^{\mu_+(\xi-\xi')}[W(\xi'+a) - W(\xi')]d\xi' \\ &\quad -\frac{1-m_+}{c(m_+-m_-)}\int_\xi^\infty e^{\mu_-(\xi-\xi')}[W(\xi'+a) - W(\xi')]d\xi'. \end{aligned} \tag{5.41}$$

It follows that

$$|U'(0)| = -U'(0) = \frac{\Lambda(0)-\Lambda(a)}{c(m_+-m_-)}, \quad |U'(-a)| = U'(-a) = \frac{\Lambda(0)-\Lambda(-a)}{c(m_+-m_-)},$$

which, together with equations (5.38) and (5.39), implies

$$\Lambda(0) - \Lambda(a) = \Lambda(0) + \chi\Lambda(-a), \quad \chi(\Lambda(0) - \Lambda(-a)) = \Lambda(a) + \chi\Lambda(0).$$

Hence, equation (5.35) is a solution provided that

$$\chi \;=\; -\frac{\Lambda(a)}{\Lambda(-a)}. \tag{5.42}$$

This is also a constructive proof that the adjoint linear operator $\mathcal{L}^*$ for a Heaviside nonlinearity has a one–dimensional nullspace spanned by $\mathbf{V}^*$.

Having found the null solution (5.35), we now determine the phase function Φ_1 given by equation (5.20) with $f \equiv \Theta$. First, the constant K of equation (5.18) is evaluated by substituting for $(A(\xi), B(\xi))$ using equation (5.35) and substituting for $(U(\xi), V(\xi))$ using equations (5.28) and (5.29). The rather lengthy expression for K is given in Appendix C. Next, we evaluate the double integral on the right–hand side of equation (5.20) by setting $\mathcal{D}_c(x) = \mathrm{e}^{ix}$ and using Fourier transforms. This gives

$$K\Phi_1\left(\frac{\phi}{\varepsilon}\right) \;=\; \frac{i}{\varepsilon}\mathrm{e}^{i\phi/\varepsilon}\int_{-\infty}^{\infty} W(x)\left[\int_{-\infty}^{\infty}\mathrm{e}^{iqx}\widetilde{A}^*(q)\widetilde{f(U)}(q+\varepsilon^{-1})\frac{\mathrm{d}q}{2\pi}\right]dx, \tag{5.43}$$

where * denotes complex conjugate and

$$\widetilde{A}(q) = \int_{-\infty}^{\infty}\mathrm{e}^{iqx}A(x)\mathrm{d}x. \tag{5.44}$$

In the case of a Heaviside nonlinearity and a pulse of width a, $f(U(\xi)) = \Theta(\xi + a) - \Theta(\xi)$, and $A(x)$ is given explicitly by the first component of the null vector in equation (5.35). Taking Fourier transforms of these expressions shows that

$$\widetilde{A}(q) = -\left(1 + \chi\mathrm{e}^{-iqa}\right)\left[\frac{\varsigma_+}{iq - \mu_+} + \frac{\varsigma_-}{iq - \mu_-}\right], \quad \widetilde{f(U)}(q) = \frac{1 - \mathrm{e}^{-iqa}}{iq - 0^+}. \tag{5.45}$$

If these Fourier transforms are now substituted into equation (5.43), we have

$$\begin{aligned} K\Phi_1\left(\frac{\phi}{\varepsilon}\right) \;=\; & \frac{\mathrm{e}^{i\phi/\varepsilon}}{\varepsilon}\int_{-\infty}^{\infty} W(x)\left[\int_{-\infty}^{\infty}\left\{\frac{\varsigma_+(1 - \mathrm{e}^{-i(q+\varepsilon^{-1})a} + \chi\mathrm{e}^{iqa} - \chi\mathrm{e}^{-ia/\varepsilon})\mathrm{e}^{iqx}}{(q + \varepsilon^{-1} + i0^+)(q - i\mu_+)}\right.\right. \\ & \left.\left. + \frac{\varsigma_-(1 - \mathrm{e}^{-i(q+\varepsilon^{-1})a} + \chi\mathrm{e}^{iqa} - \chi\mathrm{e}^{-ia/\varepsilon})\mathrm{e}^{iqx}}{(q + \varepsilon^{-1} + i0^+)(q - i\mu_-)}\right\}\frac{\mathrm{d}q}{2\pi i}\right]\mathrm{d}x. \end{aligned} \tag{5.46}$$

The resulting integral over q can be evaluated by closing the contour in the upper half or lower–half complex q–plane depending on the sign of $x, x \pm a$. We find that there are

only contributions from the poles at $q = i\mu_\pm$ with $\mu_\pm > 0$, whereas there is a removable singularity at $q = -\varepsilon^{-1} - i0^+$. Thus

$$\begin{aligned} K\Phi_1\left(\frac{\phi}{\varepsilon}\right) &= \frac{\varsigma_+ \mathrm{e}^{i\phi/\varepsilon}}{\varepsilon(\varepsilon^{-1} + i\mu_+)}\left[\left(1 - \chi \mathrm{e}^{-ia/\varepsilon}\right)\widehat{\Omega}_+(0) + \chi\widehat{\Omega}_+(-a) - \mathrm{e}^{-ia/\varepsilon}\widehat{\Omega}_+(a)\right] \\ &\quad + \frac{\varsigma_- \mathrm{e}^{i\phi/\varepsilon}}{\varepsilon(\varepsilon^{-1} + i\mu_-)}\left[\left(1 - \chi \mathrm{e}^{-ia/\varepsilon}\right)\widehat{\Omega}_-(0) + \chi\widehat{\Omega}_-(-a) - \mathrm{e}^{-ia/\varepsilon}\widehat{\Omega}_-(a)\right], \end{aligned} \tag{5.47}$$

with

$$\widehat{\Omega}_\pm(s) = \int_0^\infty W(x+s)\mathrm{e}^{-\mu_\pm x}\mathrm{d}x. \tag{5.48}$$

Taking the imaginary part of the above equation then determines the phase function $K\Phi_1$ for $\mathcal{D}_c(x) = \rho\sin(x)$. After a straightforward calculation, we find that

$$\begin{aligned} \frac{K}{\rho}\Phi_1\left(\frac{\phi}{\varepsilon}\right) &= (\Xi_+ + \Xi_-)\sin\left(\frac{\phi}{\varepsilon}\right) + (\Pi_+ + \Pi_-)\sin\left(\frac{\phi - a}{\varepsilon}\right) + \\ &\quad (\Upsilon_+ + \Upsilon_-)\cos\left(\frac{\phi}{\varepsilon}\right) + (\Psi_+ + \Psi_-)\cos\left(\frac{\phi - a}{\varepsilon}\right) \end{aligned} \tag{5.49}$$

where the explicit expressions for $\Xi_\pm, \Pi_\pm, \Upsilon_\pm, \Psi_\pm$ are given in Appendix C.

Finally, we numerically calculate the average wave speed $\bar{c}$ by substituting equation (5.49) into equation (5.21). Note that we use the exact expression for Φ_1 that includes all higher–order terms in ε, rather than keeping only the $\mathcal{O}(1)$ term, since this gives a better estimate of the wave speed. In Figure 5.4 we show some example plots of $\bar{c}$ as a function of ε and ρ. It can be seen that for each choice of parameters, $\bar{c}$ is a monotonically decreasing function of ε and ρ, with $\bar{c}$ approaching the speed c of the homogeneous wave in the limits $\varepsilon \to 0$ and $\rho \to 0$. Hence, although the periodic modulation enhances the strength of connections in some regions and reduces them in others compared to the homogeneous case, see Figure 5.1, the net result is an effective reduction in wave speed. This is consistent with our discussion of Figure 5.3 in section 5.3.1, where we used a spatial averaging argument combined with the observation that faster waves are wider to infer that regions of reduced synaptic weights affect wave propagation more than regions of enhanced weights. Figure 5.4 also suggests that for sufficiently small ε there exists a traveling wave solution for all $\rho,\ 0 \leq \rho < 1$, whereas for larger values of ε there is a critical value ρ_c beyond which propagation failure occurs. That is, $\bar{c} \to 0$ as $\rho \to \rho_c$, and this critical value decreases as the periodicity ε of the inhomogeneity increases. Similarly, for sufficiently large ρ there exists a critical period ε_c such that $\bar{c} \to 0$ as $\varepsilon \to \varepsilon_c$. Analogous results were previously

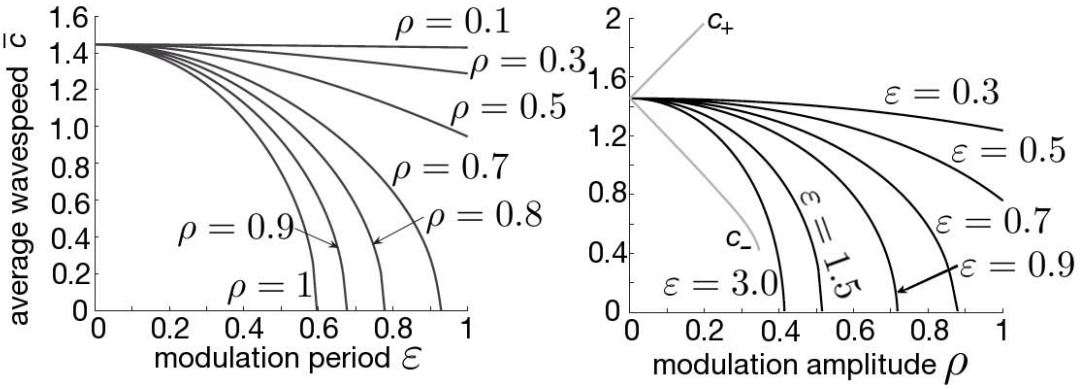

Figure 5.4. Average wave speed dependence upon modulation amplitude and period. (Left): Average wave speed $\bar{c}$ vs. ε for various values of the modulation amplitude ρ. Critical value of ε for wave propagation failure decreases as ρ increases. (Right): Average wave speed $\bar{c}$ vs. ρ for various values of the modulation period ε. For the sake of comparison, the speed curves previously plotted in Figure 5.3 for a homogeneous network are also shown (gray curves). Other parameters are $\kappa = 0.2$, $\alpha_p = 0.04$ and $\beta_p = 2.0$.

obtained for traveling fronts in a scalar equation [20]. It is important to bear in mind that the calculation of $\bar{c}$ is based on the $\mathcal{O}(\varepsilon)$ perturbation analysis of section 5.3, although we do include higher–order terms in the calculation of Φ_1. This raises the important question as to whether or not our analysis correctly predicts wave propagation failure in the full system, given that $\bar{c}$ tends to approach zero at relatively large values of ε and ρ. Moreover, the perturbation analysis does not determine the stability of the wave so that propagation failure could occur due to destabilization of the wave for $\rho < \rho_c$ or $\varepsilon < \varepsilon_c$. This will indeed turn out to be the case as we show in section 5.4, where we present numerical solutions of equation (5.1) and provide further insights into the mechanism for propagation failure.

5.3.3 Smooth nonlinearities and higher–order corrections

In the case of smooth nonlinearities, the Fourier transforms $\widetilde{A}(q)$ and $\widetilde{f(U)}(q)$ appearing in equation (5.43) no longer have simple poles and in general Φ_1 will consist of exponentially small terms. It follows that Φ_1 may be less significant than the $\mathcal{O}(\varepsilon^2)$ terms ignored in the perturbation expansion of (5.8). Therefore, following the treatment of traveling fronts [20], we carry out a perturbation expansion of system (5.8) to $\mathcal{O}(\varepsilon^2)$. This yields an equation for (u_2, v_2) of the form

$$-\frac{\partial}{\partial\tau}\begin{pmatrix} u_2(\xi,\tau) \\ v_2(\xi,\tau)/\alpha_p \end{pmatrix} + \mathcal{L}\begin{pmatrix} u_2(\xi,\tau) \\ v_2(\xi,\tau) \end{pmatrix} = -\phi_2'(\tau)\begin{pmatrix} U'(\xi) \\ V'(\xi)/\alpha_p \end{pmatrix} - \phi_1'(\tau)\begin{pmatrix} u_1'(\xi) \\ v_1'(\xi)/\alpha_p \end{pmatrix} + \begin{pmatrix} h_2(\xi,\frac{\phi}{\varepsilon}) \\ 0 \end{pmatrix} \tag{5.50}$$

where $\mathcal{L}$ is defined by equation (5.13) and

$$\begin{aligned} h_2(\xi,\frac{\phi}{\varepsilon}) &= -\frac{1}{2}\int_{-\infty}^{\infty} W(\xi-\xi')f''(U(\xi'))[u_1(\xi')]^2\mathrm{d}\xi' \\ &\quad -\int_{-\infty}^{\infty}\mathcal{D}_c\left(\frac{[\xi'+\phi]}{\varepsilon}\right)W'(\xi-\xi')f'(U(\xi'))u_1(\xi')\mathrm{d}\xi' \\ &\quad +\int_{-\infty}^{\infty}\mathcal{D}_c\left(\frac{[\xi'+\phi]}{\varepsilon}\right)W(\xi-\xi')[f'(U(\xi'))u_1'(\xi')+f''(U(\xi'))U'(\xi')u_1(\xi)]\mathrm{d}\xi'. \end{aligned} \tag{5.51}$$

The existence of a bounded solution requires the solvability conditions (5.17) and

$$K\phi_2'(\tau)+L(\tau)\phi_1'(\tau) = \int_{-\infty}^{\infty}A(\xi)h_2(\xi,\frac{\phi}{\varepsilon})\mathrm{d}\xi, \tag{5.52}$$

where

$$L(\tau)=\int_{-\infty}^{\infty}[A(\xi)\frac{\partial u_1(\xi,\tau)}{\partial\xi}+\alpha_p^{-1}B(\xi)\frac{\partial v_1(\xi,\tau)}{\partial\xi}]\mathrm{d}\xi. \tag{5.53}$$

In order to evaluate the solvability condition (5.52), we must first determine $u_1(\xi,\phi/\varepsilon)$ from equation (5.12). If we choose $\mathcal{D}_c(x)$ to be a sinusoid, then $u_1(\xi,\phi/\varepsilon)$ will include terms that are proportional to $\sin(\phi/\varepsilon)$ and $\cos(\phi/\varepsilon)$. Thus substituting $u_1(\xi/\phi/\varepsilon)$ into equation (5.51), will generate terms of the form $\sin^2(\phi/\varepsilon)$ and $\cos^2(\phi/\varepsilon)$ due to the quadratic term in u_1. Using the identities $2\sin^2(x)=1-\cos(2x)$ and $2\cos^2(x)=1+\cos(2x)$, implies that there will be an ε–independent contribution to ϕ_2'. Thus for smooth nonlinearities, we find that

$$\frac{\mathrm{d}\phi}{\mathrm{d}\tau}=c+\varepsilon^2C_2(c)+D_2\left(c,\frac{\phi}{\varepsilon}\right), \tag{5.54}$$

where C_2 is independent of ε and D_2 is exponentially small in ε. Equation (5.54) is the second–order version of the phase equation (5.19) in cases where the first–order term is exponentially small. Again the condition for wave propagation failure is that the right–hand side of equation (5.54) vanishes for some ϕ.

5.4 Numerical results

Our perturbation analysis suggests that as ρ increases, the mean speed of a traveling pulse decreases, and, at least for sufficiently large periods ε of the weight modulation,

wave propagation failure can occur. However, one of the simplifying assumptions of our analysis is that the perturbed solution is still a traveling pulse, that is, at each time t there is a single bounded interval over which the solution is above threshold, which is equal to the pulse width a of the homogeneous pulse in the limit $\varepsilon \to 0$. The inclusion of a periodic modulation of a monotonically decreasing weight function suggests that the assumption of a single pulse solution may break down as ρ increases towards unity. In this section we explore this issue by numerically solving the full system of equations (5.1) in the case of a Heaviside nonlinearity ($f = \Theta$), and show that wave propagation can persist in the presence of multiple bumps. Numerical simulations of propagating pulses employ finite difference schemes for calculating the space and time derivatives. Initial conditions are taken to be solutions to the homogeneous problem given by equations (5.28) and (5.29). We then apply backward Euler to the linear terms, and forward Euler with a Riemann sum for the convolution operator. Space and time discretizations are taken to be $\Delta t = 0.01$ and $\Delta x = 0.01$. The numerical results are stable with respect to reductions in the mesh size provided that $\Delta x \ll 2\pi\varepsilon$. Finally, boundary points evolve freely, rather than by prescription, and the domain size is wide enough so that pulses are unaffected by boundaries.

In Figure 5.5 we show some examples of traveling pulse solutions in an inhomogeneous network with weight distribution given by equations (5.2), (5.3) and (5.4). The period of the modulation is taken to be relatively small ($\varepsilon = 0.1$). We take as initial conditions the invariant profile for the corresponding homogeneous case, obtained by solving in traveling wave coordinates for the $\varepsilon = 0$ case, which gives (U, V) in equations (5.28) and (5.29). It can be seen from Figure 5.5 that as the amplitude ρ of the periodic modulation increases the wave slows down and narrows, which is consistent with our perturbation analysis. Moreover, the network activity develops a rippling within the interior of the pulse as can be seen more clearly in Figure 5.6, where we directly compare the numerical solution of the homogeneous network with that of a corresponding inhomogeneous network. Superimposing the two wave profiles at an early time ($t = 10$) illustrates the thinning of the pulse, and shows that the difference of the two wave profiles is an oscillatory component of approximately zero mean, which would correspond to u_1 in our perturbation analysis. Similarly, comparing the two wave profiles at a later time ($t = 200$) illustrates the slowing down of the pulse. As ρ increases the amplitude of the ripples also increases such that for sufficiently large ρ, activity at any given time t alternates between superthreshold

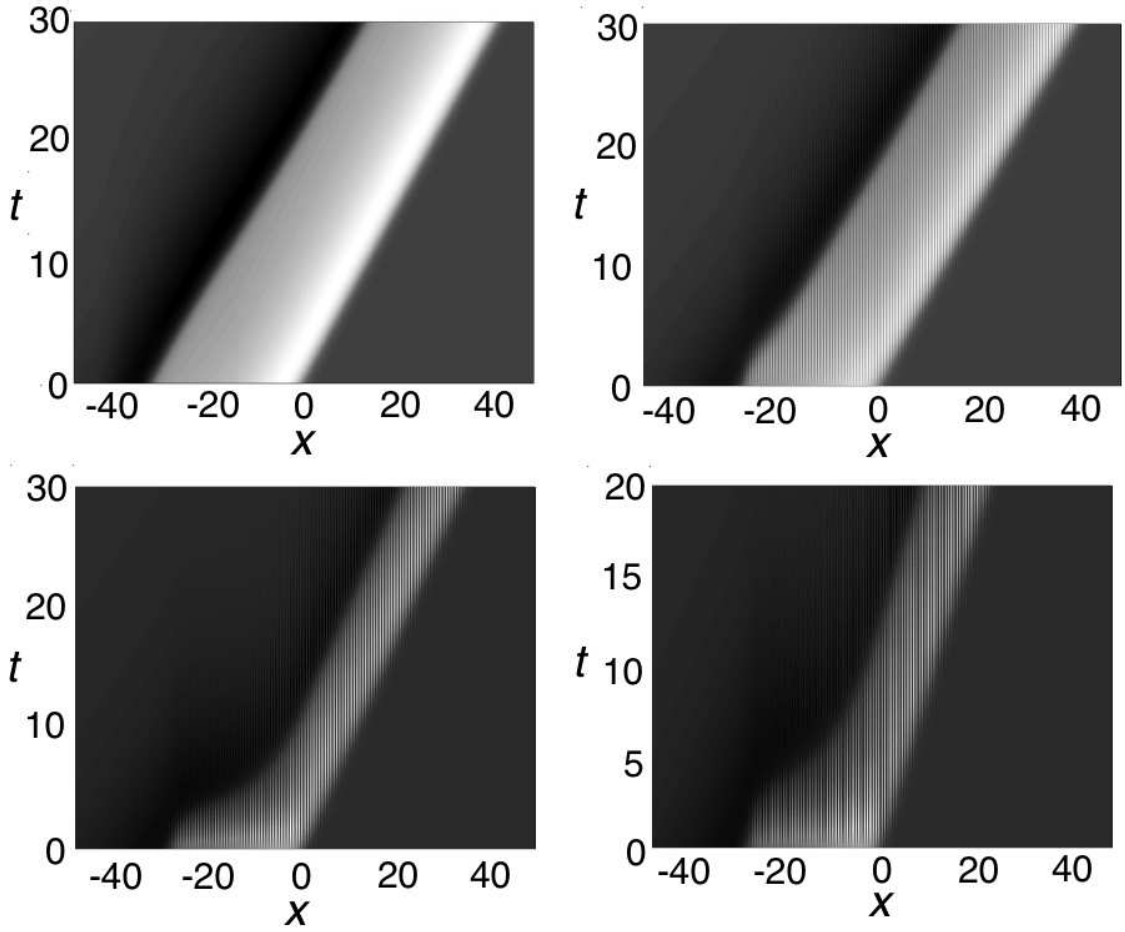

Figure 5.5. Traveling pulse dependence upon inhomogeneity modulation amplitude. (Top Left): Stable traveling pulse for a homogeneous network with exponential weight function (5.3) and fixed parameters $\kappa = 0.2$, $\beta_p = 2.0$, and $\alpha_p = 0.04$ (for all plots). (Top Right): Corresponding traveling pulse for an inhomogeneous network with weight distribution (5.2) and a sinusoidal modulation with $\varepsilon = 0.1$ and $\rho = 0.3$. We see rippling in the interior of the pulse. (Bottom Left): Using a more severe inhomogeneity, $\rho = 0.8$, leads to rippling in the active region of the pulse such that now the interior crosses below threshold periodically. (Bottom Right): For $\rho = 1$, the effect is even more severe.

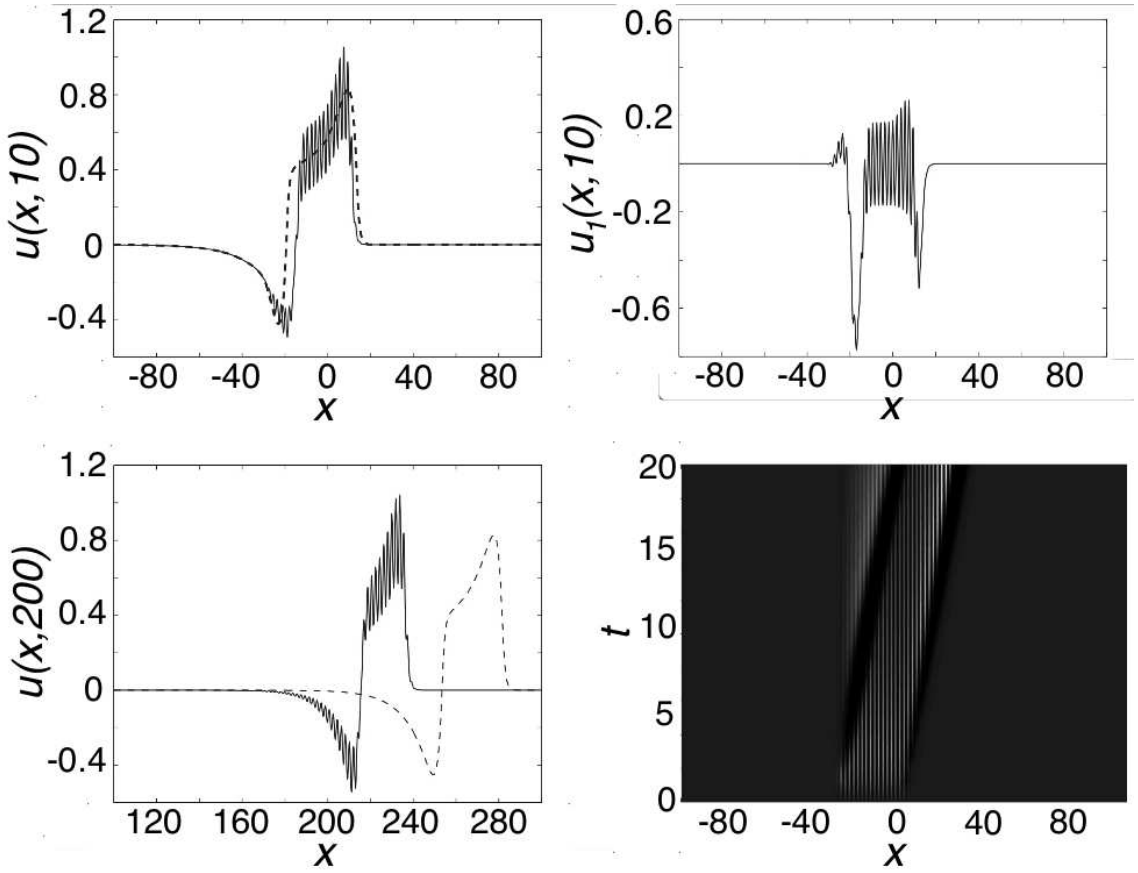

Figure 5.6. Comparison of traveling pulses in homogeneous and inhomogeneous network. (Top Left): Comparison of the wave profiles at time $t = 10$ for the homogeneous (dashed line) and the inhomogeneous (solid line) cases. Here, parameters are $\kappa = 0.2$, $\beta_p = 2.0$, $\alpha_p = 0.04$, $\varepsilon = 0.3$, and $\rho = 0.3$. Including periodic modulation clearly thins the pulse as we see its profile fits within that of the homogeneous medium. (Top Right): Subtraction of the homogeneous solution from the inhomogeneous at time $t = 10$. We see here an approximation of $u_1(x,t)$, from our perturbation analysis. The dominant detail is the oscillations with period $2\pi\varepsilon$. (Bottom Left): Profile comparison at $t = 200$. Homogeneous solution has moved well ahead of the inhomogeneous due to speed difference. (Bottom Right): Pseudocolor plot of $u_1(x,t)$, obtained by subtracting the homogeneous solution from the inhomogeneous. The dark bands delineate the underlying homogeneous solution.

and subthreshold domains. This is illustrated in Figure 5.7. A closer look at the time evolution of the wave profile when the rippling is above threshold within the interior of the pulse shows that individual ripples are nonpropagating and transient, with new ripples appearing at the leading edge of the wave and subsequently disappearing at the trailing edge, see Figure 5.7. Interestingly, such behavior persists for large ρ when the ripples cross below threshold within the interior of the pulse, see Figure 5.8. Now the pulse actually consists of multiple bumps, each of which is nonpropagating but exists for only a finite length of time. The sequence of events associated with the emergence and disappearance of these bumps generates a wave envelope that behaves very much like a single coherent traveling pulse. Hence, for sufficiently short wavelength oscillatory modulations of the weight distribution, the transient multiple bump solution can be homogenized and treated as a single traveling pulse. However, the wave speed of the multiple bump solution differs from that predicted using perturbation theory. This is shown in Figure 5.9, where we compare the $\bar{c}$ vs. ε curves obtained using perturbation theory with data obtained by directly simulating the full system (5.1). In the case of small ρ, a stable (single bump) traveling pulse persists for all $\varepsilon,\ 0 \leq \varepsilon < 1$ and $\bar{c}$ is a monotonically decreasing function of ε. Moreover, the numerically calculated value of the average wave speed agrees quite well with the first–order perturbation analysis. On the other hand, for large values of ρ, such agreement no longer holds, and we find that the traveling pulse destabilizes at a critical value of ε that is well below the value predicted from the perturbation analysis.

In Figure 5.11 we compare the behavior of traveling pulses for short wavelength ($\varepsilon = 0.2$) and long wavelength ($\varepsilon = 0.9$) periodic modulation. The amplitude is taken to be relatively large, $\rho = 0.8$, so that multiple bump solutions occur. We see that for long wavelength modulation, the initial pulse transitions into a nonpropagating multiple bump solution, with successive bumps disappearing sequentially and no additional bumps being created; the failure to generate new bumps means that activity cannot propagate. We can see this more clearly when examining a series of snapshots of the pulse/bump profiles in Figure 5.12. In conclusion, one way to understand wave propagation failure for large ρ is to note that a large amplitude periodic weight modulation can generate a pinned multiple bump solution. However, in the absence of any inhibition such a multiple bump solution is unstable [99, 144]. In the case of small ε, destabilization of the bumps generates new bumps at the leading edge of the bump such that activity can propagate in a coherent fashion. Increasing ε prevents the creation of new bumps and propagation failure occurs.

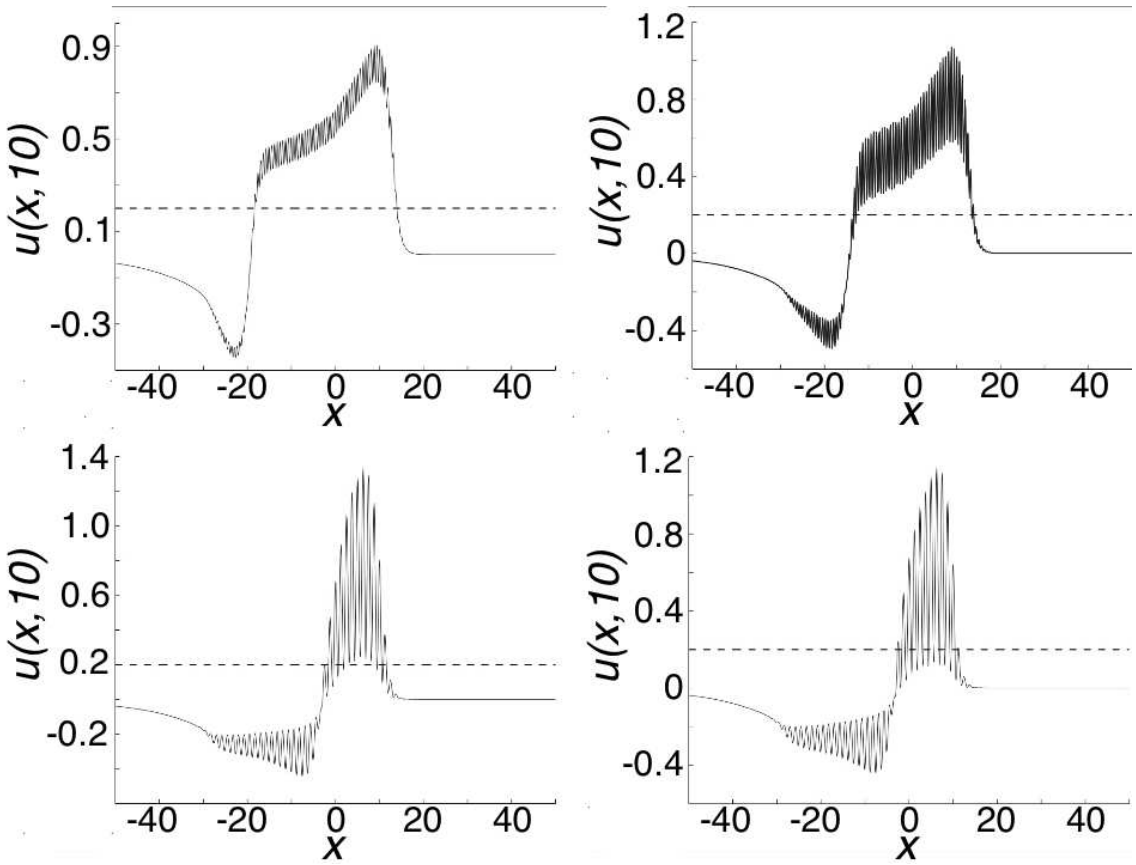

Figure 5.7. A collection of traveling wave profiles taken at time $t = 10$ for various amplitudes ρ and $\varepsilon = 0.1$. Other parameters as in Figure 5.5. (Top Left): $\rho = 0.1$. Notice that rippling of the activity does not dip below threshold within the pulse interior. (Top Right): $\rho = 0.3$. Rippling crosses below threshold at the edges of the pulse creating a couple of bumps. (Bottom Left): $\rho = 0.7$. Rippling now generates a multiple bump solution. (Bottom Right): $\rho = 0.8$.

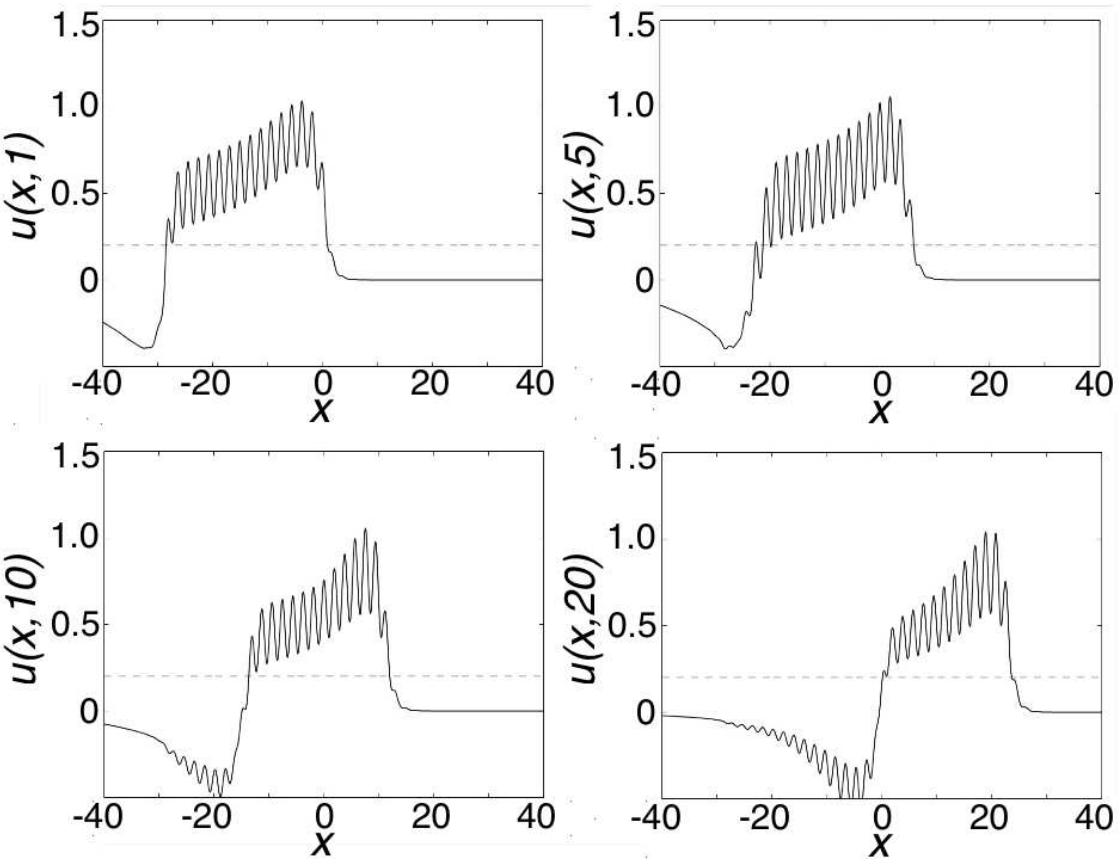

Figure 5.8. A series of snapshots in time of a traveling pulse for $\kappa = 0.2$, $\beta_p = 2.0$, $\alpha_p = 0.04$, $\rho = 0.3$, $\varepsilon = 0.3$. The interior of the pulse consists of nonpropagating, transient ripples. The disappearance of ripples at one end and the emergence of new ripples at the other end generates the propagation of activity. Notice that the solitary wave profile is not invariant, reflecting the underlying inhomogeneity. (Top Left): $t = 1$ (Top Right): $t = 5$ (Bottom Left): $t = 10$. (Bottom Right): $t = 20$.

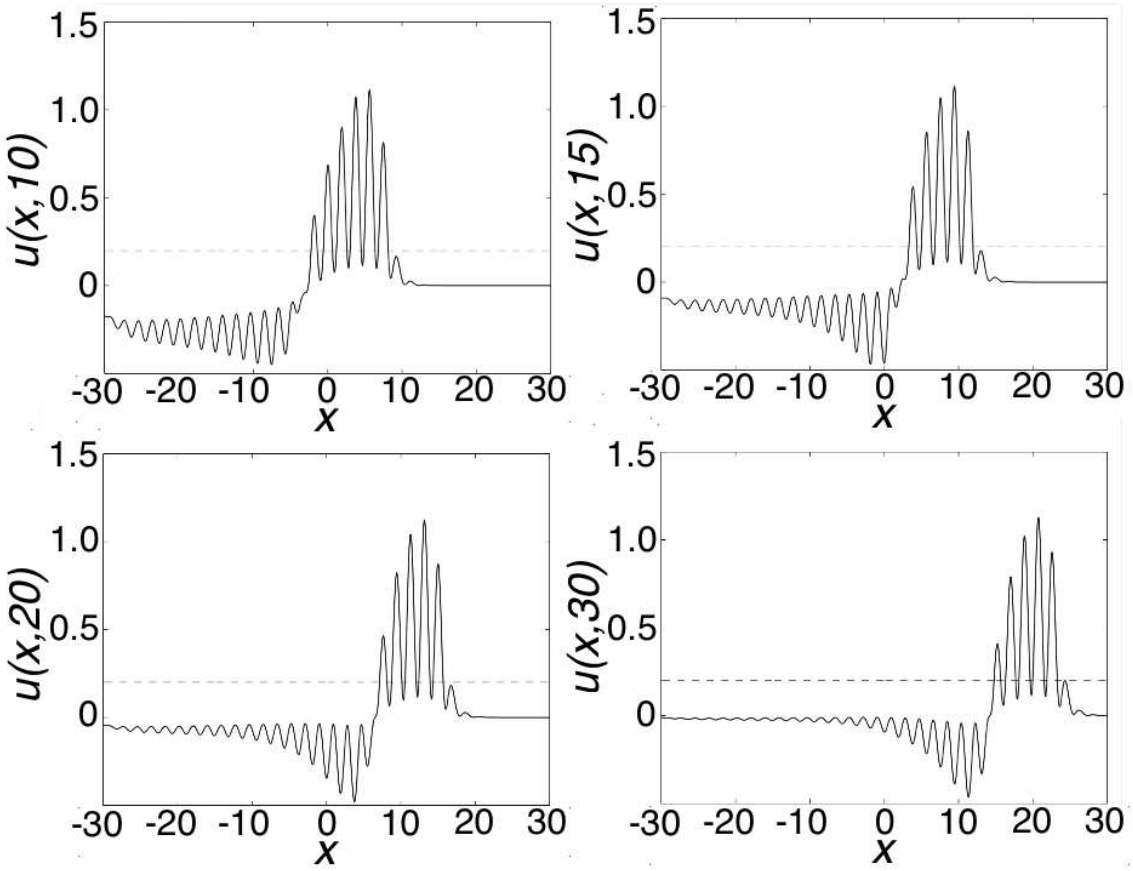

Figure 5.9. A series of snapshots in time of the "pulse" profile for $\kappa = 0.2$, $\beta_p = 2.0$, $\alpha_p = 0.04$, $\rho = 0.8$, $\varepsilon = 0.3$. The solitary pulse corresponds to the envelope of a multiple bump solution, in which individual bumps are nonpropagating and transient. The disappearance of bumps at one end and the emergence of new bumps at the other end generates the propagation of activity. Notice that the solitary wave profile is not invariant, reflecting the underlying inhomogeneity. (Top Left): $t = 10$ (Top Right): $t = 15$ (Bottom Left): $t = 20$. (Bottom Right): $t = 30$.

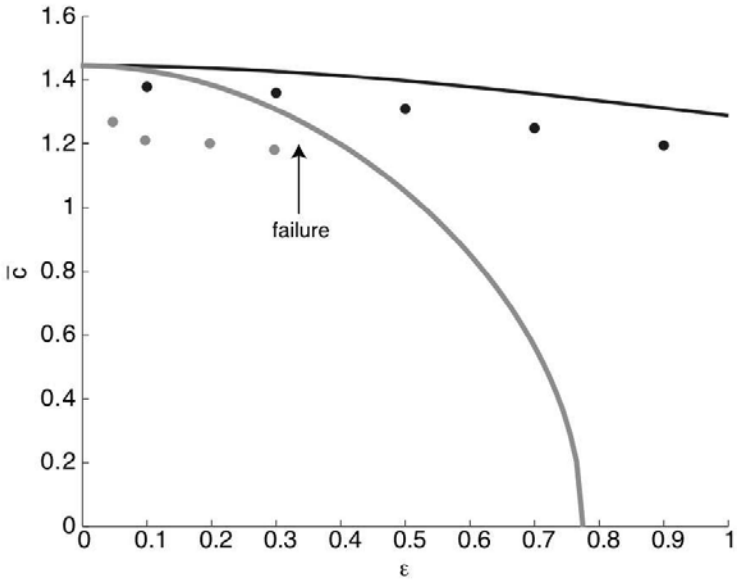

Figure 5.10. Comparison of perturbation theory with direct numerical simulations. Continuous curves show average wave speed $\bar{c}$ as a function of ε obtained using perturbation theory. Data points are the corresponding wave speeds determined from numerically solving equation (5.1). In the case of low amplitude modulation ($\rho = 0.3$, dark curve) a stable traveling pulse persists for all ε, $\varepsilon < 1$, whereas for large amplitude modulation ($\rho = 0.8$, light curve), wave propagation failure occurs as ε increases.

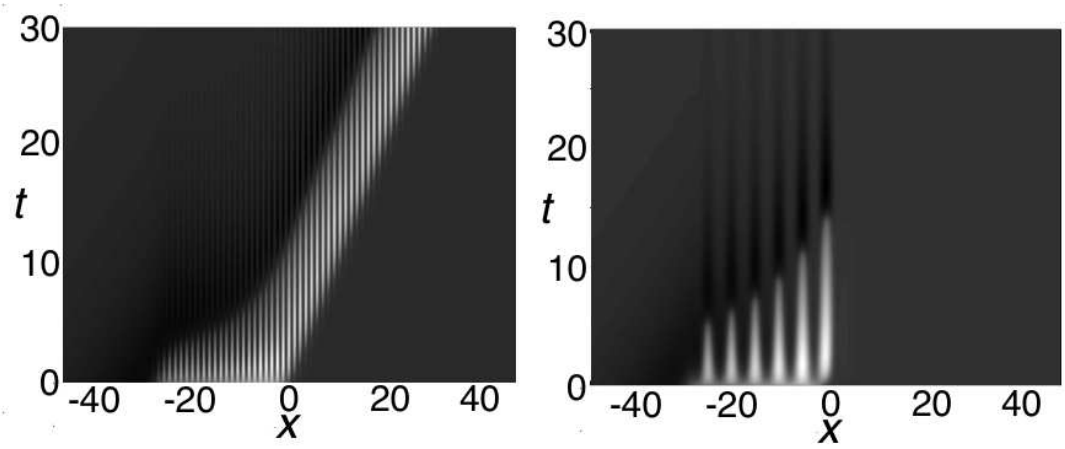

Figure 5.11. Comparison of traveling pulses in the case of short and long wavelength periodic modulation with $\rho = 0.8$ and all other parameters as in Figure 5.5. (Left): For short wavelength modulation ($\varepsilon = 0.2$) the traveling pulse shrinks and slows, but does not annihilate. (Right): For long wavelength modulation ($\varepsilon = 0.9$) wave propagation failure occurs. The initial pulse transitions into a collection of multiple equal width stationary bumps which are unstable.

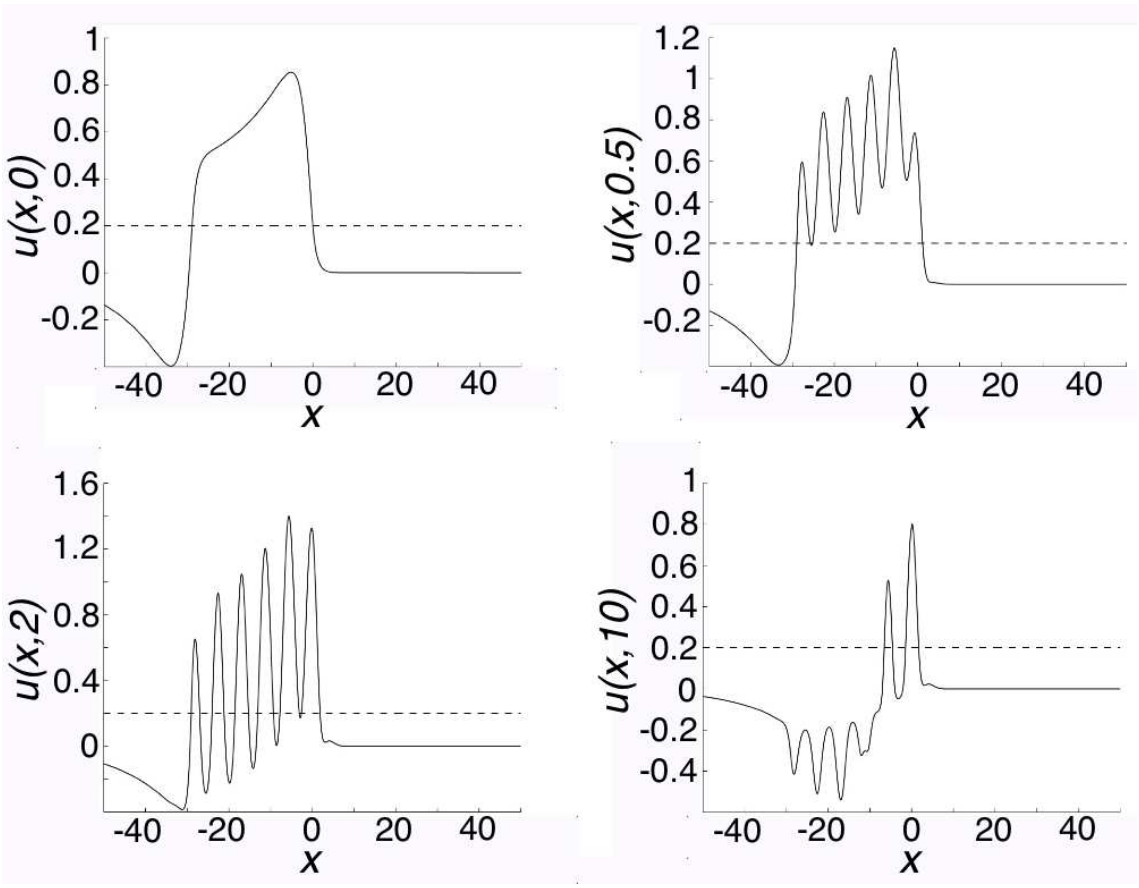

Figure 5.12. A series of snapshots in time of the "pulse" profile for the inhomogeneous network with $\kappa = 0.2$, $\beta_p = 2.0$, $\alpha_p = 0.04$, $\rho = 0.8$, $\varepsilon = 0.9$. (Top Left): The initial wave profile, which is taken to be the invariant wave profile U of the homogeneous network. (Top Right): Shortly after the simulation begins ($t = 0.5$), the interior of the pulse develops ripples such that the active region contains a subregion for which activity is subthreshold. (Bottom Left): At time $t = 2$ a multiple bump profile has emerged. We can really see here how a multiple bump solution, as defined by multiple neighboring standing profiles, emerges from the pulse profile of $t = 0$. (Bottom Right): Collapse of the pulse interior occurs due to the disappearance of the unstable bumps. Since no new bumps emerge, there is no propagating activity.

The effect of the periodic weight modulation on a different type of solution is illustrated in Figure 5.13, where, motivated by a prior numerical study of multiple bumps [99], the initial condition of the network is taken to consist of three bumps,

$$u(x,0) = \sum_{j=-1}^{1} \cos\left(\frac{x}{\varepsilon}\right) \exp\left(-\left(\frac{0.1(x-j\cdot 20)}{\varepsilon}\right)^2\right). \tag{5.55}$$

Each initial bump generates a pair of left and right moving fronts. In the homogeneous case, we see that collision of left and right moving waves results in a bidirectional front. That is, the region within the interior of the boundary formed by the two outermost fronts becomes superthreshold. In the inhomogeneous case, the collision of the waves is insufficient to maintain activity across this region, and one finds a pair of counter–propagating pulses.

5.5 Discussion

In this chapter we analyzed wave propagation in an excitatory neuronal network treated as a periodic excitable medium. The periodicity was introduced as an inhomogeneous periodic modulation in the long–range synaptic connections, and was motivated by the existence of patchy horizontal connections in cerebral cortex. We showed that for small

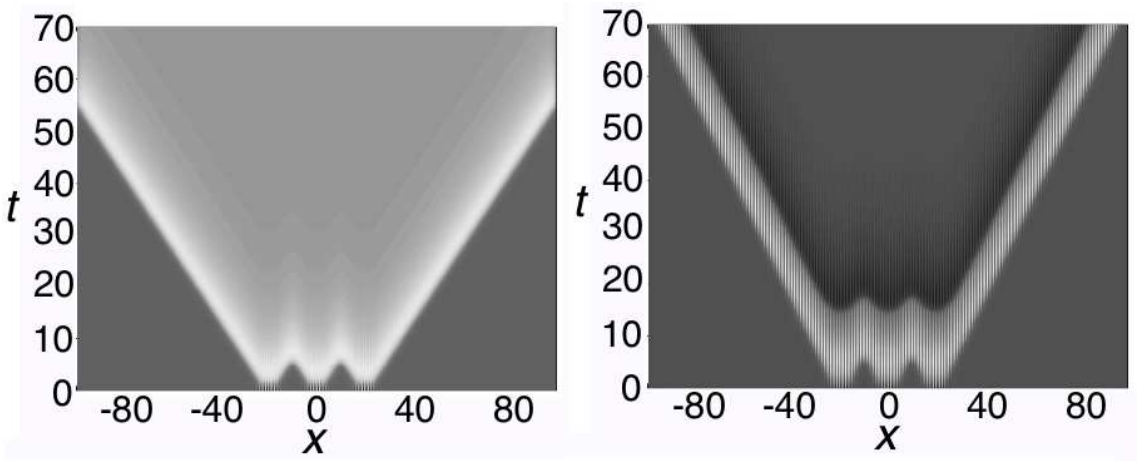

Figure 5.13. Traveling waves in homogeneous and inhomogeneous networks. (Left): In the case of a homogeneous network, a three bump initial condition evolves into a bidirectional front following the collision of left and right traveling waves. Parameters are $\kappa = 0.2$, $\beta_p = 2.0$, $\alpha_p = 0.04$. (Right): In the corresponding inhomogeneous network with $\varepsilon = 0.2$ and $\rho = 0.8$, the collision of left and right traveling waves results in a pair of counter–propagating pulses. Here the modulated synaptic interactions are insufficient to maintain activity in the region between the two pulses.

amplitude, short wavelength periodic modulation the main affect of the inhomogeneity is to slow down a traveling pulse, and the mean speed of the pulse can be estimated quite well using perturbation theory. In the case of large amplitude modulation, a stable traveling pulse still exists for sufficiently small ε, but now the pulse is the envelope of a multiple bump solution in which individual bumps are unstable and transient. Wave propagation arises via the appearance (disappearance) of bumps at the leading (trailing) edge of the pulse. As ε increases wave propagation failure occurs due to the fact that there is insufficient activity to generate new bumps.

Although the existence of multiple bump traveling "pulses" is interesting from a dynamical systems perspective, it is less clear whether such solutions can be observed in real neural tissue. Further experiments in cortical slice or *in vivo* as described in section 1.2 may reveal similar phenomena. One of the biological limitations of the integro–differential equations used in this and other studies is that although these equations support traveling waves that have speeds consistent with neurophysiology, the pulses tend to be too wide. That is, taking the range of synaptic connections to be $1mm$, the width of a stable pulse tends to vary between 5–30mm, see Figure 5.2, whereas waves in slices tend to be only $1mm$ wide [136, 139], see Figure 1.1. More realistic widths and wave speeds could be generated by taking the effective range of synaptic connections to be a few hundred μm, that is, by assuming that the predominant contribution to synaptic excitability is via local circuitry rather than via long–range patchy horizontal connections. However, inhomogeneities occurring at smaller spatial scales are unlikely to exhibit any periodic structure.

Irrespective of these particular issues, our analysis raises a more general point that would be interesting to pursue experimentally, namely, is it possible to detect the effects of network inhomogeneities by measuring the properties of traveling waves? Signatures of such inhomogeneities would include time–dependent rippling of the wave profile and variations in wave speed. However, such features may not be detectable given the current resolution of microelectrode recordings.

CHAPTER 6

FUTURE DIRECTIONS

Several additional research projects are suggested by the results of this dissertation. In particular, we have seen short–term synaptic plasticity can be a powerful mechanism for generating spatially structured activity in networks of neurons. Therefore, it behooves us to explore other forms of short–term synaptic plasticity (STSP) such as synaptic facilitation, the process by which synapses become stronger due to recurrent usage [169, 189]. Also, spike–timing–dependent–plasticity (STDP) is a mechanism of growing interest for both experimentalists and theoreticians in balancing activity, affecting sensory processes, and even for its role in pathology. It likely contributes to a great deal of cortical development and function, so it would also be worthwhile to pursue its study in networks of neurons [1]. Additionally, we could explore the effects of synaptic plasticity within the context of smaller networks ($2 - 10^3$) of spiking neurons. Such studies would indeed invite further interesting mathematical applications, like stochasticity and coupled oscillator theory. Also, with the use of more biophysically accurate models of neurons, we could address the effects of plasticity on sensory and motor processes at the single neuron level. Finally, we would like to study the effects of stochasticity in rate descriptions of large networks of neurons with synaptic depression. As we have shown, the inclusion of additive noise into the network can lead to dynamics not well predicted by the deterministic system. We could develop analytical tools for studying stochastic dynamics in networks with plasticity. We shall now discuss some of the future direction we plan to pursue.

6.1 Slow Oscillations in a Neuronal Network with Synaptic Facilitation

In this dissertation, we have studied many different forms of spatiotemporal activity that can arise within neuronal network models with short–term synaptic depression. Due to the depletion of resources within pre–synaptic boutons of active populations of neurons, synapses become less effective and excitatory activity is curtailed over time, resulting in

nonmonotonic dynamics. Short term synaptic facilitation is another plasticity process in which synapses become more effective over time. It is thought that this is due to calcium building up within the presynaptic cell, allowing the activation and release of more vesicles than the baseline level [189]. Since more neurotransmitter can be released, synaptic facilitation can lead to postsynaptic potentials tens of times greater than the original [88, 113]. Facilitation is activated over times roughly equal to the membrane time constant and has been shown to recover with a time constant 1–3s. With a slightly slower recovery time constant than synaptic depression, recent theoretical studies have proposed synaptic facilitation as a candidate mechanism for slow (0.1–1Hz) oscillations [66, 121].

Slow oscillations (0.1–1Hz) in neuronal firing rate arise spontaneously *in vivo* during sleep and reduced alertness [160, 117]. During sleep, both excitatory and inhibitory populations of the sensory, motor, and associational areas of the neocortex exhibit such slow oscillations. In fact, using electroencephalogram and magnetic resonance imaging, slow oscillations have been shown to propagate across the cortex as a traveling wave at about 1.2–7.0m/s [115]. High density EEG has shown that these waves have distinct cortical origins; they propagate across cortex and involve particular cortical structures [130]. The purpose of slow oscillations during sleep remains ambiguous, but they appear to play a role in homeostatically maintaining the balance of ionic currents and maintaining readiness for transitions to the aroused state [160]. Applying a slowly oscillating (0.75Hz) potential field to the scalp during slow wave sleep in human has been shown to improve potentiation of hippocampal declarative memory [114]. Learning tasks can even be invoked in localized regions of the neocortex, and performance can be improved by increased slow wave activity [70]. Phase–locking of slow oscillations between the neocortex and hippocampus is suggestive of its possible role in memory consolidation via plasticity [63]. Recent studies have shown partial or total sleep deprivation leads to increased slow wave activity in the following night [15]. Evidence suggests slow wave sleep is more than an epiphenomenon and is actually a sleep–regulating mechanism. Slow oscillations are often referred to as repetitive transitions between an Up state (where populations have a high firing rate) and Down state (where populations have a low firing rate) [63, 66, 6].

When neocortical slices are bathed in a medium mimicking extracellular ionic composition, slow wave oscillations are evoked both spontaneously and following glutamate stimuli [147, 146]. Isolated from other areas of the brain, slow oscillations persist due to bursts of reentrant excitation followed by longer periods of network activity failure. The

shut off of network excitation is likely due to some upregulation in inhibitory interneuron influence, since partially blocking slow inhibition with bicuculline increases the amplitude of the depolarized state. The slow oscillation also propagates horizontally along the slice at about 6–16mm/s in visual cortical slice and about 114mm/s in piriform cortical slices. Disparity between *in vivo* and *in vitro* wave speeds may result from removal of the slice from its intralayer connectivity structure.

Such robust oscillations must be sustained by a reliable mechanism that allows the transition from the Up to the Down state. In recent modeling studies, short–term synaptic plasticity has been shown to be a reliable mechanism with appropriate time constants for slow oscillations [169, 66, 121]. In particular, facilitating synapses from excitatory to inhibitory neurons behave as negative feedback that drives more inhibition when the firing rate of the excitatory population resides in the Up state. Once increased inhibition overwhelms excitation, all activity curtails to the Down state until the facilitating synapses return to their baseline utilization. Finally, low levels of excitation rekindle network activity to the Up state again [121]. Facilitation appears to be an ideal explanation as its recovery time constant is measured as 1–3s [166, 113, 156], roughly the inverse of the 0.1–1Hz frequency of slow oscillations. However, one necessary assumption has been persistent input to the network [121], whereas the slow oscillations appear to emerge spontaneously in experiment [147]. Also, as their network does not include space, one cannot observe whether oscillations generated as such will propagate or not.

Thus, we could consider a two population neuronal network model where synapses from excitatory to inhibitory populations are facilitating [169, 6, 121, 128]. Such a model allows us to study the effects of dynamic synapses in an excitatory–inhibitory network. The local level of facilitation here depends on the local firing rate $f(u)$ of the excitatory population. We take separate spatially extended excitatory and inhibitory populations, all coupled nonlocally [181]

$$\begin{aligned}\tau_e\frac{\partial u(x,t)}{\partial t} =& -u(x,t) + J_{ee}\int_{-\infty}^{\infty} w_e(x,x')f(u(x',t))\mathrm{d}x' \\ & - J_{ei}\int_{-\infty}^{\infty} w_i(x,x')f(v(x',t))\mathrm{d}x' + \eta_e(x,t) \qquad (6.1a)\\ \tau_i\frac{\partial v(x,t)}{\partial t} =& -v(x,t) + J_{ie}\int_{-\infty}^{\infty} w_e(x,x')p(x',t)f(u(x',t))\mathrm{d}x' + \eta_i(x,t) \qquad (6.1b)\\ \frac{\partial p(x,t)}{\partial t} =& \frac{\phi - p(x,t)}{\tau_f} + \gamma\phi(1-p(x,t))f(u(x,t)) \qquad (6.1c)\end{aligned}$$

Equation (6.1a) describes the evolution of the input $u(x,t)$ to the excitatory (e) evolving according to the time constant τ_e in the presence of connections between excitatory populations and feedback from the inhibitory population, via presynaptic firing rates $f(u)$ and $f(v)$. In equation (6.1b), the input $v(x,t)$ inhibitory population's (i) firing rate $v(x,t)$ evolves according to the time constant τ_i and is driven by the excitatory and inhibitory populations. The parameters $J_{\alpha\gamma} \geq 0$ denote the strength of connectivity from the γ–population to the α–population. For our study, we would initially ignore i to i connections, as they play a secondary role in the dynamics of the network. External random fluctuations to the input drives u and v are given by the spatially uncorrelated Gaussian white noise terms $\eta_e(x,t)$ and $\eta_i(x,t)$ respectively. Input from the excitatory to the inhibitory population is facilitating through the dynamic variable $p(x,t)$ that evolves according to equation (6.1c). The factor $p(x,t)$ can be interpreted as the fraction of synaptic resources currently being utilized [169], which is increased at a rate $\gamma\phi(1-p)f$ and returns to baseline fraction ϕ according to the time constant τ_f (experimentally shown to be 1–3s [113, 169, 166, 156]).

With such a model in hand, we propose to study a variety of spatiotemporal dynamics in a network with facilitating synapses from the excitatory to inhibitory populations, paying particular attention to slow oscillations. As facilitation occurs on a slower timescale than depression, we ignore effects of a dynamic depression variable in this study, and qualitative results are essentially unchanged. In the case of a linear threshold firing rate function, it has been shown the space–clamped version of such a network supports limit cycles as in [121], in the presence of an input. With this in mind, we may be able to carry out a phase reduction of the slow oscillation in the space–clamped system to project the system to a single variable. Thus, we might study the propagation of slow oscillations within a spatially extended network with synaptic facilitation as a network of coupled oscillators. In addition, we might use some of the analytical techniques to study the system in the case of a Heaviside firing rate function (1.4). It is likely that such a system will support bumps, pulses, and possibly even Turing patterns. We could then use linear stability analysis to see if any such time invariant states might destabilize to oscillatory solutions. The piecewise smooth stability analysis of standing bump solutions (section 2.2) would also be useful because the network with facilitation will have jump discontinuities in the facilitation variable. Finally, we could corroborate our results with numerical simulations of the full network for a variety of firing rate functions and parameters.

6.2 Spiking Networks with Synaptic Plasticity

In this dissertation, we have analyzed many of the effects of including synaptic depression in rate models of neuronal networks. However, many important phenomena of the brain involve dynamics that occur on finer spatial and temporal scales that cannot be reached by large scale rate approximations. Thus, we shall discuss ways of including synaptic plasticity into models of spiking neurons. As opposed to the rate models we have studied throughout this dissertation, spiking networks can be used to study many of the short–time, individual neuron dynamics that occur within the brain [89, 1]. Since these models intend to assign an equation to individual neurons, there is not the loss of detailed spike timing information that occurs through spatial averaging. There have been few studies of the role of plasticity in sensory processes of the brain to this point [45, 172]. Some minimal theory has been developed with regard to how plastic synapses may affect synchrony in spiking networks of neurons [75, 110, 35]. Therefore, we propose to carry out detailed analyses to derive biophysically appropriate models of spiking neurons with plasticity, study the various spatiotemporal activity of networks of such neurons, and apply our findings to some sensorimotor systems within the brain.

Two types of synaptic plasticity have been strongly implicated in the sub–second dynamics observed in sensory systems: short–term synaptic plasticity and spike–timing–dependent plasticity. As we have discussed so far in this dissertation, short–term synaptic plasticity (STSP) modifies the availability of resources in presynaptic cells, resulting in changes to the strength of synapses that last a few seconds. Specific forms of STSP are depression (see Chapters 2, 3, and 4), which weakens synaptic coupling, and facilitation (see section 6.1), which strengthens synaptic coupling [189]. Synchronization of central pattern generators used in locomotion [131] and the extraction of properties of visual stimuli [34] are both known experimentally to utilize STSP. Spike–timing–dependent plasticity (STDP) describes a change to the strength of a synapse that depends on the relative timing of presynaptic and postsynaptic spikes. Usually for excitatory synapses, if the presynaptic arrives before the postsynaptic spike, there is a relative strengthening in the synapse between the two cells. If the presynaptic arrives after the postsynaptic spike, a relative weakening in synaptic strength occurs. In some inhibitory cells, strengthening occurs regardless of the ordering of spikes. Evidence suggests STDP arises mostly from the modification of ion channels by intracellulular calcium [45]. Due to its submillisecond timescale precision, STDP is a well utilized mechanism of sensation [59]. Spike–timing–dependent plasticity can

modify receptive fields in visual cortex [123], resolve fine timing of auditory signals in the dorsal cochlear nucleus [172], and adapt place cells in the hippocampus [120]. Since synaptic plasticity can have such a strong influence on the neural processes of sensation, it will be quite useful to understand the many characteristics of neuronal networks with synaptic plasticity from a mathematical perspective. Thus we propose to develop mathematical models of neural oscillations in networks with plastic synapses and apply these models to sensory processing in the olfactory and auditory systems.

We shall begin by developing a new model that represents the qualitative dynamics of a network of spiking neurons whose synapses are subject to plasticity. Rather than modeling the detailed spike generation process of spiking neurons, theoretical studies often represent them using the integrate–and–fire model, employing the capacitive nature of the cell membrane. Specifically, the quadratic integrate–and–fire model is convenient as it has no hard threshold, contains intrinsic dynamics of a spike, and represents the normal form of any neuron exhibiting a saddle–node on a limit cycle bifurcation [90]. Applying a change of variables to the quadratic integrate–and–fire model makes its behavior more transparent, leading to the theta model

$$\frac{\mathrm{d}\theta}{\mathrm{d}t} = \omega(1-\cos(\theta)) + \eta(1+\cos(\theta)). \tag{6.2}$$

Thus, the neuron or oscillator is described in terms of a phase variable that lies between $-\pi$ and π. Each time $\theta = \pi$, the full model fires a spike. The constant η is proportional to any current, applied or synaptic. Thus, a network of N synaptically coupled neurons can be modeled using the theta model, where the coupling term $\eta = I + s$ involves an applied plus a dynamically changing synaptic component as

$$\frac{\mathrm{d}\theta_i}{\mathrm{d}t} = \omega_i(1-\cos(\theta_i)) + \eta_i(1+\cos(\theta_i)), \tag{6.3}$$

$$\frac{\mathrm{d}s_{ij}}{\mathrm{d}t} = -\tau_{ij}s_{ij} \qquad (j \neq i), \tag{6.4}$$

where $i = 1, ..., N$; $\eta_i = I(t)_i + \sum_{j\neq i}\alpha_j s_{ij}$; $\alpha_j \in [-1, 1]$ determines an excitatory or inhibitory strength of connection; and s_{ij} is reset to k_{ij} every time θ_j reaches π [49, 17]. Thusfar, such models have been used to study traveling waves [132, 143], standing bumps [144], synchrony [49], and gamma rhythms [17, 16]. A major extension of this model would be to explore the effects of dynamically varying k_{ij} according to various synaptic plasticity dynamics [169, 159, 75, 110].

A first research direction will be to perform a phase reduction on augmented equations that include proper forms for synaptic plasticity's dependence on ionic currents or the

membrane potential of neurons. This may lead to a phase oscillator that does not represent the normal form of a saddle–node on a limit cycle bifurcation. Therefore, we may find bifurcations and dynamics that are novel to reduced models of spiking neurons. There are a number of descriptive models of the electrophysiology of spikes in a single neuron, and we will develop conditions on the form of the spiking mechanism and plasticity that lead to certain bifurcations.

Otherwise, we will heuristically include resource dependent synaptic facilitation and/or depression in the model by assigning $k_{ij} = p_i q_i/\phi$, along the lines of [169, 121], and introducing the additional equations

$$\frac{\mathrm{d}p_i}{\mathrm{d}t} = \frac{\phi - p_i}{\tau_f} + \beta\phi(1-p_i)\psi(\theta_i), \tag{6.5}$$

$$\frac{\mathrm{d}q_i}{\mathrm{d}t} = \frac{1-q_i}{\tau_d} - \gamma p_i \psi(\theta_i), \tag{6.6}$$

where τ_f and τ_d represent the time constants of synaptic depression and facilitation respectively; β and γ are the strengths of facilitation and depression; ϕ is the baseline utilization of the synapse; and ψ is a non–negative function with a sharp maximum close to $\theta_i = \pi$, normalized to unity. Each spike of the theta model will kick the facilitation and/or depression variable, effectively scaling the weights between phase oscillators in the network. Depending on parameters, facilitation and depression may compete or one mechanism may dominate.

In addition, spike–timing–dependent plasticity (STDP) can be modeled as an abrupt change to the synaptic weight k_{ij} for every single pairing of a presynaptic spike $\theta_j = \pi$ and postsynaptic spike $\theta_i = \pi$ that occur at times t_j and t_i respectively. Based on previous experimental studies, the change to the synapse strength depends on the relative spike timing $\Delta t = t_i - t_j$ according to [11, 159]:

$$\Delta k_{ij}(\Delta t) = \begin{cases} \kappa_+ \mathrm{e}^{-\Delta t/\tau_+}, & \Delta t \geq 0, \\ -\kappa_- + \mathrm{e}^{\Delta t/\tau_-}, & \Delta t < 0, \end{cases} \tag{6.7}$$

where κ_+ (κ_-) is the strengthening (weakening) rate for positive (negative) Δt that occurs with time constant τ_+ (τ_-). To analytically study this model, we will use the assumption that changes to synaptic strength due to plasticity are slow compared to the spiking dynamics. Thus, they can be approximately calculated using the phase difference, $\Delta\theta_{ij} = \theta_i - \theta_j$, at each spike according to

$$\frac{\mathrm{d}k_{ij}}{\mathrm{d}t} = \kappa(\delta(\theta_i - \pi)) \begin{cases} (k_{max} - k_{ij})\mathrm{e}^{\Delta\theta_{ij}/\tau_+}, & \Delta\theta_{ij} \in (-\pi, 0], \\ -k_{ij}\mathrm{e}^{-\Delta\theta_{ij}/\tau_-}, & \Delta\theta_{ij} \in (0, \pi], \end{cases} \tag{6.8}$$

where κ scales the strength of STDP. Global synchronization has recently been studied in a network with STDP, but without short–term synaptic plasticity [75, 110]. Major extensions would be to study clustered states within the network, spatiotemporal dynamics, and global synchronization as influenced by either form of plasticity. Utilizing perturbation theory, phase resetting curves, and other techniques, we will analyze the existence and stability of the many possible states of the network.

With a well developed model in hand, we could then study the wide range of different synchronous firing patterns in our spiking network with plasticity. Global synchronization is a well studied problem in phase models, employing many different analytic techniques [163]. Adapting previous methods to our model, we will derive an order parameter for the level of synchronization in the network to give a clear cut bound for parameter values at which global synchrony is possible [91]. Stability will then be calculated by linearizing about each predicted state. Certainly, synaptic plasticity could modify conditions under which networks synchronize to particular frequency rhythms. Following a study of global synchrony, we will derive conditions on the physiological parameters that would ensure rotating waves, clustered states, or spiral waves. Since the strength of connections in our proposed network will be variable, we will use past methods to see how plasticity may bring the network in and out of coherent firing. We will also employ dimension reduction techniques to study variations in spatiotemporal dynamics in phase models with plasticity [94]. Additionally large but finite networks of phase oscillators have been recently analyzed using kinetic theory, where the states of the network are examined through a probability distribution [29]. Stochastic methods will be useful in analyzing the correlation of physiological parameters to the stability of synchronous firing in plastic networks, considering the small number of quanta involved in synaptic transmission.

Finally, with extensive knowledge of the dynamics supported by plastic networks of spiking neurons, we could study the importance of plasticity in networks for sensory processing. Guided by experimental data, we will use our model to study specific sensory systems. Specifically, we could study how the mitral cells of the olfactory lobe utilize STSP for proper coding [150]. Also, we could follow up on recent experimental work regarding STDP's role in audition. In particular, it would be valuable to study the problem of tinnitus, a ringing in the ears, that develops, possibly by an excess of STDP [171]. Varying $I(t)_i$ in ways similar to sensory input and studying the various stable solutions that result in the network will give insight as to the mechanisms for coding and long term changes

in sensory networks. We may learn more mechanisms that underpin the neural substrates of human experience. Framing this in a network amenable to mathematical analysis will allow us to extract general properties regarding how well certain networks handle sensory coding.

6.3 A Stochastic Neural Field with Synaptic Depression

Recently, there has been a great deal of interest in developing stochastic descriptions of neural fields [23, 30]. This allow one to model the higher order statistics of large networks of neurons such as the correlations between firing rates at different cortical locations. The models we have presented so far in this dissertation cannot describe the dynamics of these correlations. A recently proposed method of deriving stochastic neural field models is to describe the dynamics of a network by a master equation whose mean–field limit is the deterministic rate model of interest. The equations associated with the higher moments of the process can then be derived using a path integral approach from statistical physics [29, 30] or a system–size expansion [173, 23]. The moment hierarchy can then be truncated, as long as the system is not operating close to criticality. Thusfar, analyses of stochastic neural field theory have not included any local form of negative feedback but have only considered equations for the evolution of the firing rate of the neural units themselves. We plan to study the effects of including synaptic depression in such stochastic models of neural fields.

Thus, we shall construct a master equation for an appropriate Markov process, which reduces to a model of a neuronal network with resource dependent synaptic depression, as described in section 3.1 as well as in [169, 164]. To accomplish this, we will need a way to appropriately describe the stochastic evolution of such a system in this context. In [23], the number of neurons in each subpopulation is taken to be large but finite, and thus the inverse of this can be used to generate a hierarchy of moment equations as in Van Kampen [173]. In the spirit of this formalism, we shall consider a finite number of vesicles full of neurotransmitter in each subpopulation. Therefore, we can study stochastic effects within the resource pool in a similar way to that in the neural activity variable.

Initially, we need not consider the effects of spatial extension in our model. We can begin by studying stochastic oscillations in an excitatory neuronal network with synaptic depression. As we found in section 3.1.3, additive noise driving the input current of a space–clamped model can generate self–sustained oscillations in parameter regimes where

the deterministic system does not support limit cycles. These oscillations can even be quite regular, exhibiting coherence resonance [107]. It would be interesting to study the formation of oscillations in the neuronal network with synaptic depression as described by a Markov process. Then, using techniques of the system size expansion, we could determine how higher order statistics like correlations may destablize steady states of the mean field model to limit cycle oscillations. It would also be interesting to compute, if possible, the optimal system size for the most regular oscillations. With such information in hand, we could then move to an analysis of the spatially extended system to examine how noise may generate spontaneous traveling waves within the network, break the symmetry of deterministic solution like target waves, and even give rise to spiral waves. In doing such analyses, we would be able to gain insight about a great deal of noise–induced phenomena in neuronal networks with synaptic depression that escapes our current deterministic treatment.

APPENDIX A

AMARI'S STANDING BUMP ANALYSIS

In sections 2.2, 3.3, and 4.3 and Appendix B, we examine the existence and stability of standing bumps in piecewise smooth neural fields with nonlinear adaptation. Therefore, it is useful for us to review here the analysis of existence and stability of bumps in the scalar neural field (1.3) with $f = \Theta$, the Heaviside function, as was developed by Amari [3]. Equilibrium solutions of equation (1.3) satisfy

$$U(x) = \int_{-\infty}^{\infty} w(x - x')H[U(x') - \theta]dx'. \tag{A.1}$$

Let $R[U] = \{x|U(x) > \theta\}$ be the region over which the field is excited or superthreshold. Equation (A.1) can then be rewritten as

$$U(x) = \int_{R[U]} w(x - x')dx'. \tag{A.2}$$

Exploiting the fact that any solution can be arbitrarily translated so that it is centered at the origin, we define a stationary pulse solution of half–width a to be one that is excited over the interval $(-a, a)$. Let

$$W(x) = \int_0^x w(y)dy \tag{A.3}$$

and

$$W_m = \max_{x>0} W(x), \quad W_\infty = \lim_{x\to\infty} W(x) \tag{A.4}$$

such that $W(0) = 0$ and $W(-x) = -W(x)$. For a bump of half–width a, equation (A.2) reduces to the form

$$U(x) = W(a + x) - W(x - a). \tag{A.5}$$

Since $U(\pm a) = \theta$ by definition, we obtain the following necessary condition for the existence of a bump:

$$W(2a) = \theta. \tag{A.6}$$

This condition is also sufficient for a Mexican hat weight distribution [3]. It will be shown below that a bump is stable provided the condition $W'(2a) < 0$ is satisfied. The

existence and stability of activity bumps for a given θ can thus be determined graphically as illustrated in Figure A.1(b). For a certain range of values of $\theta > 0$ one finds bistability between a stable bump and a uniform rest state, $U(x) = 0$ for all $x \in \mathbf{R}$, with an unstable bump acting as a separatrix between these two solutions.

The linear stability of a stationary pulse can be determined by setting $u(x,t) = U(x) + \epsilon\psi(x,t)$ and expanding to first order in ϵ [137, 55, 41]. This leads to the eigenvalue equation

$$\psi_t(x,t) + \psi(x,t) = \int_{-\infty}^{\infty} w(x-x')\delta(U(x'))\psi(x')dx', \tag{A.7}$$

where δ is the Dirac delta distribution. Using the identity in the distribution sense

$$\delta(U(x)) = \left(\frac{\delta(x-a)}{|U'(a)|} + \frac{\delta(x+a)}{|U'(-a)|}\right), \tag{A.8}$$

and setting $|U'(a)| = U'(-a) = \gamma^{-1}$, we obtain the linear equation

$$\psi_t(x,t) + \psi(x,t) \quad = \quad \gamma(w(x-a)\psi(a,t) + w(x+a)\psi(-a,t)). \tag{A.9}$$

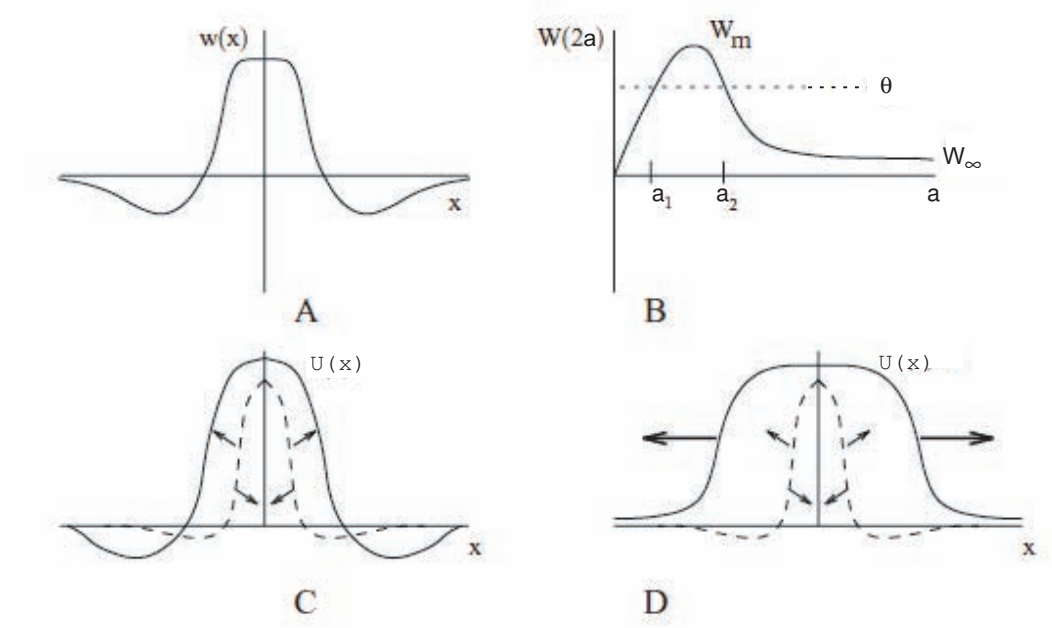

Figure A.1. Construction of a solitary pulse in the Amari model. (a) A Mexican hat weight distribution w. (b) Integral $W(x)$ of $w(x)$. Horizontal line shows the threshold θ whose intersections with $W(2a)$ determine the allowed stationary pulse solutions. If $W_\infty < \theta < W_m$ then there exists an unstable bump of half–width a_1 and a stable bump of half–width a_2. On the other hand, if $0 < \theta < W_\infty$ then there only exists an unstable bump.(c) Unstable bump (broken) acting as a separatrix between a stable bump and the uniform rest state. (d) For $0 < \theta < W_\infty$ the solitary unstable bump acts as a separatrix between a wavefront and the rest state. Adapted from [50].

Consider separable solutions of the form $\psi(x,t) = \mathrm{e}^{\lambda t}\psi(x)$, where $\psi(x)$ is a bounded and continuous function on $\mathbb{R}$ that decays to zero exponentially as $x \to \pm\infty$. Substitution of this solution into the linear equation leads to the eigenvalue problem

$$(\lambda+1)\psi(x) = \gamma\left(w(x-a)\psi(a) + w(x+a)\psi(-a)\right). \tag{A.10}$$

Following Guo and Chow [62], we define the operator $\mathcal{L} : \mathcal{C}[-a,a] \to \mathcal{C}[-a,a]$ according to

$$\mathcal{L}\psi(x) \quad = \quad \gamma(w(x-a)\psi(a) + w(x+a)\psi(-a)) \tag{A.11}$$

so that the eigenvalue problem becomes

$$(\lambda+1)\psi(x) \quad = \quad \mathcal{L}\psi(x) \quad \text{ on } \quad \mathcal{C}[-a,a]. \tag{A.12}$$

It can then be shown that [62] (i) $\mathcal{L}$ is a compact linear operator with respect to standard norms such as L^p, (ii) the eigenvalues λ are real, and (iii) $\lambda = -1$ is the only possible accumulation point of the eigenvalues. Hence, the only possible essential spectrum of the operator $\mathcal{L}$ is located at $\lambda = -1$ (spanned by functions $\psi(x)$ that vanish at all boundary points $\psi(\pm a) = 0$), implying that the discrete spectrum of $\mathcal{L}$ determines all of the linear stability properties of the bump solution. The eigenvalues can be obtained by setting $x = \pm a$ in equation (A.10):

$$(\lambda+1)\psi(a) \quad = \quad \gamma\left(w(0)\psi(a) + w(2a)\psi(-a)\right) \tag{A.13}$$

$$(\lambda+1)\psi(-a) \quad = \quad \gamma\left(w(-2a)\psi(a) + w(0)\psi(-a)\right). \tag{A.14}$$

This has the solutions $\psi(-a) = \pm\psi(a)$ with corresponding eigenvalues

$$\lambda_\pm = -1 + \gamma(w(0) \pm w(2a)). \tag{A.15}$$

Finally, using the fact that $\gamma^{-1} = w(0) - w(2a)$ we deduce that $\lambda_- = 0$ (reflecting the translation invariance of the system) and $\lambda_+ = 2\gamma w(2a)$. Thus the bump is stable provided that $w(2a) = W'(2a) < 0$.

Note that once the eigenvalues λ have been found, the corresponding eigenfunctions $\psi(x)$, $x \in \mathbb{R}$ are determined completely in terms of the perturbations $\psi(\pm a)$ and the weight distribution $w(x)$, see equation (A.10). This explains why it is also possible to analyze the stability of the bumps by restricting attention to the effects of perturbations at the boundaries of the activity bump as originally formulated [3]. In particular, if $\Delta_+(t)$

denotes a perturbation in the position of the right–hand edge of the bump so that $u(x,t) = \theta$ at $x = x + a + \epsilon\Delta_+(t)$, then

$$\begin{aligned}\theta &= U(a + \epsilon\Delta_+(t)) + \epsilon\psi(a + \epsilon\Delta_+(t), t) \\ &= U(a) + \epsilon U'(a)\Delta_+(t) + \epsilon\psi(a,t) + \mathcal{O}(\epsilon^2),\end{aligned}$$

that is,

$$\Delta_+(t) = \gamma\psi(a,t) \tag{A.16}$$

since $U(a) = \theta$ and $U'(a) = -\gamma^{-1}$. Similarly, the shift $\Delta_-(t)$ of the left–hand edge satisfies

$$\Delta_-(t) = -\gamma\psi(-a,t). \tag{A.17}$$

It follows that the eigenmode $\psi(-a,t) = \psi(a,t)$ generates a uniform expansion or contraction of the bump ($\Delta_- = -\Delta_+$) whereas $\psi(-a,t) = -\psi(a,t)$ generates a shift in the center of the bump ($\Delta_- = \Delta_+$).

APPENDIX B

STABILITY OF BUMPS IN A PIECEWISE SMOOTH NEURONAL NETWORK WITH ADAPTATION

In this appendix, we analyze the existence and stability of stationary bumps in a neuronal network with spike frequency adaptation. Spike frequency adaptation is the process by which a neuron's firing rate decays to a submaximal level, occurring when a hyperpolarizing potassium current is activated via intracellular calcium [9, 162]. Since increases in adaptation current are subtractive terms entering the sum total of all currents driving a population, they can be equivalently thought of as increases in the threshold required for a nonzero population firing rate. This phenomenon was recently incorporated into the scalar neuronal network (1.3) by introducing a dynamic threshold into the firing rate function, so that on setting $f = \Theta$ we have [42, 43]

$$\frac{1}{\alpha}\frac{\partial u(x,t)}{\partial t} = -u(x,t) + \int_{-\infty}^{\infty} w(x-x')\Theta(u(x',t) - h(x',t))\mathrm{d}x', \tag{B.1a}$$

$$\frac{\partial h(x,t)}{\partial t} = -(h(x,t) - h_0) + \kappa\Theta(u(x,t) - \theta). \tag{B.1b}$$

The threshold $h(x,t)$ increases from its baseline value h_0 to a maximum of $h_0+\kappa$, when the input drive $u(x,t)$ is above θ. In keeping with previous analyses of this model, we require the threshold parameters satisfy $h_0 < \theta < h_0 + \kappa$. However, derivations of firing rate models with spike frequency adaptation from detailed conductance based models suggest that taking $h_0 = \theta$ is more physiologically reasonable [9]. The time constant α quantifies the ratio between synaptic input dynamics and adaptation dynamics. In order to make a direct comparison with Coombes and Owen [42, 43], we take a Mexican hat weight function of the form

$$w(x) \quad = (1 - |x|)\mathrm{e}^{-|x|}. \tag{B.2}$$

Existence of Bumps

A stationary bump solution $(U(x), H(x))$ of (B.1) satisfies

$$U(x) = \int_{-\infty}^{\infty} w(x-x')\Theta(U(x')-H(x'))\mathrm{d}x', \tag{B.3}$$

$$H(x) = h_0 + \kappa\Theta(U(x)-H(x)). \tag{B.4}$$

We restrict ourselves to examining single bumps that satisfy the threshold conditions

$$U(\pm a) = h_0+\kappa, \quad U(\pm b)=\theta, \quad U(\pm c)=h_0, \tag{B.5}$$

where $a < b < c$. As opposed to bumps in the scalar and depressing networks, the stationary bump solution here will have a disconnected excited region for U, $R[U] = (-c,-b)\cup(-a,a)\cup(b,c)$, and a different excited region for H, $R[H]=(-b,b)$ so that

$$U(x) = \left(\int_{-c}^{-b} + \int_{-a}^{a} + \int_{b}^{c}\right) w(x-x')\mathrm{d}x'. \tag{B.6}$$

An example of such a bump is shown in Figure B.1. This should be contrasted with multibump solutions, whose activity in in excess of a homogeneous threshold over several disconnected subdomains [99, 98, 133]. For the Mexican hat weight function (B.2), we can explicitly evaluate the integrals in (B.6) to yield

$$U(x) = g(x+c)-g(x+b)+g(x+a)-g(x-a)+g(x-b)-g(x-c), \tag{B.7}$$

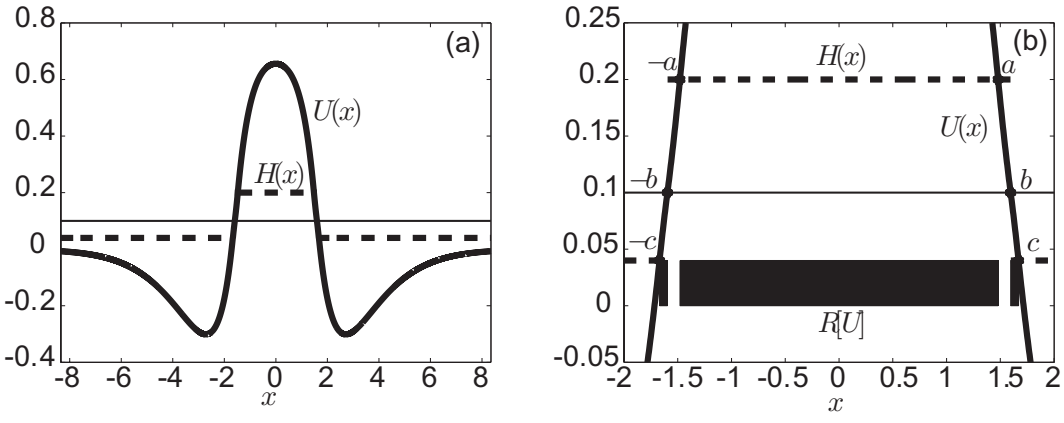

Figure B.1. Stationary bump in a network with spike frequency adaptation.(a) Bump solution $(U(x), H(x))$ with $h_0 = 0.04$, $\theta = 0.1$, and $\kappa = 0.16$. Here $a = 1.48$, $b = 1.60$, and $c = 1.67$. (b) Zoomed in version of the excited region $R[U]$, showing all of the threshold crossings at $x = \pm a, \pm b, \pm c$. Adapted from [42, 43].

where $g(x) = xe^{-|x|}$. Also note

$$H(x) = \begin{cases} h_0 + \kappa, & |x| > b, \\ h_0, & |x| < b, \end{cases} \tag{B.8}$$

implying that, as in the case of the network with depression, the negative feedback variable here will have a jump discontinuity. Applying the bump threshold conditions (B.5) to (B.7), we arrive at an implicit system relating the bump half–widths a, b, c to all other parameters

$$\begin{aligned} g(a+c) - g(a+b) + g(2a) + g(a-b) - g(a-c) &= h_0 + \kappa, \\ g(b+c) - g(2b) + g(b+a) - g(b-a) - g(b-c) &= \theta, \\ g(2c) - g(c+b) + g(c+a) - g(c-a) + g(c-b) &= h_0. \end{aligned} \tag{B.9}$$

The system of transcendental equations (B.9) can be solved numerically using a root finding algorithm. The variation of pulse width with the parameters κ and h_0 is shown in Figure B.2. The stability of the bumps is calculated below.

Stability of Bumps

As in the case of networks with synaptic depression such as the system (2.36), the Evans function approach to analyzing the stability of bumps breaks down in the high–gain limit due to the vanishing small domain over which linearization is applicable (see section 2.2.3). The construction of the Evans function for traveling pulses can still be carried out,

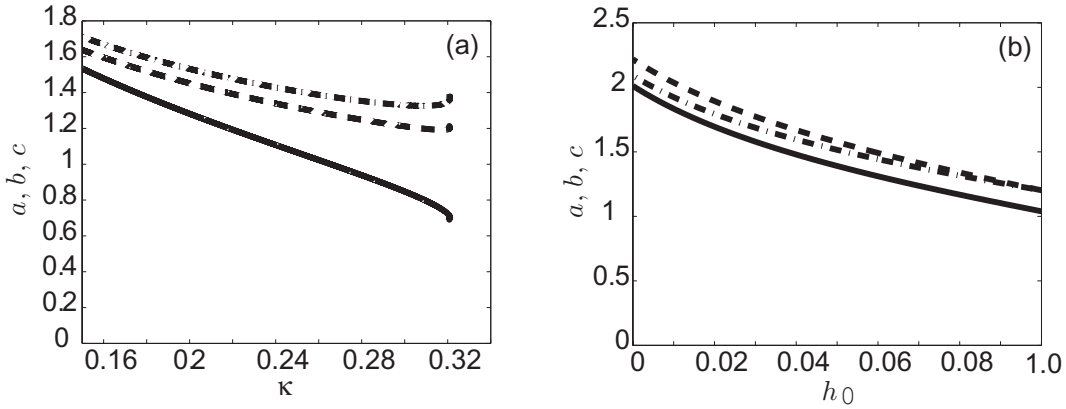

Figure B.2. Bump width dependence on strength and baseline of spike frequency adaptation. (a) Plot of bump half–widths versus κ for $\theta = 0.1$ and $h_0 = 0.04$. The bump solution exists for $\kappa < \kappa_c \approx 0.32$. (b) Plot of bump half–widths versus h_0 for $\theta = 0.1$ and $\kappa = 0.16$. The bump solution exists for $h_0 > h_c \approx 0$.

however [42, 43]. Therefore, we will proceed by considering infinitesimal perturbations of the piecewise smooth system (B.1). As we show below, there are some subtle differences between the stability analysis of the system (B.1) as compared with the system (2.36), in section 2.2.4. First, we will not be able to make a change of variables in order to smooth the dynamics of the perturbation in the h variable, as we were able to do in the case of the depression variable q. Therefore, the linear stability equations we derive here will not reflect the underlying translation invariance of the system. Also, as opposed to the depression network, when bumps are unstable, linear stability of the adapting network becomes a very poor approximation to the full system's dynamics soon after perturbations begin to evolve. This is due in part to the fact that u quickly ceases to intersect h at the same number of points as the stationary solution (see Figure B.3).

Let us set $u(x,t) = U(x) + \varepsilon\psi(x,t)$ and $h(x,t) = H(x) + \varepsilon\varphi(x,t)$ with ψ, φ smooth perturbations and $\varepsilon \ll 1$. Substituting into the full system (B.1) and imposing the stationary bump solutions (B.3) and (B.4) gives

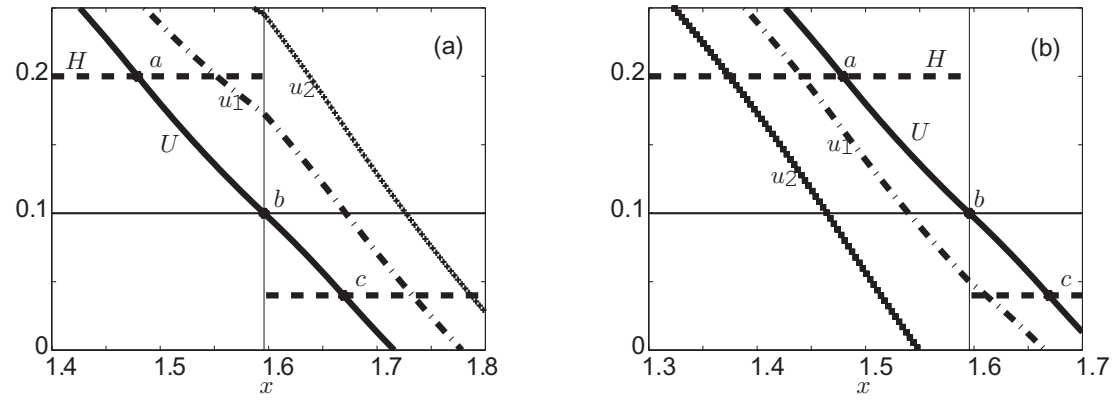

Figure B.3. Different sized perturbations of a bump. (a) Expanding a side of the bump. Zoomed–in version of the bump $(U(x), H(x))$ is shown along with perturbed solutions $u_1(x) = U(x) + \varepsilon\psi_1(x)$ and $u_2(x) = U(x) + \varepsilon\psi_2(x)$ with $\psi_i(x) > 0$. While u_1 satisfies the three threshold crossings on this side, u_2 does not, due to the condition $u_2(a + \varepsilon\Delta_+^a) = h_0 + \kappa$ being violated. (b) Contracting a side of the bump. Here, $u_1(x) = U(x) - \varepsilon\psi_1(x), (\psi_1(x) > 0)$ still satisfies all three threshold crossings, but $u_2 = U - \varepsilon\psi_2, (\psi_2 > 0)$ does not, due to $u_2(c + \varepsilon\Delta_c^+) = h_0$ being violated. Parameters are $h_0 = 0.04$, $\theta = 0.1$, $\kappa = 0.16$.

$$\begin{aligned}\frac{1}{\alpha}\frac{\partial\psi(x,t)}{\partial t} &= -\psi(x,t)+\frac{1}{\varepsilon}\int_{-\infty}^{\infty} w(x-x')\left[\Theta(U(x')+\varepsilon\psi(x',t)-H(x')-\varepsilon\varphi(x',t))\right.\\ &\quad \left.-\Theta(U(x')-H(x'))\right]\mathrm{d}x' \qquad \text{(B.10)}\\ \frac{\partial\varphi(x,t)}{\partial t} &= -\varphi(x,t)+\frac{\kappa}{\varepsilon}[\Theta(U(x)+\varepsilon\psi(x,t)-\theta)-\Theta(U(x)-\theta)]. \qquad \text{(B.11)}\end{aligned}$$

Denote the infinitesimal perturbations of the bump boundary for the u variable by $\varepsilon\Delta_{\pm}^{a}(t), \varepsilon\Delta_{\pm}^{b}(t), \varepsilon\Delta_{\pm}^{c}(t)$ such that

$$\begin{aligned}u(\pm a+\varepsilon\Delta_{\pm}^{a}(t),t) &= h(\pm a+\varepsilon\Delta_{\pm}^{a}(t),t),\\ u(\pm b+\varepsilon\Delta_{\pm}^{b}(t),t) &= \theta, \qquad \text{(B.12)}\\ u(\pm c+\varepsilon\Delta_{\pm}^{c}(t),t) &= h(\pm c+\varepsilon\Delta_{\pm}^{c}(t),t),\end{aligned}$$

for an initial time interval following the perturbation $t \in (0,T)$. The linear theory will only be valid until the time T that the existence threshold conditions are violated. It is straightforward to Taylor expand the expressions in (B.12), truncate to first order in ε, and solve for the terms

$$\begin{aligned}\Delta_{\pm}^{a}(t) &\approx \pm\frac{\psi(\pm a,t)-\varphi(\pm a,t)}{|U'(a)|},\\ \Delta_{\pm}^{b}(t) &\approx \pm\frac{\psi(\pm b,t)}{|U'(b)|}, \qquad \text{(B.13)}\\ \Delta_{\pm}^{c}(t) &\approx \pm\frac{\psi(\pm c,t)-\varphi(\pm c,t)}{|U'(c)|}.\end{aligned}$$

It is important to note that an infinitesimal shift of the point at which u crosses θ is not equivalent to shifting the boundary of the outer region of the excited region of u, due to the discontinuity in $H(x)$. As shown in Figure B.4, infinitesimal perturbations of the bump lead to changes in the excited region of u in a neighborhood of $x = \pm a, \pm c$ but not $x = \pm b$. For the excited region of u, $R[u]$, to change in the vicinity of $x = \pm b$, it would be necessary to have an $\mathcal{O}(1)$ change in the threshold h by, for example, uniformly shifting the full bump solution. Thus, while the shift of the threshold condition near $x = \pm b$ does affect the φ dynamics, it will not affect the ψ dynamics for sufficiently small perturbations. If we now express the convolution in (B.10) in terms of the bump crossings a, b, c and perturbations $\Delta_{\pm}^{a}, \Delta_{\pm}^{c}$, we have

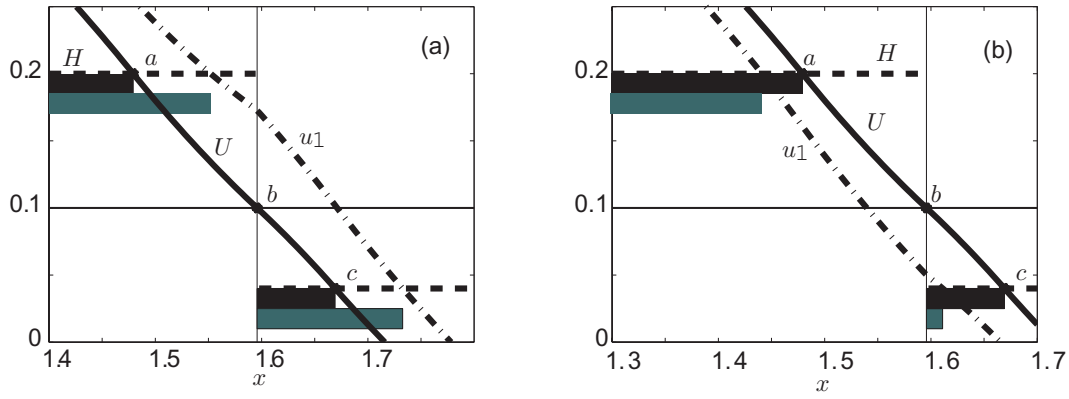

Figure B.4. Effects of perturbations on the excited region $R[U]$. (a) Zoomed–in version of the bump $(U(x), H(x))$ shows the accompanying excited region $R[U]$ (black bar). Expanding a side of the bump to the perturbed form $u_1(x) = U(x) + \varepsilon\psi_1(x), (\psi_1 > 0)$ will widen both subdomains of the excited region $R[u_1]$ (grey bars). (b) Contracting a side of the bump to the perturbed form $u_1(x) = U(x) - \varepsilon\psi_1(x), (\psi_1 > 0)$ shrinks both subdomains of the excited region $R[u_1]$ (grey bars). Parameters are $h_0 = 0.04$, $\theta = 0.1$, $\kappa = 0.16$.

$$\begin{aligned}\frac{1}{\alpha}\frac{\partial\psi(x,t)}{\partial t} &= -\psi(x,t) + \frac{1}{\varepsilon}\left[\int_{-c+\Delta_-^c}^{-b} w(x-x')\mathrm{d}x' - \int_{-c}^{-b} w(x-x')\mathrm{d}x'\right. \\ &\quad + \int_{-a+\Delta_-^a}^{a+\Delta_+^a} w(x-x')\mathrm{d}x' - \int_{-a}^{a} w(x-x')\mathrm{d}x' + \int_{b}^{c+\Delta_+^c} w(x-x')\mathrm{d}x' \\ &\quad \left. - \int_{b}^{c} w(x-x')\mathrm{d}x'\right]. \end{aligned} \tag{B.14}$$

Let us now consider an initial perturbation that only changes the activity variable u, that is, $\varphi(x,0) = 0$ for all x. We can now linearize equation (B.14) by expanding in powers of ε and collecting all $\mathcal{O}(1)$ terms, since $\varphi(\pm a, t) = 0 = \varphi(\pm c, t)$ within the linear regime, that is, infinitesimal changes in u will only perturb the threshold in a neighborhood of $x = \pm b$. Thus,

$$\frac{1}{\varepsilon}\int_{-c+\varepsilon\Delta_-^c}^{-c} w(x-x')\mathrm{d}x' \approx -\Delta_-^c w(x+c) \approx \gamma_c w(x+c)\psi(-c,t), \tag{B.15}$$

$$\frac{1}{\varepsilon}\int_{-a+\varepsilon\Delta_-^a}^{-a} w(x-x')\mathrm{d}x' \approx -\Delta_-^a w(x+a) \approx \gamma_a w(x+a)\psi(-a,t), \tag{B.16}$$

$$\frac{1}{\varepsilon}\int_{a}^{a+\varepsilon\Delta_+^a} w(x-x')\mathrm{d}x' \approx \Delta_+^a w(x-a) \approx \gamma_a w(x-a)\psi(a,t), \tag{B.17}$$

$$\frac{1}{\varepsilon}\int_{c}^{c+\varepsilon\Delta_+^c} w(x-x')\mathrm{d}x' \approx \Delta_+^c w(x-c) \approx \gamma_c w(x-c)\psi(c,t), \tag{B.18}$$

where $\gamma_y^{-1} = |U'(y)|$. This yields the linear equation

$$\begin{aligned}\frac{1}{\alpha}\frac{\partial\psi(x,t)}{\partial t} &= -\psi(x,t) + \gamma_a(w(x+a)\psi(-a,t) + w(x-a)\psi(a,t)) \\ &\quad +\gamma_c(w(x+c)\psi(-c,t) + w(x-c)\psi(c,t)). \end{aligned} \tag{B.19}$$

Assuming separability $\psi(x,t) = \mathrm{e}^{\lambda t}\psi(x)$, we derive a spectral equation that determines the linear stability of a bump solution with respect to the given restricted class of perturbations:

$$\begin{aligned}(\lambda+\alpha)\psi(x) &= \alpha\gamma_a(w(x+a)\psi(-a) + w(x-a)\psi(a)) \\ &\quad +\alpha\gamma_c(w(x+c)\psi(-c) + w(x-c)\psi(c)). \end{aligned} \tag{B.20}$$

Note that equation (B.20) is a modified version of the spectral equation for the scalar Amari equation [3] (see also analysis in Appendix A). The dynamic threshold introduces extra threshold crossing points that appear as additional pointwise terms. This is equivalent to the spectral equation one would derive for an Amari network with a spatially inhomogeneous threshold, specified by $H(x)$. Therefore, the translation invariance of the bump will no longer be implied by the linear stability equation, since translations of $H(x)$ would involve $\mathcal{O}(1)$ additions, which we must exclude from our analysis, based on our assumption that $\varphi(x)$ remains small. Setting $x = \pm a, \pm c$, we may then determine stability by solving the eigenvalue problem

$$\lambda\bar{\psi} = \alpha(\mathbf{M} - I_4)\bar{\psi},$$

where

$$\mathbf{M} = \begin{pmatrix} \gamma_a w(0) & \gamma_a w(2a) & \gamma_c w(c-a) & \gamma_c w(a+c) \\ \gamma_a w(2a) & \gamma_a w(0) & \gamma_c w(a+c) & \gamma_c w(c-a) \\ \gamma_a w(c-a) & \gamma_a w(a+c) & \gamma_c w(0) & \gamma_c w(2c) \\ \gamma_a w(a+c) & \gamma_a w(c-a) & \gamma_c w(2c) & \gamma_c w(0) \end{pmatrix}, \tag{B.21}$$

$\bar{\psi} = (\psi(-a), \psi(a), \psi(-c), \psi(c))^T$ and I_n is the $n \times n$ identity matrix. Let us define an even (odd) eigenmode as one for which $\psi(x) = \psi(-x)$ ($\psi(x) = -\psi(-x)$) at $x = a, c$. An even eigenmode corresponds to an expansion/contraction of the bump, whereas an odd eigenmode corresponds to a shift of the bump. For all parameter values that we have explored, we find that there are two positive eigenvalues, with the larger (smaller) positive eigenvalue corresponding to an odd (even) eigenmode, and a degenerate negative eigenvalue with an even/odd pair of eigenmodes. By applying the ansatz of an eigenmode

being even or odd, we can compute these eigenvalues analytically by evaluating the roots of a quadratic. In the case of even eigenmodes, the associated pair of eigenvalues is

$$\lambda_{\pm}^{\mathrm{e}} = \frac{\alpha}{2}\left(\gamma_a\Omega_+^a + \gamma_c\Omega_+^c - 2 \pm \sqrt{(\gamma_a\Omega_+^a - \gamma_c\Omega_+^c)^2 + 4\gamma_a\gamma_c\left(\Omega_+^m\right)^2}\right), \qquad \text{(B.22)}$$

and in the case of odd eigenmodes, the associated pair of eigenvalues is

$$\lambda_{\pm}^{\mathrm{o}} = \frac{\alpha}{2}\left(\gamma_a\Omega_-^a + \gamma_c\Omega_-^c - 2 \pm \sqrt{(\gamma_a\Omega_-^a - \gamma_c\Omega_-^c)^2 + 4\gamma_a\gamma_c\left(\Omega_-^m\right)^2}\right), \qquad \text{(B.23)}$$

where

$$\Omega_{\pm}^a = w(0) \pm w(2a), \quad \Omega_{\pm}^c = w(0) \pm w(2c), \quad \Omega_{\pm}^m = w(c-a) \pm w(c+a). \qquad \text{(B.24)}$$

The dependence of the eigenpairs (B.22) and (B.23) on parameters is illustrated in in Figure B.5. Clearly, varying α will not change the sign of the eigenvalues λ and thus the qualitative linear stability of bumps. In contrast to our analysis, the Evans function approach predicts that bumps are stable for sufficiently small α [42, 43] but destabilize to form a traveling pulse or breather as α increases. However, numerical simulations of the full system (B.1) confirm that bumps are always unstable once discreteness effects are taken into account. Moreover, the qualitative behavior of the resulting instabilities are consistent with our analysis (see next section).

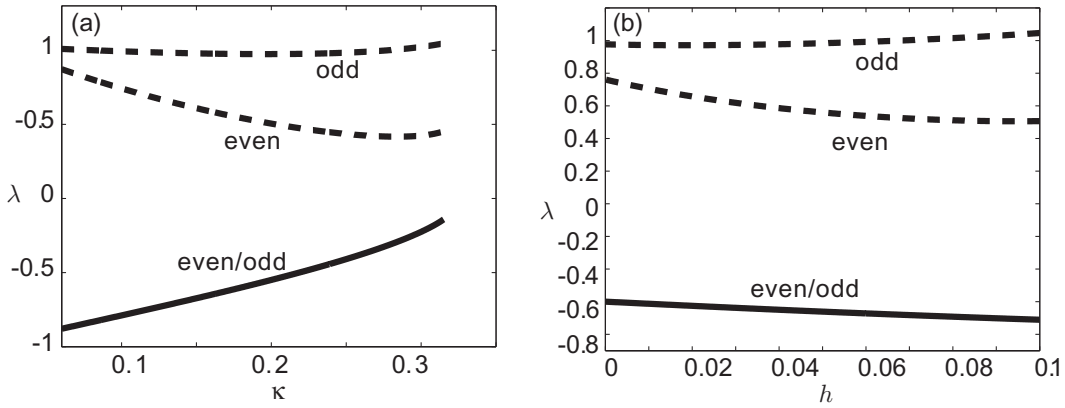

Figure B.5. Plot of eigenvalues arising from perturbations of a bump solution as a function of (a) κ with $h_0 = 0.04$, and (b) h_0 with $\kappa = 0.16$. In both plots, the positive eigenvalue associated with a shift perturbation is always larger than that associated with an expansion/contraction. Other parameters are $\theta = 0.1$ and $\alpha = 1$. Varying α has the effect of merely scaling the eigenvalues, but not changing their sign.

Numerical Simulations

We now study the full system (B.1) using a numerical approximation scheme. To evolve the system in time, we use a fourth order Runge–Kutta method with 2000–4000 spatial grid points and a time–step of $dt = 0.01$. The integral term in equation (B.1a) is approximated using Simpson's rule. For all of our numerical simulations, we begin with an initial condition $(u(x,0), h(x,0)) = (U(x), H(x))$ given by an exact bump solution specified by equations (B.7) and (B.8). After a brief period, we perturb the system according to $u(x) \to u(x) + \psi_{\pm}(x)$ with

$$\psi_{\pm}(x) = \chi(w(x+a) \pm w(x-a) + w(x+c) \pm w(x-c)), \tag{B.25}$$

and observe how the system then evolves. Leftward shifts (rightward shifts) correspond to $\psi_{-}(x,t)$ when $\chi \geq 0$ ($\chi \leq 0$), while expansions (contractions) correspond to $\psi_{+}(x,t)$ when $\chi \geq 0$ ($\chi \leq 0$). Note that the perturbation $\psi_{+}(x)$ ($\psi_{-}(x)$) is a mixture of even (odd) eigenmode solutions of equation (B.20). The resulting dynamics depends specifically on the type of perturbation applied to the bump. For each simulation, we systematically examined whether or not taking finer grids changed the stability results. We found that as the grid spacing was decreased the size of perturbation necessary to destabilize the bump also decreased. This is important because too coarse a grid can drastically alter numerical results, since discreteness can stabilize bumps that are not stable in the continuous system [62].

When shift perturbations destabilize the bump, the resulting dynamics evolves to a traveling pulse solution, as illustrated in Figure B.6(a) for a rightward shift. Coombes and Owen [42, 43] have shown that spike frequency adaptation can indeed generate stable traveling pulses for a wide range of parameters in the system (B.1). Following a perturbation by a rightward shift, the nonlinear threshold initially decays at what becomes the trailing edge of the pulse. As the leading edge moves rightward as well, the structure soon propagates invariantly, as demonstrated by the time snapshots in Figure B.7. In other simulations, we found that increasing α leads to faster traveling pulses and therefore a more obvious initial destabilization, in good agreement with the linear theory. In Figure B.6(b), we show an example of how an expansion destabilizes a bump leading to the formation of a breather, the existence of which was previously established by Coombes and Owen [42, 43]. A closer look at the corresponding snapshots in Figure B.8 shows that the breather begins contracting once the threshold h becomes higher in amplitude than u at the pulse edge. The oscillation amplitude of the breathing solution decreases as α decreases. Finally, in

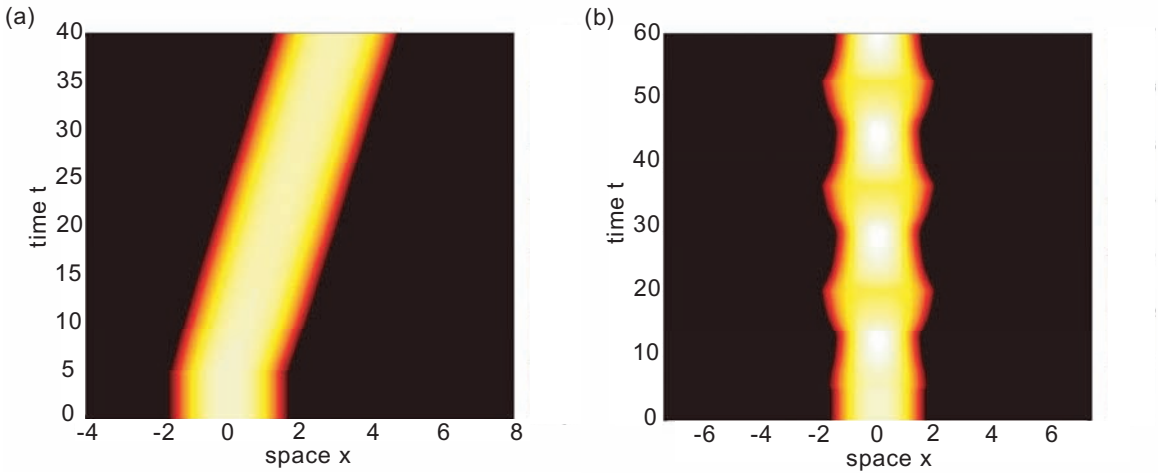

Figure B.6. Instabilities of a stationary bump solution given by equations (B.7) and (B.8). (a) Space–time plot of a bump destabilizing to form a traveling pulse for $\alpha = 1.0, \kappa = 0.16$. The activity $u(x,t)$ evolves from an initial bump solution that is perturbed by a small rightward shift at $t = 5$. (b) Space–time plot of a bump destabilizing to form a spatially localized breather for $\alpha = 1.2, \kappa = 0.16$. The activity $u(x,t)$ evolves from an initial bump solution that is perturbed by an expansion at $t = 5$. Other parameters are $\theta = 0.1$, $h_0 = 0.04$.

Figure B.9 we show an example of a shift perturbation destabilizing a bump in the case of stronger adaptation (larger κ). In this case the traveling pulse crosses threshold at five locations, rather than four points as in Figure B.7.

Discussion

In this appendix, we determined the local stability of stationary bumps in a piecewise smooth neural field model with spike frequency adaptation. We found that bumps are always unstable, and that destabilization of a bump can result in either a traveling pulse or a spatially localized breather. In future work, we will continue to explore new bifurcations and instabilities in piecewise smooth spatially extended networks. Due to the construct of our linear stability analysis, we could only study instabilities that were associated with real rather than complex eigenvalues. However, there are well known scenarios in neural field models with linear adaptation, where Hopf bifurcations can occur leading to spatially structured oscillations such as breathers and target patterns [137, 55, 57, 168]. In future work, it would be interesting to analyze generalized Hopf bifurcations in neural field models with nonlinear forms of adaptation, along the lines of recent studies of nonsmooth

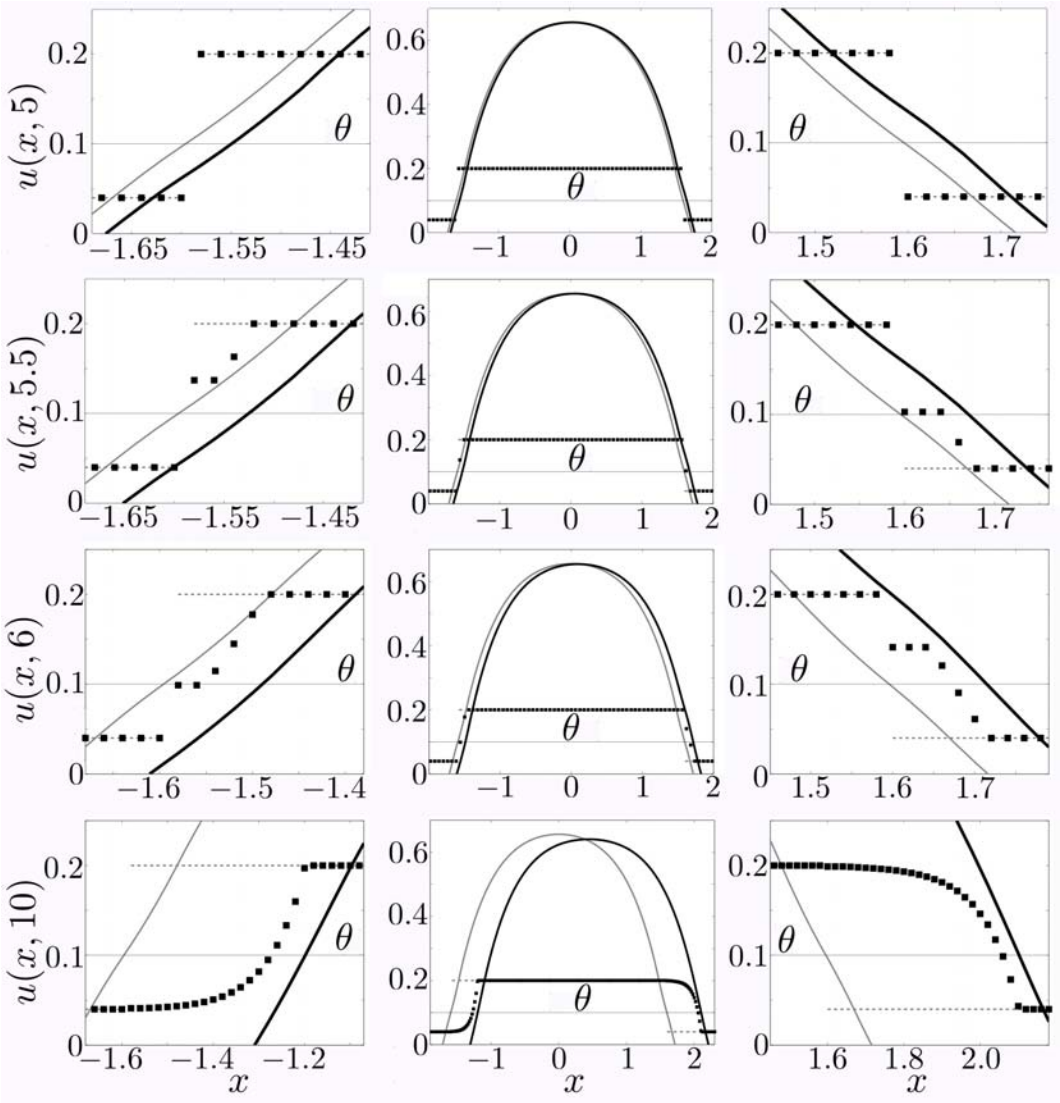

Figure B.7. Snapshots of a bump destabilizing to a traveling pulse at successive times $t = 5, 5.5, 6, 10$ (top to bottom) for $\alpha = 1.0$, and $\kappa = 0.16$. Both $u(x,t)$ (solid black curves) and $h(x,t)$ (black squares) are shown in full view (center column), at the trailing edge (left column), and at the leading edge (right column). Also shown are the initial conditions of the bump for $U(x)$ (solid grey curve) and $H(x)$ (dashed grey curve). Eventually, the threshold crossings $u(a + \varepsilon\Delta_+^a, t) = h_0 + \kappa$ and $u(-c + \varepsilon\Delta_-^c, t) = h_0$ vanish. Other parameters are $h_0 = 0.04$, $\theta = 0.1$.

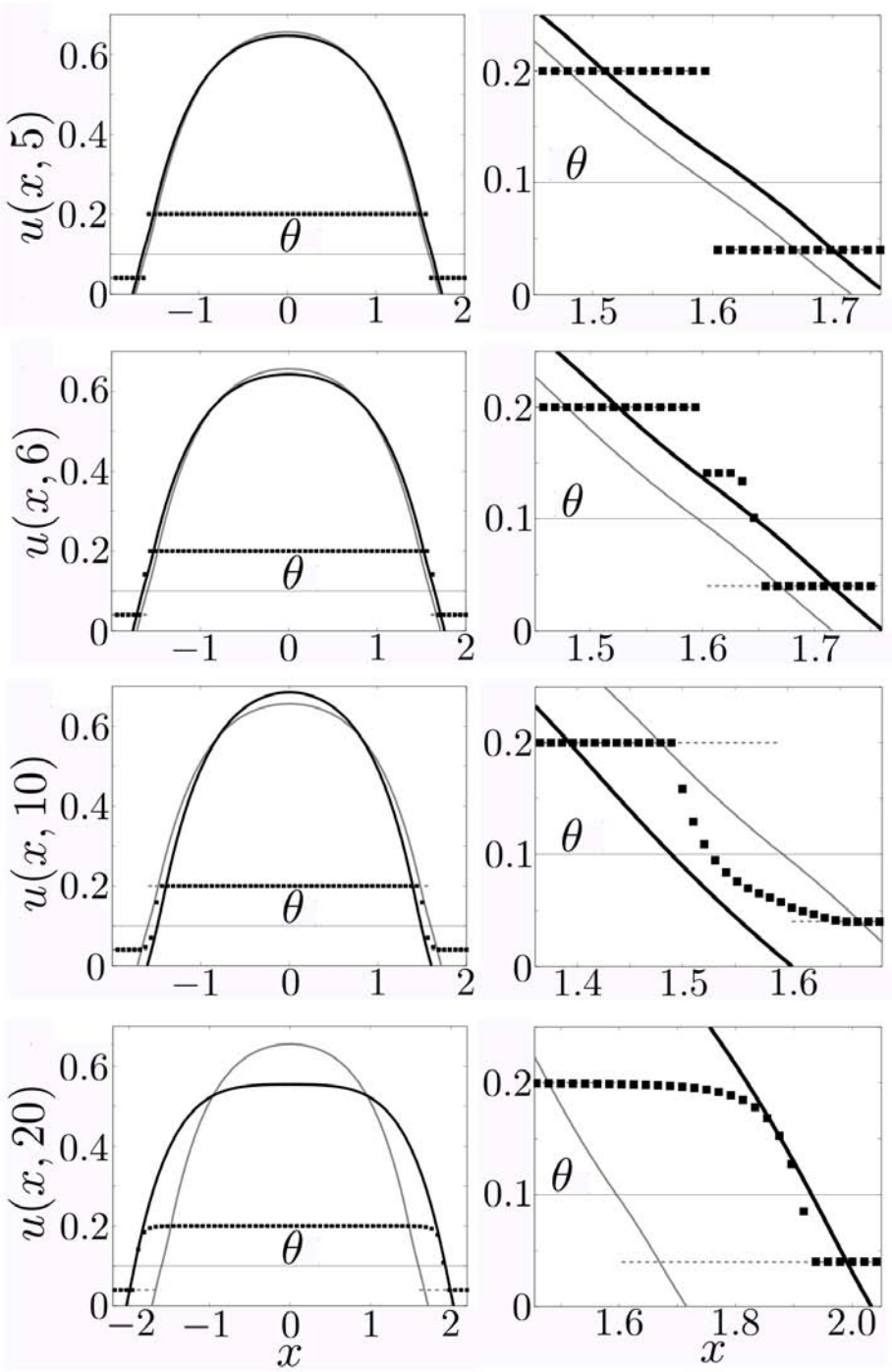

Figure B.8. Snapshots of a bump destabilizing to a breather at successive times $t = 5, 6, 10, 20$ (top to bottom) for $\alpha = 1.2$ and $\kappa = 0.16$. Both $u(x,t)$ (black curves) and $h(x,t)$ (solid black squares) are shown in full view (left column), and for the right–hand side of the bump (right column). Also shown are the initial conditions of the bump for $U(x)$ (solid grey curve) and $H(x)$ (dashed grey curve). The threshold crossings $u(\pm a + \varepsilon\Delta_{\pm}^{a}, t) = h_0 + \kappa$ and $u(\pm c + \varepsilon\Delta_{\pm}^{c}, t) = h_0$ periodically vanish. Other parameters are $h_0 = 0.04$, $\theta = 0.1$.

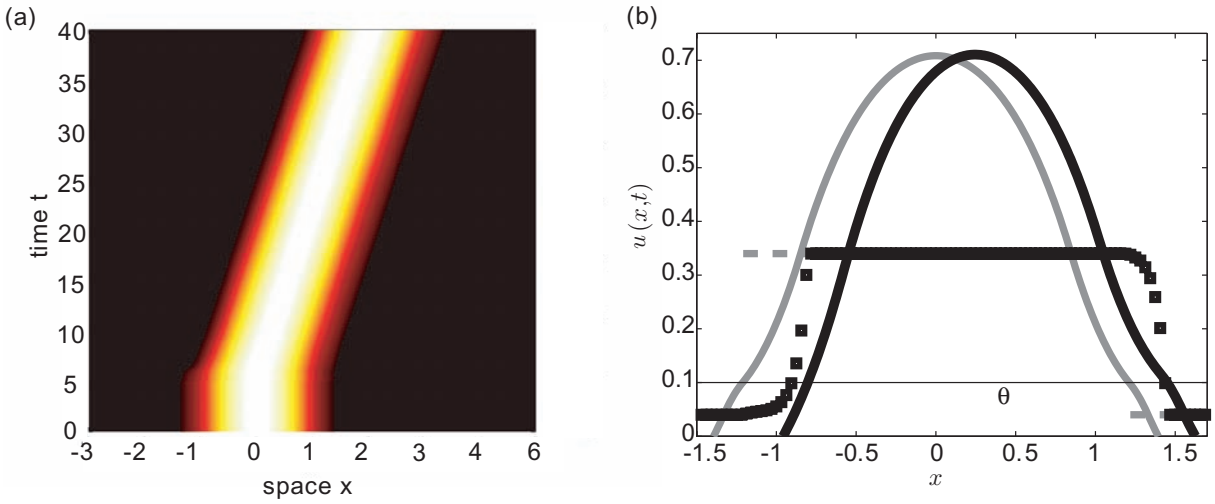

Figure B.9. Bump destabilizing to a traveling pulse for $\alpha = 2.0, \kappa = 0.3$. (a) Space–time plot of the activity $u(x,t)$ evolving from an initial bump solution that is perturbed by a small rightward shift at $t = 5$. (b) Snapshot of perturbed solution $u(x,t)$ (black solid curve) and $h(x,t)$ (black squares) at time $t = 20$, along with initial profiles $U(x)$ (grey curve) and $H(x)$ (grey dashed curve). Eventually, the threshold crossing $u(-c + \varepsilon\Delta_-^c, t) = h_0 + \kappa$ vanishes. Other parameters are $h_0 = 0.04$, $\theta = 0.1$.

dynamical systems [47]. In the case of spike frequency adaptation, it would be interesting to develop tools to analyze the nonlinear (order one) instabilities of the adaptive network (B.1). This would allow us to analytically find the period of oscillation in the breathing solutions identified using numerics.

APPENDIX C

PHASE FUNCTION PARAMETERS

In this appendix we present the explicit parameter–dependent expressions for the various coefficients appearing in the solution of the phase function Φ_1, equation (5.49). First, the constants premultiplying the periodic functions on the righthand side of equation (5.49) are as follows:

$$\begin{aligned}
\Xi_\pm &= \frac{\gamma_\pm}{1+\mu_\pm^2\varepsilon^2}\left[\frac{1}{2(1+\mu_\pm)}+\frac{\chi}{2}\left(\frac{\mathrm{e}^{-a}-\mathrm{e}^{-\mu_\pm a}}{\mu_\pm-1}+\frac{\mathrm{e}^{-\mu_\pm a}}{\mu_\pm+1}\right)\right]\\
\Pi_\pm &= \frac{\gamma_\pm}{1+\mu_\pm^2\varepsilon^2}\left[-\frac{\chi}{2(1+\mu_\pm)}-\frac{\mathrm{e}^{-a}}{2(\mu_\pm+1)}\right]\\
\Upsilon_\pm &= \frac{\gamma_\pm}{1+\mu_\pm^2\varepsilon^2}\left[-\frac{\mu_\pm\varepsilon}{2(1+\mu_\pm)}-\frac{\chi\mu_\pm\varepsilon}{2}\left(\frac{\mathrm{e}^{-a}-\mathrm{e}^{-\mu_\pm a}}{\mu_\pm-1}+\frac{\mathrm{e}^{-\mu_\pm a}}{\mu_\pm+1}\right)\right]\\
\Psi_\pm &= \frac{\gamma_\pm}{1+\mu_\pm^2\varepsilon^2}\left[\frac{\chi\mu_\pm\varepsilon}{2(1+\mu_\pm)}+\frac{\mu_\pm\varepsilon\mathrm{e}^{-a}}{2(1+\mu_\pm)}\right].
\end{aligned}$$

Second, the constant scaling factor K on the left–hand side of equation (5.49) is determined by substituting equations (5.28), (5.29) and (5.35) into equation (5.18). Using the fact that the null vector is zero for $\xi<-a$, we can expand the integral out in terms of definite integrals of exponential products with the $\mathcal{M}_\pm(\xi)$ functions

$$\begin{aligned}
K &= [\gamma_+(1-m_-)(1+\chi e^{-\mu_+ a})(1-\alpha^{-1}\beta_p^{-1}(1-m_+)^2)]\int_0^\infty e^{-\mu_+\xi}\mathcal{M}'_+(\xi)\mathrm{d}\xi\\
&\quad+[\gamma_-(1-m_-)(1+\chi e^{-\mu_- a})(1+\alpha^{-1}\beta_p^{-1}(m_+-1)(1-m_-))]\int_0^\infty e^{-\mu_-\xi}\mathcal{M}'_+(\xi)\mathrm{d}\xi\\
&\quad-[\gamma_+(1-m_+)(1+\chi e^{-\mu_+ a})(1+\alpha^{-1}\beta_p^{-1}(m_--1)(1-m_+))]\int_0^\infty e^{-\mu_+\xi}\mathcal{M}'_-(\xi)\mathrm{d}\xi\\
&\quad-[\gamma_-(1-m_+)(1+\chi e^{-\mu_- a})(1-\alpha^{-1}\beta_p^{-1}(1-m_-)^2)]\int_0^\infty e^{-\mu_-\xi}\mathcal{M}'_-(\xi)\mathrm{d}\xi\\
&\quad+\chi[\gamma_+ e^{-\mu_+ a}(1-m_-)(1-\alpha^{-1}\beta_p^{-1}(1-m_+)^2)]\int_{-a}^0 e^{-\mu_+\xi}\mathcal{M}'_+(\xi)\mathrm{d}\xi\\
&\quad+\chi[\gamma_- e^{-\mu_- a}(1-m_-)(1+\alpha^{-1}\beta_p^{-1}(m_+-1)(1-m_-))]\int_{-a}^0 e^{-\mu_-\xi}\mathcal{M}'_+(\xi)\mathrm{d}\xi
\end{aligned}$$

$$-\chi[\gamma_+ e^{-\mu_+ a}(1-m_+)(1+\alpha^{-1}\beta_p^{-1}(m_- -1)(1-m_+))]\int_{-a}^{0} e^{-\mu_+\xi}\mathcal{M}'_-(\xi)\mathrm{d}\xi$$
$$-\chi[\gamma_- e^{-\mu_- a}(1-m_+)(1-\alpha^{-1}\beta_p^{-1}(1-m_-)^2)]\int_{-a}^{0} e^{-\mu_-\xi}\mathcal{M}'_-(\xi)\mathrm{d}\xi.$$

The individual integrals can be computed as follows:

$$\int_0^\infty e^{-\mu_\pm\xi}\mathcal{M}'_\pm(\xi)\mathrm{d}\xi = \frac{e^{-a}-1}{2c(m_+-m_-)(\mu_\pm+1)^2}$$

$$\int_0^\infty e^{-\mu_+\xi}\mathcal{M}'_-(\xi)\mathrm{d}\xi = \frac{e^{-a}-1}{2c(m_+-m_-)(\mu_-+1)(\mu_++1)}$$

$$\int_0^\infty e^{-\mu_-\xi}\mathcal{M}'_+(\xi)\mathrm{d}\xi = \frac{e^{-a}-1}{2c(m_+-m_-)(\mu_++1)(\mu_-+1)}$$

and

$$\begin{aligned}\int_{-a}^{0} e^{-\mu_\pm\xi}\mathcal{M}'_\pm(\xi)\mathrm{d}\xi &= \frac{1}{2c(m_+-m_-)}\left\{\frac{a}{(\mu_\pm-1)}+\frac{1-e^{(\mu_\pm-1)a}}{(\mu_\pm-1)^2}\right.\\ &\left.+\frac{e^{-a}(e^{(\mu_\pm+1)a}-1)}{(\mu_\pm+1)^2}-\frac{a}{2(\mu_\pm+1)}\right\}\end{aligned}$$

$$\begin{aligned}\int_{-a}^{0} e^{-\mu_+\xi}\mathcal{M}'_-(\xi)\mathrm{d}\xi &= \frac{1}{2c(m_+-m_-)}\left\{\frac{1-e^{-(\mu_--\mu_+)a}}{(\mu_--\mu_+)(\mu_--1)}-\frac{e^{(\mu_+-1)a}-1}{(\mu_++1)(\mu_--1)}\right.\\ &\left.+\frac{e^{\mu_+ a}-e^{-a}}{(\mu_++1)(\mu_-+1)}-\frac{1-e^{-(\mu_--\mu_+)a}}{(\mu_-+1)(\mu_--\mu_+)}\right\}\end{aligned}$$

$$\begin{aligned}\int_{-a}^{0} e^{-\mu_-\xi}\mathcal{M}'_+(\xi)\mathrm{d}\xi &= \frac{1}{2c(m_+-m_-)}\left\{\frac{1-e^{-(\mu_+-\mu_-)a}}{(\mu_+-1)(\mu_+-\mu_-)}-\frac{e^{(\mu_--1)a}-1}{(\mu_++1)(\mu_--1)}\right.\\ &\left.+e^{-a}\frac{e^{(\mu_-+1)a}-1}{(\mu_++1)(\mu_-+1)}-\frac{1-e^{-(\mu_+-\mu_-)a}}{(\mu_++1)(\mu_+-\mu_-)}\right\}.\end{aligned}$$

REFERENCES

[1] L. F. Abbott and W. G. Regehr, *Synaptic computation*, Nature, 431 (2004), pp. 796–803.

[2] L. F. Abbott, J. A. Varela, K. Sen, and S. B. Nelson, *Synaptic depression and cortical gain control*, Science, 275 (1997), pp. 220–224.

[3] S. Amari, *Dynamics of pattern formation in lateral-inhibition type neural fields*, Biol. Cybern., 27 (1977), pp. 77–87.

[4] A. Angelucci, J. B. Levitt, E. J. S. Walton, J.-M. Hupe, J. Bullier, and J. S. Lund, *Circuits for local and global signal integration in primary visual cortex*, J. Neurosci., 22 (2002), pp. 8633–46.

[5] F. M. Atay and A. Hutt, *Stability and bifurcations in neural fields with finite propagation speed and general connectivity*, SIAM J. Appl. Math., 65 (2005), pp. 644–666.

[6] O. Barak and M. Tsodyks, *Persistent activity in neural networks with dynamic synapses*, PLoS Comput. Biol., 3 (2007), p. e35.

[7] E. Bart, S. Bao, and D. Holcman, *Modeling the spontaneous activity of the auditory cortex*, J. Comput. Neurosci., 19 (2005), pp. 357–378.

[8] R. Ben-Yishai, R. L. Bar-Or, and H. Sompolinsky, *Theory of orientation tuning in visual cortex*, Proc. Natl. Acad. Sci. USA, 92 (1995), pp. 3844–3848.

[9] J. Benda and A. V. M. Herz, *A universal model for spike-frequency adaptation*, Neural Comput., 15 (2003), pp. 2523–2564.

[10] A. Benucci, R. A. Frazor, and M. Carandini, *Standing waves and traveling waves distinguish two circuits in visual cortex*, Neuron, 55 (2007), pp. 103–17.

[11] G. Bi and M. Poo, *Synaptic modifications in cultured hippocampal neurons: dependence on spike timing, synaptic strength, and postsynaptic cell type*, J. Neurosci., 18 (1998), pp. 10464–72.

[12] R. Blake, *A primer on binocular rivalry, including current controversies*, Brain and Mind, 2 (2001), pp. 5–38.

[13] R. Blake and N. K. Logothetis, *Visual competition*, Nat. Rev. Neurosci., 3 (2002), pp. 1–11.

[14] G. G. Blasdel, *Orientation selectivity, preference, and continuity in monkey striate cortex*, J. Neurosci., 12 (1992), pp. 3139–61.

[15] A. A. Borbely and P. Achermann, *Sleep homeostasis and models of sleep regulation*, J. Biol. Rhythms, 14 (1999), pp. 557–568.

[16] C. Borgers, S. Epstein, and N. Kopell, *Gamma oscillations mediate stimulus competition and attentional selection in a cortical network model*, Proc. Natl. Acad. Sci. USA, 105 (2008), pp. 18023–18028.

[17] C. Borgers and N. J. Kopell, *Effects of noisy drive on rhythms in networks of excitatory and inhibitory neurons*, Neural Comput., 17 (2005), pp. 557–608.

[18] W. H. Bosking, Y. Zhang, B. Schofield, and D. Fitzpatrick, *Orientation selectivity and the arrangement of horizontal connections in tree shrew striate cortex*, J. Neurosci., 17 (1997), pp. 2112–27.

[19] C. J. Bossink, P. F. Stalmeier, and C. M. De Weert, *A test of Levelt's second proposition for binocular rivalry*, Vision Res., 33 (1993), pp. 1413–9.

[20] P. C. Bressloff, *Traveling fronts and wave propagation failure in an inhomogeneous neural network*, Physica D, 155 (2001), pp. 83–100.

[21] ——, *Spatially periodic modulation of cortical patterns by long-range horizontal connections*, Physica D, 185 (2003), pp. 131–157.

[22] ——, *Pattern formation in visual cortex*, in Methods and models in Neurophysics, C. C. Chow, ed., 2004.

[23] ——, *Stochastic neural field theory and the system-size expansion*, SIAM J. Appl. Math., 70 (2009), pp. 1488–1521.

[24] P. C. Bressloff and J. D. Cowan, *An amplitude equation approach to contextual effects in visual cortex*, Neural Comput., 14 (2002), pp. 493–525.

[25] P. C. Bressloff, J. D. Cowan, M. Golubitsky, P. J. Thomas, and M. C. Wiener, *Geometric visual hallucinations, Euclidean symmetry and the functional architecture of striate cortex*, Phil. Trans. Roy. Soc. Lond. B, 356 (2001), pp. 299–330.

[26] P. C. Bressloff and Z. P. Kilpatrick, *Nonlocal ginzburg-landau equation for cortical pattern formation*, Phys. Rev. E, 78 (2008), p. 041916.

[27] ——, *Two–dimensional bumps in piecewise smooth neural fields with synaptic depression*, (submitted).

[28] A. Buckthought, J. Kim, and H. R. Wilson, *Hysteresis effects in stereopsis and binocular rivalry*, Vision Res., 48 (2008), pp. 819–30.

[29] M. A. Buice and C. C. Chow, *Correlations, fluctuations, and stability of a finite-size network of coupled oscillators*, Phys. Rev. E, 76 (2007), p. 031118.

[30] M. A. Buice, J. D. Cowan, and C. C. Chow, *Systematic fluctuation expansion for neural network activity equations*, Neural Comput., 22 (2010), pp. 377–426.

[31] G. Buzsaki, *Rhythms of the Brain*, Oxford University Press, Oxford, 2006.

[32] G. Buzsaki and A. Draguhn, *Neuronal oscillations in cortical networks*, Science, 304 (2004), pp. 1926–1929.

[33] Y. Chagnac-Amitai and B. W. Connors, *Horizontal spread of synchronized activity in neocortex and its control by gaba-mediated inhibition*, J. Neurophysiol., 61 (1989), pp. 747–58.

[34] F. S. Chance, S. B. Nelson, and L. F. Abbott, *Synaptic depression and the temporal response characteristics of V1 cells*, J. Neurosci., 18 (1998), pp. 4785–4799.

[35] L. Chandrasekaran, V. Matveev, and A. Bose, *Multistability of clustered states in a globally inhibitory network*, Physica D, 238 (2009), pp. 253–263.

[36] B. Chapman, K. R. Zahs, and M. P. Stryker, *Relation of cortical cell orientation selectivity to alignment of receptive fields of the geniculocortical afferents that arborize within a single orientation column in ferret visual cortex*, J. Neurosci., 11 (1991), pp. 1347–58.

[37] R. D. Chervin, P. A. Pierce, and B. W. Connors, *Periodicity and directionality in the propagation of epileptiform discharges across neocortex*, J. Neurophysiol., 60 (1988), pp. 1695–1713.

[38] L. B. Cohen, R. D. Keynes, and B. Hille, *Light scattering and birefringence changes during nerve activity*, Nature, 218 (1968), pp. 438–41.

[39] S. Coombes, *Waves, bumps, and patterns in neural field theories*, Biol. Cybern., 93 (2005), pp. 91–108.

[40] S. Coombes, G. J. Lord, and M. R. Owen, *Waves and bumps in neuronal networks with axo–dendritic synaptic interactions*, Physica D, 178 (2003), pp. 219–241.

[41] S. Coombes and M. R. Owen, *Evans functions for integral neural field equations with heaviside firing rate function*, SIAM J. Appl. Dyn. Syst., 3 (2004), pp. 574–600.

[42] ——, *Bumps, breathers, and waves in a neural network with spike frequency adaptation*, Phys. Rev. Lett., 94 (2005), p. 148102.

[43] ——, *Exotic dynamics in a firing rate model of neural tissue with threshold accomodation*, vol. 440, AMS Contemporary Mathematics, 2007, pp. 123–144.

[44] S. Coombes and H. Schmidt, *Neural fields with sigmoidal firing rates: Approximate solutions*, Disc. Cont. Dyn. Syst. S *in press*, (2010).

[45] Y. Dan and M. M. Poo, *Spike–timing–dependent plasticity of neural circuits*, Neuron, 44 (2004), pp. 23–30.

[46] K. R. Delaney, A. Gelperin, M. S. Fee, J. S. Flores, R. Gervais, and D. W. Tank, *Waves and stimulus-modulated dynamics in an oscillating owlfactory network*, Proc. Natl. Acad. Sci. USA, 91 (1994), pp. 669–73.

[47] M. di Bernardo, C. Budd, C. A.R., and P. Kowalczyk, *Piecewise smooth dynamical systems: Theory and applications*, Springer, London, 2007.

[48] F. E. Dudek and M. Spitz, *Hypothetical mechanisms for the cellular and neurophysiological basis of secondary epileptogenesis: Proposed role for synaptic reorganization*, J. Clin. Neurophysiol., 14 (1997), pp. 90–101.

[49] G. B. Ermentrout, *Type I membranes, phase resetting curves, and synchrony*, Neural Comput., 8 (1996), pp. 979–1001.

[50] ——, *Linearization of f–I curves by adaptation*, Neural Comput., 10 (1998), pp. 1721–1729.

[51] G. B. Ermentrout and D. Kleinfeld, *Traveling electrical waves in cortex: Insights from phase dynamics and speculation on a computational role*, Neuron, 29 (2001), pp. 33–44.

[52] G. B. Ermentrout and J. B. McLeod, *Existence and uniqueness of travelling waves for a neural network*, Proc. Roy. Soc. Edin., 123A (1993), pp. 461–478.

[53] O. Faugeras, R. Veltz, and F. Grimbert, *Persistent neural states: Stationary localized activity patterns in the nonlinear continuous n–population, q–dimensional neural networks*, Neural Comput., 21 (2009), pp. 147–187.

[54] D. Ferster and K. D. Miller, *Neural mechanisms of orientation selectivity in the visual cortex*, Annu. Rev. Neurosci., 23 (2000), pp. 441–71.

[55] S. E. Folias and P. C. Bressloff, *Breathing pulses in an excitatory neural network*, SIAM J. Appl. Dyn. Syst., 3 (2004), pp. 378–407.

[56] ——, *Breathers in two–dimensional neural media*, Phys. Rev. Lett., 95 (2005), p. 208107.

[57] ——, *Stimulus–locked traveling waves and breathers in an excitatory neural network*, SIAM J. Appl. Math., 65 (2005), pp. 2067–2092.

[58] S. Funahashi, C. J. Bruce, and P. S. Goldman-Rakic, *Mnemonic coding of visual space in the monkey's dorsolateral prefrontal cortex*, J. Neurophysiol., 61 (1989), pp. 331–49.

[59] W. Gerstner, R. Kempter, J. L. van Hemmen, and H. Wagner, *A neuronal learning rule for sub-millisecond temporal coding*, Nature, 383 (1996), pp. 76–81.

[60] J. Guckenheimer and P. J. Holmes, *Nonlinear oscillations, dynamical systems, and bifurcations of vector fields*, Springer, Berlin, 1983.

[61] Y. Guo and C. C. Chow, *Existence and stability of standing pulses in neural networks: I. Existence*, SIAM J. Appl. Dyn. Syst., 4 (2005), pp. 217–248.

[62] ——, *Existence and stability of standing pulses in neural networks: II. Stability*, SIAM J. Appl. Dyn. Syst., 4 (2005), pp. 249–281.

[63] T. T. G. Hahn, B. Sakmann, and M. R. Mehta, *Phase-locking of hippocampal interneurons' membrane potential to neocortical up-down states*, Nat. Neurosci., 9 (2006), pp. 1359–1361.

[64] F. Han, N. Caporale, and Y. Dan, *Reverberation of recent visual experience in spontaneous cortical waves*, Neuron, 60 (2008), pp. 321–327.

[65] A. L. Hodgkin and A. F. Huxley, *A quantitative description of membrane current and its application to conduction and excitation in nerve*, J. Physiol., 117 (1952), pp. 500–44.

[66] D. Holcman and M. Tsodyks, *The emergence of Up and Down states in cortical networks*, PLoS Comput. Biol., 2 (2006), p. e23.

[67] X. Huang, W. C. Troy, Q. Yang, H. Ma, C. R. Laing, S. J. Schiff, and J.-Y. Wu, *Spiral waves in disinhibited mammalian neocortex*, J. Neurosci., 24 (2004), pp. 9897–9902.

[68] D. H. Hubel and T. N. Wiesel, *Receptive fields, binocular interaction and functional architecture in the cat's visual cortex*, J. Physiol., 160 (1962), pp. 106–54.

[69] ——, *Ferrier lecture. Functional architecture of macaque monkey visual cortex*, Proc. R Soc. Lond. B Biol. Sci., 198 (1977), pp. 1–59.

[70] R. Huber, M. F. Ghilardi, M. Massimini, and G. Tononi, *Local sleep and learning*, Nature, 430 (2004), pp. 78–81.

[71] J. M. Hupé, A. C. James, P. Girard, and J. Bullier, *Response modulations by static texture surround in area v1 of the macaque monkey do not depend on feedback connections from V2*, J. Neurophysiol., 85 (2001), pp. 146–63.

[72] A. Hutt, A. Longtin, and L. Schimansky-Geier, *Additive–noise induces turing transitions in spatial systems with application to neural fields and the swift-hohenberg equation*, Physica D, 237 (2008), pp. 755–773.

[73] M. A. P. Idiart and L. F. Abbott, *Propagation of excitation in neural network models*, Network, 4 (1993), pp. 285–294.

[74] E. M. Izhikevich and G. M. Edelman, *Large–scale model of mammalian thalamocortical systems*, Proc. Natl. Acad. Sci. USA, 105 (2008), pp. 3593–8.

[75] J. Karbowski and G. B. Ermentrout, *Synchrony arising from a balanced synaptic plasticity in a network of heterogeneous neural oscillators*, Phys. Rev. E, 65 (2002), p. 031902.

[76] L. C. Katz, C. D. Gilbert, and T. N. Wiesel, *Local circuits and ocular dominance columns in monkey striate cortex*, J. Neurosci., 9 (1989), pp. 1389–99.

[77] J. P. Keener, *Homogenization and propagation in the bistable equation*, Physica D, 136 (1999), pp. 1–17.

[78] ——, *Propagation of waves in an excitable medium with discrete release sites*, SIAM J. Appl. Math., 61 (2000), pp. 317–334.

[79] Z. P. Kilpatrick and P. C. Bressloff, *Effects of adaptation and synaptic depression on spatiotemporal dynamics of an excitatory neuronal network*, Physica D, 239 (2010), pp. 547–560.

[80] ——, *Spatially structured oscillations in a two-dimensional excitatory neuronal network with synaptic depression*, J. Comput. Neurosci., 28 (2010), pp. 193–209.

[81] ——, *Stability of bumps in piecewise smooth neural fields with nonlinear adaptation*, Physica D, 239 (2010), pp. 1048–1060.

[82] ——, *Binocular rivalry in a competitive neural network model with synaptic depression*, (submitted).

[83] Z. P. Kilpatrick, S. E. Folias, and P. C. Bressloff, *Traveling pulses and wave propagation failure in inhomogeneous neural media*, SIAM J. Appl. Dyn. Syst., 7 (2008), pp. 161–185.

[84] K. Kishimoto and S. Amari, *Existence and stability of local excitations in homogeneous neural fields*, J. Math. Biol., 7 (1979), pp. 303–318.

[85] D. Kleinfeld, K. R. Delaney, M. S. Fee, J. A. Flores, D. W. Tank, and A. Gelperin, *Dynamics of propagating waves in the olfactory network of a terrestrial mollusk: An electrical and optical study*, J. Neurophysiol., 72 (1994), pp. 1402–1419.

[86] W. Klimesch, *EEG alpha and theta oscillations reflect cognitive and memory performance: a review and analysis*, Brain Res. Rev., 29 (1999), pp. 169–95.

[87] C. Koch and I. Segev, eds., *Methods in neuronal modeling: From synapses to networks*, MIT Press, Cambridge, MA, USA, 1989.

[88] H. J. Koester and B. Sakmann, *Calcium dynamics associated with action potentials in single nerve terminals of pyramidal cells in layer 2/3 of the young rat neocortex*, J. Physiol., 529 (2000), pp. 625–646.

[89] N. Kopell, G. B. Ermentrout, M. A. Whittington, and R. D. Traub, *Gamma rhythms and beta rhythms have different synchronization properties*, Proc. Natl. Acad. Sci. USA, 97 (2000), pp. 1867–1872.

[90] N. J. Kopell and G. B. Ermentrout, *Symmetry and phaselocking in chains of weakly coupled oscillators*, Comm. Pure Appl. Math., 39 (1986), pp. 623–660.

[91] Y. Kuramoto, *Chemical oscillations, waves, and turbulence*, Springer, Berlin, 1984.

[92] C. Laing and S. Coombes, *The importance of different timings of excitatory and inhibitory pathways in neural field models.*, Network, 17 (2006), pp. 151–172.

[93] C. R. Laing, *Spiral waves in nonlocal equations*, SIAM J. Appl. Dyn. Syst., 4 (2005), pp. 588–606.

[94] ——, *The dynamics of chimera states in heterogeneous Kuramoto networks*, Physica D, 238 (2009), pp. 1569–1588.

[95] C. R. Laing and C. C. Chow, *Stationary bumps in networks of spiking neurons*, Neural Comput., 13 (2001), pp. 1473–94.

[96] C. R. Laing and C. C. Chow, *A spiking neuron model for binocular rivalry*, J. Comput. Neurosci., 12 (2002), pp. 39–53.

[97] C. R. Laing, T. A. Frewen, and I. G. Kevrekidis, *Coarse–grained dynamics of an activity bump in a neural field model*, Nonlinearity, 20 (2007), pp. 2127–2146.

[98] C. R. Laing and W. C. Troy, *PDE methods for nonlocal models*, SIAM J. Appl. Dyn. Syst., 2 (2003), pp. 487–516.

[99] C. R. Laing, W. C. Troy, B. Gutkin, and G. B. Ermentrout, *Multiple bumps in a neuronal model of working memory*, SIAM J. Appl. Math., 63 (2002), pp. 62–97.

[100] P. Lakatos, C.-M. Chen, M. N. O'Connell, A. Mills, and C. E. Schroeder, *Neuronal oscillations and multisensory interaction in primary auditory cortex*, Neuron, 53 (2007), pp. 279–92.

[101] Y. W. Lam, L. B. Cohen, M. Wachowiak, and M. R. Zochowski, *Odors elicit three different oscillations in the turtle olfactory bulb*, J. Neurosci., 20 (2000), pp. 749–762.

[102] U. Lee, S. Kim, and K.-Y. Jung, *Classification of epilepsy types through global network analysis of scalp electroencephalograms*, Phys. Rev. E, 73 (2006), p. 041920.

[103] D. A. Leopold and N. K. Logothetis, *Activity changes in early visual cortex reflect monkeys' percepts during binocular rivalry*, Nature, 379 (1996), pp. 549–53.

[104] W. J. M. Levelt, *On binocular rivalry*, Institute for Perception RVO–TNO, Soesterberg, The Netherlands, 1965.

[105] J. B. Levitt, D. A. Lewis, T. Yoshioka, and J. S. Lund, *Topography of pyramidal neuron intrinsic connections in macaque monkey prefrontal cortex (areas 9 and 46)*, J. Comp. Neurol., 338 (1993), pp. 360–76.

[106] D. A. Lewis and S. A. Anderson, *The functional architecture of the prefrontal cortex and schizophrenia*, Psychol. Med., 25 (1995), pp. 887–94.

[107] B. Linder, J. Garcia-Ojalvo, A. Neiman, and L. Schimansky-Geier, *Effects of noise in excitable systems*, Phys. Rep., 393 (2004), pp. 321–424.

[108] P. N. Loxley and P. A. Robinson, *Soliton model of competitive neural dynamics during binocular rivalry*, Phys. Rev. Lett., 102 (2009), p. 258701.

[109] D. V. Madison and R. A. Nicoll, *Control of the repetitive discharge of rat CA1 pyramidal neurones in vitro*, J. Physiol., 354 (1984), pp. 319–331.

[110] Y. L. Maistrenko, B. Lysyansky, C. Hauptmann, O. Burylko, and P. A. Tass, *Multistability in the Kuramoto model with synaptic plasticity*, Phys. Rev. E, 75 (2007), p. 066207.

[111] R. Malach, Y. Amir, M. Harel, and A. Grinvald, *Relationship between intrinsic connections and functional architecture revealed by optical imaging and in vivo targeted biocytin injections in primate striate cortex*, Proc. Natl. Acad. Sci. USA, 90 (1993), pp. 10469–73.

[112] H. Markram, *The blue brain project*, Nat. Rev. Neurosci., 7 (2006), pp. 153–60.

[113] H. Markram, Y. Wang, and M. Tsodyks, *Differential signaling via the same axon of neocortical pyramidal neurons.*, Proc. Natl. Acad. Sci. U S A, 95 (1998), pp. 5323–5328.

[114] L. Marshall, H. Helgadottir, M. Molle, and J. Born, *Boosting slow oscillations during sleep potentiates memory*, Nature, 444 (2006), pp. 610–613.

[115] M. Massimini, R. Huber, F. Ferrarelli, S. Hill, and G. Tononi, *The sleep slow oscillation as a traveling wave*, J. Neurosci., 24 (2004), pp. 6862–6870.

[116] V. Matveev and X. J. Wang, *Implications of all-or-none synaptic transmission and short-term depression beyond vesicle depletion: a computational study*, J. Neurosci., 20 (2000), pp. 1575–1588.

[117] D. A. McCormick and T. Bal, *Sleep and arousal: thalamocortical mechanisms*, Annu. Rev. Neurosci., 20 (1997), pp. 185–215.

[118] D. A. McCormick and D. Contreras, *On the cellular and network bases of epileptic seizures*, Annu. Rev. Physiol., 63 (2001), pp. 815–46.

[119] J. McNamara, *Cellular and molecular basis of epilepsy*, J. Neurosci., 14 (1994), pp. 3412–3425.

[120] M. R. Mehta, M. C. Quirk, and M. A. Wilson, *Experience–dependent asymmetric shape of hippocampal receptive fields*, Neuron, 25 (2000), pp. 707–15.

[121] O. Melamed, O. Barak, G. Silberberg, H. Markram, and M. Tsodyks, *Slow oscillations in neural networks with facilitating synapses*, J. Comput. Neurosci., 25 (2008), pp. 308–316.

[122] D. S. Melchitzky, S. R. Sesack, M. L. Pucak, and D. A. Lewis, *Synaptic targets of pyramidal neurons providing intrinsic horizontal connections in monkey prefrontal cortex*, J. Comp. Neurol., 390 (1998), pp. 211–24.

[123] C. D. Meliza and Y. Dan, *Receptive–field modification in rat visual cortex induced by paired visual stimulation and single–cell spiking*, Neuron, 49 (2006), pp. 183–9.

[124] R. S. Menon, S. Ogawa, J. P. Strupp, and K. Uğurbil, *Ocular dominance in human V1 demonstrated by functional magnetic resonance imaging*, J. Neurophysiol., 77 (1997), pp. 2780–7.

[125] E. K. Miller, C. A. Erickson, and R. Desimone, *Neural mechanisms of visual working memory in prefrontal cortex of the macaque*, J. Neurosci., 16 (1996), pp. 5154–67.

[126] J. Milton and P. Jung, *Epilepsy as a dynamic disease*, Springer, Berlin, 2003.

[127] J. G. Milton, P. H. Chu, and J. D. Cowan, *Spiral waves in integrate–and–fire neural networks*, in Advances in neural information processing systems, S. J. Hanson, J. D. Cowan, and C. L. Giles, eds., San Mateo, 1993, Morgan Kaufman, pp. 1001–1007.

[128] G. Mongillo, O. Barak, and M. Tsodyks, *Synaptic theory of working memory*, Science, 319 (2008), pp. 1543–1546.

[129] R. Moreno-Bote, J. Rinzel, and N. Rubin, *Noise–induced alternations in an attractor network model of perceptual bistability*, J. Neurophysiol., 98 (2007), pp. 1125–39.

[130] M. Murphy, B. A. Riedner, R. Huber, M. Massimini, F. Ferrarelli, and G. Tononi, *Source modeling sleep slow waves.*, Proc. Natl. Acad. Sci. USA, 106 (2009), pp. 1608–1613.

[131] F. Nadim and Y. Manor, *The role of short–term synaptic dynamics in motor control*, Curr. Opinion Neurobiol., 10 (2000), pp. 683–690.

[132] R. Osan, J. Rubin, and G. B. Ermentrout, *Regular traveling waves in a one dimensional network of theta neurons*, SIAM J. Appl. Math., 62 (2002), pp. 1197–1221.

[133] M. R. Owen, C. R. Laing, and S. Coombes, *Bumps and rings in a two-dimensional neural field: splitting and rotational instabilities*, New J. Phys., 9 (2007), p. 378.

[134] B. Pakkenberg, D. Pelvig, L. Marner, M. J. Bundgaard, H. J. G. Gundersen, J. R. Nyengaard, and L. Regeur, *Aging and the human neocortex*, Exp. Gerontol., 38 (2003), pp. 95–9.

[135] C. C. H. Petersen, A. Grinvald, and B. Sakmann, *Spatiotemporal dynamics of sensory responses in layer 2/3 of rat barrel cortex measured in vivo by voltage-sensitive dye imaging combined with whole-cell voltage recordings and neuron reconstructions*, J. Neurosci., 23 (2003), pp. 1298–1309.

[136] D. J. Pinto and G. B. Ermentrout, *Spatially structured activity in synaptically coupled neuronal networks: I. Traveling fronts and pulses*, SIAM J. Appl. Math., 62 (2001), pp. 206–225.

[137] ——, *Spatially structured activity in synaptically coupled neuronal networks: II. Lateral inhibition and standing pulses*, SIAM J. Appl. Math., 62 (2001), pp. 226–243.

[138] D. J. Pinto, R. K. Jackson, and C. E. Wayne, *Existence and stability of traveling pulses in a continuous neuronal network*, SIAM J. Appl. Dyn. Syst., 4 (2005), pp. 954–984.

[139] D. J. Pinto, S. L. Patrick, W. C. Huang, and B. W. Connors, *Initiation, propagation, and termination of epileptiform activity in rodent neocortex in vitro involve distinct mechanisms*, J. Neurosci., 25 (2005), pp. 8131–8140.

[140] J. C. Prechtl, L. B. Cohen, B. Pesaran, P. P. Mitra, and D. Kleinfeld, *Visual stimuli induce waves of electrical activity in turtle cortex*, Proc. Natl. Acad. Sci. USA, 94 (1997), pp. 7621–7626.

[141] K. A. Richardson, S. J. Schiff, and B. J. Gluckman, *Control of traveling waves in the mammalian cortex*, Phys. Rev. Lett., 94 (2005), p. 028103.

[142] P. R. Roelfsema, A. K. Engel, P. König, and W. Singer, *Visuomotor integration is associated with zero time-lag synchronization among cortical areas*, Nature, 385 (1997), pp. 157–61.

[143] J. Rubin, *A nonlocal eigenvalue problem for the stability of a traveling wave in a neuronal medium*, Disc. Cont. Dyn. Syst., 10 (2004), pp. 925–940.

[144] J. Rubin and A. Bose, *Localized activity patterns in excitatory neuronal networks*, Network, 15 (2004), pp. 133–158.

[145] D. Rubino, K. A. Robbins, and N. G. Hatsopoulos, *Propagating waves mediate information transfer in the motor cortex*, Nat. Neurosci., 9 (2006), pp. 1549–1557.

[146] M. V. Sanchez-Vives, V. F. Descalzo, R. Reig, N. A. Figueroa, A. Compte, and R. Gallego, *Rhythmic spontaneous activity in the piriform cortex.*, Cereb. Cortex, 18 (2008), pp. 1179–1192.

[147] M. V. Sanchez-Vives and D. A. McCormick, *Cellular and network mechanisms of rhythmic recurrent activity in neocortex.*, Nat. Neurosci., 3 (2000), pp. 1027–1034.

[148] S. J. Schiff, X. Huang, and J.-Y. Wu, *Dynamical evolution of spatiotemporal patterns in mammalian middle cortex*, Phys. Rev. Lett., 98 (2007), p. 178102.

[149] S. J. Schiff, T. Sauer, R. Kumar, and S. L. Weinstein, *Neuronal spatiotemporal pattern discrimination: The dynamical evolution of seizures*, Neuroimage, 28 (2005), pp. 1043–1055.

[150] N. E. Schoppa and N. N. Urban, *Dendritic processing within olfactory bulb circuits*, Trends Neurosci., 26 (2003), pp. 501–6.

[151] P. B. Sederberg, M. J. Kahana, M. W. Howard, E. J. Donner, and J. R. Madsen, *Theta and gamma oscillations during encoding predict subsequent recall*, J. Neurosci., 23 (2003), pp. 10809–14.

[152] H. S. Seung, *How the brain keeps the eyes still*, Proc. Natl. Acad. Sci. USA, 93 (1996), pp. 13339–44.

[153] G. M. Shepherd, *The synaptic organization of the brain*, Oxford University Press, Oxford, 5th ed ed., 2004.

[154] A. Shpiro, R. Curtu, J. Rinzel, and N. Rubin, *Dynamical characteristics common to neuronal competition models*, J. Neurophysiol., 97 (2007), pp. 462–73.

[155] V. Shusterman and W. C. Troy, *From baseline to epileptiform activity: a path to synchronized rhythmicity in large–scale neural networks*, Phys. Rev. E, 77 (2008), p. 061911.

[156] G. Silberberg and H. Markram, *Disynaptic inhibition between neocortical pyramidal cells mediated by martinotti cells*, Neuron, 53 (2007), pp. 735–746.

[157] L. C. Sincich and G. G. Blasdel, *Oriented axon projections in primary visual cortex of the monkey*, J. Neurosci., 21 (2001), pp. 4416–4426.

[158] W. Singer and C. M. Gray, *Visual feature integration and the temporal correlation hypothesis*, Annu. Rev. Neurosci., 18 (1995), pp. 555–86.

[159] S. Song, K. D. Miller, and L. F. Abbott, *Competitive Hebbian learning through spike–timing–dependent synaptic plasticity*, Nat. Neurosci., 3 (2000), pp. 919–26.

[160] M. Steriade, D. A. McCormick, and T. J. Sejnowski, *Thalamocortical oscillations in the sleeping and aroused brain*, Science, 262 (1993), pp. 679–685.

[161] C. F. Stevens and J. F. Wesseling, *Activity–dependent modulation of the rate at which synaptic vesicles become available to undergo exocytosis*, Neuron, 21 (1998), pp. 415–424.

[162] M. Stocker, M. Krause, and P. Pedarzani, *An apamin-sensitive* Ca^{2+}*–activated* K^+ *current in hippocampal pyramidal neurons*, Proc. Natl. Acad. Sci. USA, 96 (1999), pp. 4662–4667.

[163] S. Strogatz, *From Kuramoto to Crawford: Exploring the onset of synchronization in populations of coupled oscillators*, Physica D, 143 (2000), pp. 1–20.

[164] J. Tabak, W. Senn, M. J. O'Donovan, and J. Rinzel, *Modeling of spontaneous activity in developing spinal cord using activity–dependent depression in an excitatory network*, J. Neurosci., 20 (2000), pp. 3041–3056.

[165] A. L. Taylor, G. W. Cottrell, and W. B. Kristan, Jr, *Analysis of oscillations in a reciprocally inhibitory network with synaptic depression*, Neural Comput., 14 (2002), pp. 561–81.

[166] A. M. Thomson, J. Deuchars, and D. C. West, *Single axon excitatory postsynaptic potentials in neocortical interneurons exhibit pronounced paired pulse facilitation*, Neuroscience, 54 (1993), pp. 347–360.

[167] W. C. Troy, *Traveling waves and synchrony in an excitable large-scale neuronal network with asymmetric connections*, SIAM J. Appl. Dyn. Syst., 7 (2008), pp. 1247–1282.

[168] W. C. Troy and V. Shusterman, *Patterns and features of families of traveling waves in large-scale neuronal networks*, SIAM J. Appl. Dyn. Syst., 6 (2007), pp. 263–292.

[169] M. Tsodyks, K. Pawelzik, and H. Markram, *Neural networks with dynamic synapses*, Neural Comput., 10 (1998), pp. 821–835.

[170] M. V. Tsodyks and H. Markram, *The neural code between neocortical pyramidal neurons depends on neurotransmitter release probability*, Proc. Natl. Acad. Sci. USA, 94 (1997), pp. 719–723.

[171] T. Tzounopoulos, *Mechanisms of synaptic plasticity in the dorsal cochlear nucleus: Plasticity–induced changes that could underlie tinnitus*, Am. J. Audiol., 17 (2008), pp. S170–5.

[172] T. Tzounopoulos, Y. Kim, D. Oertel, and L. O. Trussell, *Cell–specific, spike timing–dependent plasticities in the dorsal cochlear nucleus*, Nat. Neurosci., 7 (2004), pp. 719–25.

[173] N. G. van Kampen, *Stochastic Processes in Physics and Chemistry*, North-Holland, 1982.

[174] J. A. Varela, K. Sen, J. Gibson, J. Fost, L. F. Abbott, and S. B. Nelson, *A quantitative description of short–term plasticity at excitatory synapses in layer 2/3 of rat primary visual cortex*, J. Neurosci., 17 (1997), pp. 7926–40.

[175] B. B. Vladimirski, J. Tabak, M. J. O'Donovan, and J. Rinzel, *Episodic activity in a heterogeneous excitatory network, from spiking neurons to mean field*, J. Comput. Neurosci., 25 (2008).

[176] X. J. Wang, *Calcium coding and adaptive temporal computation in cortical pyramidal neurons*, J. Neurophysiol., 79 (1998), pp. 1549–1566.

[177] ——, *Synaptic basis of cortical persistent activity: the importance of nmda receptors to working memory*, J. Neurosci., 19 (1999), pp. 9587–9603.

[178] H. R. Wilson, *Computational evidence for a rivalry hierarchy in vision*, Proc. Natl. Acad. Sci. USA, 100 (2003), pp. 14499–503.

[179] H. R. Wilson, R. Blake, and S. H. Lee, *Dynamics of travelling waves in visual perception*, Nature, 412 (2001), pp. 907–10.

[180] H. R. Wilson and J. D. Cowan, *Excitatory and inhibitory interactions in localized populations of model neurons*, Biophys. J., 12 (1972), pp. 1–24.

[181] ——, *A mathematical theory of the functional dynamics of cortical and thalamic nervous tissue*, Kybernetik, 13 (1973), pp. 55–80.

[182] J.-Y. Wu, *Propagating waves of activity in the neocortex: What they are, what they do*, Neuroscientist, 14 (2008), pp. 487–502.

[183] J.-Y. Wu, L. Guan, and Y. Tsau, *Propagating activation during oscillations and evoked responses in neocortical slices*, J. Neurosci., 19 (1999), pp. 5005–5015.

[184] W. Xu, X. Huang, K. Takagaki, and J.-Y. Wu, *Compression and reflection of visually evoked cortical waves*, Neuron, 55 (2007), pp. 119–129.

[185] L. C. York and M. C. W. van Rossum, *Recurrent networks with short term synaptic depression*, J. Comput. Neurosci., 27 (2009), pp. 607–20.

[186] T. Yoshioka, G. G. Blasdel, J. B. Levitt, and J. S. Lund, *Relation between patterns of intrinsic lateral connectivity, ocular dominance, and cytochrome oxidase-reactive regions in macaque monkey striate cortex*, Cereb. Cortex, 6 (1996), pp. 297–310.

[187] L. Zhang, *Existence, uniqueness, and exponential stability of traveling wave solutions of some integral differential equations arising from neuronal networks*, Differential Integral Equations, 16 (2003), pp. 513–536.

[188] ——, *Existence, uniqueness and exponential stability of traveling wave solutions of some integral differential equations arising from neuronal networks*, J. Diff. Eqns, 197 (2004), pp. 162–196.

[189] R. S. Zucker and W. G. Regehr, *Short–term synaptic plasticity*, Annu. Rev. Physiol., 64 (2002), pp. 355–405.